

**PASSIVE REALIZATIONS OF SERIES ELASTIC ACTUATION:  
EFFECTS OF PLANT AND CONTROLLER DYNAMICS ON  
PERFORMANCE AND PASSIVITY OF HAPTIC RENDERING**

by  
CELAL UMUT KENANOĞLU

Submitted to the Graduate School of Engineering and Natural Sciences  
in partial fulfillment of  
the requirements for the degree of  
Master of Science

SABANCI UNIVERSITY  
July, 2022

**PASSIVE REALIZATIONS OF SERIES ELASTIC ACTUATION:  
EFFECTS OF PLANT AND CONTROLLER DYNAMICS ON  
PERFORMANCE AND PASSIVITY OF HAPTIC RENDERING**

Approved by:

Prof. Dr. Volkan Patoğlu .....  
(Thesis Supervisor)

Prof. Dr. Çağatay Başdoğan .....

Asst. Prof. Dr. Melih Türkseven .....

Date of Approval: July 22, 2022

CELAL UMUT KENANOGLU 2022 ©

All Rights Reserved

## ABSTRACT

### PASSIVE REALIZATIONS OF SERIES ELASTIC ACTUATION: EFFECTS OF PLANT AND CONTROLLER DYNAMICS ON PERFORMANCE AND PASSIVITY OF HAPTIC RENDERING

CELAL UMUT KENANOĞLU

Mechatronics Engineering M.Sc. Thesis, 2022

Thesis Supervisor: Prof. Dr. Volkan Patoğlu

**Keywords:** Physical human-robot interaction, interaction control, haptic rendering, series (damped) elastic actuation, velocity sourced impedance control, model reference force control, network synthesis, physical realizations, coupled stability and effective impedance analysis.

Safe and natural physical human-robot interactions (pHRI) require precise control of the impedance behaviour of the robot at the interaction port. Series elastic actuation (SEA) is a commonly used interaction control paradigm for pHRI, as it can provide interactions with excellent stability robustness and high rendering fidelity. Series elastic actuation relies on a compliant element placed between the actuator and the interaction port and the utilization of the model of this compliant element to implement closed-loop force control. The compliant element relaxes the strict stability bounds on the controller gains induced due to non-collocation and bandwidth limitations and provides excellent stability robustness for interaction control.

Series damped elastic actuation (SDEA) extends SEA by introducing a viscous dissipation element parallel to the series elastic element. SDEA can, not only help increase the force control bandwidth of SEA but also provide additional advantages, in terms of improving energy efficiency, reducing undesired oscillations, and alleviating the need for D-control terms.

Velocity sourced impedance control (VSIC) is the most commonly used force control architecture for S(D)EA, as its cascaded control architecture with a robust inner motion control loop can effectively eliminate parasitic forces, leading to good rendering performance. Model reference force control (MRFC) is an alternative approach that promises to improve interaction control performance compared to VSIC, as the knowledge of the plant model enables feedforward action to react to inputs more quickly.



In this thesis, we establish the necessary and sufficient conditions for frequency domain passivity of series (damped) elastic actuation (S(D)EA) while rendering null impedance, ideal springs, and Voigt model under VSIC. Furthermore, we rigorously study the effect of omitting the damping force induced on the serial compliant element in closed-loop control and provide the necessary and sufficient conditions for the passivity of interaction when only the deflections of the serial elastic element is used to estimate the interaction forces. This model captures a common implementations of SEA, where the inherent damping effects on the serial elastic element is ignored.

We introduce passive physical equivalents for S(D)EAs under closed-loop control to help establish an intuitive understanding of the passivity bounds and to highlight the effect of different plant parameters and controller terms on the closed-loop performance of the system. Through the passive physical equivalents, we rigorously compare the effect of different plants dynamics (e.g., SEA and SDEA) and different cascaded controller architectures (e.g., P-P and P-PI) on the system performance. Moreover, we show that passive physical equivalents establish a natural means for effective impedance analysis.

Furthermore, we compare the effect of measuring and omitting the damping force of the series elastic element on the closed-loop rendering performance of the system. We also study a reduce order model for the implementation where the damping force of the series elastic element is omitted, by replacing the robust inner motion control loop by a low-pass filter. We establish passivity conditions and physical equivalents for this reduce order model and compare the results with the full-order model to study the effects of this simplifying assumption on the stability and rendering performance of the system.

We further extend our study to alternative control algorithms, such as model reference force control (MRFC). We present sufficient conditions for passivity of S(D)EA under MRFC during null impedance and ideal spring rendering. We prove that over-estimation of robot inertia and underestimation of the stiffness of the series elastic element can ensure coupled stability of interaction for SEA under MRFC during null impedance rendering, as long as a lower limit on damping compensation is not violated.

We demonstrate the validity of passivity conditions and the performance of haptic rendering through systematic simulation studies, as well as comprehensive set of physical experiments where we experimentally verify the passivity bounds and demonstrate the impedance rendering performance under different plant dynamics and different controller architectures.

## ÖZET

### SERİ ELASTİK EYLEME İÇİN PASİF GERÇEKLEŞTİRİLMELER: KONTROLCÜ VE SİSTEM DİNAMİĞİNİN HAPTİK GERİ-BESLEMENİN PASİFLİĞİNE VE PERFORMANSINA ETKİLERİ

CELAL UMUT KENANOĞLU

Mekatronik Mühendisliği Yüksek Lisans Tezi, 2022

Tez Danışmanı: Prof. Dr. Volkan Patoğlu

Anahtar Kelimeler: Fiziksel insan-robot etkileşimi, etkileşim kontrolü, haptik geri-besleme, seri (viskoelastik) elastik eyleme, hız kaynaklı empedans kontrolü, model referans kuvvet kontrolü, devre sentezi, fiziksel gerçekleştirme, bağlaşıklık kararlılık, ve etkin empedans analizi

Güvenli ve doğal fiziksel insan-robot etkileşimleri (fİRE), etkileşim noktasında robotun empedans davranışının hassas kontrolünü gerektirir. Seri elastik eyleme (SEE), yüksek stabilite gürbüzlüğü ve hassas geri-besleme doğruluğu ile etkileşimler sağlayabildiğinden, fİRE için yaygın olarak kullanılan bir etkileşim kontrol yaklaşımıdır. Seri elastik eyleme, eyleyici ile etkileşim noktası arasına yerleştirilen esnek bir elemana ve bu esnek elemanın modelinin kapalı çevrim kuvvet kontrolü için kullanılmasına dayanır. Esnek eleman, eyleyici ile sensor arasındaki dinamikler ve bant genişliği sınırlamaları nedeniyle ortaya çıkan kontrolcü kazançlarındaki sıkı kararlılık sınırlarını gevşetir ve etkileşim kontrolü için yüksek kararlılık gürbüzlüğü sağlar.

Seri viskoelastik eyleme (SVE), SEE'nin seri elastik elemanına paralel bir viskoz sönümlenme elemanı eklenerek genellenmiş halidir. SVE, yalnızca SEE'nin düşük olan kuvvet kontrol bant genişliğini arttırmaya yardımcı olmakla kalmaz, aynı zamanda enerji verimliliğini arttırma, istenmeyen salınımları azaltma ve kontrolcüde türev terimlerine olan ihtiyacı azaltma açılarından da ek avantajlar sağlayabilir.

Hız kaynaklı empedans kontrolü (HKEK), SEE/SVE için en yaygın olarak kullanılan kuvvet kontrol mimarisidir. Gürbüz bir iç hareket kontrol çevrimine sahip olan bu kademeli kontrol mimarisi bozucu kuvvetleri etkin bir şekilde ortadan kaldırarak yüksek geri-besleme performansı sağlar. Model referans kuvvet kontrolü (MRKK), sistem modelinin bilgisi sayesinde girdilere daha hızlı tepki verebildiğinden, HKEK'ye kıyasla etkileşim kontrol performansını iyileştirmeyi vaat eden alternatif bir kontrol yaklaşımıdır.

Bu tezde, seri (viskoelastik) elastik eyleme (SEE/SVE) HKEK ile sıfır empedans, sanal yay ve Voigt modeli geri-beslemesi sırasında kapalı döngü sistemin frekans bölgesi pasifliği için gerekli ve yeterli koşulları sunuyoruz. Ayrıca, kapalı çevrim kontrolde seri elastik eleman üzerinde oluşan sönümlleme kuvvetinin ihmal edilmesinin etkisini titizlikle inceleyip etkileşim kuvvetini tahmin etmek için sadece seri elastik elemanın kullanıldığı durumdaki sistemin etkileşimin pasifliği için gerekli ve yeterli koşulları sağlıyoruz. Bu model, seri elastik eleman üzerindeki doğal sönümlleme etkilerinin göz ardı edildiği genel kullanımdaki duruma denk gelmektedir.

Pasiflik sınırlarının anlaşılmasına yardımcı olmak ve farklı sistem parametrelerinin ve kontrol kazançlarının sistemin performansı üzerindeki etkilerini incelemek için kapalı çevrim kontrolü altındaki SEE/SVE'lerin pasif fiziksel gerçekleştirmelerini sunuyoruz. Pasif fiziksel gerçekleştirmeler aracılığıyla, farklı sistem dinamiklerinin (örneğin, SEE ve SVE) ve farklı kademeli kontrol mimarilerinin (örneğin, P-P ve P-PI kontrolcüler) sistem performansı üzerindeki etkilerini karşılaştırıyoruz. Ayrıca, pasif fiziksel gerçekleştirmelerin etkin empedans analizini kapsadığını gösteriyoruz.

Ayrıca, seri elastik elemandaki sönümlleme kuvvetinin ölçülmesinin veya bu kuvvetin ihmal edilmesinin sistemin kapalı çevrim geri-besleme performansı üzerindeki etkilerini karşılaştırıyoruz. Gürbüz iç hareket kontrol çevrimini bir alçak geçiren filtre ile modelleyerek, seri elastik elemanın sönümlleme kuvvetinin ihmal edildiği uygulama için derecesi azaltılmış bir model öneriyoruz. Bu varsayımın sistemin kararlılığı ve geri-beslemesi performansı üzerindeki etkilerini incelemek için bu derecesi azaltılmış model için pasiflik koşullarını ve fiziksel gerçekleştirmelerini türetiyoruz ve sonuçları tam dereceli modelle karşılaştırıyoruz.

Sonuçlarımızı, model referans kuvvet kontrolü (MRKK) gibi alternatif kontrol algoritmalarına için genişletiyoruz. MRKK altında SEE/SVE'nin sıfır empedans ve ideal yay geri-beslemesi sırasında pasifliği için yeterli koşulları sunuyoruz. Robot eylemsizliğinin fazla tahmin edilmesinin ve seri elastik elemanın sertliğinin olduğundan az tahmin edilmesinin, sönümlleme telafisinde bir alt limit ihlal edilmediği sürece, sıfır empedans geri-beslemesi sırasında MRKK altında SEE için etkileşimin bağlaşıklık kararlılığını garantiyeabileceğini kanıtıyoruz.

Pasiflik koşullarının geçerliliğini ve haptik geri-besleme performansını sistematik simülasyon çalışmalar ile deneysel olarak doğruluyor, farklı sistem dinamikleri ve farklı denetleyici mimarileri altında empedans geri-besleme performansını kapsamlı fiziksel deneyler aracılığıyla gösteriyoruz.

## ACKNOWLEDGEMENTS

Before my master's journey, I was feeling stuck and I was hoping to meet a good role model. I am blessed to have Prof. Dr. Volkan Patoğlu as a role model for my academic journey and career. His curiosity and passion for research, kindness, support, never-ending ideas, and work ethic have inspired me to be a good researcher. This thesis is truly the result of a collaboration lead by him. Not only on the research side, but I have also learned how to communicate with students and how to be a good academician from him which I will use throughout my academic journey. I will set up my expectations and standards like him rest of my life.

For this thesis, I would like to thank my jury members: Prof. Dr. Çağatay Başdoğan and Asst. Prof. Dr. Melih Türkseven for their time, interest, and valuable feedback during my thesis defense.

I have many thanks to past and present HMI lab members for their help, kindness, valuable time, and friendship: Ali Khalilian Motamed Bonab, Ali Yaşar, Alperen Kenan, Batuhan Toker, Bilal Çatkın, Cansu Öztürk, Çağatay Irmak, Deniz Ece Susuz, Harun Tolasa, Melike Cezayirlioğlu, Ömer Burak Aladağ, Özgür Taylan Kenanoğlu, and Uğur Mengilli. I also want to thank Can Önal, Mehmet Emin Mumcu, Mirvahid Mohammadpour Chehrghani, Selim Ahmet İz, Sila Akpınar, and Ömer Kemal Adak for memorable moments, friendship, and enjoyable discussions. I am lucky to meet Alperen Kenan, Çağatay Irmak, Deniz Ece Susuz, Harun Tolasa, Melike Cezayirlioğlu, Selim Ahmet İz, and Ömer Burak Aladağ. We have a lot of enjoyable activities and discussions, and they made the second year of my master's life easier and better. I want to thank Bilal Çatkın, who started master journey with me, for reliable and good friendship, and I think we walked around campus about 500 times together and we had a valuable discussions about life for each of them. I feel glad to meet with Sila Akpınar. I want to thank her for sharing valuable moments, having endless-fun conversations, motivating and reminding me for tasks when I felt bored (eg. you need to take test!), unexpected jokes (even bad ones), and the sincerest friendship. I have no doubt that she will achieve more than she ever imagined in all respects of life. Lastly, I want to thank my life-long friend (or cousin) Özgür Taylan Kenanoğlu. Growing with you is one of the luck in my life, and I have added to this luck to share same lab environment with you. You have always been a reliable and enjoyable friend to me, and I have many thanks for having made my life easier and more fun at Sabancı University and İstanbul. You have always inspired and honored me and I believe that you will maintain them.

I want to thank my friends from high-school and bachelor's: Biling Şen Erding, Canberk Önem, Emre Erğen, Erdem Kaya, Hacer Esra Çakmak, İlhan Berke Ağan, Kübra Ünlü, Meriç Büyükkoyuncu, Nilay Çınar, Olcay Uzel, Şahin Ersan, and Usay Uzunkaya. They make my life meaningful, easier, and enjoyable. I always feel their support and I always know we will do whatever we can for each other. I have a special thanks to Hacer Esra Çakmak because she has always been my biggest support from beginning to end of that journey. She has always been very kind, supportive, patient, and adoring in that journey.

The continuous, forever, and limitless thanks go to my family, my father Osman Nahit Kenanoğlu, my mother Nadire Kenanoğlu, and my big brother Asım Çağrı Kenanoğlu. I always feel their love and endless support. I feel extremely lucky to have them. All my successes until now and future are thanks to them. I want to thank them from the bottom of my heart. Also, I want to thank to all my relatives for their love and support over the years.

This work has been partially supported under TÜBİTAK Grant 216M200.

*To my beloved family*

# TABLE OF CONTENTS

<b>LIST OF TABLES .....</b>	<b>xv</b>
<b>LIST OF FIGURES .....</b>	<b>xvi</b>
<b>1. Introduction .....</b>	<b>1</b>
1.1. Motivation .....	1
1.2. Contributions .....	5
1.3. Outline .....	7
<b>2. Literature Review .....</b>	<b>8</b>
2.1. Frequency Domain Passivity of SEA .....	8
2.2. Frequency Domain Passivity of SDEA .....	9
2.3. Realization of Passive Physical Equivalents .....	10
2.4. Rendering Performance .....	11
2.5. Model Reference Force Control .....	12
<b>3. Preliminaries .....</b>	<b>13</b>
3.1. Passivity Theorems .....	15
3.2. Passive Physical Equivalents .....	16
3.2.1. An example of derivation of passive physical equivalents and effective impedance analysis .....	17
<b>4. Passivity Analysis and Passive Physical Equivalents of SEA .....</b>	<b>19</b>
4.1. Ideal Spring Rendering .....	19
4.1.1. Passive Physical Equivalent .....	20
4.1.2. Feasibility of Passive Realization vs Passivity .....	21
4.1.3. Haptic Rendering Performance .....	21
4.1.4. Effective Impedance Analysis .....	22
4.2. Null Impedance Rendering When Controllers are P-P .....	23
4.2.1. Passive Physical Equivalent .....	24
4.2.2. Feasibility of Passive Realization vs Passivity .....	24

4.2.3.	Haptic Rendering Performance.....	24
4.2.4.	Effective Impedance Analysis .....	25
4.3.	Null Impedance Rendering When Controllers are P-PI.....	25
4.3.1.	Passive Physical Equivalent .....	26
4.3.2.	Feasibility of Passive Realization vs Passivity.....	27
4.3.3.	Haptic Rendering Performance.....	28
4.3.4.	Effective Impedance Analysis .....	28
4.4.	Discussion.....	29
<b>5.</b>	<b>Passivity Analysis and Passive Physical Equivalents of SDEA ....</b>	<b>31</b>
5.1.	Voigt Model Rendering .....	31
5.1.1.	Passive Physical Equivalent .....	33
5.1.2.	Feasibility of Passive Realization vs Passivity.....	34
5.1.3.	Haptic Rendering Performance.....	34
5.1.4.	Effective Impedance Analysis .....	35
5.2.	Ideal Spring Rendering .....	37
5.2.1.	Passive Physical Equivalent: .....	38
5.2.2.	Feasibility of Passive Realization vs Passivity.....	39
5.2.3.	Haptic Rendering Performance.....	40
5.2.4.	Effective Impedance Analysis .....	40
5.3.	Null Impedance Rendering.....	42
5.3.1.	Passive Physical Equivalent: .....	43
5.3.2.	Feasibility of Passive Realization vs Passivity.....	43
5.3.3.	Haptic Rendering Performance.....	43
5.3.4.	Effective Impedance Analysis .....	44
5.4.	Discussion.....	45
<b>6.</b>	<b>Passivity Analysis and Passive Physical Equivalents of SDEA<sub>K<sub>fb</sub></sub> .</b>	<b>47</b>
6.1.	Voigt Model Rendering .....	47
6.1.1.	Passive Physical Equivalent .....	49
6.1.2.	Haptic Rendering Performance.....	50
6.1.3.	Effective Impedance Analysis .....	50
6.1.4.	Comparison of Passivity Bounds of SDEA <sub>K<sub>fb</sub></sub> with SDEA ....	51
6.2.	Ideal Spring Rendering .....	53
6.2.1.	Passive Physical Equivalent: .....	54
6.2.2.	Haptic Rendering Performance.....	54
6.2.3.	Effective Impedance Analysis .....	55
6.3.	Null Impedance Rendering.....	56
6.3.1.	Passive Physical Equivalent: .....	57
6.3.2.	Feasibility of Passive Realization vs Passivity.....	58



6.3.3.	Haptic Rendering Performance.....	58
6.3.4.	Effective Impedance Analysis .....	58
6.4.	Discussion.....	60
<b>7.</b>	<b>Passivity Analysis and Passive Physical Equivalents of Reduce Order Model of Different Implementations of SEA.....</b>	<b>62</b>
7.1.	Reduce Order Model for $SDEA_{K_{fb}}$ .....	63
7.1.1.	Voigt Model Rendering.....	63
7.1.1.1.	Passive Physical Equivalent .....	64
7.1.1.2.	Haptic Rendering Performance .....	65
7.1.1.3.	Effective Impedance Analysis .....	66
7.1.1.4.	Comparison of Passivity Bounds of $SDEA_{K_{fb}}$ vs $SDEA_{K_{red}}$ .....	66
7.1.2.	Ideal Spring Rendering.....	68
7.1.2.1.	Passive Physical Equivalent:.....	69
7.1.2.2.	Haptic Rendering Performance .....	69
7.1.2.3.	Effective Impedance Analysis .....	70
7.1.3.	Null Impedance Rendering .....	71
7.1.3.1.	Passive Physical Equivalent .....	72
7.1.3.2.	Haptic Rendering Performance .....	72
7.1.3.3.	Effective Impedance Analysis .....	73
7.2.	Reduce Order Model for $SDEA$ .....	74
7.2.1.	Voigt Model Rendering.....	74
7.2.1.1.	Passive Physical Equivalent .....	75
7.2.1.2.	Comparison of Passivity Bounds of $SDEA_{K_{red}}$ with $SDEA$ .....	76
7.3.	Reduce Order Model for $SEA$ .....	78
7.3.1.	Ideal Spring Rendering.....	78
7.3.1.1.	Passive Physical Equivalent .....	79
7.3.1.2.	Comparison of Passivity Bounds of $SEA_{red}$ with $SEA$ .....	79
7.4.	Discussion.....	80
<b>8.</b>	<b>Haptic Rendering Performance.....</b>	<b>82</b>
8.1.	Effects of Controller Gains on Null Impedance Rendering Performance .....	86
8.1.1.	Effects of Controller Gains on Ideal Spring Rendering Performance .....	88
8.1.2.	Effects of Physical Plant and Filter Parameters on Null Impedance Rendering Performance .....	91
8.1.3.	Effects of Physical Plant and Filter Parameters on Ideal Spring Rendering Performance .....	92

8.1.4.	Rendering Performance Comparison of SEA vs SDEA.....	95
8.1.5.	Comparison of Loss Factor for SEA and SDEA.....	97
8.1.6.	Voigt Model Rendering Performance of SDEA.....	98
8.1.7.	Physical Filter Damping Effect for SDEA .....	99
8.1.8.	Physical Filter Damping Effect for SDEA <sub>K<sub>fb</sub></sub> .....	100
8.1.9.	Performance Comparison of SDEA, SDEA <sub>K<sub>fb</sub></sub> , SDEA <sub>K<sub>red</sub></sub> , and SEA .....	101
8.1.10.	Maximum Renderable Virtual Stiffness Comparison for SDEA, SDEA <sub>K<sub>fb</sub></sub> , and SDEA <sub>K<sub>red</sub></sub> .....	105
<b>9.</b>	<b>Experimental Evaluations .....</b>	<b>108</b>
9.1.	Experimental Setup.....	108
9.2.	System Identification .....	111
9.2.1.	Torque Controller Tuning .....	114
9.3.	Series Elastic Actuation .....	116
9.3.1.	Impedance Rendering Performance .....	116
9.3.1.1.	Null Impedance Rendering .....	116
9.3.1.2.	Spring Rendering .....	117
9.3.2.	Verification of Passivity Bounds .....	121
9.3.2.1.	Null Impedance Rendering .....	121
9.3.2.2.	Spring Rendering Rendering .....	122
9.4.	Series Damped Elastic Actuation .....	124
9.4.1.	Impedance Rendering Performance .....	124
9.4.1.1.	Null Impedance Rendering .....	124
9.4.1.2.	Spring Rendering .....	125
9.4.1.3.	Voigt Model Rendering .....	129
9.4.2.	Verification of Passivity Bounds .....	131
9.4.2.1.	Voigt Model Rendering .....	131
9.4.2.2.	Spring Rendering .....	132
9.5.	Series Elastic Actuation with Omitted Damping Effect .....	134
9.5.1.	Impedance Rendering Performance .....	134
9.5.1.1.	Null Impedance Rendering .....	134
9.5.1.2.	Spring Rendering .....	135
9.5.1.3.	Voigt Model Rendering .....	139
9.5.2.	Verification of Passivity Bounds .....	141
9.5.2.1.	Voigt Model Rendering .....	141
9.5.2.2.	Spring Rendering .....	142
<b>10.</b>	<b>Model Reference Force Control .....</b>	<b>144</b>
10.1.	System Description .....	144

10.2. Passivity Analysis .....	146
10.3. Numerical Evaluations .....	151
10.4. Experimental Validations .....	153
10.4.1. System Identification .....	153
10.4.2. Experimental Validation of Passivity Limits .....	153
10.4.3. Experimental Evaluation of Performance of MRFC .....	155
<b>11. Conclusion and Future Work .....</b>	<b>156</b>
<b>BIBLIOGRAPHY .....</b>	<b>159</b>

# LIST OF TABLES

Table 8.1. Comparison of Physical Realizations of S(D)EA under VSIC...	83
Table 8.2. Parameters of the S(D)EA plant .....	84
Table 8.3. Numerical values for the inerter and damping terms of the passive physical equivalents for SEA and SDEA for various controller gains $G_m$ , $G_t$ , $I_m$ , and $K_d$ . (Inerter is in $kg\,m^2$ and damper is in $Nm\,\frac{s}{rad}$ .) .....	84
Table 8.4. Numerical values for serial-inerter damper element for various values of $G_t$ , $G_m$ , $I_m$ , and $K_d$ for SEA during null impedance render- ing when controllers are PI-P and for SDEA during spring rendering when controllers are P-P. ....	96
Table 8.5. Numerical values for the inerter and damping terms of the passive physical equivalents for SDEA during Voigt model rendering for various controller gains $G_m$ , $G_t$ , $K_d$ , and $B_d$ . (Inerter is in $kg\,m^2$ and damper is in $Nm\,\frac{s}{rad}$ .) .....	99
Table 8.6. Physical parameters of 3 different systems .....	106
Table 9.1. Experimentally characterized system parameters for the SEA brake pedal .....	114
Table 10.1. Parameters for SEA under MRFC .....	151
Table 10.2. Experimentally characterized system parameters for the SEA brake pedal .....	153

# LIST OF FIGURES

Figure 3.1. Schematic representation of SDEA (SEA if $B_f = 0$ ) .....	13
Figure 3.2. Block diagram of S(D)EA under VSIC .....	14
Figure 3.3. Block diagram of SDEA $_{K_{fb}}$ under VSIC, for which interaction forces are estimated by only utilizing the deflections of the physical spring .....	14
Figure 3.4. Relationship between mechanical and electrical networks .....	16
Figure 3.5. Step 1 of realization .....	17
Figure 3.6. Step 2 of realization .....	18
Figure 3.7. Step 3 of realization .....	18
Figure 4.1. Passive physical equivalent of SEA under VSIC during spring rendering when the motion and force controllers are taken as P con- trollers .....	21
Figure 4.2. Passive physical equivalent of SEA under VSIC during null impedance rendering when both controllers are P .....	24
Figure 4.3. Passive physical equivalent of SEA under VSIC during null impedance rendering when the motion controller is PI and the force controller is P .....	27
Figure 4.4. Alternative passive physical equivalents of SEA under VSIC during null impedance rendering when the force controller is P and the motion controller is PI .....	29
Figure 4.5. Passive physical equivalent of SEA under VSIC during null impedance rendering when both controllers are PI .....	30
Figure 5.1. Passive physical equivalent of SDEA under VSIC during Voigt model rendering when both controllers are P .....	33
Figure 5.2. Realization of SDEA under VSIC during spring rendering when controllers are P .....	39
Figure 5.3. Realization of SDEA under VSIC during null impedance ren- dering when both controllers are P .....	43

Figure 5.4. Alternative passive physical equivalents of SDEA under VSIC during spring rendering when both controllers are P .....	45
Figure 5.5. Passive physical equivalent of SDEA under VSIC during null impedance rendering when both controllers are PI .....	46
Figure 6.1. Passive physical equivalent of $SDEA_{K_{fb}}$ under VSIC during Voigt model rendering .....	49
Figure 6.2. Passive physical equivalent of $SDEA_{K_{fb}}$ under VSIC during ideal spring rendering .....	55
Figure 6.3. Passive physical equivalent of $SDEA_{K_{fb}}$ under VSIC during null impedance rendering .....	57
Figure 6.4. Alternative passive physical equivalents of $SDEA_{K_{fb}}$ .....	60
Figure 7.1. Block diagram of impedance control with reduce order model $SDEA_{K_{red}}$ , for which the interaction forces are estimated by only utilizing the deflections of the physical spring .....	62
Figure 7.2. Passive physical equivalent of $SDEA_{K_{red}}$ under VSIC during Voigt model rendering .....	65
Figure 7.3. Passive physical equivalent of $SDEA_{K_{red}}$ under VSIC during spring rendering rendering .....	69
Figure 7.4. Passive physical equivalent of $SDEA_{K_{red}}$ under VSIC during null impedance rendering rendering .....	72
Figure 7.5. Block diagram of impedance control with reduce order model S(D)EA .....	74
Figure 7.6. Passive physical equivalent of $SDEA_{red}$ under VSIC during Voigt model rendering .....	76
Figure 7.7. Passive physical equivalent of $SEA_{red}$ under VSIC during ideal spring rendering .....	79
Figure 7.8. Alternative passive physical equivalents of $SDEA_{K_{red}}$ .....	80
Figure 8.1. Effect of $G_t$ and $G_m$ on null impedance rendering performance of SEA when both controllers are P .....	86
Figure 8.2. Effect of $G_t$ , $G_m$ , and $I_m$ on null impedance rendering performance for SEA when the force controller is P and the motion controller is PI .....	87
Figure 8.3. Effect of $G_t$ and $G_m$ on null impedance rendering performance of SDEA when both controllers are P .....	88
Figure 8.4. Effect of $G_t$ , $G_m$ , and $K_d$ on the spring rendering performance of SEA during when both controllers are P .....	89

Figure 8.5. Effect of $G_t$ , $G_m$ , and $K_d$ on the spring rendering performance of SDEA during when both controllers are P .....	90
Figure 8.6. Effect of plant parameters $J_m$ and $B_m$ on performance for SEA and SDEA during null impedance rendering when both controllers are P .....	92
Figure 8.7. Effect of physical filter parameters $K$ - $B_f$ on performance for SEA and SDEA during null impedance rendering when both controllers are P .....	93
Figure 8.8. Effect of plant parameters $J_m$ and $B_m$ on performance for SEA and SDEA during ideal spring rendering when both controllers are P .....	94
Figure 8.9. Effect of physical filter parameters $K$ - $B_f$ on performance for SEA and SDEA during ideal spring rendering when both controllers are P .....	95
Figure 8.10. Rendering performance comparison between SEA and SDEA ..	96
Figure 8.11. Loss Factor of SEA vs SDEA .....	97
Figure 8.12. Effect of $G_t$ , $G_m$ , $K_d$ , and $B_d$ on the voigt model rendering performance of SDEA during when both controllers are P .....	98
Figure 8.13. Effect of physical parameters $B_f$ on performance SDEA during Voigt model rendering, spring rendering, and null impedance rendering	100
Figure 8.14. Effect of unmeasured physical parameters $B_f$ on performance SDEA $_{K_{fb}}$ during Voigt model rendering, spring rendering, and null impedance rendering .....	101
Figure 8.15. Performance comparison of SDEA, SDEA $_{K_{fb}}$ , SDEA $_{K_{red}}$ , and SEA .....	102
Figure 8.16. Effective damping and spring plots of SDEA and SDEA $_{K_{fb}}$ for Voigt model .....	103
Figure 8.17. Effective impedance comparison for SDEA, SDEA $_{K_{fb}}$ , and SEA for spring rendering .....	104
Figure 8.18. Effective impedance comparison for SDEA, SDEA $_{K_{fb}}$ , and SEA for null impedance rendering .....	105
Figure 8.19. Performance comparison of SDEA, SDEA $_{K_{fb}}$ , SDEA $_{K_{red}}$ for spring rendering for 3 different parameters set .....	107
Figure 9.1. Components of experimental setup .....	110
Figure 9.2. Closed loop motion controlled system .....	111
Figure 9.3. Bode plot of inner loop .....	112
Figure 9.4. Identification of stiffness of physical filter .....	113
Figure 9.5. Details of arrangement of magnet .....	113
Figure 9.6. Damping identification .....	114
Figure 9.7. Measured torque vs desired torque .....	115

Figure 9.8. Chip test for 3 different $G_t$ .....	116
Figure 9.9. Null impedance rendering performance when interacting with human .....	117
Figure 9.10. Rendering two virtual stiffness experimentally when $G_t = 25$ rad/sNm .....	118
Figure 9.11. Rendering two virtual stiffness experimentally when $G_t = 30$ rad/sNm .....	118
Figure 9.12. When human interacting with the SEA brake pedal when $K_d =$ 50 Nm/rad .....	119
Figure 9.13. When human interacting with the SEA brake pedal when $K_d =$ 100 Nm/rad .....	120
Figure 9.14. When human interacting with the SEA brake pedal when $K_d =$ 50 Nm/rad with $G_t = 30$ rad/sNm .....	120
Figure 9.15. $G_t$ - $I_m$ plot for experimentally coupled stability for null impedance rendering .....	122
Figure 9.16. $G_t$ - $K_{vir}$ plot for experimentally coupled stability for spring rendering .....	123
Figure 9.17. Chip test for 3 different $G_t$ for SDEA .....	124
Figure 9.18. Null impedance rendering performance when interacting with human for SDEA .....	125
Figure 9.19. Rendering two virtual stiffness experimentally when $G_t = 25$ rad/sNm for SDEA .....	126
Figure 9.20. Rendering two virtual stiffness experimentally when $G_t = 30$ rad/sNm .....	126
Figure 9.21. When human interacting with the SDEA brake pedal when $K_d = 50$ Nm/rad .....	127
Figure 9.22. When human interacting with the SDEA brake pedal when $K_d = 100$ Nm/rad .....	128
Figure 9.23. When human interacting with the SDEA brake pedal when $K_d = 50$ Nm/rad with $G_t = 30$ rad/sNm for SDEA .....	128
Figure 9.24. When human interacting with the SDEA brake pedal when $K_d = 100$ Nm/rad and $B_d = 0.01$ Nms/rad .....	129
Figure 9.25. When human interacting with the SDEA brake pedal when $K_d = 100$ Nm/rad and $B_d = 0.01$ Nms/rad with $G_t = 30$ rad/sNm ...	130
Figure 9.26. When human interacting with the SDEA brake pedal when $K_d = 100$ Nm/rad and $B_d = 0.05$ Nms/rad with $G_t = 30$ rad/sNm ...	130
Figure 9.27. $B_d$ - $K_{vir}$ plot for experimentally coupled stability for spring rendering for SDEA .....	131



Figure 9.28. $G_t$ - $K_{vir}$ plot for experimentally coupled stability for spring rendering for SDEA .....	132
Figure 9.29. Chip test for 3 different $G_t$ for SDEA $_{Kfb}$ .....	134
Figure 9.30. Null impedance rendering performance when interacting with human for SDEA $_{Kfb}$ .....	135
Figure 9.31. Rendering two virtual stiffness experimentally when $G_t = 25$ rad/sNm for SDEA $_{Kfb}$ .....	136
Figure 9.32. Rendering two virtual stiffness experimentally when $G_t = 30$ rad/sNm for SDEA $_{Kfb}$ .....	136
Figure 9.33. When human interacting with the SDEA $_{Kfb}$ brake pedal when $K_d = 50$ Nm/rad for SDEA $_{Kfb}$ .....	137
Figure 9.34. When human interacting with the SDEA $_{Kfb}$ brake pedal when $K_d = 100$ Nm/rad for SDEA $_{Kfb}$ .....	138
Figure 9.35. When human interacting with the SDEA $_{Kfb}$ brake pedal when $K_d = 50$ Nm/rad with $G_t = 30$ rad/sNm for SDEA $_{Kfb}$ .....	138
Figure 9.36. When human interacting with the SDEA $_{Kfb}$ brake pedal when $K_d = 100$ Nm/rad and $B_d = 0.01$ Nms/rad .....	139
Figure 9.37. When human interacting with the SDEA $_{Kfb}$ brake pedal when $K_d = 100$ Nm/rad and $B_d = 0.01$ Nms/rad with $G_t = 30$ rad/sNm ...	140
Figure 9.38. When human interacting with the SDEA $_{Kfb}$ brake pedal when $K_d = 100$ Nm/rad and $B_d = 0.05$ Nms/rad with $G_t = 30$ rad/sNm ...	141
Figure 9.39. $B_d$ - $K_{vir}$ plot for experimentally coupled stability for spring rendering for SDEA $_{Kfb}$ .....	142
Figure 9.40. $G_t$ - $K_{vir}$ plot for experimentally coupled stability for spring rendering for SDEA $_{Kfb}$ .....	143
Figure 10.1. 2-port impedance-admittance block diagram of uncontrolled system .....	144
Figure 10.2. Block diagram of S(DEA) under MRFC .....	145
Figure 10.3. 2-port block diagram of SEA under MRFC .....	146
Figure 10.4. Bode plots for null rendering for various $\hat{K}$ .....	151
Figure 10.5. Bode plots for null rendering for various $\hat{J}_m$ .....	152
Figure 10.6. Bode plots for null rendering for various $\hat{B}_m$ .....	152
Figure 10.7. Closed loop motion controlled system .....	153
Figure 10.8. Experimental verification of the $\hat{K}$ bound .....	154
Figure 10.9. Experimental verification of the $\hat{J}_m$ bound .....	155
Figure 10.10. Chip test of MRFC .....	155

# Chapter 1

## Introduction

### 1.1 Motivation

Establishing safe and natural physical human-robot interactions (pHRI) is vital in many applications, including collaborative manufacturing, service, surgical, assistive, and rehabilitation robotics. Safe and natural pHRI necessitate precise control of the impedance characteristics of the robot at the interaction port [1, 2].

There are robotic applications which rely on open-loop force/impedance control which eliminate negative impacts of force sensor. End-effector force/impedance is directly translated to the motor torques/impedance for open-loop systems. However, transparency of mechanical design is critical to provide sufficient performance for open-loop system. To ensure good performance by limiting parasitic forces, the robot's mechanical design should have high stiffness, low inertia, and high passive backdrivability. There are optimization approaches available to assist in the design of transparent robots [3, 4]. However, making the construction of highly transparent robots challenging, if not unachievable. Because high force/impedance levels are required while backdrivable high torque/power density actuators are not available.

Alternatively, closed-loop force control is used in many robotic applications to compensate parasitic force from the mechanical design. However, it is a challenging problem to achieve coupled stability for closed-loop force control because of unavoidable bounds on the controller gains due to non-collocation and bandwidth limitations of sensors and actuators which enforce a fundamental trade-off between stability robustness and control performance [5, 6, 7]. The gains should be selected carefully to not make closed-loop system unstable.

When traditional high-stiffness force sensors are used in the control loop, the sys-

tem’s stable loop gain is mostly allocated to the force sensing element, severely limiting the upper bound available for controller gains to achieve fast response and good robustness properties from the controlled system. As a result, high-quality actuators/power transmission elements are commonly used in force control architectures to avoid hard-to-model parasitic effects like friction and torque ripple, which may not be effectively compensated by robust controllers based on aggressive force-feedback controller gains.

Series elastic actuation (SEA) is a commonly employed interaction control paradigm that has been introduced in [8, 9, 10] to address the fundamental trade-off between the stability robustness and control performance of closed-loop force control systems [5, 6, 7]. SEA relies on an intentionally introduced compliant element between the actuator and the interaction port, and utilizes the model of this compliant element to implement closed-loop force control. Thanks to SEA, the strict stability bounds on the controller gains induced due to non-collocation and bandwidth limitations can be relaxed, leading to excellent stability robustness and good rendering performance. Through closed-loop impedance control of high power density actuators, SEA can also provide active backdrivability within the force control bandwidth of the device by modulating its output impedance to a desirable level. Moreover, SEA acts like a low-pass filter for the parasitic forces. SEA is also preferred because of cost. SEA’s cost is lower than other traditional force sensors. Because the orders of magnitude more compliant force sensing elements in SEA experience significantly larger deflections than commercial force sensors, regular position sensors, such as optical encoders, can be used to measure these deflections, allowing the implementation of low-cost digital force sensing elements without signal conditioning.

On the negative side, the introduction of the compliant element significantly decreases the system bandwidth; consequently, the control effort increases quickly for high-frequency interactions, resulting in actuator (velocity and/or torque) saturation. Other issues of SEA designs, depending on the application, include possible end-effector oscillations, especially when SEA is not in touch, and the potential energy storage of the elastic element.

Series damped elastic actuation (SDEA) extends SEA by introducing a viscous dissipation element parallel to the series elastic element [11, 12, 13, 14, 15]. SDEA can, not only help increase the force control bandwidth of SEA [11] but also provide additional advantages, in terms of improving energy efficiency [13], reducing undesired oscillations [14], and alleviating the need for D-control terms [15].

Consideration of the damping term in the serial elastic element has major consequences in the high frequency response of the system. When causal controllers

roll-off, the dynamics of the uncontrolled plant is recovered and the high frequency response of SDEA is dominated by the dynamics of the physical filter serially attached to the plant. Accordingly, at high frequencies, while SEA acts as the spring of the series elastic element, the dynamics of SDEA is dominated by the damping of its physical filter. Consequently, the frequency response of SDEA and SEA are significantly different from each other, leading to different haptic rendering performance.

Coupled stability of interactions with S(D)EA has commonly been studied through the frequency domain passivity analysis [2]. Given that inanimate environments are passive and non-malicious human interactions do not intentionally aim to destabilize a system, frequency domain passivity can be utilized to conclude coupled stability of interactions [16]. While frequency domain passivity analysis is known to be conservative, closed-form analytical passivity conditions derived through such analysis are informative, as they provide insights on how system parameters affect stability robustness.

Passive physical equivalents are studied in the field of network synthesis, which aims to rigorously describe physically realizable behaviours in a given domain with specified components. In particular, the goal in network synthesis is to design a passive network of fundamental elements to realize a given driving-point impedance. Passive physical equivalents gives insight of effects of gains on performance and passivity bound. Moreover, passive physical equivalents give understanding of which plant parameters are controllable or uncontrollable [17]. While network synthesis in the electrical domain has received much attention during the era of analogue circuits, diminished attention has been renewed during the last decade, especially in the mechanical domain, with the introduction of inerter element and demonstration of its successful applications in the design of passive suspensions [18, 19, 20, 21, 22, 23, 24].

Effective impedance is very useful to give physical intuition To provide physical intuition to the characteristics of the impedance at the interaction port, it is common practice to decompose the impedance into its basic *mechanical primitives* through effective impedance analysis [25, 26, 27, 28, 29, 30]. While effective impedance analysis is quite useful, the use of passive physical equivalents extends this concept, as a feasible realization also provides a topological connection of fundamental mechanical elements. Along these lines, passive physical equivalents subsume effective impedance analysis, and provide a more intuitive understanding of system behaviour and its underlying components.

Natural admittance control (NAC) has been proposed as a robust model-based interaction control strategy to ensure coupled stability of interaction [7, 31, 32]. NAC is

used to plant parameters and NAC can provide selection of higher controller gains under perfect cancellation. Rejection of parasitic dynamics and performance increase with selection of higher gains. Despite selection of higher gains, performance of the closed-loop system at low frequency is limited by the physical system which exists an asymptote at the high frequency [7, 33].

## 1.2 Contributions

In this thesis, firstly, the commonly utilized cascaded control architecture for impedance control of S(D)EA is analyzed. The cascaded control architecture, also named velocity source impedance control (VSIC), consists of an inner-most velocity loop, an intermediate torque loop, and an outer-most impedance loop.

We rigorously study the frequency domain passivity of VSIC acting on different plants dynamics, such as SEA, SDEA,  $SDEA_{Kfb}$  (denoting SEA with unmeasured damping effect on the sensor) and their reduce order models.

We introduce passive physical equivalents for S(D)EAs under closed-loop control to help establish an intuitive understanding of the passivity bounds and to highlight the effect of different plant parameters and controller terms on the closed-loop performance of the system.

Furthermore, we extend our results to an alternative control architecture, called model reference force control (MRFC).

We demonstrate the validity of passivity conditions and the performance of haptic rendering through systematic simulation studies, as well as comprehensive set of physical experiments.

Contributions of the thesis may be summarized as follows:

- We rigorously study the passivity of S(D)EA to establish closed-form analytical solutions for the necessary and sufficient conditions for frequency domain passivity of S(D)EA while rendering ideal springs and null impedance, without imposing an assumption on the non-negativeness of the controller gains. Also, we rigorously study the passivity of SDEA to establish closed-form analytical solutions for the necessary and sufficient conditions for frequency domain passivity of SDEA while rendering Voigt models.
- We provide novel physical insights to these passivity conditions by deriving *passive physical equivalents* of S(D)EAs under closed-loop control for rendering Voigt model, ideal spring, and null impedance. Thanks to passive physical equivalents, we study effects of different plant parameters and controller terms on the closed-loop rendering performance.
- We rigorously study the effect of omitting the damping force induced on the serial elastic element in closed-loop control and provide necessary and sufficient conditions for the passivity of interaction when only the deflections of the serial spring element is used to estimate the interaction forces. This model,

called  $\text{SDEA}_{Kfb}$ , captures the most common implementations of SEA, where the inherent damping effects on the serial elastic element is ignored. We also provide physical equivalents of SEA with omitting the damping force induced on the serial elastic element.

- We show that passive physical equivalents establish a natural means for effective impedance analysis. Furthermore, we compare different plant dynamics, such as SEA and SDEA, with insight of passive physical equivalents. Passive physical equivalents promote co-design of S(D)EAs by enforcing simultaneous consideration of controller and plant dynamics on the closed-loop system performance. Furthermore, through the passive physical equivalents, we compare the effect of measuring and omitting the damping force on the series elastic element on the closed-loop rendering performance of the system.
- We also study reduce order models for the common implementations of SEA, where the robust inner motion control loop is replaced by a low-pass filter. We establish passivity conditions and physical equivalents for these reduce order models and compare the results with the full order systems to study the effects of this simplifying assumption on the analysis of coupled stability and haptic rendering performance.
- We propose the use of MRFC for S(D)EA as a control scheme and present the sufficient conditions for one-port passivity of SEA under MRFC during null impedance and ideal spring rendering.
- We provide validations of our theoretical results through a set of systematic simulations. We also experimentally validate the theoretical passivity bounds and haptic rendering performance for SEA, SDEA,  $\text{SDEA}_{Kfb}$  using a single degree of freedom haptic interface.

## 1.3 Outline

The rest of thesis organized as follows:

Chapter 2 presents comprehensive review of the related works on coupled stability of the series elastic actuation, passive physical equivalents, rendering performance analysis related to effective impedance, and model reference force control.

Chapter 3 overviews the concepts of series elastic actuation, presents the theorems that are used in frequency domain passivity analysis. In addition to them, it overviews passive physical equivalents, and provides a sample realization.

Chapter 4 presents the frequency domain passivity analysis of series elastic actuation, as well as its passive physical equivalents. Also, effective impedance and haptic rendering performance analyses are presented with the insight provided by passive physical equivalents.

Chapter 5 presents the frequency domain passivity analysis of series-damped elastic actuation, as well as its passive physical equivalents. Also, effective impedance and haptic rendering performance analyses are presented with the insight provided by passive physical equivalents.

Chapter 6 presents the frequency domain passivity analysis of series elastic actuation when the damping effect on the sensor is omitted, as well as its passive physical equivalents. Also, effective impedance and haptic rendering performance analyses are presented with the insight provided by passive physical equivalents.

Chapter 7 presents frequency domain passivity analysis of reduce order models of different series elastic actuation implementations, as well as their passive physical equivalents. Also, effective impedance and haptic rendering performance analyses are presented with the insight provided by passive physical equivalents.

Chapter 8 presents haptic rendering performance evaluation for different series elastic actuation implementations through Bode plots.

Chapter 9 presents the experimental setup and experimental verification of the theoretical results presented in the previous chapters.

Chapter 10 presents frequency domain passivity analysis of model reference force control for series elastic actuation during null impedance rendering, and experimental verification of the theoretical passivity bounds.

Chapter 11 concludes the paper and discusses the future research directions.



# Chapter 2

## Literature Review

In this section, we discuss the related works on frequency domain passivity of S(D)EA, and review the classical results and recent developments in the realization of passive networks.

### 2.1 Frequency Domain Passivity of SEA

Pratt *et al.* have presented the first passivity analysis for SEA, and provided sufficient conditions for an SEA under a filtered PID force controller with feedforward compensation [9]. Since the introduction of velocity-sourced impedance control (VSIC) for SEA [8, 34, 35, 36], passivity of SEA under VSIC has been studied extensively [37, 38, 39, 40, 41]. VSIC has become the most popular force control architecture for SEA, as its cascaded control architecture with inner motion control loop can effectively eliminate parasitic forces, leading to good rendering performance [8, 10, 36, 42]. Furthermore, VSIC is easy-to-use, since this controller does not rely on the dynamic model of the plant and the controller gains can be empirically tuned.

In terms of null impedance and ideal spring rendering with SEA under VSIC, Vallery *et al.* have provided a set of sufficient conditions [37, 38]. They have also proved that the passively renderable stiffness of an SEA under VSIC is upper bounded by the physical stiffness of the compliant element of SEA [38]. Tagliamonte *et al.* have provided less conservative sufficient conditions for passivity of SEA under VSIC during null impedance, linear stiffness, and Maxwell body rendering [39]. They have also proved that Voigt model cannot passively rendered with SEA under VSIC and shown that the maximum renderable stiffness not only depends on the physical stiffness, but also the physical damping in the system. Calanca *et al.* have presented sufficient conditions for passivity of SEA under four

different control architectures: VSIC, basic impedance, collocated admittance, and collocated impedance controllers [40]. They have shown that passively renderable virtual stiffness of all of these control architectures are also limited by the physical stiffness of the compliant element. They have also demonstrated that Voigt model cannot be rendered passively with SEA under VSIC [40].

Tosun and Patoglu [41] have presented the necessary and sufficient conditions for the passivity of SEA under VSIC for null impedance and linear spring rendering. The earlier sufficiency bounds on controller gains have been relaxed and the range of impedances that can be passively rendered has been extended in this study. Furthermore, it has been shown that integral gain of the motion controller is required to render stiffness if the force controller utilizes an integral term.

Recently, model reference force control (MRFC) has been proposed for SEA and provided passivity analysis of this control scheme, under model mismatch. In particular, sufficient conditions for passivity of SEA under MRFC during null impedance rendering are presented in [43].

## 2.2 Frequency Domain Passivity of SDEA

SDEA generalizes SEA by introducing a viscous dissipation element parallel to the series elastic element. Accordingly, the passivity analysis of SDEA subsumes the passivity analysis of SEA, as most SEA results can be recovered as the effect of the dissipation element approaches to zero. Passivity analysis of SDEA has received relatively less attention in the literature since the resulting closed-form solutions are more complex and harder to interpret [44, 12, 45, 46].

The passive range of virtual stiffness and damping parameters for SDEA under a cascaded impedance controller with an inner torque loop acting on a velocity compensated plant and load dynamics has been studied in [44]. In this controller, a positive velocity feedback loop provides velocity compensation by attempting to extend the bandwidth of the torque control loop under the passivity constraints.

Oblak and Matjacic [12] have conducted a frequency domain passivity analysis of SDEA under an unconventional basic impedance controller. In this controller, a force sensor is employed after the end-effector inertia to measure the human interface force, and this force is used for closed-loop force control, in addition to the series damped elastic element. It has been demonstrated that a sufficient level of mechanical damping in the compliant element is required to ensure the passivity of linear stiffness rendering using this control architecture. Sufficient conditions to passively render linear springs have been proposed, which include a lower bound on

the required level of physical damping.

Recently, Mengilli *et al.* have presented the sufficient conditions for passivity of series damped elastic actuation (SDEA) under VSIC for the null impedance, pure spring, and Voigt model rendering [46]. Furthermore, they have extended these results to absolute stability analysis and derived the *necessary and sufficient conditions* for two-port passivity of SDEA under VSIC with a virtual coupler [45].

## 2.3 Realization of Passive Physical Equivalents

Colgate and Hogan have advocated the use of passive physical equivalents for the analysis of contact instability observed in interaction control. Through passive realizations of force controlled systems, they have shown a fundamental limitation on inertia cancellation under passivity constraints for force-feedback systems with sensor-actuator non-collocation [17]. Ortega *et al.* have presented physical equivalents to establish an intuitive understanding of passivity-based control [47].

Similar to [17, 47], this paper also focuses on linear passive mechanical networks, built utilizing springs, dampers, and inerters—a recently introduced fundamental element for the mechanical domain [18, 48]. Inerter element completes the force-current analogy between the electrical and mechanical domains by introducing an ideal linear two-terminal energy storage element equivalent to an ungrounded capacitor. The completion of the analogy has a major impact, as it enables all of the previously established results in electrical network synthesis to be equivalently expressed in the mechanical domain. Thanks to this analogy, all classical results, including Foster’s reactance theorem [49] characterizing lossless networks, Brune’s construction method [50] for realization of general positive-real functions using resistors, inductors, capacitors, and transformers, and Bott-Duffin theorem [51] indicating transformers are not necessary in the synthesis of positive-real impedances, can be directly used for network synthesis in the mechanical domain.

Kalman has also advocated for renewed focus on network synthesis to establish a general theory of the subject, pointing out high potential of this field to have wider impact in a broad range of applications [52]. Accordingly, recent results have been established to extend the classical ones. Chen and Smith have studied the most general class of mechanical impedances that can be realized using one damper, one inerter, and an arbitrary number of spring elements, while allowing no levers [20]. Jiang and Smith have studied realizability conditions for positive-real biquadratic impedance functions which can be realized by five-element [53] and six-element [54] networks. Chen *et al.* have extended their earlier results in [22] and established

realizability conditions to two special class of mechanical networks: networks with biquadratic functions with an extra pole at the origin [23] and networks that are constituted of one inerter, one damper, and at most three springs [24]. Hughes and Smith have extended the classical results on Bott–Duffin realization procedure by discussing minimality and uniqueness of these realizations among all series-parallel networks realizing biquadratic minimum functions [55]. Hughes has further extended these results and established minimal network realizations for the class of impedances realized by series-parallel networks containing at most three energy storage elements [56, 57]. Morelli and Smith have presented an enumerative approach to passive network synthesis and provided a classification for networks of restricted complexity [58]. Readers are referred to the survey by Hughes *et al.* for a review of recent developments [59].

## 2.4 Rendering Performance

While the coupled stability of pHRI systems constitutes an imperative design criterion, the performance of the system is also significant for natural interactions. Transparency is a commonly used concept in evaluation of the haptic rendering, as it quantifies the match between the mechanical impedance of the virtual environment and the impedance felt by the operator, with the requirement of identical force/velocity responses [60, 61].  $Z_{\text{width}}$  is another commonly used metric that quantifies the difference between the minimum and the maximum passively renderable impedances [62].

Given that the rendered impedance is a function of frequency, both of these metrics are also quantified as such; however, the frequency dependence of these metrics make their interpretation challenging. To provide physical intuition to the characteristics of the impedance at the interaction port, it is common practice to decompose the impedance into its basic *mechanical primitives* through effective impedance analysis [25, 26, 27, 28, 29, 30]. In particular, effective impedance definitions partition the frequency dependent impedance transfer function into its real and imaginary parts, assign the real positive part to effective damping, while imaginary part is mapped to effective spring and effective mass components based on the phase response of the impedance.

While effective impedance analysis is quite useful, the use of passive physical equivalents extends this concept, as a feasible realization also provides a topological connection of fundamental mechanical elements. Along these lines, passive physical equivalents subsume effective impedance analysis, and provide a more intuitive understanding of system behaviour and its underlying components.

## 2.5 Model Reference Force Control

Natural admittance control (NAC) has been proposed as a robust model-based interaction control strategy to ensure coupled stability of interaction [7, 31, 32]. Newman has noted that causal controllers cannot alter the high frequency behaviour of the closed loop system; hence, the maximum achievable performance is limited by this high frequency asymptote. Passivity necessitates the high frequency dynamic behaviour not to be modified by any controller [7] and this inherent restriction imposes bounds on how the system admittance at low-frequencies can be modified to match this high frequency behaviour without violating phase limitations imposed by passivity [7, 31, 32].

As a model-based control approach, NAC utilizes feed-forward action to react to inputs more quickly and effectively reject parasitic forces, such as internal friction, to achieve high interaction control performance [31, 32]. Passivity of NAC under model uncertainty has been studied for compliant manipulators equipped with force sensors and underestimation of the damping and overestimation the inertia parameters have been established as sufficient conditions for these systems [7]. Passivity bounds for this system has also been studied numerically [63]. Hart and Niemeyer [33] have explicitly shown the equivalence of NAC with model reference force control (MRFC) for rigid manipulators and rigorously proved the passivity limitations imposed on the low-frequency inertial behaviour of the system due to the high-frequency asymptote of the system dynamics. They have also established overestimation of robot inertia and Coriolis affects as a sufficient condition for passivity of MRFC for a rigid manipulator. In all of these earlier studies, the force sensor is located after the end-effector inertia, such that the high frequency dynamic behaviour of the system is dominated by inertia. MRFC of SEA is significantly different from these studies as the force sensing element is located before the end-effector inertia and the high frequency dynamic behaviour of the system is dominated by compliance.

# Chapter 3

## Preliminaries

Figure 3.1 depicts a schematic representation of a single degree of freedom SDEA plant without its controller. The reflected inertia of the actuator is denoted by  $J_m$ , the viscous friction of the actuator including the reflected motor damping is denoted by  $B_m$ , the physical compliant element and viscous damper, arranged in parallel between the end-effector and the actuator, are denoted by  $K$  and  $B_f$ , respectively. Symbols  $\omega_m$  and  $\omega_{end}$  denote the actuator and end-effector velocities, respectively. The actuator torque is shown with  $\tau_m$ , while  $M_{end}$  represents the inertia of the end-effector.

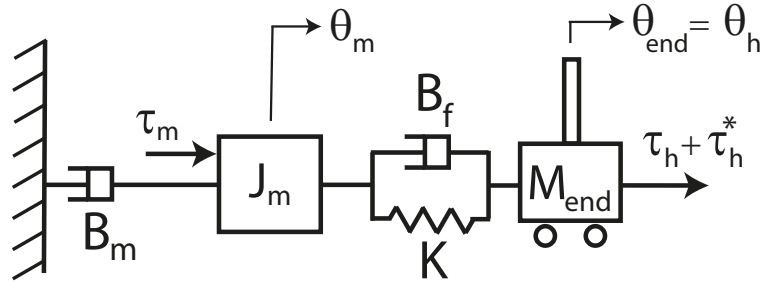


Figure 3.1 Schematic representation of SDEA (SEA if  $B_f = 0$ )

The torque  $\tau_{sea}$  on the damped compliant element, also called the physical filter, is equal to the sum of the torques induced on the linear spring and the viscous damper elements. Figure 3.1 represents an SEA, when  $B_f$  is set to 0. In this case,  $\tau_{sea}$  can be computed using the deflections of the linear spring  $K$ , according to Hooke's law.

Human interaction is modeled with two components:  $\tau_h$  represents the passive component of the applied torques while  $\tau_h^*$  is the deliberately applied active component that is assumed to be independent of system states [16]. We assume that the non-malicious human interactions do not intentionally aim to destabilize the system.

It is considered that the end-effector inertia of SDEA is negligible such that  $\tau_{sea}(s) \approx \tau_h + \tau_h^*$ ; hence, the impedance at the human/environment interaction port can be defined as  $Z_{out}(s) = -\frac{\tau_{sea}(s)}{\omega_{end}(s)}$ , where the spring-damper torque is considered as positive when these elements are in compression.

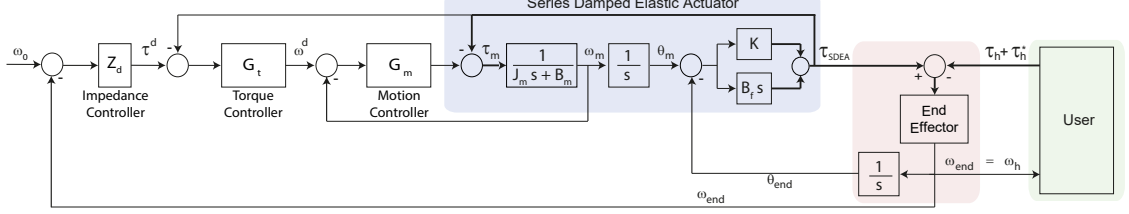


Figure 3.2 Block diagram of S(D)EA under VSIC

Figure 3.2 depicts the block diagram of SDEA under VSIC, where thick lines present physical forces. In this cascaded controller, the inner velocity control loop of the cascaded controller renders the system into an ideal motion source and acts on references generated by the outer torque control loop to keep the spring-damper deflection at the desired level to match the reference force for SDEA.  $G_t$  and  $G_m$  denote the torque and velocity controllers, respectively.

The torque  $\tau_{SDEA}$  on the physical filter, modeled as a damped compliant element, is equal to the sum of the torques induced on the linear spring and the viscous damper elements. Figure 3.2 represents an SEA, when  $B_f = 0$ . In this case,  $\tau_{SEA}$  can be computed using the deflections of the linear spring  $K$ , according to the Hooke's law. As a third case,  $B_f$  is not equal to zero, but  $B_f$  is omitted in feedback which call as  $SDEA_{Kfb}$ . In the case of  $SDEA_{Kfb}$ ,  $\tau_{sea}$  can be computed using deflections of the linear spring  $K$  while  $B_f$  is not equal to zero. The control diagram of  $SDEA_{Kfb}$  is presented in Figure 3.3.

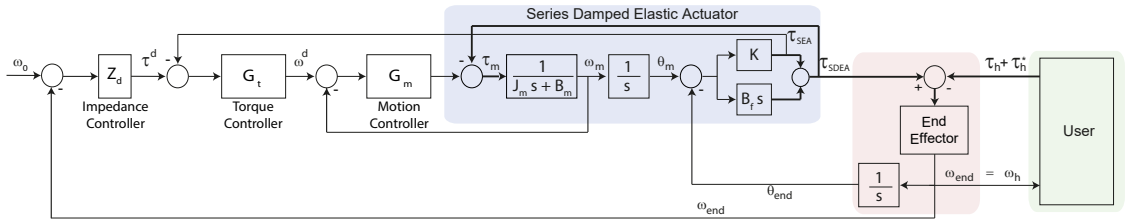


Figure 3.3 Block diagram of  $SDEA_{Kfb}$  under VSIC, for which interaction forces are estimated by only utilizing the deflections of the physical spring

The following assumptions are considered for the analysis:

- A linear time-invariant (LTI) model is considered. Therefore, nonlinear effects, such as backlash, stiction, and actuator saturation are neglected.

- Electrical dynamics are neglected and actuator velocity is assumed to be available with a negligible time delay.
- Both the deflection induced on the physical filter and its time derivative are assumed to be measured with a negligible time delay.
- Without loss of generality, a zero motion reference ( $\omega_d=0$ ) is assumed for the virtual environment and the transmission ratio is set to 1.
- Physical plant parameters are assumed to be positive, while the controller gains are allowed to be negative.

### 3.1 Passivity Theorems

Passivity of an LTI network in the frequency domain is equivalent to the positive realness of its impedance transfer function  $Z(s)$ . The positive realness of  $Z(s)$  can be studied according to Theorem 1 as follows.

**Theorem 1** ([2, 64]). *An impedance transfer function  $Z(s)$  is passive if and only if:*

- (1)  $Z(s)$  has no poles in the right half plane.
- (2)  $\text{Re}[Z(jw)] \geq 0$  for all  $w$ .
- (3) Any poles of  $Z(s)$  on the imaginary axis are simple with positive and real residues.

Following useful lemmas have been established in the literature to determine the necessary and sufficient conditions for the frequency domain passivity of LTI systems.

**Lemma 1.** *Let  $Z(s) = N(s)/D(s)$  be an impedance transfer function. Then,  $\text{Re}[Z(jw)] \geq 0$  if and only if  $P(w) \geq 0$  for any value of  $w$ , where  $P(w) = \text{Re}[N(jw)D(-jw)] = \sum_{i=0}^n d_i w^i$ .*

**Lemma 2.** *Let  $f(s) = a_3 s^3 + a_2 s^2 + a_1 s + a_0$  for  $a_i \geq 0$  be the third-order characteristic equation of a system. Then,  $f(s)$  has no roots in the open right half plane iff  $a_3 \geq 0$ ,  $a_2 \geq 0$ ,  $a_0 \geq 0$ , and  $a_1 a_2 - a_0 a_3 \geq 0$ . If these inequalities are strictly greater than zero, then the system has no roots on the imaginary axis.*

**Lemma 3** ([45]). *A polynomial of the form  $p(x) = p_2 x^2 + p_1 x + p_0$ ,  $p(x) \geq 0$  for all  $x \geq 0$  if and only if  $p_2 \geq 0$ ,  $p_0 \geq 0$  and  $p_1 \geq -2\sqrt{p_0 p_2}$ .*



## 3.2 Passive Physical Equivalents

In the force-current analogy between mechanical and electrical domains, forces are considered to be analogous to currents while velocities are analogous to voltages. Accordingly, Figure 3.4 presents the force-current analogy between fundamental two-terminal elements in both domains.

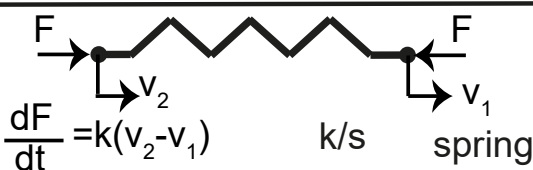
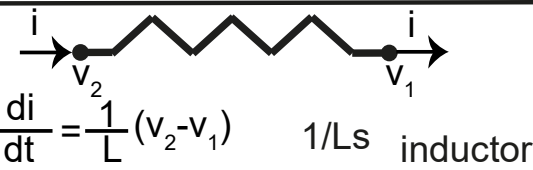
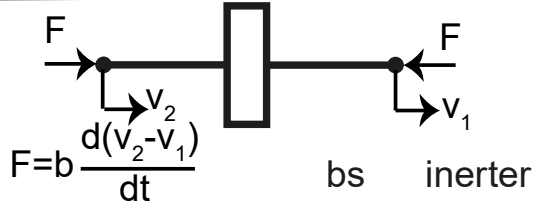
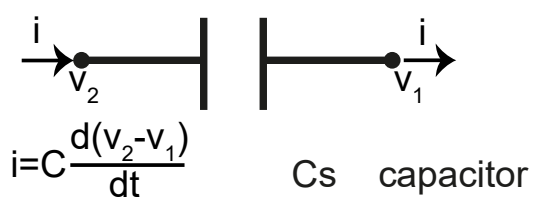
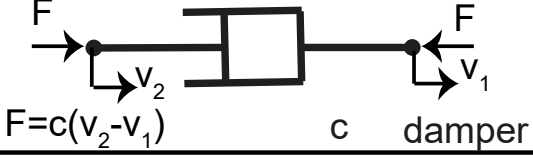
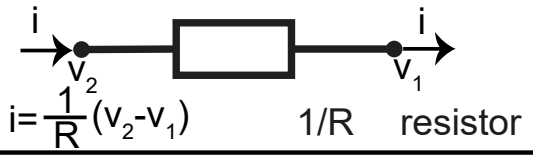
Mechanical	Electrical
 $\frac{dF}{dt} = k(v_2 - v_1)$ $k/s$ spring	 $\frac{di}{dt} = \frac{1}{L}(v_2 - v_1)$ $1/Ls$ inductor
 $F = b \frac{d(v_2 - v_1)}{dt}$ $bs$ inerter	 $i = C \frac{d(v_2 - v_1)}{dt}$ $Cs$ capacitor
 $F = c(v_2 - v_1)$ $c$ damper	 $i = \frac{1}{R}(v_2 - v_1)$ $1/R$ resistor

Figure 3.4 Relationship between mechanical and electrical networks

Inerter is a relatively recently introduced ideal energy storage element that completes the force-current analogy between the mechanical and electrical domains [18, 48]. Particularly, inerter is an ideal linear two-terminal energy storage element in the mechanical domain that is equivalent to an ungrounded capacitor in the electrical domain. Inerter element generalizes the more familiar mass/inertia element in the mechanical domain, which is analogous to the more restricted case of a grounded capacitor in the electrical domain.

### 3.2.1 An example of derivation of passive physical equivalents and effective impedance analysis

Let's consider the following impedance transfer function:

$$Z_{out}(s) = \frac{J_m K s^2 + K(B_m + G_m) s + K K_d \alpha}{J_m s^3 + (B_m + G_m) s^2 + K(\alpha + 1) s} \quad (3.1)$$

#### Step 1

Firstly, the virtual stiffness can be separated as:

$$Z_{s1}(s) = Z_{out}(s) - \frac{\alpha K_d}{(\alpha + 1)s} \quad (3.2)$$

where  $\alpha = G_m G_t$ .

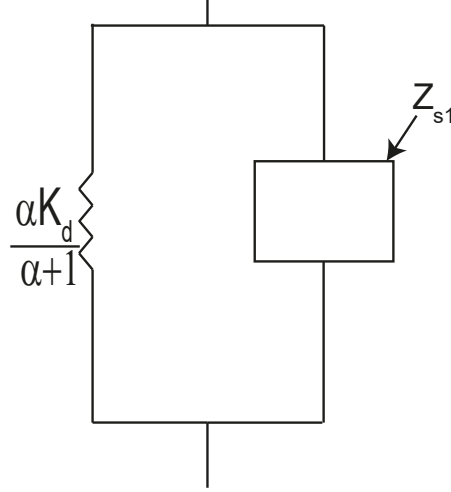


Figure 3.5 Step 1 of realization

Eqn. (3.2) is equal to:

$$Z_{s1}(s) = \frac{J_m (K(\alpha + 1) - K_d \alpha) s + K(B_m + G_m) + \alpha(B_m K - B_m K_d + G_m K - G_m K_d)}{J_m (\alpha + 1) s^2 + (\alpha + 1)(B_m + G_m) s + K(\alpha + 1)^2} \quad (3.3)$$

**Step 2** Then, physical filter can be separated as:

$$Z_{s2}(s) = (Z_{s1}(s))^{-1} - ((K - \frac{\alpha}{\alpha + 1} K_d)/s)^{-1} \quad (3.4)$$

Eqn. (3.4) is equal to:

$$Z_{s2}(s) = \frac{J_m (K(\alpha + 1) - K_d \alpha) s + K(B_m + G_m) + \alpha(B_m K - B_m K_d + G_m K - G_m K_d)}{K(\alpha + 1)^2} \quad (3.5)$$

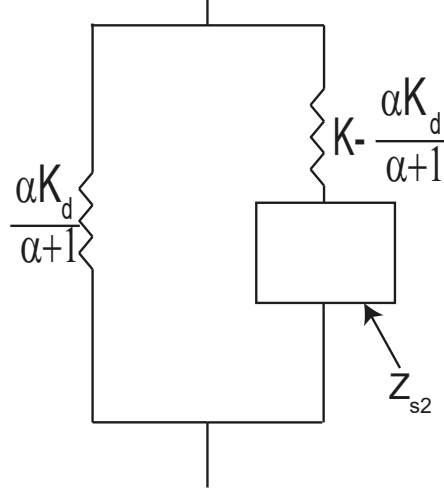


Figure 3.6 Step 2 of realization

### Step 3

Eqn. (3.5) has a form of  $\frac{As+B}{C}$  which equals to transfer function of parallel inerter and damper terms. Inerter term is equal to  $A/C$  and damper term is equal to  $B/C$ . The realization of Eqn. (3.1) where  $\sigma = \frac{1}{\alpha+1} - \frac{\alpha}{(\alpha+1)^2} \frac{K_d}{K}$ .

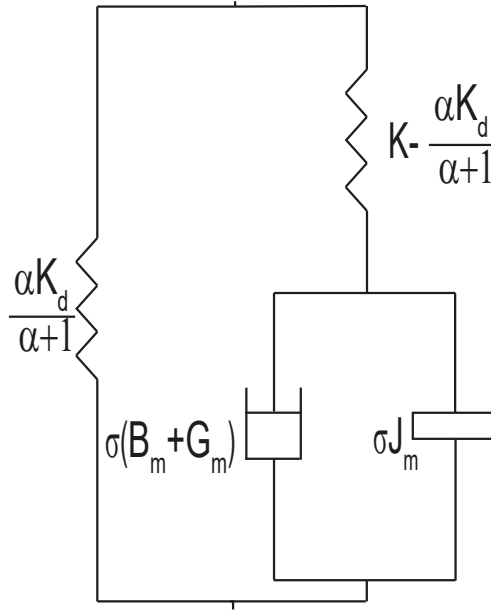


Figure 3.7 Step 3 of realization

### An example of effective impedance analysis:

If virtual stiffness and physical filter is separated, the output impedance transfer function is equal to  $Z_{s2}(s)$ . For effective impedance analysis, we can use [26]. To derive effective damping of  $Z_{s2}(s)$ , we need to find real part of  $Z_{s2}(jw)$ . Furthermore, we need to find positive part of imaginary part of  $Z_{s2}(jw)$  for effective mass of  $Z_{s2}(s)$ . From Figure 3.7, we can see that effective damping of  $Z_{s2}$  is equal to  $\sigma(B_m + G_m)$  and effective mass of  $Z_{s2}$  is equal to  $\sigma J_m$ .

## Chapter 4

# Passivity Analysis and Passive Physical Equivalents of SEA

In this chapter, we present the necessary and sufficient conditions for frequency domain passivity of SEA under VSIC (with P and PI controllers) while rendering null impedance and linear springs without imposing non-negativity assumption of the controller gains, introduce passive physical equivalents of these models, and conduct their feasibility analysis. Also, effective impedance and haptic rendering analyses are made through passive physical equivalents.

### 4.1 Ideal Spring Rendering

When both the motion and force controllers are taken as proportional (P) controllers, the impedance at the interaction port of SEA under VSIC during spring rendering equals to

$$Z_{spring}^{SEA^{P-P}}(s) = \frac{J_m K s^2 + (B_m + G_m) K s + \alpha K K_d}{J_m s^3 + (B_m + G_m) s^2 + (\alpha + 1) K s} \quad (4.1)$$

where  $\alpha = G_m G_t$ . Note that when  $(\alpha + 1) = 0$ , the rendering of virtual springs is no longer possible.

The passivity of  $Z_{spring}^{SEA^{P-P}}(s)$  is checked according to Theorem 1. Theorem 2 presents necessary and sufficient conditions for one-port passivity of SEA under VSIC while rendering spring, when  $G_t$  and  $G_m$  consist of proportional gains and without imposing non-negative controller gains.

**Theorem 2.** *Consider spring rendering for SEA under VSIC as in Figure 3.2 while  $B_f = 0$ , where  $G_t$  and  $G_m$  consist of proportional gains. Let physical plant parameters be positive, while the controller gains are allowed to be negative. Then, the*

following expressions constitute necessary and sufficient conditions for passivity of  $Z_{spring}^{SEA^{P-P}}(s)$ .

- (i)  $K \geq \frac{\alpha}{\alpha+1} K_d$ , and
- (ii)  $\frac{\alpha}{\alpha+1} K_d > 0$ , and
- (iii)  $\alpha + 1 > 0$ , and
- (iv)  $(B_m + G_m) \geq 0$ .

*Proof.* 1)  $Z(s)$  has no poles in the right half plane. If we apply Routh-Hurwitz stability criterion,  $Z_{spring}^{SEA^{P-P}}(s)$  has no roots in the open right half plane, if  $(B_m + G_m)$  and  $(\alpha + 1)$  are non-negative.

2)  $Re[Z(jw)] \geq 0$  for all  $w$ . Invoking Lemma 1, the sign of  $Re[Z_{spring}^{SEA^{P-P}}(jw)]$  can be checked by the sign of  $H(jw) = d_2 w^2$ , where  $d_2 = K^2 (\alpha + 1) (B_m + G_m) - \alpha K K_d (B_m + G_m)$ . Here,  $d_2$  is guaranteed to be non-negative if

$$K \geq \frac{\alpha}{\alpha + 1} K_d \quad (4.2)$$

Note that, if  $G_m$  is negative,  $G_t$  should also be negative to ensure that  $\frac{\alpha}{\alpha+1} K_d$  is positive.

3) Any poles of  $Z(s)$  on the imaginary axis are simple with positive and real residues. If  $(B_m + G_m)$  and  $(\alpha + 1)$  are positive, then the only possible root on the imaginary axis is at zero with a residue of  $\frac{\alpha}{\alpha+1} K_d$ . For the special case, when  $(B_m + G_m) = 0$ , there exist simple poles on the imaginary axis whose residues are  $\frac{J_m (K - K_d)}{2} - \frac{J_m K_d}{2 B_m G_t - 2}$ . This residue is positive if the condition in Eqn. (4.2) is satisfied. Note that, when  $(\alpha + 1) = 0$ , the output impedance transfer function becomes equal to  $\frac{(J_m K) s^2 + (B_m + G_m) K s - K K_d}{J_m s^3 + (B_m + G_m) s^2}$  and Condition 3 of Theorem 1 is violated as double poles exist at  $s = 0$ .  $\square$

#### 4.1.1 Passive Physical Equivalent

A realization of Eqn. (4.1) characterizing SEA under VSIC during spring rendering when both controllers are proportional is presented in Figure 4.1, where  $\sigma = \frac{1}{\alpha+1} - \frac{\alpha}{(\alpha+1)^2} \frac{K_d}{K}$ .

For the realization in Figure 4.1 to be physically feasible, all of components of the model should be non-negative. All components in the realization are guaranteed to be non-negative, if  $(B_m + G_m)$  is non-negative, and  $\frac{\alpha}{\alpha+1} K_d$  and  $\alpha + 1$  are positive.

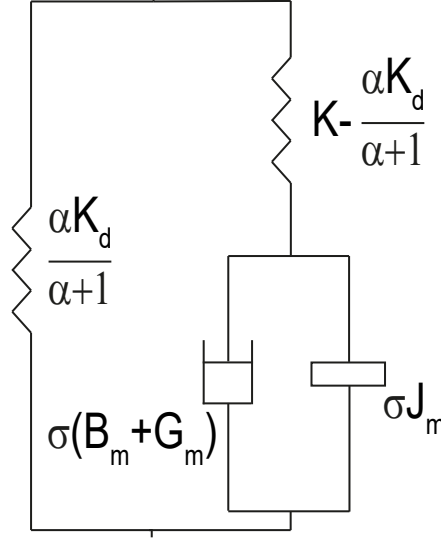


Figure 4.1 Passive physical equivalent of SEA under VSIC during spring rendering when the motion and force controllers are taken as P controllers

#### 4.1.2 Feasibility of Passive Realization vs Passivity

The conditions for feasibility of realization in Figure 4.1 are equivalent to the necessary and sufficient conditions for passivity of Eqn. (4.1) according to Theorem 1: if  $(B_m + G_m)$  is non-negative, and  $(\alpha + 1)$  and  $\frac{\alpha}{\alpha+1} K_d$  are positive, then Eqn. (4.1) is passive and all components in Figure 4.1 are non-negative.

#### 4.1.3 Haptic Renderin Performance

Physical realization of SEA during ideal spring rendering in Figure 4.1 indicates two branches in parallel: an ideal spring  $\frac{\alpha K_d}{(\alpha+1)}$  whose stiffness approaches to the desired spring  $K_d$  as the controller gains gets large and parasitic dynamics governed by a damper-inertance pair in parallel that is coupled to the system with a spring in series. The stiffness of the coupling spring is given by  $K - \frac{\alpha K_d}{(\alpha+1)}$ ; hence, the parasitic dynamics gets more decoupled from the system as the controller gains  $G_t$  and  $G_m$  increase. Note that, since the coupling spring needs to be positive for feasibility, this spring imposes an upper bound on  $K_d$  that can be passively rendered. The parasitic damper-inertance dynamics is scaled by  $\sigma = \frac{1}{\alpha+1} - \frac{\alpha}{(\alpha+1)^2} \frac{K_d}{K}$ , indicating that  $G_t$  has a significant effect for damper term, while both  $G_m$  and  $G_t$  equally affect the inerter term. Furthermore, the parasitic dynamics decrease with the choice of higher  $K_d$  values. When  $K_d = 0$ , the parasitic dynamics converges to that of null impedance rendering.

#### 4.1.4 Effective Impedance Analysis

The effective impedance of the controllable part of the realization in Figure 4.1, that is, the remaining system dynamics after parallel  $\frac{\alpha}{\alpha+1}K_d$  and the serial physical filter  $K - \frac{\alpha}{\alpha+1}K_d$  is extracted, is dominated by the damper term  $\sigma(B_m + G_m)$  in the low frequency range. Therefore, the spring rendering performance can be increased in the low frequency range by attenuating the affects of this damper term. Similarly, the high frequency behaviour of these parasitic dynamics is dictated by the inerter  $\sigma J_m$  term. Hence, the passive physical equivalentents provide an explicit representation for the effective impedance analysis.

## 4.2 Null Impedance Rendering When Controllers are P-P

When the force and the motion controllers taken as proportional (P) controllers, the impedance at the interaction port of SEA under VSIC during null impedance rendering is

$$Z_{null}^{SEA^{P-P}}(s) = \frac{J_m K s + (B_m + G_m) K}{J_m s^2 + (B_m + G_m) s + (1 + \alpha) K} \quad (4.3)$$

where  $\alpha = G_t G_m$ .

The passivity of  $Z_{null}^{SEA^{P-P}}(s)$  is checked according to Theorem 1. Theorem 3 presents necessary and sufficient conditions for one-port passivity of SEA under VSIC while rendering null impedance, when  $G_t$  and  $G_m$  consist of proportional gains and without imposing non-negative controller gains.

**Theorem 3.** *Consider null impedance rendering for SEA under VSIC as in Figure 3.2 while  $B_f = 0$ , where  $G_t$  and  $G_m$  consist of proportional gains. Let physical plant parameters be positive, while the controller gains are allowed to be negative. Then, the following expressions constitute necessary and sufficient conditions for passivity of  $Z_{null}^{SEA^{P-P}}(s)$ .*

(i)  $(B_m + G_m) \geq 0$ , and

(ii)  $\alpha + 1 \geq 0$ .

*Proof.* 1)  $Z(s)$  has no poles in the right half plane. If we apply Routh-Hurwitz stability criterion,  $Z_{null}^{SEA^{P-P}}(s)$  has no roots in the open right half plane if  $(B_m + G_m)$  and  $(\alpha + 1)$  are non-negative.

2)  $Re[Z(jw)] \geq 0$  for all  $w$ . Invoking Lemma 1, the sign of  $Re[Z_{null}^{SEA^{P-P}}(jw)]$  can be checked by the sign of  $H(jw) = K^2(\alpha + 1)(B_m + G_m)$ .  $Re[Z_{null}^{SEA^{P-P}}]$  is guaranteed to be non-negative if  $(B_m + G_m)$  and  $(\alpha + 1)$  are non-negative.

3) Any poles of  $Z(s)$  on the imaginary axis are simple with positive and real residues. There exists no poles on imaginary axis if  $(\alpha + 1)$ , and  $(B_m + G_m)$  are positive. Given that plant parameters  $J_m$  and  $K$  are positive, Eqn. (4.3) is passive when  $(\alpha + 1) = 0$ , since Eqn. (4.3) equals to  $\frac{K}{s}$ , which models a passive physical spring. A special case occurs when  $(B_m + G_m) = 0$ , for which there exist poles on the imaginary axis. The residues of these imaginary poles equal to  $\frac{J_m K}{2}$ , which is positive.  $\square$



### 4.2.1 Passive Physical Equivalent

A realization of Eqn. (4.3) characterizing SEA under VSIC during null impedance rendering when both controllers are P is presented in Figure 4.2.

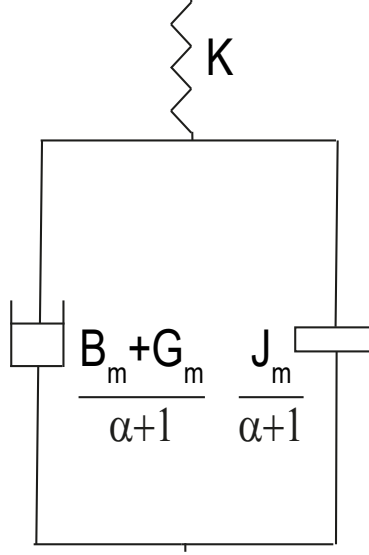


Figure 4.2 Passive physical equivalent of SEA under VSIC during null impedance rendering when both controllers are P

For the realization in Figure 4.2 to be feasible, all physical components in the model should be non-negative, that is,  $(B_m + G_m)$  and  $(\alpha + 1)$  should be non-negative, given the plant parameters  $J_m$ ,  $B_m$ , and  $K$  are positive. In the special case when  $(\alpha + 1) = 0$ , the damper and inerter elements converge to  $\infty$  and the system behaves as a pure spring.

### 4.2.2 Feasibility of Passive Realization vs Passivity

The conditions for feasibility of realization in Figure 4.2 are equivalent to the necessary and sufficient conditions for passivity of Eqn. (4.3) according to Theorem 1: if the  $(B_m + G_m) \geq 0$  and  $(\alpha + 1) \geq 0$ , then Eqn. (4.3) is passive and all components in Figure 4.2 are non-negative.

### 4.2.3 Haptic Rendering Performance

Figure 4.2 indicates that the parasitic effect of the damper  $(B_m + G_m)/(\alpha + 1)$  and inerter  $J_m/(\alpha + 1)$  terms decrease with choice of high controller gains for SEA during null impedance rendering when both controllers are P. It can be observed from Figure 4.2 that  $G_t$  has a more dominant effect on the damper term, while  $G_m$  and  $G_t$  gains affect the inerter term in the same manner, as their effects are multiplicative.

#### 4.2.4 Effective Impedance Analysis

The effective impedance of the controllable part of the realization in Figure 4.2, that is, the remaining system dynamics after the serial physical filter  $K$  is extracted, is dominated by the damper term  $(B_m + G_m)/(\alpha + 1)$  in the low frequency range. Therefore, the null impedance rendering performance can be increased in the low frequency range by attenuating the affects of this damper term. Similarly, the high frequency behaviour of these parasitic dynamics is dictated by the inerter  $J_m/(\alpha + 1)$  term. Hence, the passive physical equivalents provide an explicit representation for the effective impedance analysis.

### 4.3 Null Impedance Rendering When Controllers are P-PI

When the force controller is taken as proportional (P) and the motion controller is taken as proportional-integral (PI) controller, the impedance at the interaction port of SEA under VSIC during null impedance rendering equals to

$$Z_{null}^{SEA^{P-PI}}(s) = \frac{J_m K s^2 + (B_m + G_m) K s + I_m K}{J_m s^3 + (B_m + G_m) s^2 + (I_m + (1 + \alpha) K) s + G_t I_m K} \quad (4.4)$$

where  $\alpha = G_m G_t$ . The passivity of  $Z_{null}^{SEA^{P-PI}}(s)$  is checked according to Theorem 1. Theorem 4 presents necessary and sufficient conditions for one-port passivity of SEA under VSIC while rendering null impedance, when  $G_t$  is taken as proportional (P) and the  $G_m$  is taken as proportional-integral (PI) controller and without imposing non-negative controller gains.

**Theorem 4.** *Consider null impedance rendering for SEA under VSIC as in Figure 3.2 while  $B_f = 0$ , where  $G_t$  is taken as proportional gain and  $G_m$  is taken as proportional-integral gain. Let physical plant parameters be positive, while the controller gains are allowed to be negative. Then, the following expressions constitute necessary and sufficient conditions for passivity of  $Z_{null}^{SEA^{P-PI}}(s)$ .*

- (i)  $J_m \leq \frac{(\alpha+1)(B_m+G_m)}{G_t I_m}$ , and
- (ii)  $\alpha + 1 > 0$ , and
- (iii)  $B_m + G_m > 0$ , and
- (iv)  $G_t \geq 0$ , and
- (v)  $I_m \geq 0$ .

*Proof.* 1)  $Z(s)$  has no poles in the right half plane. If we apply Routh-Hurwitz stability criterion,  $Z_{null}^{SEAP-PI}(s)$  has no roots in the open right half plane if  $(B_m + G_m)$  and  $G_t I_m$  are non-negative and the following condition is satisfied.

$$J_m \leq \frac{(B_m + G_m)(I_m + (1 + \alpha)K)}{G_t I_m K} \quad (4.5)$$

2)  $Re[Z(jw)] \geq 0$  for all  $w$ . Invoking Lemma 1, the sign of  $Re[Z_{null}^{SEAP-PI}(jw)]$  can be checked by the sign of  $H(jw) = d_2 w^2 + d_0$  where

$$d_0 = G_t I_m^2 K^2 \quad (4.6)$$

$$d_2 = -G_t I_m K^2 J_m + K^2 (B_m + G_m)(\alpha + 1) \quad (4.7)$$

$Re[Z_{null}^{SEAP-PI}]$  is non-negative if  $G_t \geq 0$  as required for non-negativeness of  $d_0$ , and  $(\alpha + 1) > 0$ ,  $(B_m + G_m) > 0$  and Eqn. (4.8) holds as required for non-negativeness of  $d_2$ . Note that if Eqn. (4.8) holds, then Eqn. (4.5) is also guaranteed to hold.

$$J_m \leq \frac{(\alpha + 1)(B_m + G_m)}{G_t I_m} \quad (4.8)$$

3) Any poles of  $Z(s)$  on the imaginary axis are simple with positive and real residues. No roots exists on the imaginary axis if  $(B_m + G_m)$  and  $G_t I_m$  are positive. For the special case when  $G_t = 0$ , there is a pole on the imaginary axis whose residue is  $\frac{I_m K}{I_m + K}$ . Note that,  $G_t \geq 0$  and  $G_t I_m \geq 0$  imply that  $I_m \geq 0$ . When  $I_m = 0$ , Eqn. (4.4) reduces to Eqn. (4.3) as analysed in the previous subsection.  $\square$

### 4.3.1 Passive Physical Equivalent

A realization of Eqn. (4.4) characterizing SEA under VSIC during null impedance rendering when the motion controller is PI and the force controller is P is presented in Figure 4.3, where  $c_{1n} = \frac{1}{G_t}$ ,  $c_{2n} = \frac{B_m - \frac{1}{G_t}}{\alpha + 1} - \frac{G_t I_m J_m}{(\alpha + 1)^2}$ , and  $b_{1n} = \frac{B_m G_t - 1}{G_t^2 I_m} - \frac{J_m}{\alpha + 1}$ .

For the realization in Figure 4.3 to be feasible, all physical components in the model should be non-negative. Therefore,  $(\alpha + 1)$  should be non-negative from the inerter term, while  $G_t$  should be non-negative for a non-negative  $c_{1n}$ . The non-negativeness of  $b_{1n}$  imposes

$$J_m \leq \frac{(\alpha + 1)(B_m G_t - 1)}{G_t^2 I_m} \quad (4.9)$$

If  $I_m \geq 0$ , then Eqn. (4.9) ensures non-negativeness of  $c_{2n}$ , while also indicating that  $(B_m G_t - 1)$  and  $(\alpha + 1)$  should be positive. It is not possible to select  $I_m < 0$ , as the non-negativeness of  $c_{2n}$  conflicts with Eqn. (4.9) in this case.

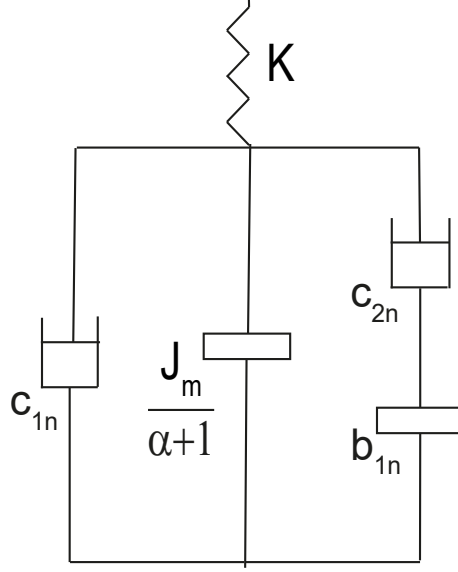


Figure 4.3 Passive physical equivalent of SEA under VSIC during null impedance rendering when the motion controller is PI and the force controller is P

### 4.3.2 Feasibility of Passive Realization vs Passivity

Given  $(\alpha + 1) > 0$  as necessitated by the feasibility of the realization in Figure 4.3 and the passivity of Eqn. (4.4), Eqn. (4.8) and Eqn. (4.9) can be expressed together as

$$\frac{J_m}{(\alpha + 1)} \leq \frac{(B_m G_t - 1)}{G_t^2 I_m} < \frac{(B_m + G_m)}{G_t I_m} \quad (4.10)$$

Consequently, Eqn. (4.9) presents a more conservative bound and its satisfaction ensures that Eqn. (4.8) is also satisfied. Lastly, it can be shown that when  $(B_m G_t - 1) > 0$  is summed with  $(\alpha + 1) > 0$ , the result is equivalent to  $(B_m + G_m) > 0$ , which is known to be positive as  $G_t > \frac{1}{B_m}$ .

Hence, the conditions for feasibility of realization in Figure 4.3 provide sufficient conditions for the passivity of Eqn. (4.4) according to Theorem 1. In particular, Eqn. (4.9) implies Eqn. (4.8) if  $(\alpha + 1) > 0$ , as necessitated by non-negativeness of  $c_{2n}$  term. Furthermore, the condition  $(B_m G_t - 1) > 0$  imposed by the non-negativeness of  $c_{2n}$  implies  $(B_m + G_m) > 0$ , when considered with  $(\alpha + 1) > 0$ .

To summarize, the realization in Figure 4.3 is feasible and the sufficient conditions for passivity of Eqn. (4.4) are satisfied if  $(B_m G_t - 1)$  and  $(\alpha + 1)$  are positive,  $I_m$  is non-negative, and Eqn. (4.9) is satisfied. The necessary and sufficient conditions for passivity of Eqn. (4.4) can be enforced if Eqn. (4.8) is imposed instead of Eqn. (4.9), and  $G_t \geq 0$  and  $(B_m + G_m) > 0$  are imposed instead of  $(B_m G_t - 1) > 0$ .

### 4.3.3 Haptic Rendering Performance

Deeper insights may be gained by comparing the physical realization of these systems. In comparison with Figure 4.2, Figure 4.3 indicates that the addition of an integral term to the motion controller modifies the damping term by splitting it into two parts: a regular damper  $c_{1n}$  whose damping coefficient is inversely proportional to  $G_t$  and a newly introduced element that consists of a damper  $c_{2n}$  in series with an inerter  $b_{1n}$ . The newly introduced serial damper-inerter term introduces frequency dependent dissipation to the system that increases with frequency.

### 4.3.4 Effective Impedance Analysis

Effective impedance analysis of the controllable part of the realization in Figure 4.3. In particular, the effective damping for Eqn. (4.4) after removing the uncontrollable serial compliant element  $K$  can be computed as

$$c_{effP-PI}^{SEA}(\omega) = \frac{((B_m + G_m)(\alpha + 1) - G_t I_m J_m) \omega^2 + G_t I_m^2}{(\alpha + 1)^2 \omega^2 + G_t^2 I_m^2} \quad (4.11)$$

At low frequencies (as  $\omega \rightarrow 0$ ), Eqn. (4.11) converges to  $c_{1n}$ . At high frequencies (as  $\omega \rightarrow \infty$ ), Eqn. (4.11) approaches to  $c_{1n} + c_{2n}$ .

Similarly, the effective inertence for Eqn. (4.4) after removing the serial compliant element  $K$  can be computed as

$$b_{effP-PI}^{SEA}(\omega) = \frac{J_m(\alpha + 1) \omega^2 + I_m(B_m G_t - 1)}{(\alpha + 1)^2 \omega^2 + G_t^2 I_m^2} \quad (4.12)$$

At low frequencies (as  $\omega \rightarrow 0$ ), Eqn. (4.12) converges to  $\frac{J_m}{(\alpha+1)} + b_{1n}$ . At high frequencies (as  $\omega \rightarrow \infty$ ), Eqn. (4.12) approaches to  $\frac{J_m}{\alpha+1}$ .

Hence, null impedance rendering performance at the low frequency range is dominated by the parasitic damping of  $c_{1n}$ , while a parasitic inertence of  $\frac{J_m}{(\alpha+1)} + b_{1n}$  acts at this frequency range. The parasitic damping term  $c_{1n}$  is inversely proportional to  $G_t$  and can be attenuated by the force controller. Similarly, the parasitic inertance  $\frac{B_m G_t - 1}{G_t^2 I_m}$  at the low frequency range can be attenuated by  $G_t$  and  $I_m$  gains. As can be observed from the physical realization,  $I_m$  and  $G_m$  do not affect  $c_{1n}$ . Furthermore,  $G_m$  does not affect parasitic inertence at the low frequency range. At intermediate frequencies,  $c_{2n}$  slightly reduces with higher  $I_m$  selections, so the performance of null impedance rendering can be mildly improved by  $I_m$ .

## 4.4 Discussion

We have presented passivity analysis of SEA under VSIC during null impedance and spring rendering. Also, we have provided passive physical equivalents of SEA under VSIC during null impedance and spring rendering. Through passive physical equivalents, we have provided analysis of effective impedance and haptic rendering performance. It is important to note that, in general, passive physical realizations for a given impedance transfer function are not unique. While the feasibility conditions for a passive physical realization provides sufficient conditions for passivity as shown in previous Sections, the necessary conditions may not be easily established through such analysis, as it requires studying feasibility of all passive physical realizations.

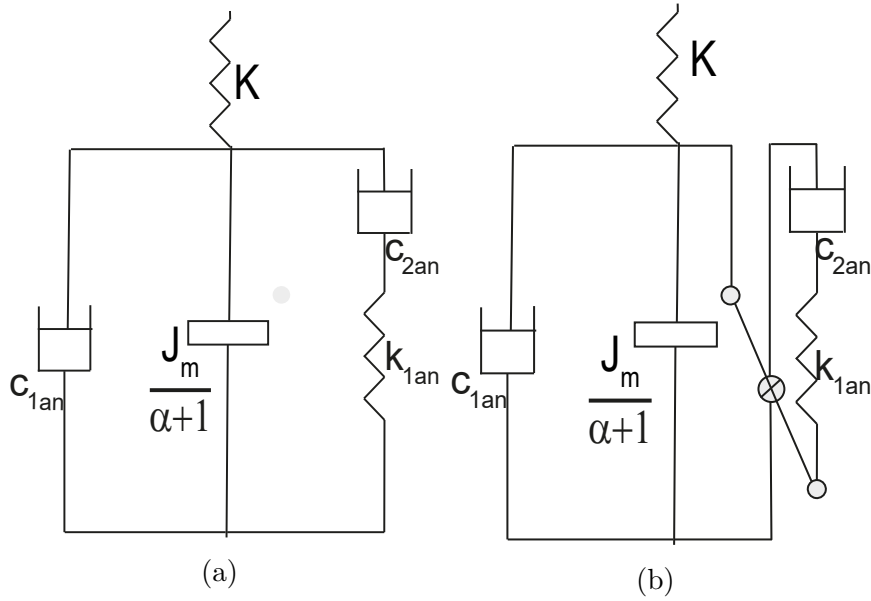


Figure 4.4 Alternative passive physical equivalents of SEA under VSIC during null impedance rendering when the force controller is P and the motion controller is PI

Figure 4.4 depicts alternative passive physical realizations of SEA under VSIC during null impedance rendering when the force controller is P and the motion controller is PI. In particular, Figure 4.3 and Figures 4.4a and 4.4b present the realizations for the impedance transfer function in Eqn. (4.4). This chapter presents feasibility conditions for Figure 4.3 and prove that they establish a set of sufficient conditions for passivity. Figure 4.4a and 4.4b are alternative realizations, where the serial inerter-damper term introduced due to the integral controller is realized through a serial spring-damper. The feasibility conditions for these realizations provide a different set of sufficient conditions for passivity. While Bott-Duffin theorem [51] establishes that ideal transformers (levers) can be avoided in physical realizations, we present Figures 4.4a and 4.4b as a set of alternative realizations, since the feasibility conditions of these two realizations nicely complement each other to recover the necessary and sufficient conditions for passivity of Eqn. (4.4) and the explicit use

of a lever to change direction provides an understanding on how negative values of fundamental elements (e.g.,  $k_{1an}$  and  $c_{2an}$ ) can be avoided in realizations.

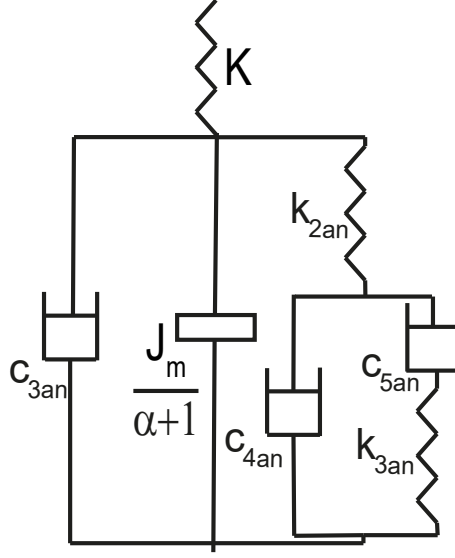


Figure 4.5 Passive physical equivalent of SEA under VSIC during null impedance rendering when both controllers are PI

Realizations become more complicated as controllers become more involved, making their interpretation harder. For instance, Figure 4.5 presents passive physical realizations for SEA under VSIC during null impedance rendering, when both controllers are PI.

# Chapter 5

## Passivity Analysis and Passive Physical Equivalents of SDEA

In this chapter, we present the necessary and sufficient conditions for frequency domain passivity of SDEA under VSIC with P controllers, while rendering null impedance, linear springs, and Voigt model, introduce passive physical equivalents of these models, and conduct their feasibility analysis. Also, effective impedance and haptic rendering analyses are made through passive physical equivalents. In this chapter, ideal spring rendering and null impedance rendering analyses are provided without imposing an assumption on the non-negativeness of the controller gains, but Voigt model rendering analysis is provided under assumption of non-negative parameters.

### 5.1 Voigt Model Rendering

When the force and the motion controllers taken as proportional (P) controllers, the impedance at the interaction port of SDEA under VSIC during Voigt model rendering is  $Z_{Voigt}^{SDEA^{P-P}}(s) =$

$$\frac{B_f J_m s^3 + [B_f (B_m + G_m) + J_m K + B_d B_f \alpha] s^2 + [K (B_m + G_m + B_d \alpha) + B_f K_d \alpha] s + K K_d \alpha}{J_m s^3 + [B_m + G_m + B_f (1 + \alpha)] s^2 + K (1 + \alpha) s} \quad (5.1)$$

where  $\alpha = G_m G_t$ .

The passivity of  $Z_{Voigt}^{SDEA^{P-P}}(s)$  is checked according to Theorem 1. Theorem 5 presents necessary and sufficient conditions for one-port passivity of SDEA under VSIC while rendering Voigt model, when  $G_t$  and  $G_m$  consist of proportional gains.



**Theorem 5.** Consider Voigt model rendering for SDEA under VSIC as in Figure 3.2, where  $G_t$  and  $G_m$  consist of proportional gains. Let all parameters be positive. Then, the following expressions constitute necessary and sufficient conditions for passivity of  $Z_{Voigt}^{SDEA^{P-P}}(s)$ .

- (i)  $K \geq K_d \frac{\alpha}{(\alpha+1)} \frac{B_m+G_m}{B_m+G_m+B_d\alpha}$ , and
- (ii)  $-2J_m \sqrt{B_f K [(B_m+G_m+B_d\alpha)K(\alpha+1) - (B_m+G_m)K_d\alpha]} \leq B_f (B_m+G_m+B_d\alpha) [B_m+G_m+B_f(\alpha+1)] - (B_d K + B_f K_d) J_m \alpha$ .

*Proof.* 1)  $Z(s)$  has no poles in the right half plane. If we apply Routh-Hurwitz stability criterion,  $Z_{Voigt}^{SDEA^{P-P}}(s)$  has no poles in the open right half plane, since all coefficients of denominator of  $Z_{Voigt}^{SDEA^{P-P}}(s)$  are positive.

2)  $\text{Re}[Z(jw)] \geq 0$  for all  $w$ . Invoking Lemma 1, the sign of  $\text{Re}[Z_{voigt}^{SDEA^{P-P}}(jw)]$  can be checked by the sign of  $H(jw) = d_6 w^6 + d_4 w^4 + d_2 w^2$ , where

$$d_2 = K^2 (\alpha + 1) (B_m + G_m + B_d \alpha) - (B_m + G_m) K K_d \alpha \quad (5.2)$$

$$d_4 = B_f (B_m + G_m + B_d \alpha) [B_m + G_m + B_f (\alpha + 1)] - (B_d K + B_f K_d) J_m \alpha \quad (5.3)$$

$$d_6 = B_f J_m^2 \quad (5.4)$$

Applying Lemma 3,  $d_6$  is positive, since  $B_f$  is positive. The non-negativeness of  $d_2$  imposes the following constraint:

$$K \geq K_d \frac{\alpha}{(\alpha + 1)} \frac{B_m + G_m}{B_m + G_m + B_d \alpha} \quad (5.5)$$

The last necessary and sufficient condition can be derived as:

$$\begin{aligned} & -2 J_m \sqrt{B_f K [(B_m + G_m + B_d \alpha) K (\alpha + 1) - (B_m + G_m) K_d \alpha]} \\ & \leq B_f (B_m + G_m + B_d \alpha) [B_m + G_m + B_f (\alpha + 1)] - (B_d K + B_f K_d) J_m \alpha \end{aligned} \quad (5.6)$$

Accordingly, Eqns. (5.5) and (5.6) provide the necessary and sufficient conditions to ensure that  $\text{Re}[Z_{voigt}^{SDEA^{P-P}}(jw)] > 0$ . Together with Eqn. (5.5), a simpler but more conservative set of sufficient conditions can be derived by imposing non-negativeness of  $d_4$  instead of Eqn. (5.6) as follows:

$$J_m \leq \frac{B_f (B_m + G_m + B_d \alpha) [B_m + G_m + B_f (1 + \alpha)]}{(B_f K_d + B_d K) \alpha} \quad (5.7)$$

3) Any poles of  $Z(s)$  on the imaginary axis are simple with positive and real residues. There exists no poles on the imaginary axis, except at  $s = 0$ , as long as all controller gains and physical parameters are positive. For the pole at  $s = 0$ , the residue equals to  $\frac{\alpha}{(\alpha+1)} K_d$  which is also positive for positive controller gains.  $\square$

### 5.1.1 Passive Physical Equivalent

A realization of Eqn. (5.1) characterizing SDEA under VSIC during Voigt model rendering when both controllers are proportional is presented in Figure 5.1.

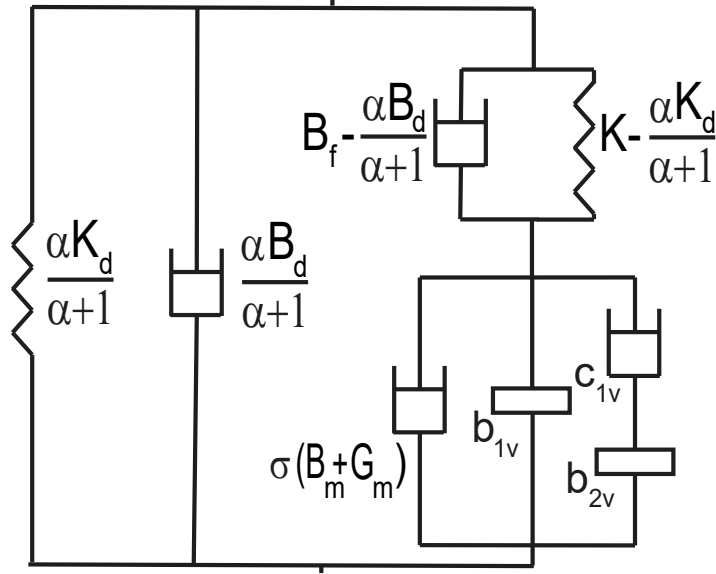


Figure 5.1 Passive physical equivalent of SDEA under VSIC during Voigt model rendering when both controllers are P

The parameters of this physical realization can be listed as follows

$$b_{1v} = \frac{J_m}{(\alpha+1)^2} - \frac{\alpha}{(\alpha+1)^2} \frac{(B_d - B_f)}{B_f} J_m \quad (5.8)$$

$$c_{1v} = \frac{\alpha}{(\alpha+1)^2} \frac{(B_f K_d - B_d K) [B_f (B_m + G_m) - J_m K]}{B_f^2 K} \quad (5.9)$$

$$b_{2v} = \frac{\alpha}{(\alpha+1)^2} \frac{(B_f K_d - B_d K) [B_f (B_m + G_m) - J_m K]}{B_f K^2} \quad (5.10)$$

with  $\sigma = \frac{1}{\alpha+1} - \frac{\alpha}{(\alpha+1)^2} \frac{K_d}{K}$ .

For the realization in Figure 5.1 to be feasible, all of components of the model should be non-negative. Hence, the non-negativeness of terms imposes

$$K \geq \frac{\alpha}{\alpha + 1} K_d \quad (5.11)$$

$$B_f \geq \frac{\alpha}{\alpha + 1} B_d \quad (5.12)$$

$$\frac{B_f}{K} \geq \frac{J_m}{(B_m + G_m)} \quad (5.13)$$

In particular, substituting Eqn. (5.12) into  $(B_f K_d - B_d K)$  and invoking Eqn. (5.11), one can prove that  $(B_f K_d - B_d K) \geq 0$ . Eqns. (5.11) and (5.12) impose upper bounds on passively renderable stiffness and damping levels. In Eqn. (5.13),  $\frac{J_m}{(B_m + G_m)}$  captures the time constant of the controlled mass-damper system, while  $\frac{B_f}{K}$  is the time constant of the serial physical filter. The condition given in Eqn. (5.13) imposes the intuitive constraint that the controlled mass-damper model of the plant should respond faster than the interaction forces filtered by the physical filter, such that the system can keep up with these inputs to adequately cancel out and superpose the dynamics according to the desired impedance.

### 5.1.2 Feasibility of Passive Realization vs Passivity

The feasibility conditions in Eqns. (5.11)–(5.13) serve as a set of sufficient conditions for passivity. In particular, Eqn. (5.11) is a more conservative condition than Eqn. (5.5) as shown below:

$$K \geq K_d \frac{\alpha}{(\alpha + 1)} \geq K_d \frac{\alpha}{(\alpha + 1)} \frac{B_m + G_m}{B_m + G_m + B_d \alpha} \quad (5.14)$$

Similarly, Eqn. (5.13) imposes a constraint that is more conservative than the sufficiency condition in Eqn. (5.7), as can be shown by substituting Eqn. (5.5) into Eqn. (5.7) and noting that the plant parameters are positive.

$$J_m \leq \frac{B_f}{K} (B_m + G_m) \leq \frac{B_f (B_m + G_m + B_d \alpha) [B_m + G_m + B_f (1 + \alpha)]}{(B_f K_d + B_d K) \alpha} \quad (5.15)$$

Consequently, the feasibility of Figure 5.1 provides sufficient conditions for the frequency domain passivity of Eqn. (5.1).

### 5.1.3 Haptic Rendering Performance

Physical realization of SDEA during Voigt model rendering in Figure 5.1 indicates three main branches in parallel: an ideal spring-damper pair  $\left(\frac{\alpha}{(\alpha+1)} K_d\right) - \left(\frac{\alpha}{(\alpha+1)} B_d\right)$  in parallel that converges to the Voigt model to be rendered, and a branch capturing

the parasitic dynamics governed by a complex topology of damper-inertance terms that are coupled to the system in series through a coupling filter.

The coupling filter consists of a spring-damper pair in parallel, where the stiffness and damping of the filter are given by  $K - \frac{\alpha}{(\alpha+1)} K_d$  and  $B_f - \frac{\alpha}{(\alpha+1)} B_d$ , respectively. The coupling filter indicates that the parasitic dynamics gets more decoupled from the system as the controller gains  $G_t$  and  $G_m$  increase. Furthermore, given that the coupling filter terms need to be positive for feasibility, upper bounds are imposed on  $K_d$  and  $B_d$  parameters of Voigt models that can be passively rendered.

The parasitic dissipation effects are split into two parts: a damper term scaled by  $\frac{1}{\alpha+1} - \frac{\alpha}{(\alpha+1)^2} \frac{K_d}{K}$  indicating a significant effect of the force control gain  $G_t$  on this damper term, and a serial damper-inerter term that introduces frequency dependent dissipation to the system that increases with frequency. The parasitic inertance is scaled by  $\frac{1}{(\alpha+1)^2} - \frac{\alpha}{(\alpha+1)^2} \frac{(B_d - B_f)}{B_f}$ , indicating both control gains  $G_m$  and  $G_t$  equally affect this inerter term.

The realization of ideal spring rendering can be recovered with SDEA from the realization of Voigt model rendering with SDEA by setting  $B_d = 0$ , while the realization of null impedance rendering with SDEA can be recovered from the realization of Voigt model rendering with SDEA by setting  $B_d = 0$  and  $K_d = 0$ . Similarly, realizations with SEA can be recovered from the SDEA realizations by simply setting  $B_f = 0$ .

#### 5.1.4 Effective Impedance Analysis

Deeper insights may be gained about the parasitic dynamics by studying the effective impedance of the realization. The effective impedance analysis of the realization in Figure 5.1, after removing the rendered Voigt model  $\left(\frac{\alpha}{(\alpha+1)} K_d\right) - \left(\frac{\alpha}{(\alpha+1)} B_d\right)$  and the serial coupling filter  $\left(B_f - \frac{\alpha}{(\alpha+1)} B_d\right) - \left(K - \frac{\alpha}{(\alpha+1)} K_d\right)$  pairs, indicates that the effective damping of the parasitic dynamics can be computed as

$$c_{effVoigt}^{SDEA}(\omega) = \frac{[B_f^2 [(B_m + G_m)(1 + \alpha)] - B_d B_f \alpha (B_m + G_m) + J_m \alpha (B_d K - B_f K_d)] \omega^2 + K (B_m + G_m) [K + \alpha (K - K_d)]}{B_f^2 (\alpha + 1)^2 \omega^2 + K^2 (\alpha + 1)^2} \quad (5.16)$$

At low frequencies (as  $\omega \rightarrow 0$ ), Eqn. (5.16) converges to  $\sigma(B_m + G_m)$ . At high frequencies (as  $\omega \rightarrow \infty$ ), Eqn. (5.16) approaches to  $\sigma(B_m + G_m) + c_{1v}$ .

Similarly, the effective inertance of the parasitic dynamics can be computed as

$$b_{effVoigt}^{SDEA}(\omega) = \frac{B_f [B_f J_m - \alpha J_m (B_d - B_f)] \omega^2 + J_m K^2 (1 + \alpha) + \alpha (B_f K_d - B_d K) (B_m + G_m) - J_m K K_d \alpha}{B_f^2 (\alpha + 1)^2 \omega^2 + K^2 (\alpha + 1)^2} \quad (5.17)$$

At low frequencies (as  $\omega \rightarrow 0$ ), Eqn. (5.17) converges to  $b_{1v} + b_{2v}$ . At high frequencies (as  $\omega \rightarrow \infty$ ), Eqn. (5.17) approaches to  $b_{1v}$ .

Accordingly, the parasitic damping of  $\sigma(B_m + G_m)$  affects the Voigt model rendering performance at the low frequency range, while a parasitic inertance of  $b_{1v} + b_{2v}$  also acts at this frequency range. Hence, parasitic damping at low frequencies can be effectively attenuated by the force controller  $G_t$ . The effective parasitic damping increases with frequency and  $c_{1v}$  is added to  $\sigma(B_m + G_m)$  at the high frequency range. On the other hand, the effective parasitic inertance decreases with frequency and the effect of  $b_{1v}$  becomes more dominant at high frequencies. Hence, the effect of inertance at the low frequency range can be attenuated by  $G_t$  and  $G_m$  gains.

Note that, for large controller gains  $G_t$  and  $G_m$ , the dynamics of the parasitic impedance is more effectively decoupled from the rendered impedance  $\left(\frac{\alpha}{(\alpha+1)} K_d\right) - \left(\frac{\alpha}{(\alpha+1)} B_d\right)$  through the serial coupling filter. Furthermore, the rendered impedance converges to the desired  $K_d - B_d$  parameters of the Voigt model.

## 5.2 Ideal Spring Rendering

When the force and the motion controllers taken as proportional (P) controllers, the impedance at the interaction port of SDEA under VSIC during spring rendering equals to

$$Z_{spring}^{SDEA^{P-P}}(s) = \frac{B_f J_m s^3 + (B_f (B_m + G_m) + J_m K) s^2 + (K (B_m + G_m) + B_f K_d \alpha) s + K K_d \alpha}{J_m s^3 + (B_f (1 + \alpha) + B_m + G_m) s^2 + K (\alpha + 1) s} \quad (5.18)$$

where  $\alpha = G_t G_m$ . The passivity of  $Z_{spring}^{SDEA^{P-P}}(s)$  is checked according to Theorem 1. Theorem 6 presents necessary and sufficient conditions for one-port passivity of SDEA under VSIC while rendering spring, when  $G_t$  and  $G_m$  consist of proportional gains and without imposing non-negative controller gains.

**Theorem 6.** *Consider spring rendering for SDEA under VSIC as in Figure 3.2, where  $G_t$  and  $G_m$  consist of proportional gains. Let physical plant parameters be positive, while the controller gains are allowed to be negative. Then, the following expressions constitute necessary and sufficient conditions for passivity of  $Z_{spring}^{SDEA^{P-P}}(s)$ .*

- (i)  $K \geq \frac{\alpha}{\alpha+1} K_d$ , and
- (ii)  $\frac{\alpha}{\alpha+1} K_d > 0$ , and
- (iii)  $-2 J_m \sqrt{B_f K (B_m + G_m) (K + \alpha (K - K_d))} \leq B_f ((B_m + G_m) (B_f (1 + \alpha) + B_m + G_m) - \alpha J_m K_d)$ , and
- (iv)  $\alpha + 1 > 0$ , and
- (v)  $(B_m + G_m) > 0$ .

*Proof.* 1)  $Z(s)$  has no poles in the right half plane. Invoking Lemma 2 imposes  $(\alpha + 1) (B_m + G_m + B_f (\alpha + 1)) \geq 0$ . Accordingly,  $Z_{spring}^{SDEA^{P-P}}(s)$  has no roots in the open right half plane if  $(\alpha + 1)$  and  $B_m + G_m + B_f (\alpha + 1)$  are non-negative.

2)  $Re[Z(jw)] \geq 0$  for all  $w$ . Invoking Lemma 1, the sign of  $Re[Z_{spring}^{SDEA^{P-P}}(jw)]$  can be checked by the sign of  $H(jw) = d_6 w^6 + d_4 w^4 + d_2 w^2$  where

$$d_2 = K (B_m + G_m) (K (\alpha + 1) - \alpha K_d) \quad (5.19)$$

$$d_4 = B_f ((B_m + G_m) (B_m + G_m + B_f (\alpha + 1)) - \alpha J_m K_d) \quad (5.20)$$

$$d_6 = B_f J_m^2 \quad (5.21)$$

From Lemma 3, the non-negativeness of  $d_2$  imposes

$$K \geq \frac{\alpha}{\alpha + 1} K_d \quad (5.22)$$

Furthermore, non-negativeness of  $d_6$  is guaranteed as the plant parameter  $B_f$  is positive. The last condition of Lemma 3 imposes

$$\begin{aligned} & -2 J_m \sqrt{B_f K (B_m + G_m) (K + \alpha (K - K_d))} \\ & \leq B_f ((B_m + G_m) (B_f (1 + \alpha) + B_m + G_m) - \alpha J_m K_d) \end{aligned} \quad (5.23)$$

which indicates  $(B_m + G_m) > 0$ .

3) Any poles of  $Z(s)$  on the imaginary axis are simple with positive and real residues. If  $B_m + G_m + B_f(\alpha + 1)$  and  $(\alpha + 1)$  are positive, then the only possible root on the imaginary axis is at zero with a residue of  $\frac{\alpha}{\alpha+1} K_d$ . Note that  $B_m + G_m + B_f(\alpha + 1) > 0$ , since Eqn. (5.23) implies that  $(B_m + G_m) > 0$ , and  $(\alpha + 1) > 0$  due to the stability condition. When  $(\alpha + 1) = 0$ , the output impedance transfer function becomes equal to  $\frac{B_f J_m s^3 + (B_f (B_m + G_m) + J_m K) s^2 + (K (B_m + G_m) - B_f K_d) s - K K_d}{J_m s^3 + (B_m + G_m) s^2}$  and Condition 3 of Theorem 1 is violated as double poles exist at  $s = 0$ . Hence, when  $(\alpha + 1) = 0$ , passive virtual springs cannot be rendered.

□

### 5.2.1 Passive Physical Equivalent:

A realization of Eqn. (5.18) characterizing SDEA under VSIC during spring rendering when both controllers are proportional is presented in Figure 5.2, where  $c_{1s} = \frac{K_d \alpha (B_f (B_m + G_m) - J_m K)}{B_f K (\alpha + 1)^2}$ ,  $b_{1s} = \frac{K_d \alpha (B_f (B_m + G_m) - J_m K)}{K^2 (\alpha + 1)^2}$ , and  $\sigma = \frac{1}{\alpha + 1} - \frac{\alpha}{(\alpha + 1)^2} \frac{K_d}{K}$ .

For the realization in Figure 5.2 to be feasible, all of components of the model should be non-negative. Hence,  $(\alpha + 1)$  should be non-negative. Furthermore, the non-negativeness of the right spring imposes the condition expressed in Eqn. (5.22). The non-negativeness  $\sigma(B_m + G_m)$  is guaranteed if  $(B_m + G_m) \geq 0$  and Eqn. (5.22) are simultaneously satisfied. As  $\frac{\alpha}{\alpha+1} K_d$  approaches to zero, the outer spring which represents the virtual stiffness to be rendered, converges to zero. The conditions for non-negativeness of  $c_{1s}$  and  $b_{1s}$  can be derived as

$$J_m \frac{K}{B_f} \leq (B_m + G_m) \quad (5.24)$$

which indicates  $(B_m + G_m) > 0$ .

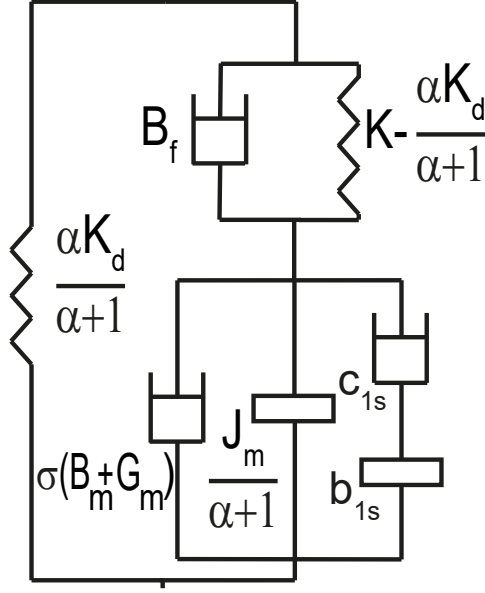


Figure 5.2 Realization of SDEA under VSIC during spring rendering when controllers are P

### 5.2.2 Feasibility of Passive Realization vs Passivity

The feasibility conditions for the realization in Figure 5.2 provide sufficient conditions for passivity of Eqn. (5.18). This can be shown by first considering a sufficient condition for passivity that is ensured by imposing a non-negative value to  $d_4$  as follows

$$J_m \leq \frac{(B_m + G_m)(B_m + G_m + B_f(\alpha + 1))}{\alpha K_d} \quad (5.25)$$

Note that replacing the condition provided in Eqn. (5.23) with the non-negativeness of  $d_4$  provide (more conservative) sufficient condition for passivity. This condition still needs to be considered together with the other necessary conditions of non-negative  $d_2$  and  $d_6$ . Eqns. (5.24) and (5.25) can be arranged together as

$$J_m \leq \frac{(B_m + G_m) B_f}{K} \leq \frac{(B_m + G_m)(B_m + G_m + B_f(\alpha + 1))}{\alpha K_d} \quad (5.26)$$

Given Eqn. (5.22) as necessitated by the feasibility of the realization in Figure 5.2 and the passivity of Eqn. (5.18), this inequality is always satisfied. Therefore, Eqn. (5.24) is a more conservative sufficient condition than the one provided in Eqn. (5.25) and when Eqn. (5.24) is satisfied, Eqn. (5.23) is guaranteed to hold.

Hence, the realization in Figure 5.2 is feasible and the sufficient conditions for passivity of Eqn. (5.18) are satisfied if the  $(B_m + G_m)$ ,  $(\alpha + 1)$ , and  $\frac{\alpha}{\alpha+1} K_d$  are positive, and Eqn. (5.24) is satisfied. If Eqn. (5.23) replaced with Eqn. (5.24), then the necessary and sufficient conditions for passivity of Eqn. (5.18) can be recovered.



### 5.2.3 Haptic Rendering Performance

Physical realization of SDEA during ideal spring rendering is related to that of SEA in a number of ways. Similar to the case for SEA, Figure 5.2 indicates two branches in parallel: an ideal spring  $\frac{\alpha K_d}{(\alpha+1)}$  whose stiffness approaches to the desired spring  $K_d$  as the controller gains gets large and parasitic dynamics governed by damper-inertance elements that are serially coupled to the system with a spring-damper pair in parallel. The main differences are due to the physical filter damping  $B_f$  appearing in parallel to the coupling spring  $K - \frac{\alpha K_d}{(\alpha+1)}$  and the more complicated form of the parasitic damper-inertance dynamics.

Existence of the physical filter damping  $B_f$  in parallel to the coupling spring indicates that, unlike the case in SEA, the parasitic dynamics cannot be completely decoupled from the system as the as the controller gains  $G_t$  and  $G_m$  increase, since  $B_f$  term dominates the coupling at intermediate and high frequencies. Similar to the case with SEA, Figure 5.2 indicates that the parasitic effect of the damper  $\sigma(B_m + G_m)$  and inerter  $J_m/(\alpha + 1)$  terms decrease with the choice of high controller gains. Once again,  $G_t$  has a more dominant effect on the damper term, while  $G_m$  and  $G_t$  gains affect the inerter term in the same manner, as their effects are multiplicative. In comparison with Figure 4.1, Figure 5.2 indicates that the addition of an physical damping  $B_f$  to the filter appends the parastic dissipation effects by introducing a serial damper-inerter term that introduces frequency dependent dissipation to the system whose effect increases with frequency.

Since the high frequency dynamics of SDEA is governed by the damping of the physical filter, all Bode plots converges to this dynamics. Along these lines, high frequency behaviour of SDEA is significantly different from that of SEA.

### 5.2.4 Effective Impedance Analysis

Effective impedance analysis of the parasitic dynamics of the realization in Figure 5.2. In particular, the effective damping for Eqn. (5.18) after removing the serial coupling filter  $B_f - (K - \frac{\alpha K_d}{(\alpha+1)})$  pair and the rendered stiffness  $\frac{\alpha K_d}{(\alpha+1)}$  can be computed as

$$c_{effPP}^{SDEA} = \frac{B_f (B_f (B_m + G_m)(\alpha + 1) - J_m K_d \alpha) \omega^2 + K (K (B_m + G_m)(\alpha + 1) - K_d \alpha (B_m + G_m))}{B_f^2 (\alpha + 1)^2 \omega^2 + K^2 (\alpha + 1)^2} \quad (5.27)$$

At low frequencies (as  $\omega \rightarrow 0$ ), Eqn. (5.27) converges to  $\sigma(B_m + G_m)$ . At high frequencies (as  $\omega \rightarrow \infty$ ), Eqn. (5.27) approaches to  $\sigma(B_m + G_m) + c_{1s}$ .

Similarly, the effective inertence for the parasitic dynamics of Eqn. (5.18) can be

computed as

$$b_{effPP}^{SDEA} = \frac{\left(B_f^2 J_m(\alpha + 1)\right) \omega^2 + J_m K^2(\alpha + 1) + B_f K_d \alpha (B_m + G_m) - J_m K K_d \alpha}{B_f^2 (\alpha + 1)^2 \omega^2 + K^2 (\alpha + 1)^2} \quad (5.28)$$

At low frequencies (as  $\omega \rightarrow 0$ ), Eqn. (5.28) converges to  $\frac{J_m}{\alpha+1} + b_{1s}$ . At high frequencies (as  $\omega \rightarrow \infty$ ), Eqn. (5.28) approaches to  $\frac{J_m}{\alpha+1}$ .

Hence, similar to the case with SEA, ideal spring impedance rendering performance at the low frequency range is dominated by the parasitic damping of  $\sigma(B_m + G_m)$ , while a parasitic inertance of  $\frac{J_m}{(\alpha+1)} + b_{1s}$  acts at this frequency range. Hence, parasitic damping at low frequencies can be effectively attenuated by the force controller  $G_t$ . Similarly, the parasitic inertance  $\frac{J_m}{(\alpha+1)}$  at the high frequency range can be attenuated by  $G_t$  and  $G_m$  gains.

### 5.3 Null Impedance Rendering

When the force and the motion controllers taken as proportional (P) controllers, the impedance at the interaction port of SDEA under VSIC during null impedance rendering equals to

$$Z_{null}^{SDEA^{P-P}}(s) = \frac{B_f J_m s^2 + (B_f (B_m + G_m) + J_m K) s + K(B_m + G_m)}{J_m s^2 + (B_f (1 + \alpha) + B_m + G_m) s + K(\alpha + 1)} \quad (5.29)$$

where  $\alpha = G_t G_m$ . Note that when  $(\alpha + 1) = 0$ , Eqn. (5.29) equals to  $B_f + \frac{K}{s}$ , which is passive.

The passivity of  $Z_{null}^{SDEA^{P-P}}(s)$  is checked according to Theorem 1. Theorem 7 presents necessary and sufficient conditions for one-port passivity of SDEA under VSIC while rendering null impedance, when  $G_t$  and  $G_m$  consist of proportional gains and without imposing non-negative controller gains.

**Theorem 7.** *Consider null impedance rendering for SEA under VSIC as in Figure 3.2, where  $G_t$  and  $G_m$  consist of proportional gains. Let physical plant parameters be positive, while the controller gains are allowed to be negative. Then, the following expressions constitute necessary and sufficient conditions for passivity of  $Z_{null}^{SDEA^{P-P}}(s)$ .*

$$(i) \quad (B_m + G_m) \geq 0, \text{ and}$$

$$(ii) \quad \alpha + 1 \geq 0.$$

*Proof.* 1)  $Z(s)$  has no poles in the right half plane. If we apply Routh-Hurwitz stability criterion,  $Z_{null}^{SDEA^{P-P}}(s)$  has no poles in the right half plane if  $B_m + G_m + B_f(\alpha + 1)$  and  $(\alpha + 1)$  are non-negative.

2)  $Re[Z(jw)] \geq 0$  for all  $w$ . Invoking Lemma 1, the sign of  $Re[Z_{null}^{SDEA^{P-P}}(jw)]$  can be checked by the sign of  $H(jw) = d_4 w^4 + d_2 w^2 + d_0$  where

$$d_0 = K^2 (\alpha + 1) (B_m + G_m) \quad (5.30)$$

$$d_2 = B_f (B_m + G_m) (B_m + G_m + B_f(\alpha + 1)) \quad (5.31)$$

$$d_4 = B_f J_m^2 \quad (5.32)$$

$Re[Z_{null}^{SDEA^{P-P}}]$  is non-negative if  $B_m + G_m + B_f(\alpha + 1)$ ,  $(\alpha + 1)$ , and  $(B_m + G_m)$  are non-negative.

3) Any poles of  $Z(s)$  on the imaginary axis are simple with positive and real residues. When  $B_m + G_m + B_f(\alpha + 1)$  and  $(\alpha + 1)$  are posi-

tive, this condition is satisfied. For the special case, when  $(\alpha + 1) = 0$ , Eqn. (5.29) reduces to  $B_f + \frac{K}{s}$ , which is always passive. There exists a pole on the imaginary axis when  $B_m + G_m + B_f(\alpha + 1) = 0$ . However,  $B_m + G_m + B_f(\alpha + 1) = 0$ , if and only if  $(\alpha + 1) = 0$ , since  $(B_m + G_m) \geq 0$  and  $(\alpha + 1) \geq 0$ .  $\square$

### 5.3.1 Passive Physical Equivalent:

A realization of Eqn. (5.29) characterizing SDEA under VSIC during null impedance rendering when both controllers are proportional is presented in Figure 5.3.

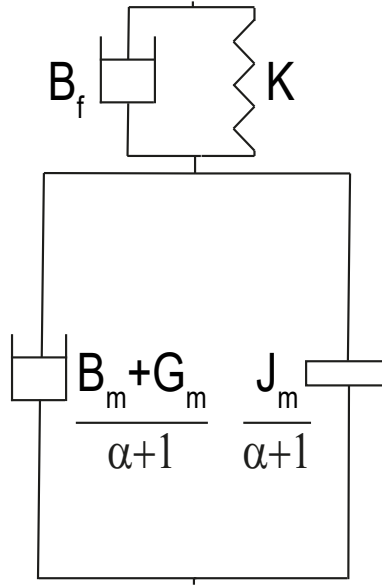


Figure 5.3 Realization of SDEA under VSIC during null impedance rendering when both controllers are P

For the realization in Figure 5.3 to be feasible, all physical components in the model should be non-negative, that is,  $(B_m + G_m)$  and  $(\alpha + 1)$  should be non-negative.

### 5.3.2 Feasibility of Passive Realization vs Passivity

The conditions for feasibility of realization in Figure 5.3 are equivalent to the necessary and sufficient conditions for passivity of Eqn. (5.29) according to Theorem 1: if  $(B_m + G_m) \geq 0$  and  $(\alpha + 1) \geq 0$ , then Eqn. (5.29) is passive and all components in Figure 5.3 are non-negative.

### 5.3.3 Haptic Rendering Performance

Physical realization of SDEA during null impedance rendering is identical to that of SEA, except the fact that the physical filter of SDEA includes a physical damping

term  $B_f$  parallel to the physical spring  $K$ . Similar to the case with SEA, Figure 5.3 indicates that the parasitic effect of the damper  $(B_m + G_m)/(\alpha + 1)$  and inerter  $J_m/(\alpha + 1)$  terms decrease with choice of high controller gains for SDEA during null impedance rendering when both controllers are P.  $G_t$  has a more dominant effect on the damper term, while  $G_m$  and  $G_t$  gains affect the inerter term in the same manner, as their effects are multiplicative.

### 5.3.4 Effective Impedance Analysis

The effective impedance of the controllable part of the realization in Figure 5.3, that is, the remaining system dynamics after the serial physical filter consisting of  $K$ - $B_f$  terms is extracted, is dominated by the damper term  $(B_m + G_m)/(\alpha + 1)$  in the low frequency range. Therefore, the null impedance rendering performance can be increased in the low frequency range by attenuating the affects of this damper term. Similarly, the high frequency behaviour of the parasitic dynamics is dictated by the inerter  $J_m/(\alpha + 1)$  term.

## 5.4 Discussion

We have presented passivity analysis of SdEA under VSIC during null impedance, spring rendering, and Voigt model rendering. Also, we have provided passive physical equivalents of SDEA under VSIC during null impedance, spring rendering, and Voigt model rendering. Through passive physical equivalents, we have provided analysis of effective impedance and haptic rendering performance. It is important to note that, in general, passive physical realizations for a given impedance transfer function are not unique. Similarly Section 4.4, Figure 5.4 depicts alternative passive physical equivalents for the impedance in Eqn. (5.18) for SDEA under VSIC during spring rendering when both controllers are P. Here, Figures 5.4a and 5.4b complement each other to provide the same sufficient conditions as presented for Figure 5.2.

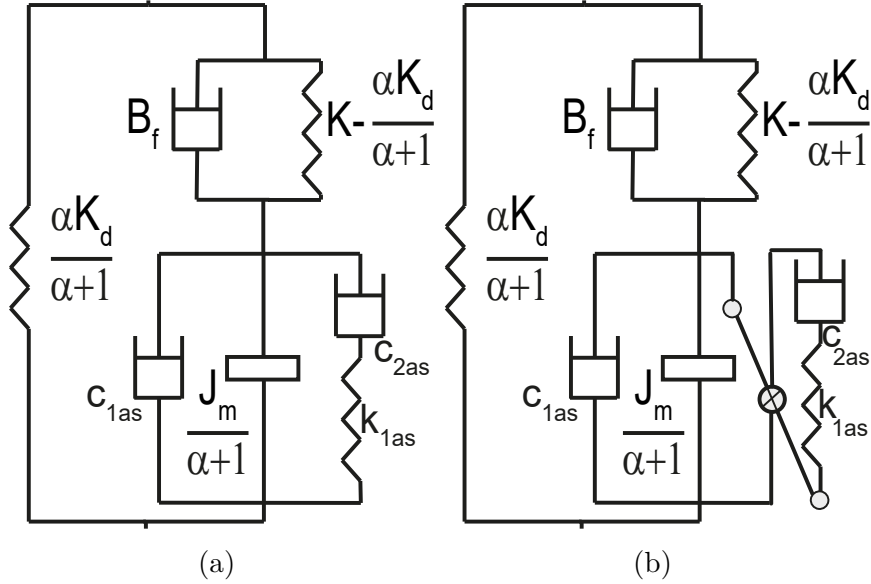


Figure 5.4 Alternative passive physical equivalents of SDEA under VSIC during spring rendering when both controllers are P

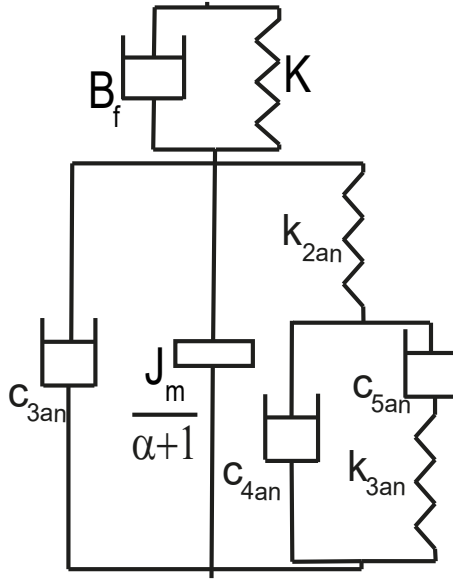


Figure 5.5 Passive physical equivalent of SDEA under VSIC during null impedance rendering when both controllers are PI

Realizations become more complicated as controllers become more involved, making their interpretation harder. For instance, Figure 5.5 presents passive physical realizations for SDEA under VSIC during null impedance rendering, when both controllers are PI.

# Chapter 6

## Passivity Analysis and Passive Physical Equivalents of SDEA<sub>K<sub>fb</sub></sub>

In this chapter, we study the effect of omitting the damping force induced on the serial compliant element in closed-loop control, and provide necessary and sufficient conditions for the passivity and passive physical equivalents of interaction when only the deflections of the serial elastic element is used to estimate the interaction forces. This model, depicted in Figure 3.3 and named SDEA<sub>K<sub>fb</sub></sub>, captures the most common implementations of SEA, where the inherent damping effect on the serial elastic element is ignored. Furthermore, effective impedance and haptic rendering analyses are made through passive physical equivalents. Also, we compare the passivity bounds of SDEA<sub>K<sub>fb</sub></sub> with SDEA.

### 6.1 Voigt Model Rendering

The impedance at the interaction port of SDEA<sub>K<sub>fb</sub></sub> under VSIC during Voigt model rendering when both controllers are proportional is  $Z_{Voigt}^{SDEA_{K_{fb}}}(s) =$

$$\frac{B_f J_m s^3 + (B_f(B_m + G_m + B_d \alpha) + J_m K) s^2 + (K(B_m + G_m) + \alpha(B_d K + B_f K_d)) s + K K_d \alpha}{J_m s^3 + (B_f + B_m + G_m) s^2 + K(1 + \alpha) s} \quad (6.1)$$

where  $\alpha = G_m G_t$ . The passivity of  $Z_{Voigt}^{SDEA_{K_{fb}}}(s)$  is checked according to Theorem 1. Theorem 8 presents necessary and sufficient conditions for one-port passivity of SDEA<sub>K<sub>fb</sub></sub> under VSIC while rendering Voigt model, when  $G_t$  and  $G_m$  consist of proportional gains.

**Theorem 8.** *Consider Voigt model rendering for SDEA<sub>K<sub>fb</sub></sub> under VSIC as in Fig-*



ure 3.3, where  $G_t$  and  $G_m$  consist of proportional gains. Let all parameters be positive. Then, the following expressions constitute necessary and sufficient conditions for passivity of  $Z_{V_{oigt}}^{SDEA_{K_{fb}}}(s)$ .

$$(i) \ K \geq K_d \frac{\alpha}{(\alpha+1)} \frac{B_m+G_m-B_f\alpha}{B_m+G_m+B_d\alpha}, \text{ and}$$

$$(ii) -2\sqrt{\gamma} \leq B_f(B_m+G_m+B_d\alpha)(B_f+B_m+G_m) - \alpha J_m(B_f(K+K_d) + KB_d)$$

where

$$\begin{aligned} \gamma &= B_f J_m^2 (K(\alpha+1)(K(B_m+G_m+B_d\alpha) + B_f\alpha K_d) \\ &\quad - \alpha K K_d (B_f+B_m+G_m)). \end{aligned}$$

*Proof.* 1)  $Z(s)$  has no poles in the right half plane. If we apply Routh-Hurwitz stability criterion,  $Z_{V_{oigt}}^{SDEA_{K_{fb}}}(s)$  has no poles in the open right half plane, since all coefficients of denominator of  $Z_{V_{oigt}}^{SDEA_{K_{fb}}}(s)$  are positive.

2)  $Re[Z(jw)] \geq 0$  for all  $w$ . Invoking Lemma 1, the sign of  $Re[Z_{V_{oigt}}^{SDEA_{K_{fb}}}(jw)]$  can be checked by the sign of  $H(jw) = d_6w^6 + d_4w^4 + d_2w^2$ , where

$$d_2 = K(K(B_m+G_m+B_d\alpha) + B_f K_d \alpha)(\alpha+1) - K K_d \alpha (B_f+B_m+G_m) \quad (6.2)$$

$$d_4 = B_f(B_f+B_m+G_m)(B_m+G_m+B_d\alpha) - J_m \alpha (K(B_d+B_f) + B_f K_d) \quad (6.3)$$

$$d_6 = B_f J_m^2 \quad (6.4)$$

Here,  $d_6$  is positive, since  $B_f$  is positive. The non-negativeness of  $d_2$  imposes the following constraint:

$$K \geq K_d \frac{\alpha}{(\alpha+1)} \frac{B_m+G_m-B_f\alpha}{B_m+G_m+B_d\alpha} \quad (6.5)$$

The last necessary and sufficient condition can be derived as:

$$-2\sqrt{\gamma} \leq \frac{B_f(B_m+G_m+B_d\alpha)(B_f+B_m+G_m)}{-\alpha J_m(B_f(K+K_d) + KB_d)} \quad (6.6)$$

where  $\gamma = B_f J_m^2 (K(\alpha+1)(K(B_m+G_m+B_d\alpha) + B_f\alpha K_d) - \alpha K K_d (B_f+B_m+G_m))$ .

Accordingly, Eqns. (6.5) and (6.6) provide the necessary and sufficient conditions to ensure that  $Re[Z_{V_{oigt}}^{SDEA_{K_{fb}}}(jw)] > 0$ . Together with Eqn. (6.5), a simpler but more conservative set of sufficient conditions can be derived by imposing non-negativeness of  $d_4$  instead of Eqn. (6.6) as follows:

$$J_m \leq \frac{B_f (B_f + B_m + G_m) (B_m + G_m + B_d \alpha)}{\alpha (K (B_d + B_f) + B_f K_d)} \quad (6.7)$$

3) Any poles of  $Z(s)$  on the imaginary axis are simple with positive and real residues. There exists no poles on the imaginary axis, except at  $s = 0$ , as long as all controller gains and physical parameters are positive. For the pole at  $s = 0$ , the residue equals to  $\frac{\alpha}{\alpha+1} K_d$ , which is positive for positive controller gains.

Eqn. (6.5) and Eqn. (6.6) are necessary and sufficient condition for passivity of Eqn. (6.1) when all parameters are positive.  $\square$

### 6.1.1 Passive Physical Equivalent

A realization of Eqn. (6.1) characterizing  $SDEA_{K_{fb}}$  under VSIC during Voigt model rendering when both controllers are proportional is presented in Figure 6.1. The parameters of this realization include  $k_{1v} = K - \frac{K_d \alpha}{\alpha+1} - \frac{B_f (B_f - B_d \alpha)}{J_m}$  and  $c_{2v} = \frac{B_m - B_f + G_m + B_d \alpha - B_f \alpha}{\alpha+1} - \frac{K_d \alpha (B_m + G_m - B_f \alpha)}{K (\alpha+1)^2}$ . The rest of terms are long and complicated; hence, are presented as a Matlab script that allows for a numerical means of checking for the non-negativeness of each element<sup>1</sup>.

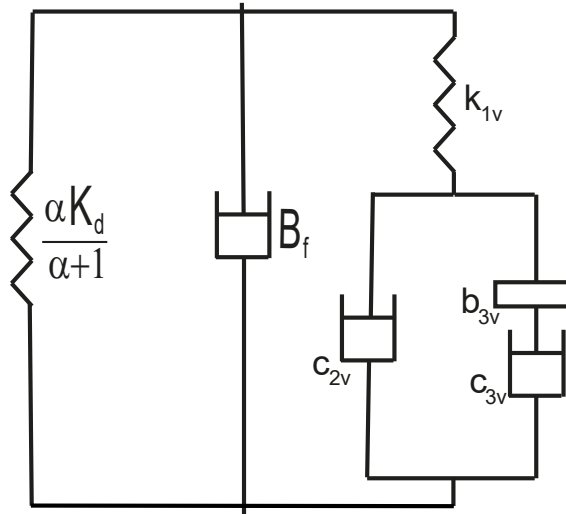


Figure 6.1 Passive physical equivalent of  $SDEA_{K_{fb}}$  under VSIC during Voigt model rendering

<sup>1</sup>The Matlab script that presents parameters of the realization in Figure 6.1 is available for download at xxxxx.

### 6.1.2 Haptic Rendering Performance

Physical realization of  $\text{SDEA}_{K_{fb}}$  during Voigt model rendering in Figure 6.1 indicates three main branches in parallel: a spring-damper pair  $\left(\frac{\alpha}{(\alpha+1)} K_d\right) - B_f$  in parallel, and a branch capturing the parasitic dynamics governed by a complex topology of damper-inertance terms that are coupled to the system in series through a spring. The parallel spring-damper pair of  $\left(\frac{\alpha}{(\alpha+1)} K_d\right) - B_f$  indicates that, while  $\text{SDEA}_{K_{fb}}$  can render the desired spring levels, it cannot render the desired damping, since the controller terms have no effect on  $B_f$ . Accordingly,  $\text{SDEA}_{K_{fb}}$  cannot render desired Voigt models, unlike SDEA which has direct control over the desired damping term in addition to the spring term. According to the  $\text{SDEA}_{K_{fb}}$  realization, the uncontrollable damping term  $B_f$  acts as a parasitic effect working against the rendering performance.

For the physical realization of  $\text{SDEA}_{K_{fb}}$ , the coupling filter consists of the spring  $k_{1v}$  whose stiffness can get large for large controller gains or  $B_d$ . Hence, unlike the case for SDEA, larger controller gains do not necessarily decouple the parasitic dynamics from the rendered impedance for  $\text{SDEA}_{K_{fb}}$ . When the coupling is strong, the parasitic dissipation effects due to the last branch in the  $\text{SDEA}_{K_{fb}}$  realization can be split into two parts: a damper  $c_{2v}$  and a serial damper-inerter term that introduces frequency dependent dissipation that increases with frequency. Unlike in the SDEA realization,  $\text{SDEA}_{K_{fb}}$  does not have a pure inerter term that dominates the parasitic dynamics at high frequencies.

The third row of Table 8.1 presents realizations for  $\text{SDEA}_{K_{fb}}$  while rendering Voigt, spring, and null impedance models. Table 8.1 indicates that there exists continuity among the realizations; that is, one can recover the realization of ideal spring rendering with  $\text{SDEA}_{K_{fb}}$  from the realization of Voigt model rendering with  $\text{SDEA}_{K_{fb}}$  by setting  $B_d = 0$ , while the realization of null impedance rendering with  $\text{SDEA}_{K_{fb}}$  can be recovered from the realization of Voigt model rendering with  $\text{SDEA}_{K_{fb}}$  by setting  $B_d = 0$  and  $K_d = 0$ . Similarly, realizations with SEA can also be recovered from the  $\text{SDEA}_{K_{fb}}$  realizations by simply setting  $B_f = 0$ .

### 6.1.3 Effective Impedance Analysis

Further insights may be gained about the parasitic dynamics by studying the effective impedance of the realization. Effective impedance analysis of the realization in Figure 6.1, after removing  $\left(\frac{\alpha}{(\alpha+1)} K_d\right) - B_f$  and the serial coupling filter  $k_{1v}$ , indicates that, at low frequencies (as  $\omega \rightarrow 0$ ), the effective damping of the parasitic dynamics converges to  $c_{2v}$ , while at high frequencies (as  $\omega \rightarrow \infty$ ), the effective damping of

the parasitic dynamics approaches to  $c_{2v} + c_{3v}$ .

Similarly, the effective inertance of the parasitic dynamics at low frequencies (as  $\omega \rightarrow 0$ ) converges to  $b_{3v}$ , while at high frequencies (as  $\omega \rightarrow \infty$ ), the effective inertance of the parasitic dynamics approaches to zero.

Accordingly, in addition to the parasitic effect of  $B_f$ , through the coupling spring, the parasitic damping of  $c_{2v}$  affects the Voigt model rendering performance at the low frequency range, while a parasitic inertance of  $b_{3v}$  also acts at this frequency range. The effective parasitic damping increases with frequency and  $c_{2v}$  is added to  $c_{3v}$  at the high frequency range. On the other hand, the effective parasitic inertance decreases to zero with increasing frequency.

Comparison of the effective impedance of the realization of  $\text{SDEA}_{K_{fb}}$  with SDEA at the high frequency range indicates that the effective inertance of the parasitic dynamics of  $\text{SDEA}_{K_{fb}}$  goes to zero, while the effective inertance of the parasitic dynamics of SDEA at the high frequency goes to  $b_{1v}$ ; hence, the effective inertance of the parasitic dynamics for SDEA is higher than that of  $\text{SDEA}_{K_{fb}}$ . A numerical comparison of the effective damping of  $\text{SDEA}_{K_{fb}}$  with SDEA at the low frequency range is presented in Chapter 8.

#### 6.1.4 Comparison of Passivity Bounds of $\text{SDEA}_{K_{fb}}$ with SDEA

Comparison of the necessary conditions presented in Eqns. (5.5) and (6.5) that impose upper bounds on  $K_d$  for SDEA and  $\text{SDEA}_{K_{fb}}$  respectively, indicates that the bound for  $\text{SDEA}_{K_{fb}}$  is more relaxed as follows:

$$K \geq K_d \frac{\alpha}{(\alpha + 1)} \frac{B_m + G_m}{B_m + G_m + B_d \alpha} \geq K_d \frac{\alpha}{(\alpha + 1)} \frac{B_m + G_m - B_f \alpha}{B_m + G_m + B_d \alpha} \quad (6.8)$$

Accordingly, Eqn. (6.8) shows that  $\text{SDEA}_{K_{fb}}$  can passively render virtual springs  $K_b$  that are stiffer than the virtual springs that can be passively rendered by SDEA.

Comparison of the sufficient conditions of SDEA and  $\text{SDEA}_{K_{fb}}$  presented in Eqns. (5.7) and (6.7) indicate that

$$\begin{aligned} J_m &\leq \frac{B_f (B_m + G_m + B_d \alpha) [B_m + G_m + B_f (1 + \alpha)]}{(B_f K_d + B_d K) \alpha} \\ &\leq \frac{B_f (B_m + G_m + B_d \alpha) (B_m + G_m + B_f)}{[B_f K_d + K (B_d + B_f)] \alpha} \end{aligned} \quad (6.9)$$

Consequently, while  $\text{SDEA}_{K_{fb}}$  can passively render more stiff virtual spring compared to SDEA according to Eqn. (6.8),  $\text{SDEA}_{K_{fb}}$  also possesses a more strict passivity bound on  $J_m$  as expressed in Eqn. (6.9).

## 6.2 Ideal Spring Rendering

When  $B_d = 0$  in Eqn. (6.1), the output impedance transfer function becomes equal to the transfer function for the ideal spring rendering. The impedance at the interaction port of  $SDEA_{K_{fb}}$  under VSIC during ideal spring rendering becomes  $Z_{spring}^{SDEA_{K_{fb}}}(s) =$

$$\frac{B_f J_m s^3 + (B_f B_m + B_f G_m + J_m K) s^2 + (B_m K + G_m K + B_f \alpha K_d) s + \alpha K K_d}{J_m s^3 + (B_f + B_m + G_m) s^2 + K (1 + \alpha) s} \quad (6.10)$$

where  $\alpha = G_m G_t$ . The passivity of  $Z_{spring}^{SDEA_{K_{fb}}}(s)$  is checked according to Theorem 1. Theorem 9 presents necessary and sufficient conditions for one-port passivity of  $SDEA_{K_{fb}}$  under VSIC while rendering spring, when  $G_t$  and  $G_m$  consist of proportional gains.

**Theorem 9.** *Consider spring rendering for  $SDEA_{K_{fb}}$  under VSIC as in Figure 3.3, where  $G_t$  and  $G_m$  consist of proportional gains. Let all parameters be positive. Then, the following expressions constitute necessary and sufficient conditions for passivity of  $Z_{spring}^{SDEA_{K_{fb}}}(s)$ .*

- (i)  $K \geq K_d \frac{\alpha}{(\alpha+1)} \frac{(B_m+G_m-B_f \alpha)}{(B_m+G_m)}$ , and
  - (ii)  $-2 \sqrt{\gamma} \leq B_f (B_m + G_m) (B_f + B_m + G_m) - B_f \alpha J_m (K + K_d)$
- where
- $$\gamma = B_f J_m^2 (K (\alpha + 1) (K (B_m + G_m) + B_f \alpha K_d) - \alpha K K_d (B_f + B_m + G_m)).$$

*Proof.* 1)  $Z(s)$  has no poles in the right half plane. If we apply Routh-Hurwitz stability criterion,  $Z_{spring}^{SDEA_{K_{fb}}}(s)$  has no poles in the open right half plane, since all coefficients of denominator of  $Z_{spring}^{SDEA_{K_{fb}}}(s)$  are positive.

2)  $Re[Z(jw)] \geq 0$  for all  $w$ . Invoking Lemma 1, the sign of  $Re[Z_{spring}^{SDEA_{K_{fb}}}(jw)]$  can be checked by the sign of  $H(jw) = d_6 w^6 + d_4 w^4 + d_2 w^2$ , where

$$d_2 = K(\alpha + 1)[K(B_m + G_m) + B_f \alpha K_d] - \alpha K K_d (B_m + G_m + B_f) \quad (6.11)$$

$$d_4 = B_f [(B_m + G_m)(B_m + G_m + B_f) - \alpha J_m (K + K_d)] \quad (6.12)$$

$$d_6 = B_f J_m^2 \quad (6.13)$$

Applying Lemma 3,  $d_6$  is positive, since  $B_f$  is positive. The non-negativeness of  $d_2$  imposes the following constraint:

$$K \geq K_d \frac{\alpha}{(\alpha+1)} \frac{(B_m + G_m - B_f \alpha)}{(B_m + G_m)} \quad (6.14)$$

The last necessary and sufficient condition can be derived as:

$$-2\sqrt{\gamma} \leq B_f (B_m + G_m) (B_f + B_m + G_m) - B_f \alpha J_m (K + K_d) \quad (6.15)$$

where  $\gamma = B_f J_m^2 (K (\alpha + 1) (K (B_m + G_m) + B_f \alpha K_d) - \alpha K K_d (B_f + B_m + G_m))$ .

A simpler but more conservative set of sufficient conditions can be expressed by using Eqn. (6.14) together with Eqn. (6.16) instead of Eqn. (6.15) as follows

$$J_m \leq \frac{(B_m + G_m) (B_m + G_m + B_f)}{(K_d + K) \alpha} \quad (6.16)$$

□

### 6.2.1 Passive Physical Equivalent:

A realization of Eqn. (6.10) characterizing  $\text{SDEA}_{K_{fb}}$  under VSIC during ideal spring rendering when both controllers are proportional is presented in Figure 6.2. The parameters of this realization include  $k_{1s} = K - \frac{B_f^2}{J_m} - \frac{K_d \alpha}{\alpha+1}$ ,  $c_{2s} = \frac{B_m + G_m}{\alpha+1} - B_f - \frac{K_d \alpha (B_m + G_m - B_f \alpha)}{K (\alpha+1)^2}$ . The rest of terms are still complicated and presented as a Matlab script which is presented before with giving  $B_d = 0$ .

### 6.2.2 Haptic Rendering Performance

Physical realization of  $\text{SDEA}_{K_{fb}}$  during ideal spring rendering in Figure 6.2 indicates three main branches in parallel: a spring-damper pair  $\left(\frac{\alpha}{(\alpha+1)} K_d\right) - B_f$  in parallel, and a branch capturing the parasitic dynamics governed by a complex topology of damper-inertance terms that are coupled to the system in series through a spring. The parallel spring-damper pair of  $\left(\frac{\alpha}{(\alpha+1)} K_d\right) - B_f$  indicates that, while  $\text{SDEA}_{K_{fb}}$  can render desired spring levels and the controller terms have no affect on  $B_f$ . Accordingly,  $\text{SDEA}_{K_{fb}}$  can render desired ideal spring like SDEA. According to the  $\text{SDEA}_{K_{fb}}$  realization, the uncontrollable damping term  $B_f$  acts as a parasitic effect working against rendering performance.

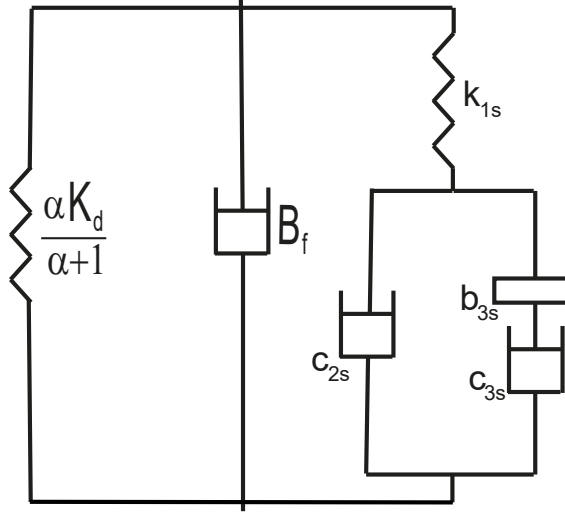


Figure 6.2 Passive physical equivalent of  $\text{SDEA}_{K_{fb}}$  under VSIC during ideal spring rendering

### 6.2.3 Effective Impedance Analysis

Further insights may be gained about the parasitic dynamics by studying the effective impedance of the realization. Effective impedance analysis of the realization in Figure 6.2, after removing  $\left(\frac{\alpha}{(\alpha+1)} K_d\right) - B_f$  and the serial coupling filter  $k_{1s}$ , indicates that at low frequencies (as  $\omega \rightarrow 0$ ) the effective damping of the parasitic dynamics converges to  $c_{2s}$ . At high frequencies (as  $\omega \rightarrow \infty$ ), the effective damping of the parasitic dynamics approaches to  $c_{2s} + c_{3s}$ .

Similarly, the effective inertance of the parasitic dynamics at low frequencies (as  $\omega \rightarrow 0$ ) converges to  $b_{3s}$ . At high frequencies (as  $\omega \rightarrow \infty$ ), the effective inertance of the parasitic dynamics approaches to 0.

Accordingly, in addition to the parasitic effect of  $B_f$ , through the coupling spring, the parasitic damping of  $c_{2s}$  affects the spring rendering performance at the low frequency range, while a parasitic inertance of  $b_{3s}$  also acts at this frequency range. The effective parasitic damping increases with frequency and  $c_{2s}$  is added to  $c_{3s}$  at the high frequency range. On the other hand, the effective parasitic inertance decreases to zero with increasing frequency.

Comparison of the effective impedance of the realization of  $\text{SDEA}_{K_{fb}}$  with SDEA at the high frequency range indicates that the effective inertance of the parasitic dynamics of  $\text{SDEA}_{K_{fb}}$  goes to zero, while the effective inertance of the parasitic dynamics of SDEA at the high frequency goes to  $J_m/(\alpha + 1)$ ; hence, the effective inertance of the parasitic dynamics for SDEA is higher than that of  $\text{SDEA}_{K_{fb}}$ . A numerical comparison of the effective damping of  $\text{SDEA}_{K_{fb}}$  with SDEA at the low frequency range is presented in Chapter 8.



### 6.3 Null Impedance Rendering

When  $K_d = 0$  in Eqn. (6.10), the output impedance transfer function becomes equal to the transfer function for null impedance rendering. The impedance at the interaction port of  $SDEA_{K_{fb}}$  under VSIC during null impedance rendering becomes  $Z_{null}^{SDEA_{K_{fb}}}(s) =$

$$\frac{B_f J_m s^2 + (B_f B_m + B_f G_m + J_m K) s + K(B_m + G_m)}{J_m s^2 + (B_f + B_m + G_m) s + K(1 + \alpha)} \quad (6.17)$$

where  $\alpha = G_m G_t$ . The passivity of  $Z_{null}^{SDEA_{K_{fb}}}(s)$  is checked according to Theorem 1. Theorem 10 presents a necessary and sufficient condition for one-port passivity of  $SDEA_{K_{fb}}$  under VSIC while rendering null impedance, when  $G_t$  and  $G_m$  consist of proportional gains.

**Theorem 10.** *Consider null impedance rendering for  $SDEA_{K_{fb}}$  under VSIC as in Figure 3.3, where  $G_t$  and  $G_m$  consist of proportional gains. Let all parameters be positive. Then, the following expression constitute the necessary and sufficient condition for passivity of  $Z_{null}^{SDEA_{K_{fb}}}(s)$ .*

$$(i) \quad -2 J_m K \sqrt{B_f(\alpha + 1)(B_m + G_m)} \leq B_f((B_m + G_m)(B_f + B_m + G_m) - \alpha J_m K).$$

*Proof.* 1)  $Z(s)$  has no poles in the right half plane.  $Z_{null}^{SDEA_{K_{fb}}}(s)$  has no roots in the open right half plane if all coefficients of denominator of  $Z_{null}^{SDEA_{K_{fb}}}(s)$  are positive.

2)  $Re[Z(jw)] \geq 0$  for all  $w$ . Invoking Lemma 1, the sign of  $Re[Z_{null}^{SDEA_{K_{fb}}}(jw)]$  can be checked by the sign of  $H(jw) = d_4 w^4 + d_2 w^2 + d_0$  where

$$d_0 = K^2(\alpha + 1)(B_m + G_m) \quad (6.18)$$

$$d_2 = B_f(B_m + G_m)(B_f + B_m + G_m) - B_f \alpha J_m K \quad (6.19)$$

$$d_4 = B_f J_m^2 \quad (6.20)$$

From Lemma 3,  $d_0$  and  $d_4$  are always positive while gains are positive, while the following condition is also imposed: When all parameters are positive, the necessary and sufficient condition for the passivity of Eqn. (6.17) can be derived as

$$-2 J_m K \sqrt{B_f(\alpha + 1)(B_m + G_m)} \leq B_f((B_m + G_m)(B_f + B_m + G_m) - \alpha J_m K) \quad (6.21)$$

Hence, Eqn. (6.21) provides the necessary and sufficient condition for  $Re[Z_{null}^{SDEA_{K_{fb}}}(jw)]$ .

A simpler but more conservative sufficient condition can be provided as

$$J_m \leq \frac{(B_m + G_m)(B_f + B_m + G_m)}{\alpha K} \quad (6.22)$$

3) Any poles of  $Z(s)$  on the imaginary axis are simple with positive and real residues. There is a no poles on the imaginary axis while all controller gains and physical parameters are positive.  $\square$

### 6.3.1 Passive Physical Equivalent:

A realization of Eqn. (6.17) characterizing  $SDEA_{K_{fb}}$  under VSIC during null impedance rendering when both controllers are P is presented in Figure 6.3, where  $b_{1n} = \frac{B_f \alpha (B_m + G_m)}{K(\alpha + 1)^2} - \frac{\alpha J_m}{\alpha + 1}$  and  $c_{1n} = \frac{\alpha (B_m + G_m)}{\alpha + 1} - \frac{\alpha J_m K}{B_f}$ .

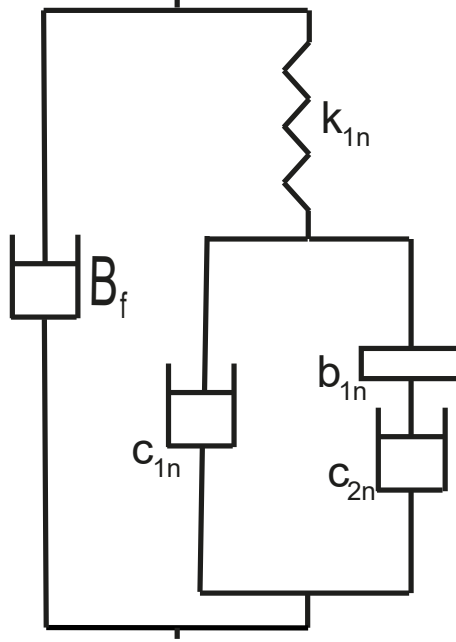


Figure 6.3 Passive physical equivalent of  $SDEA_{K_{fb}}$  under VSIC during null impedance rendering

For the realization in Figure 6.3 to be physically feasible, all components in the model should be non-negative. Non-negative controller gains and physical parameters guarantee non-negativeness of all components, except  $b_{1n}$  and  $c_{1n}$ . The non-negativeness of  $b_{1n}$  and  $c_{1n}$  imposes

$$J_m \leq \frac{B_f (B_m + G_m)}{K(\alpha + 1)} \quad (6.23)$$

Note that there exists an alternative passive physical equivalent of Eqn. (6.17) which possesses a more similar topology with the realization in Figure 6.2 with  $K_d = 0$ .

In this section, we have preferred to present the realization in Figure 6.3, as the parameters of this realization are less complicated, leading to more compact and intuitive symbolic expressions for passivity.

### 6.3.2 Feasibility of Passive Realization vs Passivity

Eqn. (6.23) imposes a constraint that is more conservative than the sufficiency condition in Eqn. (6.22). Therefore, Eqn. (6.23) not only ensures feasibility of the realization in Figure 6.3, but also provides a sufficient condition for passivity of Eqn. (6.17) when all gains and physical parameters are positive.

### 6.3.3 Haptic Rendering Performance

Physical realization of  $\text{SDEA}_{K_{fb}}$  during null impedance rendering in Figure 6.3 indicates two main branches in parallel: a damper  $B_f$ , and a branch capturing the parasitic dynamics governed by a complex topology of damper-inertance terms that are coupled to the system in series through a spring. A damper term  $B_f$  shows that the controller terms have no effect on  $B_f$ . According to the  $\text{SDEA}_{K_{fb}}$  realization, the uncontrollable damping term  $B_f$  acts as a parasitic effect working against rendering performance.

### 6.3.4 Effective Impedance Analysis

Further insights may be gained about the parasitic dynamics by studying the effective impedance of the realization. Effective impedance analysis of the realization in Figure 6.3, after removing  $B_f$  and the serial coupling filter  $k_{1n}$ , indicates that at low frequencies (as  $\omega \rightarrow 0$ ) the effective damping of the parasitic dynamics converges to  $c_{1n}$ . At high frequencies (as  $\omega \rightarrow \infty$ ), the effective damping of the parasitic dynamics approaches to  $c_{1n} + c_{2n}$ .

Similarly, the effective inertance of the parasitic dynamics at low frequencies (as  $\omega \rightarrow 0$ ) converges to  $b_{1n}$ . At high frequencies (as  $\omega \rightarrow \infty$ ), the effective inertance of the parasitic dynamics approaches to 0.

Accordingly, in addition to the parasitic effect of  $B_f$ , the parasitic damping of  $c_{1n}$  affects the null impedance rendering performance at the low frequency range, while a parasitic inertance of  $b_{1n}$  also acts at this frequency range. The effective parasitic damping increases with frequency and  $c_{1n}$  is added to  $c_{2n}$  at the high frequency range. On the other hand, the effective parasitic inertance decreases to zero with increasing frequency.

Comparison of the effective impedance of the realization of  $\text{SDEA}_{K_{fb}}$  with SDEA at the high frequency range indicates that the effective inertance of the parasitic dynamics of  $\text{SDEA}_{K_{fb}}$  goes to zero, while the effective inertance of the parasitic dynamics of SDEA at the high frequency goes to  $J_m/(\alpha + 1)$ ; hence, the effective inertance of the parasitic dynamics for SDEA is higher than that of  $\text{SDEA}_{K_{fb}}$ . A numerical comparison of the effective damping of  $\text{SDEA}_{K_{fb}}$  with SDEA at the low frequency range is presented in Chapter 8.

## 6.4 Discussion

We have provided necessary and sufficient conditions of  $SDEA_{Kfb}$  under VSIC during rendering Voigt model, spring, and null impedance. Also, we have provided passive physical equivalents of  $SDEA_{Kfb}$  under VSIC during rendering Voigt model, spring, and null impedance. Through passive physical equivalents, analysis of effective impedance and haptic rendering performance are provided. Furthermore, we compare the passivity bounds of SDEA and  $SDEA_{Kfb}$ .

In general, passive physical realizations for a given impedance transfer function are not unique and the feasibility conditions for a passive physical realization only provides sufficient conditions for passivity. Hence, the necessary conditions are not easy established through such analysis, as it requires studying feasibility of all passive physical realizations.

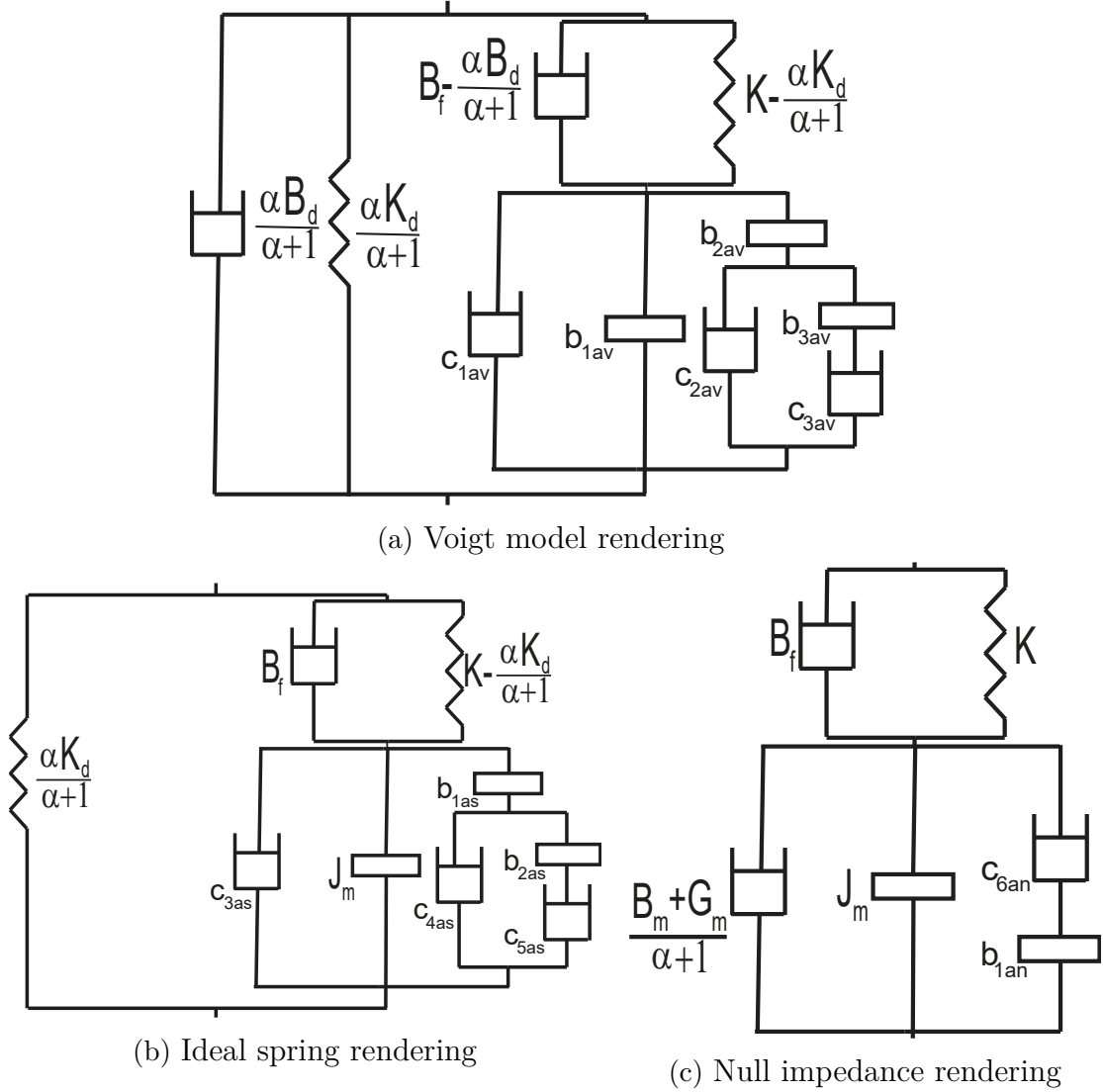


Figure 6.4 Alternative passive physical equivalents of  $SDEA_{Kfb}$

Figure 6.4 depicts alternative passive physical equivalents of  $\text{SDEA}_{K_{fb}}$  under VSIC during Voigt model, ideal spring, and null impedance rendering. In particular, Figure 6.4a and Figure 6.1 present the realizations for the impedance transfer function in Eqn. 6.1, Figure 6.4b and Figure 6.2 present the realizations for the ideal spring rendering when  $B_d$  is set to zero in Eqn. 6.1, and Figure 6.4c and Figure 6.3 present the realizations for null impedance rendering when  $B_d$  and  $K_d$  are set to zero in Eqn. 6.1. We have used in our analysis Figures 6.1, 6.2, and 6.3 instead of Figure 6.4a, 6.4b, and 6.4c because of simplicity of the terms and easier to give intuitive for performance comparison.  $B_f$  exists alone in Figures 6.1, 6.2, and 6.3 where we can easily see that  $B_f$  is not affected by any controller terms and parasitic effect of  $B_f$  for performance.

# Chapter 7

## Passivity Analysis and Passive Physical Equivalents of Reduce Order Model of Different Implementations of SEA

In this chapter, we study the effect of utilizing a reduce order model for SEA, SDEA, and  $SDEA_{K_{fb}}$ . In particular, in the reduce order model, depicted in Figure 7.1 and called  $SDEA_{K_{red}}$ , the inner motion controller is assumed to render the system into an ideal motion source and replaced with a low-pass filter of the form  $w_a/(s + w_a)$ , where  $w_a$  captures the bandwidth limitation of the motion controlled system.

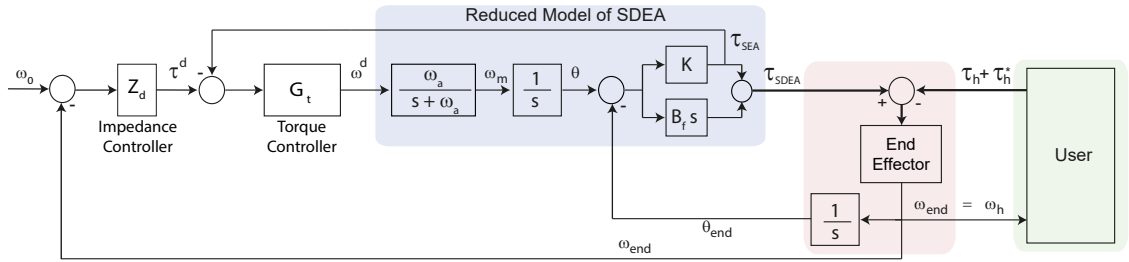


Figure 7.1 Block diagram of impedance control with reduce order model  $SDEA_{K_{red}}$ , for which the interaction forces are estimated by only utilizing the deflections of the physical spring

The physical interaction force that is applied to the actuator as a disturbance is omitted in the reduce order model, as it is assumed that this force is partially cancelled out with a feed-forward control action and the motion controlled system is sufficiently robust to effectively compensate for the interaction force within its bandwidth.

The reduce order model is commonly employed as it provides simpler analysis; how-

ever, the results obtained through the analysis of the reduce order model necessitate rigorous validation with respect to the full order model. In this chapter, we provide necessary and sufficient conditions for passivity and passive physical equivalents of reduce models. Furthermore, effective impedance and haptic rendering analyses are made through passive physical equivalents. Also, we compare passivity bounds with full order model.

## 7.1 Reduce Order Model for SDEA<sub>Kfb</sub>

In this section, we have studied reduce order model for SDEA<sub>Kred</sub> where block diagram is provided in Figure 7.1.

### 7.1.1 Voigt Model Rendering

The impedance at the interaction port of SDEA<sub>Kred</sub> under VSIC during Voigt model rendering when both controllers are proportional is  $Z_{Voigt}^{SDEA_{Kred}}(s) =$

$$\frac{B_f s^3 + (K + B_f w_a(1 + B_d G_t)) s^2 + w_a(K + B_d G_t K + B_f G_t K_d) s + G_t K K_d w_a}{s^3 + w_a s^2 + G_t K w_a s} \quad (7.1)$$

The passivity of  $Z_{Voigt}^{SDEA_{Kred}}(s)$  is checked according to Theorem 1. Theorem 11 presents necessary and sufficient conditions for one-port passivity of SDEA<sub>Kred</sub> under VSIC while rendering Voigt model, when  $G_t$  consists of proportional gains.

**Theorem 11.** *Consider Voigt model rendering for SDEA<sub>Kred</sub> under VSIC as in Figure 7.1, where  $G_t$  consists of proportional gains. Let all parameters be positive. Then, the following expressions constitute necessary and sufficient conditions for passivity of  $Z_{Voigt}^{SDEA_{Kred}}(s)$ .*

$$(i) \ K \geq \frac{K_d(1 - B_f G_t)}{B_d G_t + 1}, \text{ and}$$

$$(ii) \ w_a \geq \frac{G_t(K + K_d)}{(B_d G_t + 1)} - \frac{2\sqrt{B_f G_t K (K(B_d G_t + 1) + K_d(B_f G_t - 1)) - B_d G_t K}}{B_f (B_d G_t + 1)}.$$

*Proof.* 1)  $Z(s)$  has no poles in the right half plane.  $Z_{Voigt}^{SDEA_{Kred}}(s)$  has no roots in the open right half plane if all coefficients of denominator of  $Z_{Voigt}^{SDEA_{Kred}}(s)$  are positive.

2)  $Re[Z(jw)] \geq 0$  for all  $w$ . Invoking Lemma 1, the sign of  $Re[Z_{Voigt}^{SDEA_{Kred}}(jw)]$  can be checked by the sign of  $H(jw) = d_6 w^6 + d_4 w^4 + d_2 w^2$  where



$$d_2 = G_t(B_d G_t + 1) K^2 w_a^2 + G_t K_d (B_f G_t - 1) K w_a^2 \quad (7.2)$$

$$d_4 = B_f w_a^2 - B_d G_t w_a (K - B_f w_a) - B_f G_t K w_a - B_f G_t K_d w_a \quad (7.3)$$

$$d_6 = B_f \quad (7.4)$$

Here,  $d_6$  is positive, since  $B_f$  is positive. The non-negativeness of  $d_2$  imposes

$$K \geq \frac{K_d (1 - B_f G_t)}{B_d G_t + 1} \quad (7.5)$$

When Lemma 3 is applied, the last necessary and sufficient condition for passivity can be derived as

$$w_a \geq \frac{G_t (K + K_d)}{(B_d G_t + 1)} - \frac{2\sqrt{B_f G_t K (K (B_d G_t + 1) + K_d (B_f G_t - 1)) - B_d G_t K}}{B_f (B_d G_t + 1)} \quad (7.6)$$

A simpler but more conservative sufficient condition can be presented by imposing non-negativeness of  $d_4$  instead of Eqn. (7.6) as

$$w_a \geq \frac{G_t [K (B_d + B_f) + B_f K_d]}{B_f (B_d G_t + 1)} \quad (7.7)$$

3) Any poles of  $Z(s)$  on the imaginary axis are simple

with positive and real residues. There is a no poles on the imaginary axis except at  $s = 0$ , when all controller gains and  $w_a$  are positive. There is a pole when  $s = 0$ , for which the residue equals to  $K_d$ , which is positive.

Hence, Eqns. (7.5) and (7.6) constitute the necessary and sufficient conditions for the passivity of Eqn. (7.1) when all parameters are positive.

□

#### 7.1.1.1 Passive Physical Equivalent

A realization of Eqn. (7.1) characterizing  $SDEA_{K_{red}}$  under VSIC during Voigt model rendering when both controllers are proportional is presented in Figure 7.2, where  $k_{2v} = K - K_d + B_d B_f G_t w_a$ ,  $c_{4v} = \frac{B_d G_t - B_f G_t + 1}{G_t} + \frac{K_d (B_f G_t - 1)}{G_t K}$ ,  $b_{4v} = \frac{(w_a B_f (G_t B_f - 1) + K) (w_a B_d (G_t B_d K + K - K_d) + (K - K_d)^2)}{G_t K^2 w_a (K - K_d + B_d B_f G_t w_a)}$ , and  $c_{5v} = \frac{(w_a B_f (G_t B_f - 1) + K) (w_a B_d (G_t B_d K + K - K_d) + (K - K_d)^2)}{G_t K w_a (B_f K - B_d K - B_f K_d + B_d B_f w_a)}$ .

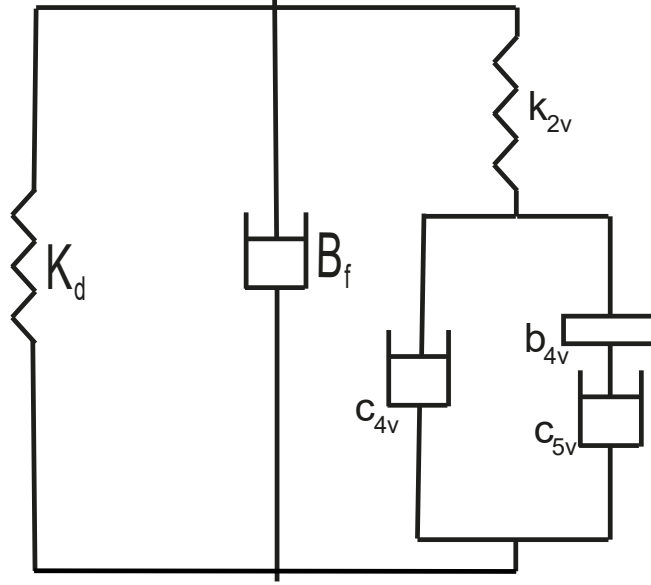


Figure 7.2 Passive physical equivalent of  $\text{SDEA}_{K_{red}}$  under VSIC during Voigt model rendering

#### 7.1.1.2 Haptic Rendering Performance

Physical realization of  $\text{SDEA}_{K_{red}}$  during Voigt model rendering in Figure 7.2 indicates three main branches in parallel: a spring-damper pair  $K_d-B_f$  in parallel, and a branch capturing the parasitic dynamics governed by a complex topology of damper-inertance terms that are coupled to the system in series through a spring. The parallel spring-damper pair of  $K_d-B_f$  shows that, while  $\text{SDEA}_{K_{red}}$  can render the desired spring levels, it cannot render the desired damping, since the controller terms have no effect on  $B_f$ . Hence,  $\text{SDEA}_{K_{red}}$  cannot render desired Voigt models, unlike SDEA which has direct control over the damping term in addition to the spring term. Similar to the case with the  $\text{SDEA}_{K_{fb}}$  realization, according to the  $\text{SDEA}_{K_{red}}$  realization, the uncontrollable damping term  $B_f$  acts as a parasitic effect working against the rendering performance.

For the physical realization of  $\text{SDEA}_{K_{red}}$ , the coupling filter consists of a spring, whose stiffness can get large for large controller gains or  $B_d$ . Hence, unlike the case for SDEA, larger controller gains do not necessarily decouple these parasitic dynamics from the rendered impedance. When the coupling is strong, the parasitic dissipation effects due to the last branch in  $\text{SDEA}_{K_{red}}$  realization can be split into two parts: a damper  $c_{4v}$  and a serial damper-inerter term that introduces frequency dependent dissipation to the system that increases with frequency. Similar to  $\text{SDEA}_{K_{fb}}$  and unlike the SDEA realizations,  $\text{SDEA}_{K_{red}}$  does not have a pure inerter term that dominates the parasitic dynamics at high frequencies.

The fourth row of Table 8.1 presents realizations for  $\text{SDEA}_{K_{red}}$  while rendering Voigt,

spring, and null impedance models. Table 8.1 indicates that there exists continuity among realizations; that is, one can recover the realization of ideal spring rendering with  $\text{SDEA}_{K_{red}}$  from the realization of Voigt model rendering with  $\text{SDEA}_{K_{red}}$  by setting  $B_d = 0$ , while the realization of null impedance rendering with  $\text{SDEA}_{K_{red}}$  can be recovered from the realization of Voigt model rendering with  $\text{SDEA}_{K_{red}}$  by setting  $B_d = 0$  and  $K_d = 0$ .

### 7.1.1.3 Effective Impedance Analysis

Further insights may be gained about the parasitic dynamics by studying the effective impedance of the realization. The effective impedance of the realization in Figure 7.2, after removing  $K_d$ - $B_f$  and the serial coupling spring  $k_{2v}$ , indicates that, at low frequencies (as  $\omega \rightarrow 0$ ), the effective damping of the parasitic dynamics converges to  $c_{4v}$ , while at high frequencies (as  $\omega \rightarrow \infty$ ), the effective damping of the parasitic dynamics approaches to  $c_{4v} + c_{5v}$ .

Similarly, at low frequencies (as  $\omega \rightarrow 0$ ), the effective inertance of the parasitic dynamics converges to  $b_{4v}$ , while at high frequencies (as  $\omega \rightarrow \infty$ ), the effective inertance of the parasitic dynamics approaches to zero.

Accordingly, in addition to the parasitic effect of  $B_f$ , through the coupling spring, the parasitic damping of  $c_{4v}$  affects the Voigt model rendering performance at the low frequency range, while a parasitic inertance of  $b_{4v}$  also acts at this frequency range. The effective parasitic damping increases with frequency and  $c_{4v}$  is added to  $c_{5v}$  at the high frequency range. On the other hand, the effective parasitic inertance decreases to zero with increasing frequency.

If we compare the effective impedance of  $\text{SDEA}_{K_{fb}}$  to  $\text{SDEA}_{K_{red}}$ , at the high frequency range, the effective inertance of the parasitic dynamics of both  $\text{SDEA}_{K_{fb}}$  and  $\text{SDEA}_{K_{red}}$  goes to zero. While the effective dampings of  $\text{SDEA}_{K_{fb}}$  and  $\text{SDEA}_{K_{red}}$  at low frequencies converge to  $c_{2v}$  and  $c_{4v}$ , respectively, for large torque controller gains (as  $G_t \rightarrow \infty$ ), both of these parasitic damping terms converge to  $B_d - B_f + \frac{B_f K_d}{K}$ . Finally, both  $\text{SDEA}_{K_{fb}}$  and  $\text{SDEA}_{K_{red}}$  possess frequency dependent parasitic dissipation terms.

### 7.1.1.4 Comparison of Passivity Bounds of $\text{SDEA}_{K_{fb}}$ vs $\text{SDEA}_{K_{red}}$

While the reduce order model  $\text{SDEA}_{K_{red}}$  provides simpler passivity conditions, these conditions need to be rigorously validated with respect to the full-order model  $\text{SDEA}_{K_{fb}}$ .

Comparison of the necessary conditions presented in Eqns. (6.5) and (7.5) that

impose upper bounds on  $K_d$  for  $\text{SDEA}_{K_{fb}}$  and  $\text{SDEA}_{K_{red}}$ , respectively indicates that the bound for  $\text{SDEA}_{K_{red}}$  may be more relaxed. In particular, it is easy to show that for relatively large controller gains such that  $\alpha/(\alpha + 1) \approx 1$  and for  $B_m + G_m(1 - B_f G_t) \geq 0$ , the following condition holds

$$K \geq K_d \frac{\alpha}{(\alpha + 1)} \frac{B_m + G_m(1 - B_f G_t)}{B_m + G_m(B_d G_t + 1)} \geq K_d \frac{(1 - B_f G_t)}{(B_d G_t + 1)} \quad (7.8)$$

Eqn. (7.35) indicates that the  $K_d$  bound according to the reduce order model  $\text{SDEA}_{K_{red}}$  may mislead the analyst into thinking that stiff virtual springs  $K_b$  that are impossible to passively render with the full-order model  $\text{SDEA}_{K_{fb}}$  can be passive. Therefore, the selection of maximum  $K_d$  according to the  $\text{SDEA}_{K_{red}}$  bound can be fallacious, as rendering implementations are always performed on a physical hardware whose dynamics is better captured by the full-order model  $\text{SDEA}_{K_{fb}}$ . Note that, if  $B_m + G_m(1 - B_f G_t) \leq 0$ , the necessary conditions of  $\text{SDEA}_{K_{fb}}$  and  $\text{SDEA}_{K_{red}}$  given in Eqns. (6.5) and (7.5) are trivially satisfied.

If the cut-off frequency of the reduce order model is selected to satisfy  $w_a \leq \frac{B_m + G_m}{J_m}$ , then it can be shown that the passivity bound of  $\text{SDEA}_{K_{red}}$  in Eqn. (7.7) provides a sufficient condition for the passivity bound of  $\text{SDEA}_{K_{fb}}$  in Eqn. (6.7). In particular, the comparison of the sufficient conditions of presented in Eqns. (6.7) and (7.7) indicates that

$$\begin{aligned} J_m &\leq \frac{B_f (B_d G_t + 1)(B_m + G_m)}{G_t (K (B_d + B_f) + B_f K_d)} \\ &\leq \frac{B_f (B_f + B_m + G_m)(B_m + G_m + B_d \alpha)}{\alpha (K (B_d + B_f) + B_f K_d)} \end{aligned} \quad (7.9)$$

Accordingly, if  $w_a \leq \frac{B_m + G_m}{J_m}$ , then Eqn. (7.7) presents a more conservative bound than Eqn. (6.7). In other words, if the cut-off frequency of the reduce order model is selected to underestimate the inner-motion control bandwidth of the full-order model, then the passivity bound of  $\text{SDEA}_{K_{fb}}$  in Eqn. (6.7) is ensured.

Furthermore, in addition to  $w_a \leq \frac{B_m + G_m}{J_m}$ , if it can also be imposed that  $\frac{B_m + G_m}{J_m} \leq \frac{B_f G_m G_t}{J_m}$ , then passivity of renderings with the full-order model  $\text{SDEA}_{K_{fb}}$  can be ensured, since this condition ensures that  $B_m + G_m(1 - B_f G_t) \leq 0$ ; hence, the necessary condition in Eqn. (6.7) for the passivity of the full-order model is also satisfied. Otherwise, the necessary condition presented in Eqns. (6.5) needs to be imposed (instead of Eqn. (7.5)) for  $\text{SDEA}_{K_{red}}$  to ensure passivity of the rendering implementations.

### 7.1.2 Ideal Spring Rendering

When  $B_d = 0$  in Eqn. (7.1), the output impedance transfer function at the interaction port reduces to that of  $SDEA_{K_{red}}$  under VSIC during ideal spring rendering as  $Z_{spring}^{SDEA_{K_{red}}}(s) =$

$$\frac{B_f s^3 + (K + B_f w_a) s^2 + w_a (K + B_f G_t K_d) s + G_t K K_d w_a}{s^3 + w_a s^2 + G_t K w_a s} \quad (7.10)$$

The passivity of  $Z_{spring}^{SDEA_{K_{red}}}(s)$  is checked according to Theorem 1. Theorem 12 presents necessary and sufficient conditions for one-port passivity of  $SDEA_{K_{red}}$  under VSIC while rendering spring, when  $G_t$  consists of proportional gains.

**Theorem 12.** *Consider spring rendering for  $SDEA_{K_{red}}$  under VSIC as in Figure 7.1, where  $G_t$  consists of proportional gains. Let all parameters be positive. Then, the following expressions constitute necessary and sufficient conditions for passivity of  $Z_{spring}^{SDEA_{K_{red}}}(s)$ .*

$$(i) \quad K \geq K_d(1 - B_f G_t), \text{ and}$$

$$(ii) \quad w_a \geq G_t (K + K_d) - \frac{2\sqrt{B_f G_t K (K - K_d(1 - B_f G_t))}}{B_f}.$$

*Proof.* 1)  $Z(s)$  has no poles in the right half plane.  $Z_{spring}^{SDEA_{K_{red}}}(s)$  has no roots in the open right half plane if all coefficients of denominator of  $Z_{spring}^{SDEA_{K_{red}}}(s)$  are positive.

2)  $Re[Z(jw)] \geq 0$  for all  $w$ . Invoking Lemma 1, the sign of  $Re[Z_{spring}^{SDEA_{K_{red}}}(jw)]$  can be checked by the sign of  $H(jw) = d_6 w^6 + d_4 w^4 + d_2 w^2$  where

$$d_2 = G_t K w_a^2 (K - K_d + B_f G_t K_d) \quad (7.11)$$

$$d_4 = B_f w_a (w_a - G_t K - G_t K_d) \quad (7.12)$$

$$d_6 = B_f \quad (7.13)$$

From Lemma 3,  $d_6$  is always positive if  $B_f$  is positive. Non-negativeness of  $d_2$  imposes:

$$K \geq K_d(1 - B_f G_t) \quad (7.14)$$

When Lemma 3 is applied, the following equation can be derived:

$$w_a \geq G_t (K + K_d) - \frac{2\sqrt{B_f G_t K (K - K_d(1 - B_f G_t))}}{B_f} \quad (7.15)$$

Non-negative  $d_4$  is the sufficient condition of  $Re[Z_{spring}^{SDEA_{K_{red}}}(jw)]$  when  $d_2$  and  $d_6$  are non-negative which imposes: A simpler but more conservative set of sufficient conditions can be derived by using Eqn. (7.14) together with Eqn. (7.16) instead of Eqn. (7.15), where

$$w_a \geq G_t (K + K_d) \quad (7.16)$$

3) Any poles of  $Z(s)$  on the imaginary axis are simple with positive and real residues. There is a no poles on the imaginary axis except  $s = 0$  while all controller gains and  $w_a$  are positive. There is a pole when  $s = 0$  where residue equals to  $K_d$  which is always positive with positive  $K_d$ .  $\square$

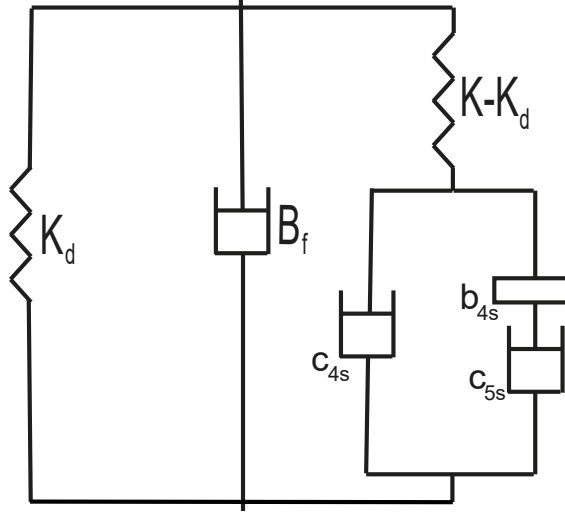


Figure 7.3 Passive physical equivalent of  $SDEA_{K_{red}}$  under VSIC during spring rendering

#### 7.1.2.1 Passive Physical Equivalent:

A realization of Eqn. (7.10) characterizing  $SDEA_{K_{red}}$  under VSIC during spring rendering when both controllers are proportional is presented in Figure 7.3, where  $c_{4s} = \frac{(1-B_f G_t)(K-K_d)}{G_t K}$ ,  $b_{4s} = \frac{(K-K_d)(G_t w_a B_f^2 - w_a B_f + K)}{G_t K^2 w_a}$ , and  $c_{5s} = \frac{(B_f G_t - 1)(K-K_d)}{G_t K} + \frac{K-K_d}{B_f G_t w_a}$ .

#### 7.1.2.2 Haptic Rendering Performance

Physical realization of  $SDEA_{K_{red}}$  during spring rendering in Figure 7.3 indicates three main branches in parallel: a spring-damper pair  $K_d-B_f$  in parallel, and a branch capturing the parasitic dynamics governed by a complex topology of damper-inertance terms that are coupled to the system in series through a spring. The

parallel spring-damper pair of  $K_d$ - $B_f$  shows that, while  $\text{SDEA}_{K_{red}}$  can render desired spring and the controller terms have no affect on  $B_f$ . Hence,  $\text{SDEA}_{K_{red}}$  can render desired spring like SDEA. Similar to the case with the  $\text{SDEA}_{K_{fb}}$  realization, according to the  $\text{SDEA}_{K_{red}}$  realization, the uncontrollable damping term  $B_f$  acts as a parasitic effect working against rendering performance.

For the physical realization of  $\text{SDEA}_{K_{red}}$ , the filter consists of a spring. Hence, unlike the case for SDEA, larger controller gains do not necessarily decouple these parasitic dynamics from the rendered impedance. When the coupling is strong, the parasitic dissipation effects due to the last branch in  $\text{SDEA}_{K_{red}}$  realization can be split into two parts: a damper  $c_{4s}$  and a serial damper-inerter term that introduces frequency dependent dissipation to the system that increases with frequency. Similar to  $\text{SDEA}_{K_{fb}}$  and unlike in the SDEA realizations,  $\text{SDEA}_{K_{red}}$  does not have a pure inerter term that dominates the high frequency parasitic dynamics.

### 7.1.2.3 Effective Impedance Analysis

Insights may be gained about the parasitic dynamics by studying the effective impedance of the realization. The effective impedance of the realization in Figure 7.3, after removing  $K_d$ - $B_f$  and the serial coupling spring  $K - K_d$ , indicates that at low frequencies (as  $\omega \rightarrow 0$ ), the effective damping of the parasitic dynamics converges to  $c_{4s}$ . At high frequencies (as  $\omega \rightarrow \infty$ ), the effective damping of the parasitic dynamics approaches to  $c_{4s} + c_{5s}$ .

Similarly, at low frequencies (as  $\omega \rightarrow 0$ ), the effective inertance of the parasitic dynamics converges to  $b_{4s}$ . At high frequencies (as  $\omega \rightarrow \infty$ ), the effective inertance of the parasitic dynamics approaches to zero.

Accordingly, in addition to the parasitic effect of  $B_f$ , through the coupling spring, the parasitic damping of  $c_{4s}$  affects the spring rendering performance at the low frequency range, while a parasitic inertance of  $b_{4s}$  also acts at this frequency range. The effective parasitic damping increases with frequency and  $c_{4s}$  is added to  $c_{5s}$  at the high frequency range. On the other hand, the effective parasitic inertance decreases to zero with increasing frequency.

### 7.1.3 Null Impedance Rendering

When  $K_d = 0$  in Eqn. (7.10), the output impedance transfer function at the interaction port reduces to that of  $SDEA_{K_{red}}$  under VSIC during null impedance rendering as

$$Z_{null}^{SDEA_{K_{red}}}(s) = \frac{B_f s^2 + (K + B_f w_a) s + K w_a}{s^2 + w_a s + G_t K w_a} \quad (7.17)$$

The passivity of  $Z_{null}^{SDEA_{K_{red}}}(s)$  is checked according to Theorem 1. Theorem 13 presents the necessary and sufficient condition for one-port passivity of  $SDEA_{K_{red}}$  under VSIC while rendering null impedance, when  $G_t$  consists of proportional gains.

**Theorem 13.** *Consider null impedance rendering for  $SDEA_{K_{red}}$  under VSIC as in Figure 7.1, where  $G_t$  consists of proportional gains. Let all parameters be positive. Then, the following expression constitute the necessary and sufficient condition for passivity of  $Z_{null}^{SDEA_{K_{red}}}(s)$ .*

$$(i) \quad w_a \geq G_t K - \frac{2K \sqrt{B_f G_t}}{B_f}.$$

*Proof.* 1)  $Z(s)$  has no poles in the right half plane.  $Z_{null}^{SDEA_{K_{red}}}(s)$  has no roots in the open right half plane if all coefficients of denominator of  $Z_{null}^{SDEA_{K_{red}}}(s)$  are positive.

2)  $Re[Z(jw)] \geq 0$  for all  $w$ . Invoking Lemma 1, the sign of  $Re[Z_{null}^{SDEA_{K_{red}}}(jw)]$  can be checked by the sign of  $H(jw) = d_4 w^4 + d_2 w^2 + d_0$  where

$$d_0 = G_t K^2 w_a^2 \quad (7.18)$$

$$d_2 = B_f w_a (w_a - G_t K) \quad (7.19)$$

$$d_4 = B_f \quad (7.20)$$

From Lemma 3,  $d_0$  and  $d_4$  are always positive while all controller gains and  $w_a$  are positive.

When Lemma 3 is applied, the following equation can be derived: When all parameters are positive, the necessary and sufficient condition for the passivity of Eqn. (7.17) becomes

$$w_a \geq G_t K - \frac{2K \sqrt{B_f G_t}}{B_f} \quad (7.21)$$



Non-negative  $d_2$  is the sufficient condition of non-negative  $Re[Z_{null}^{SDEA_{K_{red}}}(jw)]$  when  $d_0$  and  $d_4$  are non-negative which imposes A simpler but more conservative sufficient condition can be derived as

$$w_a \geq G_t K \quad (7.22)$$

3) Any poles of  $Z(s)$  on the imaginary axis are simple with positive and real residues. There is a no poles on the imaginary axis while all controller gains and  $w_a$  are positive.  $\square$

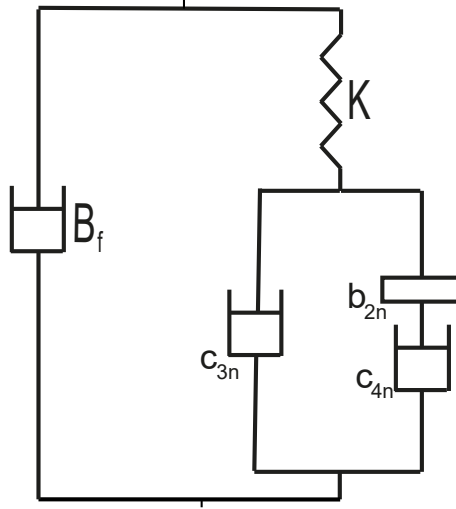


Figure 7.4 Passive physical equivalent of  $SDEA_{K_{red}}$  under VSIC during null impedance rendering

### 7.1.3.1 Passive Physical Equivalent

A realization of Eqn. (7.17) characterizing  $SDEA_{K_{red}}$  under VSIC during null impedance rendering when both controllers are proportional is presented in Figure 7.4, where  $c_{2n} = \frac{1}{G_t} - B_f$ ,  $b_{2n} = \frac{1}{G_t w_a} + \frac{B_f (B_f G_t - 1)}{G_t K}$ , and  $c_{3n} = B_f + \frac{K - B_f w_a}{B_f G_t w_a}$ .

### 7.1.3.2 Haptic Rendering Performance

Physical realization of  $SDEA_{K_{red}}$  during null impedance rendering in Figure 7.4 indicates two main branches in parallel: a damper  $B_f$ , and a branch capturing the parasitic dynamics governed by a complex topology of damper-inertance terms that are coupled to the system in series through a spring. A damper term  $B_f$  shows that the controller terms have no affect on  $B_f$ . According to the  $SDEA_{K_{red}}$  realization, the uncontrollable damping term  $B_f$  acts as a parasitic effect working against rendering performance.

### 7.1.3.3 Effective Impedance Analysis

Further insights may be gained about the parasitic dynamics by studying the effective impedance of the realization. Effective impedance analysis of the realization in Figure 7.4, after removing  $B_f$  and the serial coupling filter  $K$ , indicates that at low frequencies (as  $\omega \rightarrow 0$ ) the effective damping of the parasitic dynamics converges to  $c_{3n}$ . At high frequencies (as  $\omega \rightarrow \infty$ ), the effective damping of the parasitic dynamics approaches to  $c_{3n} + c_{4n}$ .

Similarly, the effective inertance of the parasitic dynamics at low frequencies (as  $\omega \rightarrow 0$ ) converges to  $b_{2n}$ . At high frequencies (as  $\omega \rightarrow \infty$ ), the effective inertance of the parasitic dynamics approaches to 0.

Accordingly, in addition to the parasitic effect of  $B_f$ , the parasitic damping of  $c_{3n}$  affects the null impedance rendering performance at the low frequency range, while a parasitic inertance of  $b_{2n}$  also acts at this frequency range. The effective parasitic damping increases with frequency and  $c_{4n}$  is added to  $c_{3n}$  at the high frequency range. On the other hand, the effective parasitic inertance decreases to zero with increasing frequency. A numerical comparison of the effective damping of  $\text{SDEA}_{K_{red}}$  with SDEA at the low frequency range is presented in Chapter 8.

## 7.2 Reduce Order Model for SDEA

In this section, we have studied reduce order model for SDEA. where block diagram is provided in Figure 7.5.

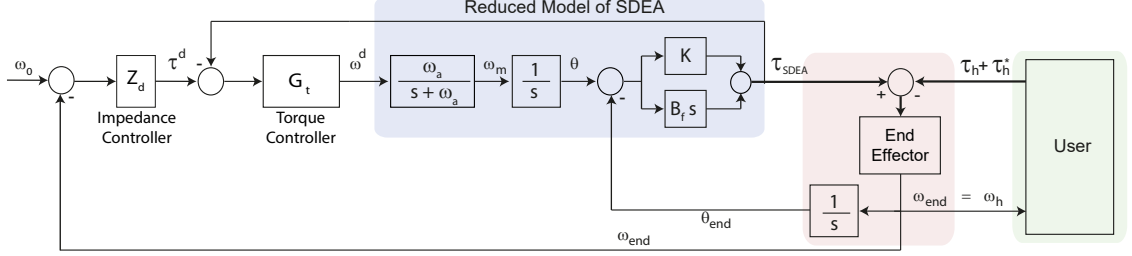


Figure 7.5 Block diagram of impedance control with reduce order model S(D)EA

### 7.2.1 Voigt Model Rendering

The impedance at the interaction port of reduce order model of  $SDEA_{red}$  under VSIC during Voigt model rendering becomes:

$$Z_{Voigt}^{SDEA_{red}}(s) = \frac{B_f s^3 + (K + B_f w_a(1 + B_d G_t)) s^2 + (K w_a + G_t w_a(B_d K + B_f K_d)) s + G_t K K_d w_a}{s^3 + (w_a + B_f G_t w_a) s^2 + G_t K w_a s} \quad (7.23)$$

The passivity of  $Z_{Voigt}^{SDEA_{red}}(s)$  is checked according to Theorem 1. Theorem 14 presents necessary and sufficient conditions for one-port passivity of  $SDEA_{red}$  under VSIC while rendering Voigt model, when  $G_t$  consists of proportional gains.

**Theorem 14.** *Consider Voigt model rendering for  $SDEA_{red}$  under VSIC as in Figure 7.5, where  $G_t$  consists of proportional gains. Let all parameters be positive. Then, the following expressions constitute necessary and sufficient conditions for passivity of  $Z_{Voigt}^{SDEA_{red}}(s)$ .*

- (i)  $K \geq \frac{K_d}{B_d G_t + 1}$ , and
- (ii)  $-\frac{2\sqrt{B_f G_t K(K - K_d + B_d G_t K)} - G_t(B_d K + B_f K_d)}{B_f(B_d G_t + 1)(B_f G_t + 1)} \leq w_a$ .

*Proof.* 1)  $Z(s)$  has no poles in the right half plane.  $Z_{Voigt}^{SDEA_{red}}(s)$  has no roots in the open right half plane if all coefficients of denominator of  $Z_{Voigt}^{SDEA_{red}}(s)$  are positive.

2)  $Re[Z(jw)] \geq 0$  for all  $w$ . Invoking Lemma 1, the sign of  $Re[Z_{Voigt}^{SDEA_{red}}(jw)]$  can be checked by the sign of  $H(jw) = d_6 w^6 + d_4 w^4 + d_2 w^2$  where

$$d_2 = G_t K w_a^2 (K - K_d + B_d G_t K) \quad (7.24)$$

$$d_4 = B_f w_a^2 (B_d G_t + 1)(B_f G_t + 1) - B_d G_t K w_a - B_f G_t K_d w_a \quad (7.25)$$

$$d_6 = B_f \quad (7.26)$$

From Lemma 3,  $d_6$  is always positive since  $B_f$  is positive. Non-negativeness of  $d_2$  imposes:

$$K \geq \frac{K_d}{B_d G_t + 1} \quad (7.27)$$

When Lemma 3 is applied, the following equation can be derived:

$$-\frac{2\sqrt{B_f G_t K (K - K_d + B_d G_t K)} - G_t (B_d K + B_f K_d)}{B_f (B_d G_t + 1) (B_f G_t + 1)} \leq w_a \quad (7.28)$$

Non-negative  $d_4$  is the sufficient condition of  $Re[Z_{Voigt}^{SDEA_{red}}(jw)]$  when  $d_2$  and  $d_6$  are non-negative which imposes:

$$\frac{G_t (B_d K + B_f K_d)}{B_f (B_d G_t + 1) (B_f G_t + 1)} \leq w_a \quad (7.29)$$

3) Any poles of  $Z(s)$  on the imaginary axis are simple with positive and real residues. There is a no poles on the imaginary axis except  $s = 0$  while all controller gains and  $w_a$  are positive. There is a pole when  $s = 0$  where residue equals to  $K_d$  which is always positive with positive  $K_d$ .  $\square$

### 7.2.1.1 Passive Physical Equivalent

A realization of Eqn. (7.23) characterizing  $SDEA_{red}$  under VSIC during Voigt model rendering when both controllers are proportional is presented in Figure 7.6.

The parameters of this realization include  $c_{6v} = \frac{K - K_d}{G_t K}$ ,  $b_{5v} = \frac{B_f - B_d}{B_f G_t w_a}$ ,  $c_{7v} = \frac{(B_f K_d - B_d K)(B_f w_a - K)}{B_f^2 G_t K w_a}$ , and  $b_{6v} = \frac{(B_f K_d - B_d K)(B_f w_a - K)}{B_f G_t K^2 w_a}$

For the realization in Figure 7.6 to be feasible, all of components of the model should be non-negative. Hence, the non-negativeness of terms impose:

$$K \geq K_d \quad (7.30)$$

$$B_f \geq B_d \quad (7.31)$$

$$\frac{K}{B_f} \leq w_a \quad (7.32)$$

$$\frac{B_f}{K} \geq \frac{B_d}{K_d} \quad (7.33)$$

Eqn. (7.30) imposes a constraint that is more conservative than the sufficiency condition in Eqn. (7.27). Eqn. (7.32) imposes a more conservative bound than Eqn. (7.29) while Eqn. (7.33) holds.

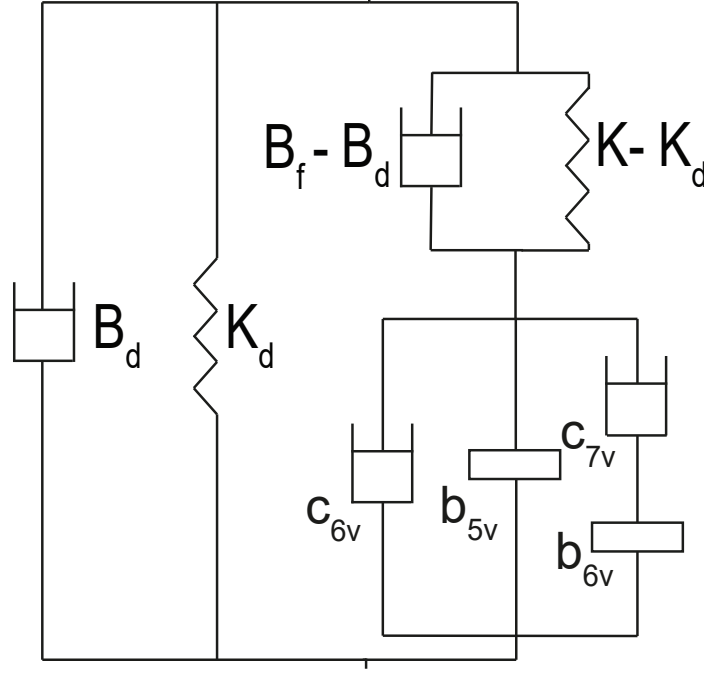


Figure 7.6 Passive physical equivalent of  $\text{SDEA}_{red}$  under VSIC during Voigt model rendering

Consequently, the feasibility of Figure 7.6 provides sufficient conditions for the frequency domain passivity of Eqn. (7.23).

#### 7.2.1.2 Comparison of Passivity Bounds of $\text{SDEA}_{K_{red}}$ with SDEA

Inner loop of  $(\frac{\omega_m}{\omega_d})$  SDEA full-order model equals to:

$$\frac{G_m}{J_m s + B_m + G_m} \quad (7.34)$$

Comparison of the necessary conditions presented in Eqns. (7.27) and (5.5) indicates that:

$$K \geq \frac{K_d}{B_d G_t + 1} \geq K_d \frac{\alpha}{(\alpha + 1)} \frac{B_m + G_m}{B_m + G_m + B_d \alpha} \quad (7.35)$$

Accordingly, Eqn. (7.35) shows that  $\text{SDEA}_{K_{red}}$  presents a more conservative bounds than SDEA while the following equation holds:

$$0 \leq B_m + G_m + B_d \alpha (1 - B_m G_t) \quad (7.36)$$

which is can be rearranged as:

$$w_a \geq \frac{B_d \alpha (B_m G_t - 1)}{J_m} \quad (7.37)$$

If  $1 - B_m G_t \geq 0$ , no need to check Eqns. (7.36) or (7.37) and Eqn. (7.35) always holds. If  $1 - B_m G_t < 0$  and the cut-off frequency of the reduce order model is selected to satisfy Eqn. (7.37), then it can be shown that the passivity bound of  $\text{SDEA}_{K_{red}}$  in Eqn. (7.27) provides a sufficient condition for the passivity bound of SDEA in Eqn. (5.5). In particular, the comparison of the sufficient conditions of presented in Eqns. (7.29) and (5.7) indicates that

$$\begin{aligned} J_m &\leq \frac{B_f(B_d G_t + 1)(B_f G_t + 1)(B_m + G_m)}{(B_f K_d + B_d K) G_t} \\ &\leq \frac{B_f (B_m + G_m + B_d \alpha) [B_m + G_m + B_f (1 + \alpha)]}{(B_f K_d + B_d K) \alpha} \end{aligned} \quad (7.38)$$

Accordingly, if  $w_a \leq \frac{B_m + G_m}{J_m}$ , then Eqn. (7.29) presents a more conservative bound than Eqn. (5.7) while the following equation holds:

$$0 \leq B_d B_f \alpha (1 - B_m G_t) + (B_m + G_m)(B_m + B_f) \quad (7.39)$$

which is can be rearranged as:

$$w_a \geq \frac{B_d B_f \alpha (B_m G_t - 1)}{J_m (B_m + B_f)} \quad (7.40)$$

If  $1 - B_m G_t \geq 0$ , no need to check Eqns. (7.39) or (7.40) and Eqn. (7.38) always holds. If  $1 - B_m G_t < 0$  and the cut-off frequency of the reduce order model is selected to underestimate the inner-motion control bandwidth of the full-order model and Eqn. (7.40), then the passivity bound of SDEA in Eqn. (5.7) is ensured while Eqn. (7.40) is satisfied. However, Eqn. (7.37) presents a more conservative bounds than Eqn. (7.40).

As a result, if  $1 - B_m G_t \geq 0$ ,  $\text{SDEA}_{K_{red}}$  presents sufficient conditions of SDEA while the cut-off frequency of the reduce order model is selected to underestimate the inner-motion control bandwidth of the full-order model. If  $1 - B_m G_t < 0$ ,  $\frac{B_d \alpha (B_m G_t - 1)}{J_m} \leq w_a \leq \frac{B_m + G_m}{J_m}$ ,  $\text{SDEA}_{K_{red}}$  presents sufficient conditions of SDEA.

## 7.3 Reduce Order Model for SEA

In this section, we have studied reduce order model for SEA where block diagram is provided in Figure 7.5, but  $B_f$  is equal to zero.

### 7.3.1 Ideal Spring Rendering

The impedance at the interaction port of reduce order model of SEA under VSIC during spring rendering becomes:

$$Z_{spring}^{SEA_{red}}(s) = \frac{K s^2 + K w_a s + G_t K K_d w_a}{s^3 + w_a s^2 + G_t K w_a s} \quad (7.41)$$

The passivity of  $Z_{spring}^{SEA_{red}}(s)$  is checked according to Theorem 1. Theorem 15 presents necessary and sufficient conditions for one-port passivity of  $SEA_{red}$  under VSIC while rendering spring model, when  $G_t$  consists of proportional gains.

**Theorem 15.** *Consider spring rendering for  $SEA_{red}$  under VSIC as in Figure 7.5 while  $B_f = 0$ , where  $G_t$  consists of proportional gains. Let all parameters be positive. Then, the following expressions constitute necessary and sufficient conditions for passivity of  $Z_{spring}^{SEA_{red}}(s)$ .*

$$(i) \quad K \geq K_d.$$

*Proof.* 1)  $Z(s)$  has no poles in the right half plane.  $Z_{Spring}^{SEA_{red}}(s)$  has no roots in the open right half plane if all coefficients of denominator of  $Z_{Spring}^{SEA_{red}}(s)$  are positive.

2)  $Re[Z(jw)] \geq 0$  for all  $w$ . Invoking Lemma 1, the sign of  $Re[Z_{Spring}^{SEA_{red}}(jw)]$  can be checked by the sign of  $H(jw) = d_2 w^2$  where

$$d_2 = G_t K w_a^2 (K - K_d) \quad (7.42)$$

Non-negativeness of  $d_2$  imposes:

$$K \geq K_d \quad (7.43)$$

3) Any poles of  $Z(s)$  on the imaginary axis are simple with positive and real residues. There is a no poles on the imaginary axis except  $s = 0$  while all controller gains and  $w_a$  are positive. There is a pole when  $s = 0$  where residue equals to  $K_d$  which is always positive with positive  $K_d$ .  $\square$

### 7.3.1.1 Passive Physical Equivalent

A realization of Eqn. (7.23) characterizing  $SDEA_{red}$  under VSIC during Voigt model rendering when both controllers are proportional is presented in Figure 7.6. The parameters of this realization include  $c_{6s} = \frac{K w_a - K_d w_a}{G_t K w_a}$  and  $b_{5s} = \frac{K - K_d}{G_t K w_a}$ .

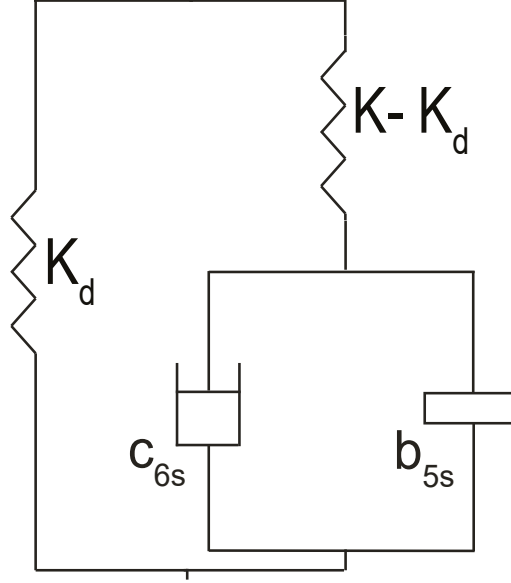


Figure 7.7 Passive physical equivalent of  $SEA_{red}$  under VSIC during ideal spring rendering

For the realization in Figure 7.7 to be feasible, all physical components in the model should be non-negative. Feasibility of  $c_{6s}$  and  $b_{5s}$  imposes necessary and sufficient condition of Eqn. (7.41) while all parameters are positive.

### 7.3.1.2 Comparison of Passivity Bounds of $SEA_{red}$ with SEA

If Eqn. (7.43) is satisfied, ideal spring rendering of full-order model for SEA is ensured which is the Eqn. (4.2).

The necessary and sufficient condition of  $SEA_{red}$  during spring rendering equals to  $K \geq K_d$  while all parameters are positive.  $K \geq K_d$  presents sufficient condition of full-order model of SEA under VSIC during ideal spring rendering when controllers P-P.



## 7.4 Discussion

We have provided necessary and sufficient conditions of reduce order model of SEA, SDEA, and  $SDEA_{Kfb}$  under VSIC during rendering Voigt model, spring, and null impedance. Also, we have provided passive physical equivalents of  $S(D)EAs_{red}$  under VSIC during rendering Voigt model, spring, and null impedance. Through passive physical equivalents, analysis of effective impedance and haptic rendering performance are provided. Furthermore, we compare the passivity bounds of full order model and reduce order model of  $S(D)EAs$ .

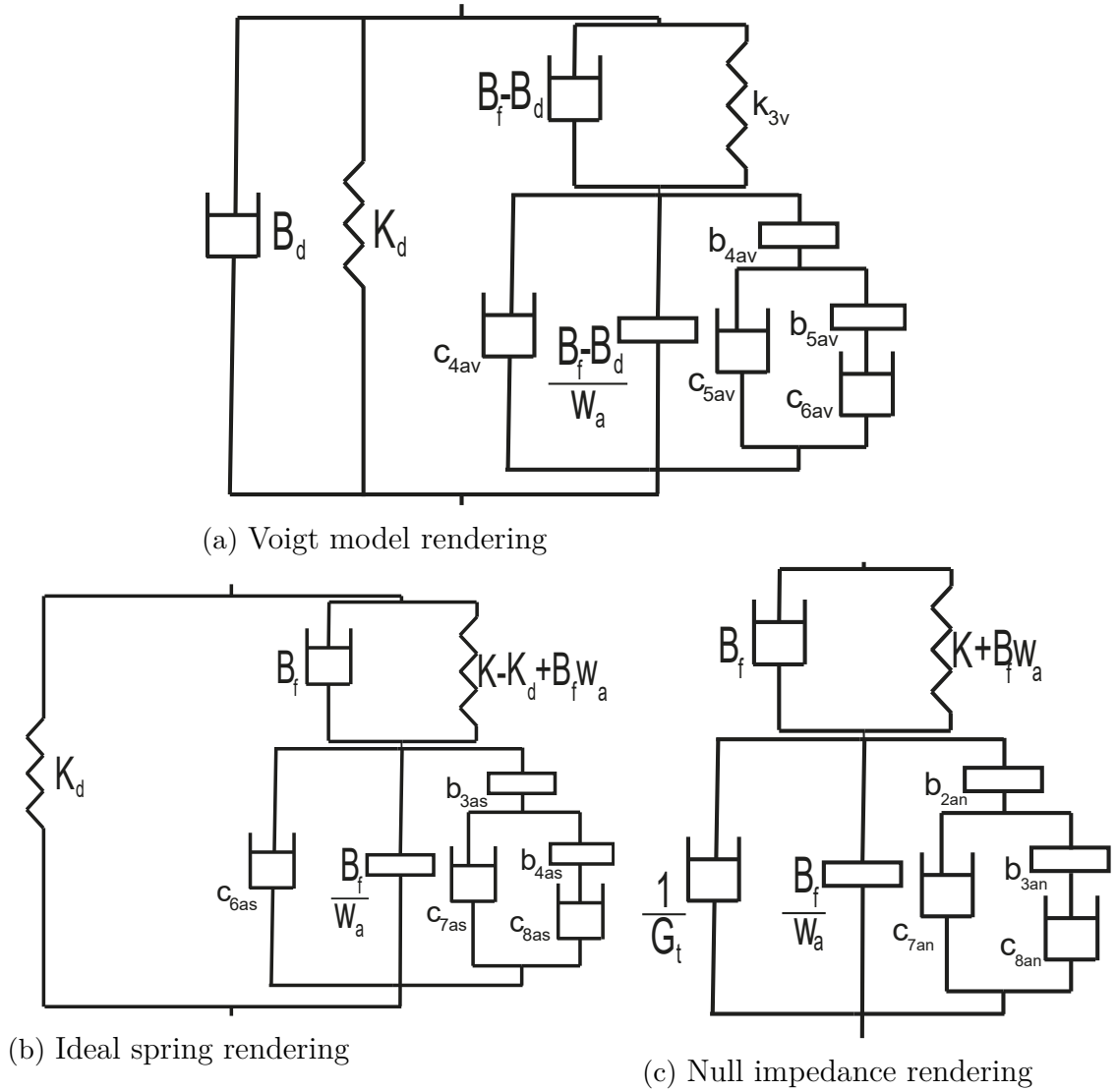


Figure 7.8 Alternative passive physical equivalents of  $SDEA_{K_{red}}$

Similarly Section 6.4, Figure 7.8 depicts alternative passive physical equivalents of  $SDEA_{K_{red}}$  under VSIC during Voigt model, ideal spring, and null impedance rendering. In particular, Figure 7.8a and Figure 7.2 present the realizations for the impedance transfer function in Eqn. 7.1, Figure 7.8b and Figure 7.3 present the realizations for the ideal spring rendering when  $B_d$  is set to zero in Eqn. 7.1, and

Figure 7.8c and Figure 7.4 present the realizations for the null impedance rendering when  $B_d$  and  $K_d$  are set to zero in Eqn. 7.1. We have used Figures 7.2, 7.3, and 7.4 instead of Figure 7.8a, 7.8b, and 7.8c because similarity between passive physical equivalents with  $\text{SDEA}_{K_{fb}}$  and easier performance evaluation in Section 8. Similarly physical passive equivalents of  $\text{SDEA}_{K_{fb}}$ ,  $B_f$  is occurred alone which has a parasitic effect for performance.

# Chapter 8

## Haptic Rendering Performance

In this section, we study the effects of the physical plant parameters and the controller gains on the rendering performance through Bode plots. We provide performance comparisons between different plant (SEA vs SDEA) and controller (P-P vs P-PI) architectures, using the insight gained through the passive realizations of the closed-loop systems.

The passive physical equivalents in Table 8.1 explicitly show that, when causal controllers roll-off, the dynamics of the uncontrolled plant is recovered. Accordingly, the high frequency response of all realizations are dominated by the dynamics of the physical filters (spring and damper) serially attached to the plant; hence, passive physical realizations indicate that SEAs act as a physical spring  $K$ , while an SDEAs act as a physical spring  $K$  and damping  $B_f$  in parallel, at high frequencies.

In Table 8.1, all passive physical equivalents include an inerter and a damper term in parallel. This damper term significantly affects the low frequency range of null impedance and spring rendering, as well as the bandwidth of spring rendering. The inerter term affects the transition from intermediate to high frequency range.

Furthermore, in Table 8.1, the passive physical equivalents for spring rendering include a spring with  $\frac{\alpha}{\alpha+1} K_d$ , parallel to all other components. For large controller gains, this spring converges to the desired virtual spring  $K_d$  to be rendered. As controllers are selected to include integral terms, additional components are included to the passive physical realizations, in parallel with the terms discussed above.

Table 8.1 Comparison of Physical Realizations of S(D)EA under VSIC

	Voigt Rendering	Spring Rendering	Null Rendering
SDEA	(a)	(b)	(c)
SEA	No passive realization exists.	(d)	(e)
SDEA_{K_{fb}}	(f)	(g)	(h)
SDEA_{K_{red}}	(i)	(j)	(k)

Table 8.2 Parameters of the S(D)EA plant

Parameter	Value
$J_m$	0.002 kgm <sup>2</sup>
$B_m$	1.22 Nms/rad
$K$	360 Nm/rad
$B_f$	0.5 Nms/rad

Table 8.2 presents the physical parameters of the S(D)EA plant used in simulations to evaluate the system performance. The proportional controller gains are set as  $G_m = 10$  Nms/rad and  $G_t = 5$  rad/sNm, while the integral gain of motion controller is set as  $I_m = 10$  Nm/rad. Table 8.3 presents the numerical values selected for the parallel inerter and damping terms of the passive physical equivalents in Figures 4.2–5.2 for various controller gains  $G_m$ ,  $G_t$ ,  $I_m$ , and desired stiffness levels  $K_d$ .

Table 8.3 Numerical values for the inerter and damping terms of the passive physical equivalents for SEA and SDEA for various controller gains  $G_m$ ,  $G_t$ ,  $I_m$ , and  $K_d$ . (Inerter is in  $kg\,m^2$  and damper is in  $Nm\,\frac{s}{rad}$ .)

	SEA						SDEA			
	Null Impedance Rendering				Spring Rendering		Null Impedance Rendering		Spring Rendering	
	P-P		P-PI		P-P		P-P		P-P	
	Inerter	Damper	Inerter	Damper ( $c_{1n}$ )	Inerter	Damper	Inerter	Damper	Inerter	Damper
$G_t = 5$	$3.92e^{-5}$	0.220	$3.92e^{-5}$	0.200	$2.32e^{-5}$	0.130	$3.92e^{-5}$	0.220	$3.92e^{-5}$	0.130
$G_t = 50$	$3.99e^{-6}$	0.022	$3.99e^{-6}$	0.020	$2.33e^{-6}$	0.013	$3.99e^{-6}$	0.022	$3.99e^{-6}$	0.013
$G_t = 100$	$2.00e^{-6}$	0.011	$2.00e^{-6}$	0.010	$1.17e^{-6}$	0.007	$2.00e^{-6}$	0.011	$2.00e^{-6}$	0.007
$G_m = 10$	$3.92e^{-5}$	0.220	$3.92e^{-5}$	0.200	$2.32e^{-5}$	0.130	$3.92e^{-5}$	0.220	$3.92e^{-5}$	0.130
$G_m = 50$	$7.97e^{-6}$	0.204	$7.97e^{-6}$	0.200	$4.66e^{-6}$	0.119	$7.97e^{-6}$	0.204	$7.97e^{-6}$	0.119
$G_m = 100$	$3.99e^{-6}$	0.202	$3.99e^{-6}$	0.200	$2.33e^{-6}$	0.118	$3.99e^{-6}$	0.202	$3.99e^{-6}$	0.118
$I_m = 10$	-	-	$3.92e^{-5}$	0.200	-	-	-	-	-	-
$I_m = 50$	-	-	$3.92e^{-5}$	0.200	-	-	-	-	-	-
$I_m = 100$	-	-	$3.92e^{-5}$	0.200	-	-	-	-	-	-
$K_d = 150$	-	-	-	-	$2.32e^{-5}$	0.130	-	-	$3.92e^{-5}$	0.130
$K_d = 200$	-	-	-	-	$1.79e^{-5}$	0.100	-	-	$3.92e^{-5}$	0.100
$K_d = 250$	-	-	-	-	$1.25e^{-5}$	0.070	-	-	$3.92e^{-5}$	0.070

Please note that only the parallel inerter and damper terms common to all realizations are presented in Table 8.3 for SEA and SDEA except Voigt model rendering. The numerical values used for additional elements in the realizations are presented in Table 8.4 in Section 8.1.4.

The null impedance rendering performance increases as the parallel inerter and damper terms in the physical equivalents decrease. From Table 8.3, it can be observed that these parallel inerter and damper terms decrease with the choice of higher proportional gains  $G_t$  and  $G_m$ . For all physical equivalents,  $G_t$  has a larger effect on decreasing the damper term than  $G_m$ . Furthermore, the integral controller gain  $I_m$  does not have any significant effect on these parasitic inerter and damper terms, for the realizations considered, but results in frequency dependent damping effect that increases with frequency.

The spring rendering performance also improves as the parasitic inerter and damper terms in the physical equivalents decrease. From Table 8.3, it can be observed

that these parallel inerter and damper terms decrease with the choice of higher proportional gains  $G_t$  and  $G_m$ . For all physical equivalents,  $G_t$  has a larger effect on decreasing the damper term than  $G_m$ . Higher desired stiffness  $K_d$  decreases these parallel inerter and damper terms for SEA, while  $K_d$  decreases only the damper term for SDEA and has no effect on the inerter term for SDEA.

Tables 8.3 and 8.4 show that the parasitic components of the physical realization approach to zero as the controller gains are increased; however, passivity bounds limit these gains to ensure that physical components cannot be negative, resulting in a trade-off between the rendering performance and the stability robustness. Similarly, passivity bounds impose a upper bound on  $K_d$  during spring rendering, as demonstrated by high  $K_d$  terms necessitating negative damping in realizations.

## 8.1 Effects of Controller Gains on Null Impedance Rendering Performance

P-P controllers for SEA:

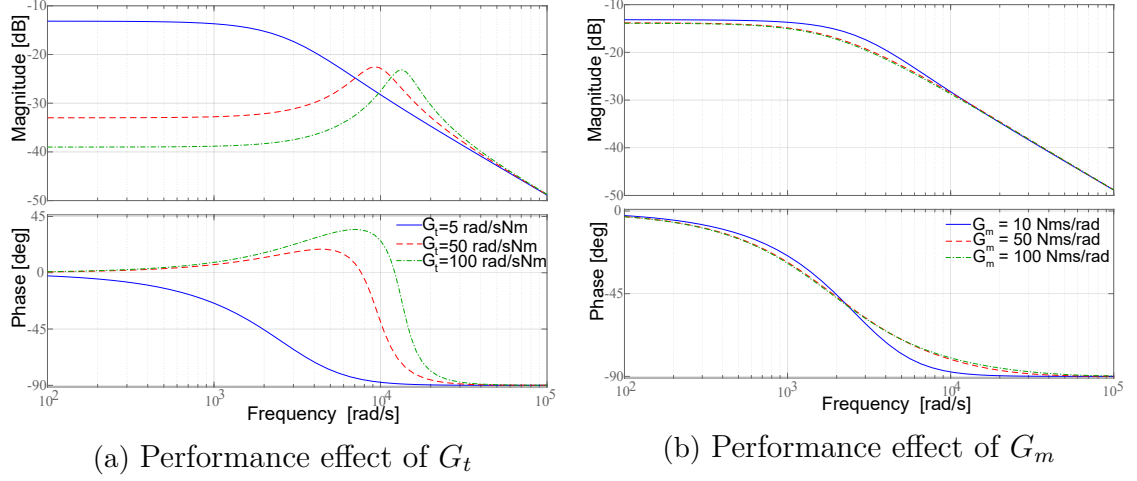


Figure 8.1 Effect of  $G_t$  and  $G_m$  on null impedance rendering performance of SEA when both controllers are P

Figure 8.1 presents Bode plots of system performance for various  $G_m$  and  $G_t$  controller gains. It can be observed from the Bode plots that the output impedance converges to the dynamics of the physical spring  $K$  at the high frequency range and the controller gains can shape this transition. Figure 8.1a indicates that null impedance rendering performance can be significantly improved by employing higher  $G_t$  gains, leading to attenuated damping effects. Figure 8.1b shows that the effect of  $G_m$  gain is much less in the low frequency range. Figures 8.1a and 8.1b indicate that higher  $G_t$  and  $G_m$  gains enable smoother the transition from the intermediate frequency range to the high frequency range and reduce the resonant peak. Table 8.3 can be used to verify that the damper term of passive physical equivalent decreases with choice of higher force controller gain  $G_t$  and the inerter term decreases with choice of high controller gains  $G_t$  and  $G_m$ .

P-PI controllers for SEA:

The Bode plots in Figures 8.2a and 8.2b indicate that the system response under P-PI controller is quite similar to the behaviour under the P-P control architecture. In Figure 8.2c, the effect of  $I_m$  on Bode plots of the null impedance rendering performance seems quite low.

$I_m$  does not display a noticeable effect on the null impedance rendering performance, as shown in Figure 8.2c,  $I_m$  significantly affects the disturbance rejection performance of the system, as the disturbance rejection performance is improved by

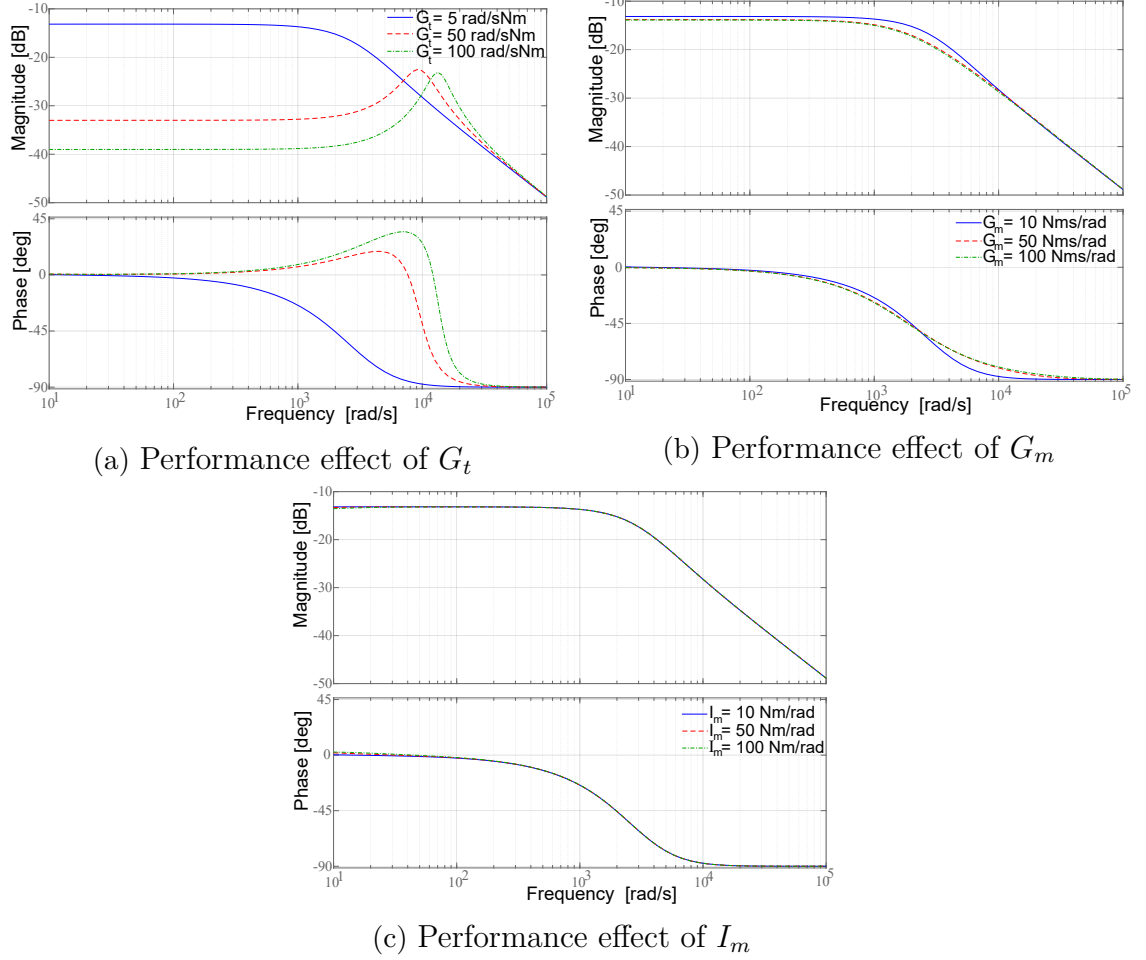


Figure 8.2 Effect of  $G_t$ ,  $G_m$ , and  $I_m$  on null impedance rendering performance for SEA when the force controller is P and the motion controller is PI

larger  $I_m$  gains. Further insight into the disturbance rejection performance can also be gained through physical realizations. In particular, if we consider a disturbance force  $F_{dist}$  acting on the system at the same location with the actuator input in Figure 3.2, the disturbance response of the closed-loop system under P-PI VSIC controller during null impedance rendering can be derived as

$$Y_{f_{null}}^{SEA^{P-PI}}(s) = \frac{\omega_{end}}{F_{dist}} \Big|_{\tau_{sea}=0} = \frac{s}{J_m s^2 + (B_m + G_m) s + I_m} \quad (8.1)$$

The disturbance transfer function  $Y_{f_{null}}^{SEA^{P-PI}}$  in Eqn. (8.1) is in the form of a passive admittance of an inerter  $J_m$ , damper  $(B_m + G_m)$  and spring  $I_m$  in parallel; hence,  $Y_{f_{null}}^{SEA^{P-PI}}$  decreases with  $I_m$ , indicating better disturbance attenuation. The physical realization of  $Y_{f_{null}}^{SEA^{P-PI}}$  emphasizes the effect of  $I_m$  as the restoring spring that counteracts disturbances.

When a P-P controller that omits the integral term is utilized under VSIC, no restoring spring exists for the disturbance response and much larger steady state



errors are likely be induced due to disturbances. Also note that larger  $G_m$  gains positively impact the disturbance response of both systems.

P-P controllers for SDEA:

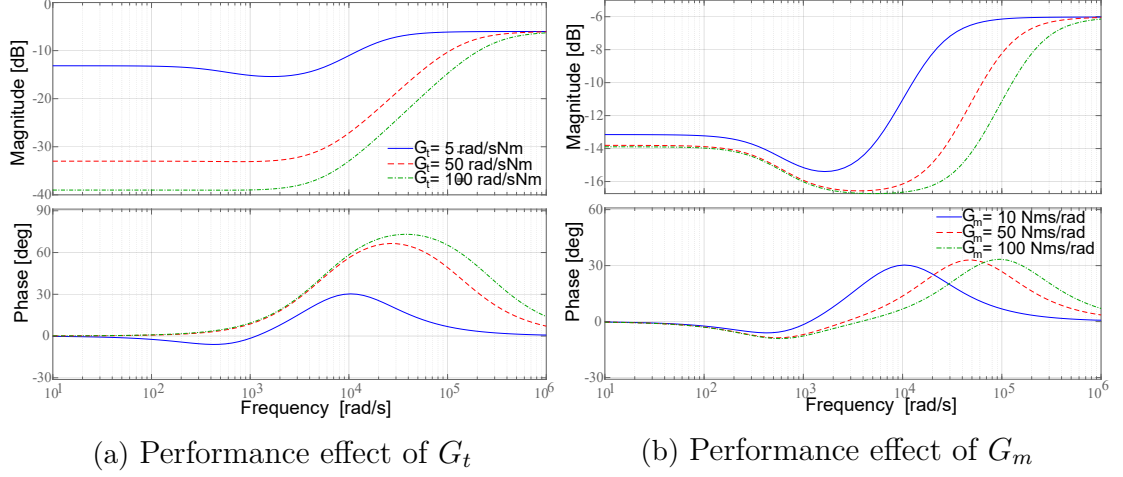


Figure 8.3 Effect of  $G_t$  and  $G_m$  on null impedance rendering performance of SDEA when both controllers are P

Figure 8.3 presents Bode plots of system performance for various  $G_m$  and  $G_t$  controller gains. It can be observed from the Bode plots that the output impedance converges to the dynamics of the physical damper  $B_f$  at the high frequency range and the controller gains can shape this transition.

Figure 8.3a indicates that null impedance rendering performance can be significantly improved by employing higher  $G_t$  gains, leading to attenuated damping effects. Figure 8.3b shows that the effect of  $G_m$  gain is less in the low frequency range. Figures 8.3a and 8.3b indicate that higher  $G_t$  and  $G_m$  gains enable smoother the transition from the intermediate frequency range to the high frequency range.

### 8.1.1 Effects of Controller Gains on Ideal Spring Rendering Performance

P-P Controllers for SEA:

High frequency dynamics of SEA is governed by the spring of the physical filter, all Bode plots converges to this dynamics. Figure 8.4a shows that as the force controller gain  $G_t$  is increased, the frequency range over which the virtual stiffness is successfully rendered can be significantly increased. Figures 8.4a and 8.4b indicate that, a smoother transition takes place at the intermediate frequency range, from the rendered virtual spring at the low frequency range to the spring of the physical filter at the the high frequency range, when higher P-gains are utilized. Similarly,

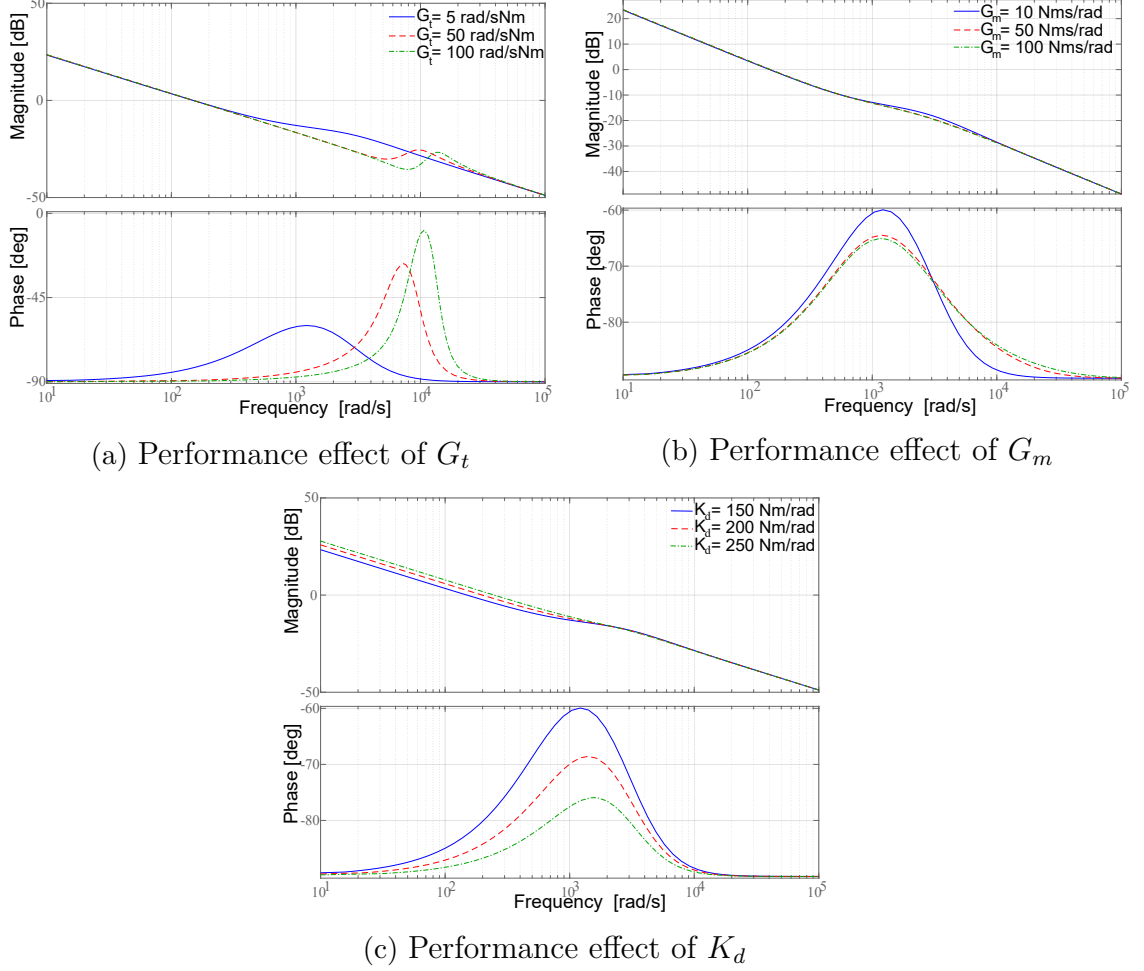


Figure 8.4 Effect of  $G_t$ ,  $G_m$ , and  $K_d$  on the spring rendering performance of SEA during when both controllers are P

Figure 8.4c shows that higher virtual stiffness levels can be rendered for higher  $K_d$  selections, and for such selections the transition at the intermediate frequency range is smoother. Figure 8.4b indicates that  $G_m$  gains do not result in significant rendering performance differences at the low frequency range; however,  $G_m$  gains positively impact the disturbance response of the system, as shown in the previous subsection. Furthermore, the effects of controller gains on parameters of the realization can also be verified through the numerical values presented in Table 8.3.

Insight into the disturbance rejection performance of SEA during spring rendering can also be gained through physical realizations. In particular, if we consider a disturbance force  $F_{dist}$  acting on the system at the same location with the actuator input in Figure 3.2, the disturbance response of the closed-loop SEA system under P-P VSIC controller during spring impedance rendering can be derived as

$$Y_{f_{spring}}^{SEA^{P-P}}(s) = \frac{\omega_{end}}{F_{dist}} \Big|_{\tau_{sea}=0} = \frac{s}{J_m s^2 + (B_m + G_m)s + G_m G_t K_d} \quad (8.2)$$

The disturbance transfer function  $Y_{f_{spring}}^{SEAP-P}$  in Eqn. (8.2) is in the form of a passive admittance of an inerter  $J_m$ , damper  $(B_m + G_m)$  and spring  $G_m G_t K_d$  in parallel; hence,  $Y_{f_{spring}}^{SEAP-P}$  decreases with larger controller gains and  $K_d$ , indicating better disturbance attenuation. The physical realization of  $Y_{f_{spring}}^{SEAP-P}$  emphasizes the effect of  $G_m G_t K_d$  as the restoring spring that counteracts disturbances. Note that when  $K_d \rightarrow 0$ , the disturbance response for null impedance rendering case is recovered.

#### P-P Controllers for SDEA:

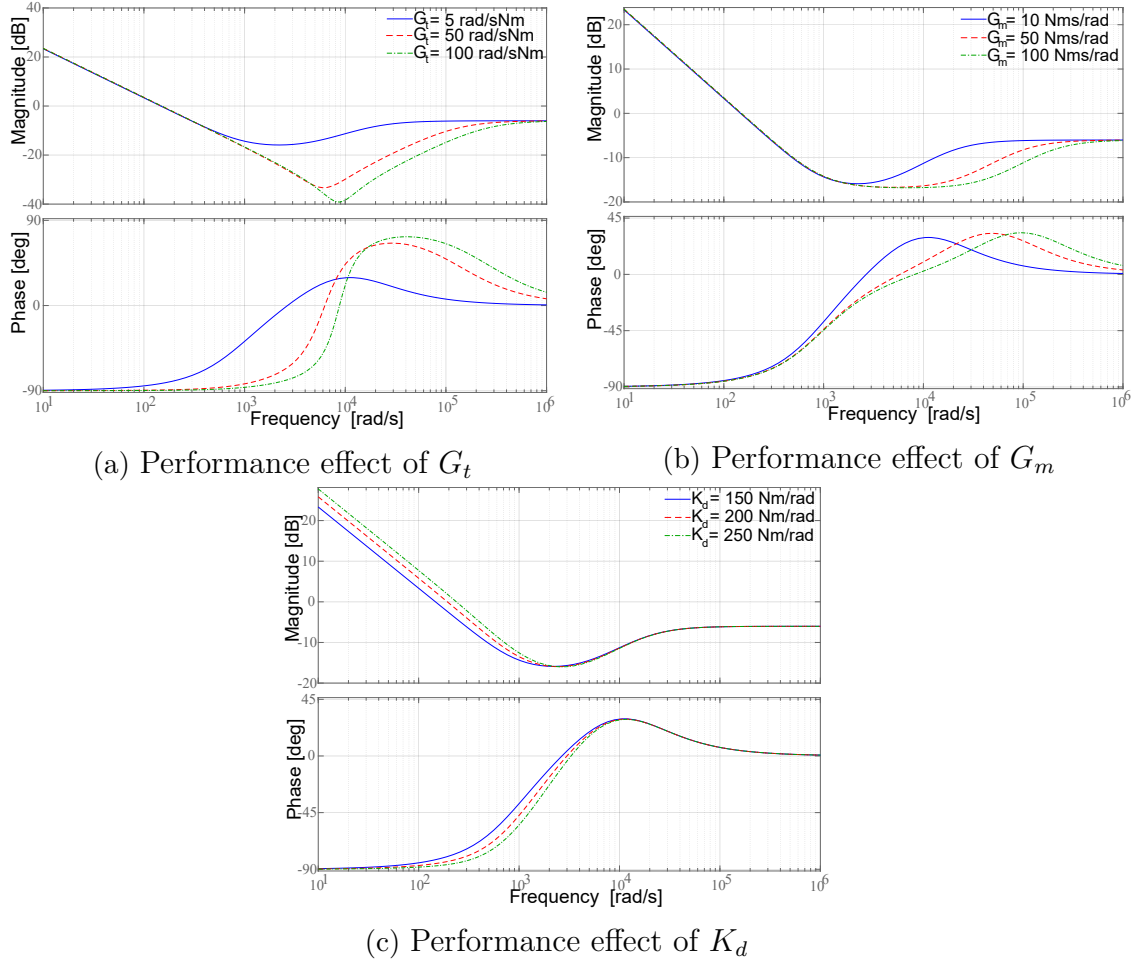


Figure 8.5 Effect of  $G_t$ ,  $G_m$ , and  $K_d$  on the spring rendering performance of SDEA during when both controllers are P

Figure 8.5a shows that as the force controller gain  $G_t$  is increased, the frequency range over which the virtual stiffness is successfully rendered can be significantly increased. Figures 8.5a and 8.5b indicate that, a smoother transition takes place at the intermediate frequency range, from the rendered virtual spring at the low frequency range to the damping of the physical filter at the high frequency range, when higher P-gains are utilized. Similarly, Figure 8.5c shows that higher virtual stiffness levels can be rendered for higher  $K_d$  selections, and for such selections, the transition at the intermediate frequency range is smoother. Figure 8.5b shows that

$G_m$  gains do not result in significant rendering performance differences at the low frequency range; however,  $G_m$  gains positively impact the disturbance response of the system. The effects of controller gains on parameters of the realizations can also be verified through the numerical values presented in Table 8.3.

If we consider a disturbance force  $F_{dist}$  acting on the system at the same location with the actuator input in Figure 3.2, the disturbance response  $Y_{f_{spring}}^{SDEA^{P-P}}(s)$  of the closed-loop SDEA system under P-P VSIC controller during spring impedance rendering is identical to that of SEA given in Eqn. (8.2). Hence, the addition of  $B_f$  to the physical filter does not affect this disturbance response.

### 8.1.2 Effects of Physical Plant and Filter Parameters on Null Impedance Rendering Performance

Passive physical equivalents do not distinguish between the plant and the controller parameters and promote co-design thinking by enforcing simultaneous consideration of controller and plant dynamics on the closed-loop system performance [65, 66].

#### Effects of Plant Parameters:

Table 8.1c and 8.1e indicate that the inerter term is equal to  $\frac{J_m}{\alpha+1}$  for S(D)EA during null impedance rendering when both controllers are P. Hence, the parasitic effect of this intertence can be reduced, either by redesigning the plant with lower  $J_m$  or selecting higher controller gains. Figures 8.6a and 8.6c show that better null impedance rendering performance can be achieved by employing a plant with lower  $J_m$  for S(D)EA plants.

Similarly, Table 8.1c and 8.1e indicate that the damper term is equal to  $\frac{B_m+G_m}{\alpha+1}$  for S(D)EA during null impedance rendering when both controllers are P. Hence, the parasitic effect of this damper can be reduced, either by redesigning the plant with lower  $B_m$  or selecting higher controller gains, especially higher  $G_t$ . Figures 8.6b and 8.6d show that the null impedance rendering performance can be improved by employing a plant with lower  $B_m$  for S(D)EA plants.

#### Effects of Physical Filter Parameters:

Table 8.1c and 8.1e indicate that the physical filter affects the system performance as a serially connected mechanical low-pass filter and does not have any influence on the remaining parasitic dynamics. Figures 8.7a and 8.7b indicate that the null impedance rendering bandwidth of S(D)EA improves for the selection of higher filter stiffness  $K$ , when both controllers are P.

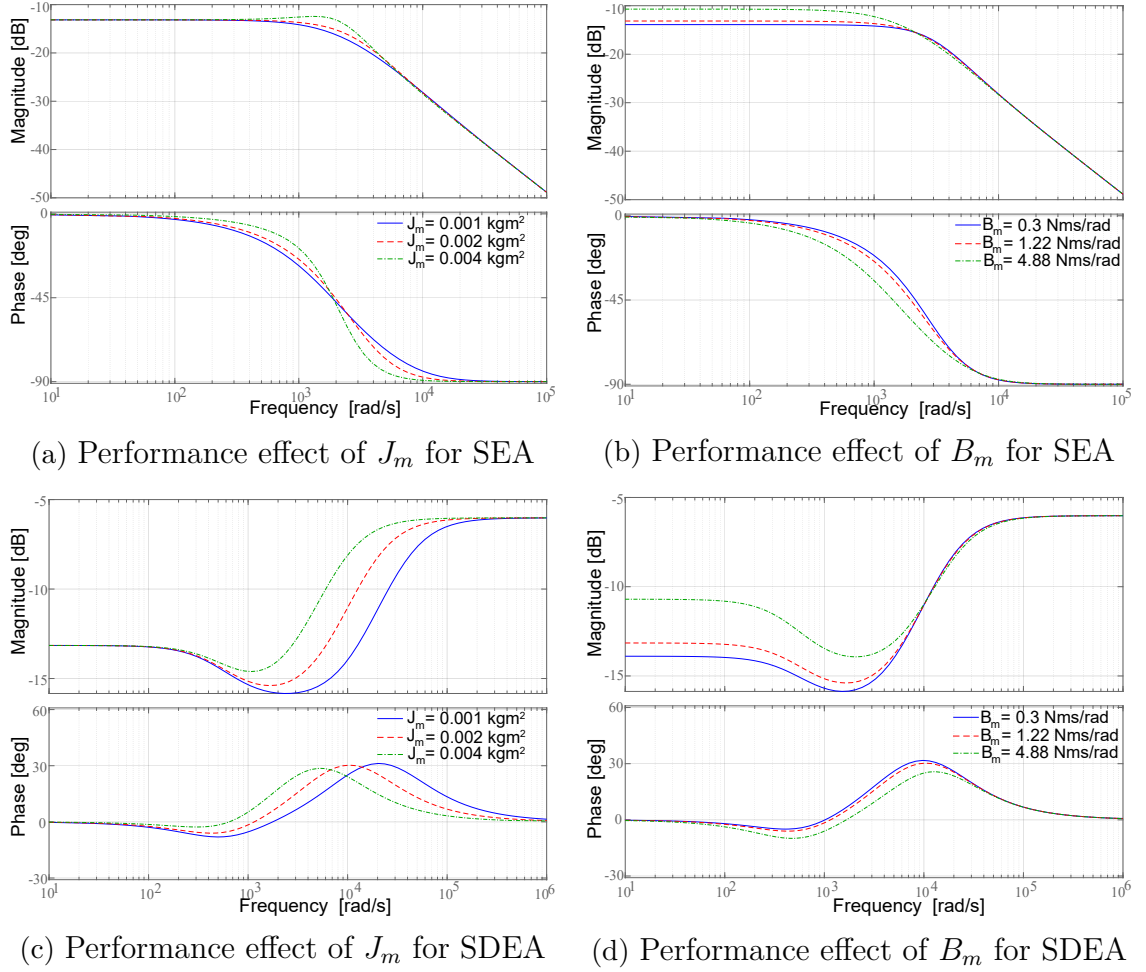


Figure 8.6 Effect of plant parameters  $J_m$  and  $B_m$  on performance for SEA and SDEA during null impedance rendering when both controllers are P

This performance improvement is due to the improved bandwidth of the physical filter; however, employing a stiffer mechanical filters come with the cost of reduced force sensing resolution and less disturbance attenuation under impulsive disturbances acting at the interaction port.

Figure 8.7c shows that the damping of the physical filter  $B_f$  dominate the high frequency dynamic behaviour of SDEA.

### 8.1.3 Effects of Physical Plant and Filter Parameters on Ideal Spring Rendering Performance

Effects of Plant Parameters:

Table 8.1b and 8.1d indicate that the inerter terms are equal  $\sigma J_m$  and  $\frac{J_m}{\alpha+1}$  for SEA and SDEA, respectively, during ideal spring rendering when both controllers are P. Hence, the parasitic effect of these intertences can be reduced, either by redesigning the plant with lower  $J_m$  or selecting higher controller gains. Figures 8.8a and 8.8c

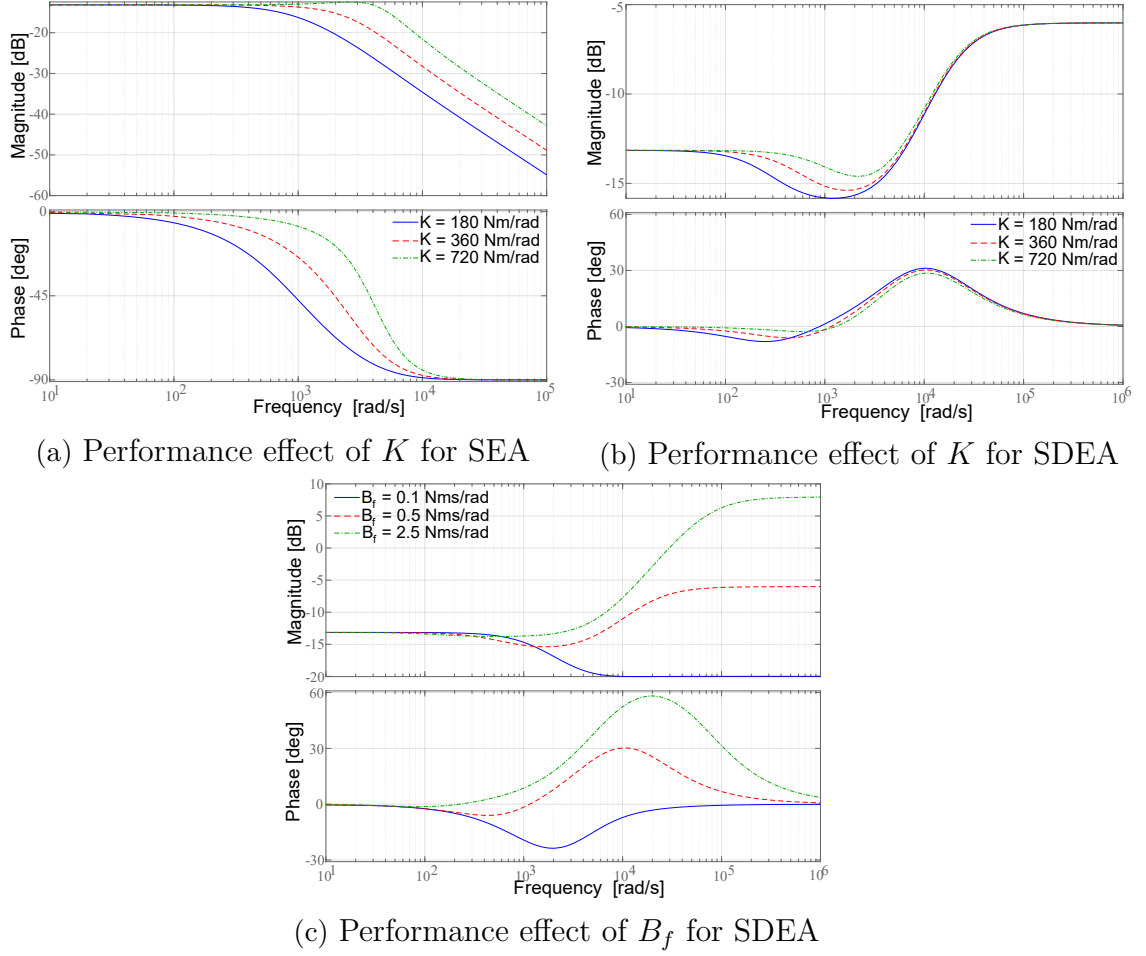


Figure 8.7 Effect of physical filter parameters  $K$ - $B_f$  on performance for SEA and SDEA during null impedance rendering when both controllers are P

show that better virtual spring rendering performance can be achieved by employing a plant with lower  $J_m$  for S(D)EA plants.

Similarly, Table 8.1b and 8.1d indicate that the low frequency dominant damper term is equal to  $\sigma(B_m + G_m)$  for both SEA and SDEA during ideal spring rendering when both controllers are P. Hence, the parasitic effect of this damper can be reduced, either by redesigning the plant with lower  $B_m$  or selecting higher controller gains, especially higher  $G_t$ . Figures 8.8b and 8.8d show that the virtual spring rendering performance can be improved by employing a plant with lower  $B_m$  for S(D)EA plants.

#### Effects of Physical Filter Parameters:

Table 8.1b and 8.1d indicate that the physical filter directly affects the virtual spring rendering performance of the system, as it acts as the coupling element between the parasitic system dynamics and spring to be rendered. In particular, the coupling spring is in the form of  $K - \frac{\alpha K_d}{\alpha+1}$ , whose feasibility of implementation imposes an

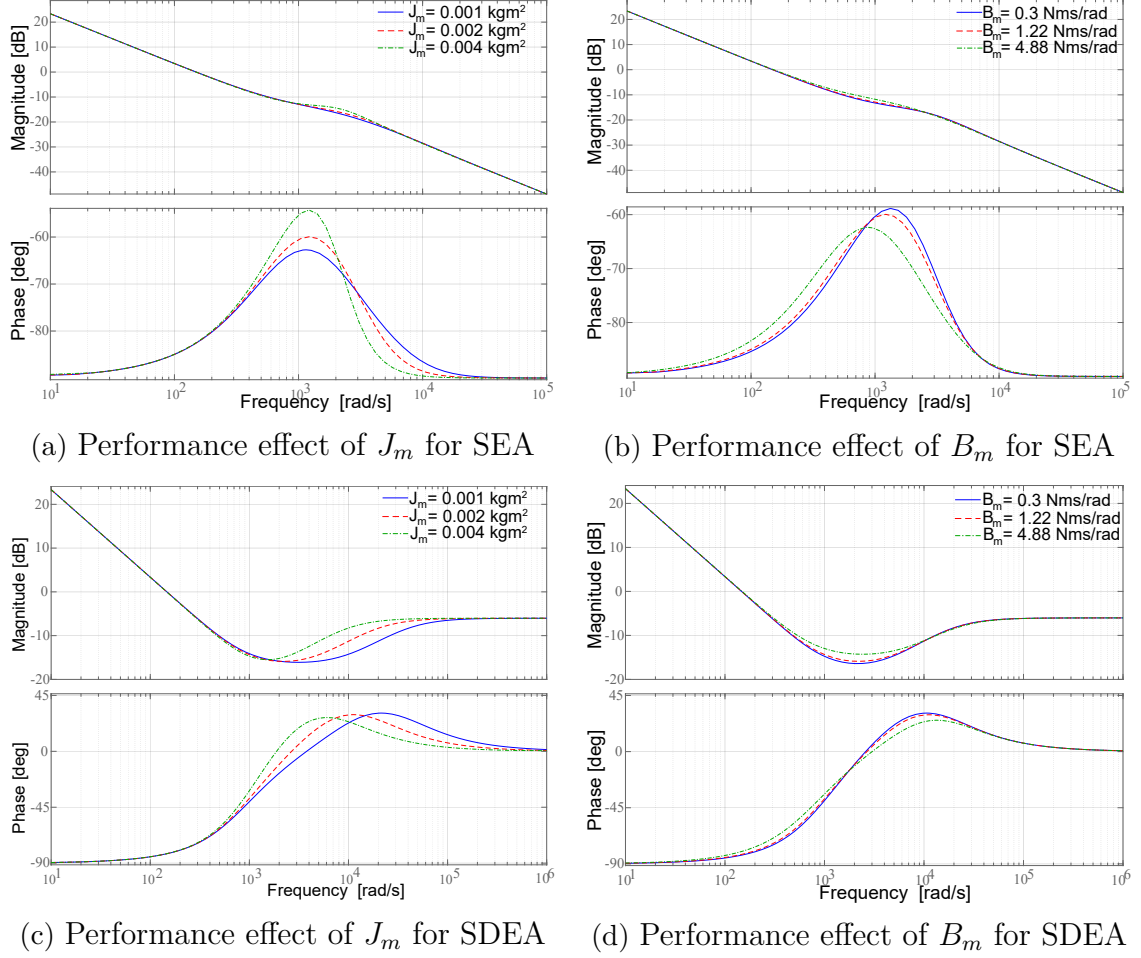


Figure 8.8 Effect of plant parameters  $J_m$  and  $B_m$  on performance for SEA and SDEA during ideal spring rendering when both controllers are P

upper bound on the virtual springs  $K_d$  that can be passively rendered. The effect of coupling through this spring element can be reduced by using a physical filter with lower stiffness  $K$ .

Furthermore, the stiffness of the physical filter  $K$  has a direct effect on the term  $\sigma$  that scales parasitic dynamic effects. In particular,  $\sigma = \frac{1}{\alpha+1} - \frac{\alpha}{(\alpha+1)^2} \frac{K_d}{K}$  can be reduced by the use of lower filter stiffness  $K$ , positively affecting the parasitic inertance and damping effects for SEA, and damping effects for SDEA, respectively.

Table 8.1d indicates that the damper of the physical filter  $B_f$  directly affects the coupling behaviour and lower  $B_f$  increases range of virtual stiffness, while accuracy of virtual stiffness decreases.

Figures 8.9a and 8.9b show that the frequency range over which desired virtual spring is rendered can be improved if the stiffness of the physical filter  $K$  is selected to be close to  $K_d$ . Figure 8.9c indicates that the virtual spring rendering performance is improved for lower  $B_f$ , as this damping dominates the high frequency behaviour and



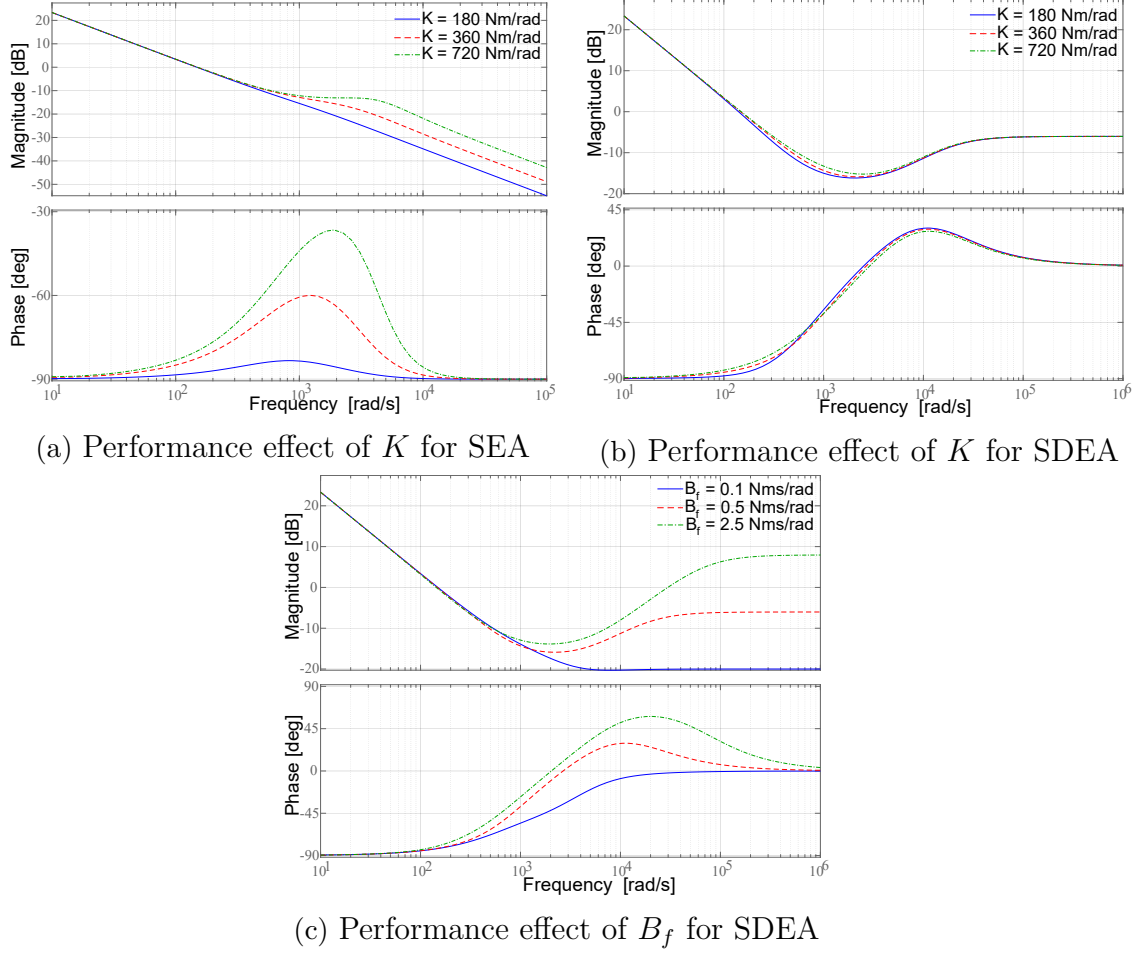


Figure 8.9 Effect of physical filter parameters  $K$ - $B_f$  on performance for SEA and SDEA during ideal spring rendering when both controllers are P

the transition from desired spring to  $B_f$  needs to take place earlier for larger  $B_f$ .

#### 8.1.4 Rendering Performance Comparison of SEA vs SDEA

For null impedance rendering, Table 8.1c and 8.1e indicate that both SEA and SDEA have identical parasitic dynamics consisting of a damper and inerter in parallel and the effects of controller gains on these elements are the same. Hence, only difference is due to the damper term  $B_f$  in the physical filter of SDEA. Figure 8.10a presents a comparison the null impedance rendering performance of SEA and SDEA when the controller gains are selected to be the same. As can be verified from Table 8.3, the inerter and damper terms of physical equivalents of SEA and SDEA have the same values. Figure 8.10a indicates that the performance of SEA and SDEA are very close in the low frequency range. However, as expected, the high frequency dynamics of SEA is dominated by the stiffness  $K$  of the physical filter, while the high frequency dynamics of SDEA is dominated by the damping  $B_f$  of the physical filter. Accordingly, the transition from null impedance rendering to high frequency



dynamics differs significantly for SEA and SDEA.

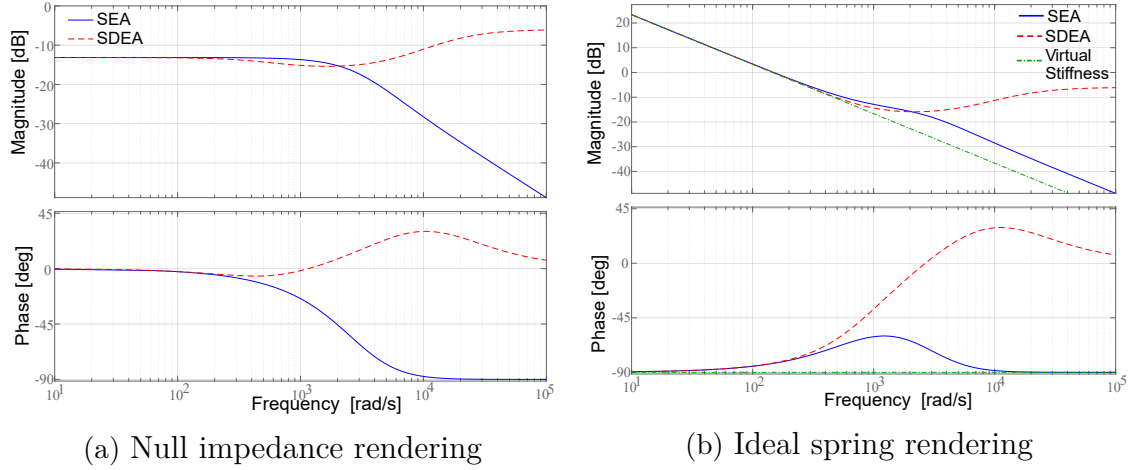


Figure 8.10 Rendering performance comparison between SEA and SDEA

Table 8.4 Numerical values for serial-inerter damper element for various values of  $G_t$ ,  $G_m$ ,  $I_m$ , and  $K_d$  for SEA during null impedance rendering when controllers are PI-P and for SDEA during spring rendering when controllers are P-P.

	S(D)EA P-PI (Null Impedance)		SDEA P-P (Spring Rendering)	
	Inerter ( $b_{1n}$ )	Damper ( $c_{2n}$ )	Inerter ( $b_{1s}$ )	Damper ( $c_{1s}$ )
$G_t = 5$	0.0204	0.0200	$10^{-4}$	0.078
$G_t = 50$	0.0024	0.0024	$10^{-5}$	0.008
$G_t = 100$	0.0012	0.0012	$10^{-5}$	0.004
$G_m = 10$	0.0204	0.0200	$10^{-4}$	0.078
$G_m = 50$	0.0204	0.0041	$10^{-4}$	0.082
$G_m = 100$	0.0204	0.0020	$10^{-4}$	0.083
$I_m = 10$	0.0204	0.0200	-	-
$I_m = 50$	0.0040	0.0198	-	-
$I_m = 100$	0.0020	0.0196	-	-
$K_d = 150$	-	-	$10^{-4}$	0.078
$K_d = 200$	-	-	$10^{-4}$	0.104
$K_d = 250$	-	-	$2e^{-4}$	0.131

For ideal spring rendering, Table 8.1b and 8.1d indicate that both SEA and SDEA include identical parasitic damper terms, but the parasitic inerter terms are different. Furthermore, SDEA includes an extra branch with frequency dependent damping effect that increases with frequency. As can be verified from Table 8.3, the inerter effects are lower for SEA, compared to SDEA, while the low frequency damping effects are identical. Table 8.4 presents the numerical values for the elements that provide the frequency dependent damping effect. Figure 8.10b presents a comparison the ideal spring impedance rendering performance of SEA and SDEA when the controller gains are selected to be the same. Figure 8.10b indicates that the performance of SEA and SDEA are quite close to each other in the low frequency range. However, similar to the the null impedance rendering case, the high

frequency dynamics of SEA is dominated by the stiffness  $K$  of the physical filter, while the high frequency dynamics of SDEA is dominated by the damping  $B_f$  of the physical filter. Accordingly, the transition from spring rendering to high frequency dynamics differs significantly for SEA and SDEA.

### 8.1.5 Comparison of Loss Factor for SEA and SDEA

Dissipation in a system can be quantified using the concept of the loss coefficient. The loss coefficient is defined as the ratio of the energy dissipated per radian and the total strain energy [67] that is  $\frac{\Delta W}{2\pi W}$  where  $\Delta W$  is dissipated energy and  $W$  is total energy. Loss factor (loss coefficient) defines the equation of motion of a single degree-freedom system with internal damping which is:

$$\frac{\text{Energy dissipated during 1 cycle of harmonic displacement/radian}}{\text{Maximum strain energy in cycle}} \quad (8.3)$$

Figure 8.11 presents a comparison of loss factors of SEA and SDEA while both systems are rendering an ideal spring.

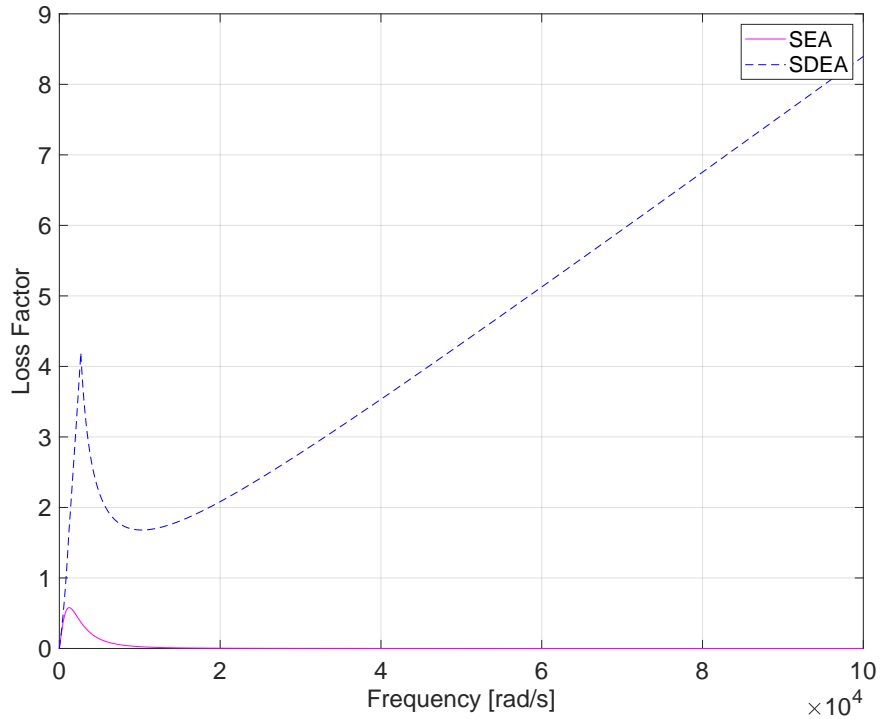


Figure 8.11 Loss Factor of SEA vs SDEA

Figure 8.11 shows that loss factor of SDEA is higher than that of SEA, as SDEA includes more damping compared to SEA.

### 8.1.6 Voigt Model Rendering Performance of SDEA

During Bode plot and numeric evaluation as in Figure 8.12 and Table 8.5, Table 8.2 is used while  $K_d = 150 \text{ Nm/rad}$  and  $B_d = 0.2 \text{ Nms/rad}$ .

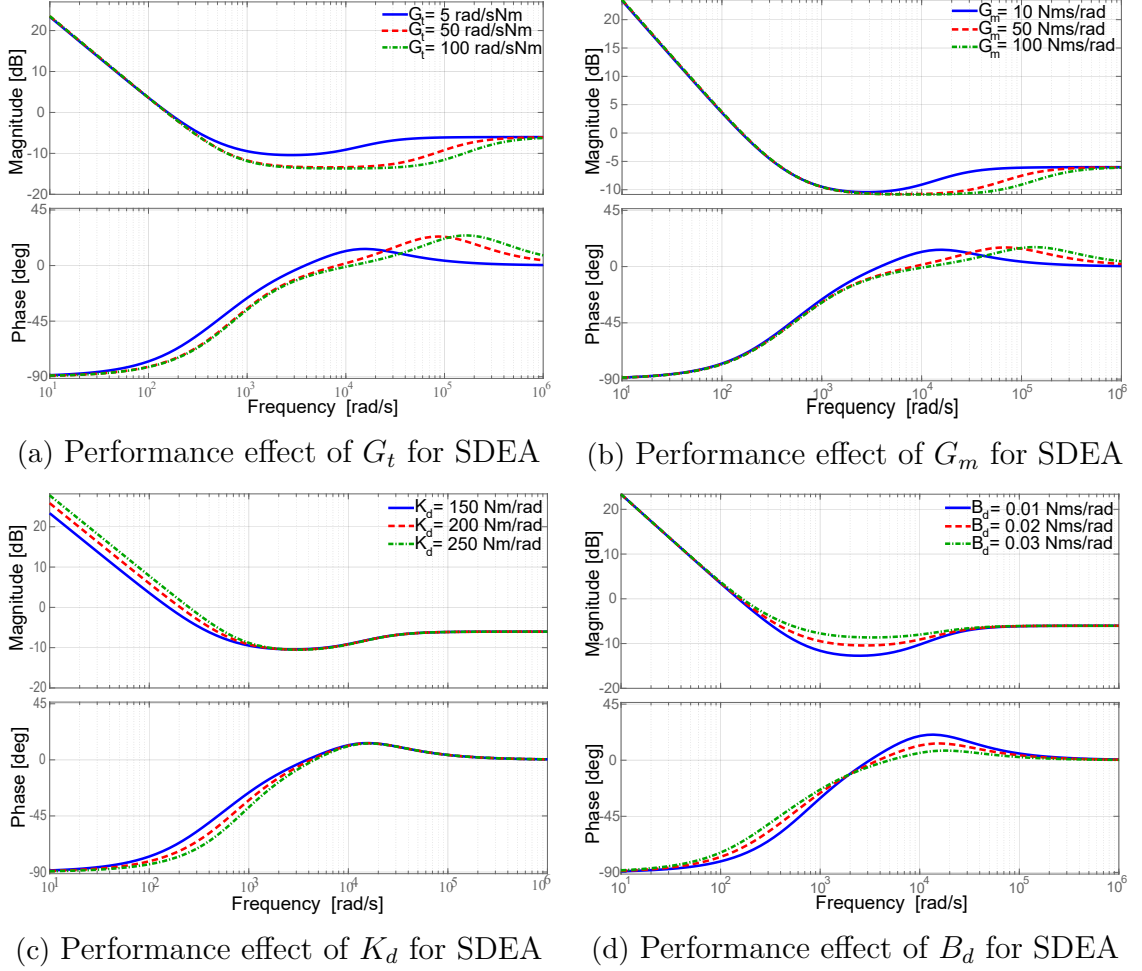


Figure 8.12 Effect of  $G_t$ ,  $G_m$ ,  $K_d$ , and  $B_d$  on the voigt model rendering performance of SDEA during when both controllers are P

Figure 8.12a shows that as the force controller gain  $G_t$  is increased, the frequency range over which the virtual stiffness and virtual damping are successfully rendered can be significantly increased. Figure 8.12b shows that  $G_m$  gains do not result in significant rendering performance differences at the spring rendering range; however, Figure 8.12b indicates that, range of virtual damping is increased with higher  $G_m$  gains. Higher  $K_d$  increases virtual stiffness and slightly reduces the virtual damping because  $\sigma(B_m + G_m)$  reduces with higher  $K_d$  as shows in Figure 8.12c. Figure 8.12d indicates that higher  $B_d$  increases virtual damping. Also, higher  $B_d$  increases range of the virtual damping due to lower inerter term. The effects of controller gains on parameters of the realizations can also be verified through the numerical values presented in Table 8.5.

Since the high frequency dynamics of SDEA is governed by the damping of the

Table 8.5 Numerical values for the inerter and damping terms of the passive physical equivalents for SDEA during Voigt model rendering for various controller gains  $G_m$ ,  $G_t$ ,  $K_d$ , and  $B_d$ . (Inerter is in  $kg\ m^2$  and damper is in  $Nm\ \frac{s}{rad}$ .)

	$b_{1s}$	$\sigma(B_m + G_m)$
$G_t=5$	$2.4e^{-5}$	0.130
$G_t=50$	$2e^{-6}$	0.013
$G_t=100$	$e^{-6}$	0.007
$G_m=10$	$2.4e^{-5}$	0.130
$G_m=50$	$5e^{-6}$	0.119
$G_m=100$	$2e^{-6}$	0.118
$K_d=150$	$2.4e^{-5}$	0.130
$K_d=200$	$2.4e^{-5}$	0.100
$K_d=250$	$2.4e^{-5}$	0.070
$B_d=0.1$	$3.2e^{-5}$	0.130
$B_d=0.2$	$2.4e^{-5}$	0.130
$B_d=0.3$	$1.6e^{-5}$	0.130

physical filter, all Bode plots converges to this dynamics.

Performance evaluation of ideal spring rendering and null impedance rendering for SDEA with insight of passive physical equivalents are provided in Table 8.1.

### 8.1.7 Physical Filter Damping Effect for SDEA

During Bode plot evaluation as in Figure 8.13, Table 8.2 is used while  $K_d = 150\ Nm/rad$  and  $B_d = 0.2\ Nms/rad$ .

Table 8.1a, 8.1b, and 8.1c are passive physical equivalents for SDEA for Voigt model rendering, ideal spring rendering, and null impedance rendering, respectively. All passive physical equivalents include physical filter term which consists of parallel damping and spring terms. Figure 8.13 presents performance of Voigt model rendering, ideal spring rendering, and null impedance rendering for SDEA when controllers are P. Figure 8.13a shows that Voigt model rendering performance is the worst for the lowest  $B_f$ . There is no significant difference between  $B_f = 0.5\ Nms/rad$  and  $B_f = 1\ Nms/rad$ . Figure 8.13b shows that when  $B_f$  is the lowest, range of spring rendering is the largest, but it is less accurate for the larger part. As a results of Figure 8.13b, there is no significant difference between different  $B_f$ . Figure 8.13c shows that the performance is the worst for the lowest  $B_f$ . There is no significant difference between  $B_f = 0.5\ Nms/rad$  and  $B_f = 1\ Nms/rad$ . All Bode plots in Figure 8.13 show that goes to  $B_f$  in the high frequency, but the high frequency behaviours change with different  $B_f$ .

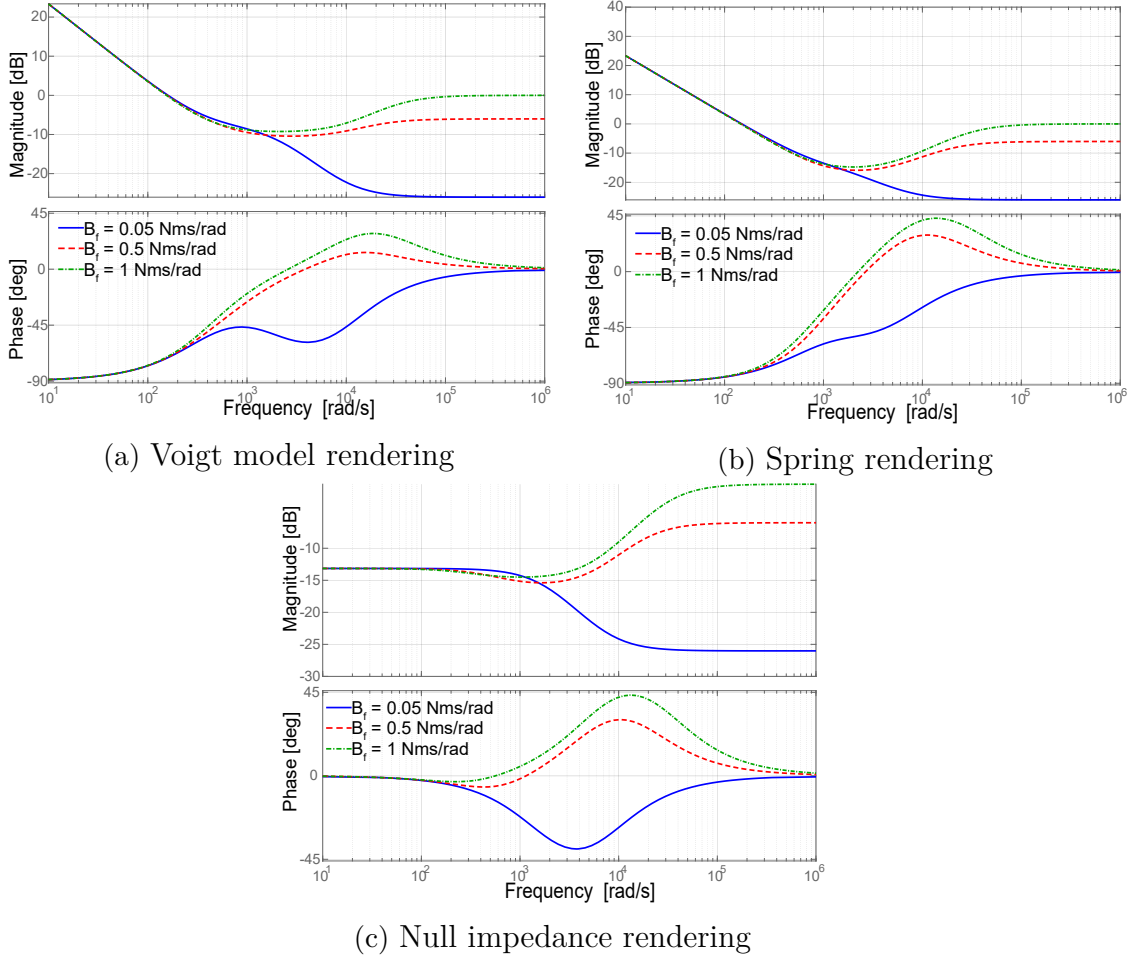


Figure 8.13 Effect of physical parameters  $B_f$  on performance SDEA during Voigt model rendering, spring rendering, and null impedance rendering

### 8.1.8 Physical Filter Damping Effect for $SDEA_{K_{fb}}$

During Bode plot evaluation as in Figure 8.14, Table 8.2 is used while  $K_d = 150 \text{ Nm/rad}$  and  $B_d = 0.2 \text{ Nms/rad}$ .

Table 8.1f, 8.1g, and 8.1h are passive physical equivalents for  $SDEA_{K_{fb}}$  for Voigt model rendering, ideal spring rendering, and null impedance rendering, respectively. All passive physical equivalents have the physical filter damping  $B_f$  as a parallel term with the all terms and this uncontrollable  $B_f$  is not measured for  $SDEA_{K_{fb}}$ .

Figure 8.14 presents effect of  $B_f$  on performance for Voigt model rendering, spring rendering, and null impedance rendering. Figure 8.14a and 8.14b show that range of the virtual stiffness in the low frequency range are larger with lower  $B_f$  because of lower physical filter damping term in Table 8.1f and 8.1g. Figure 8.14c shows that range of the low frequency range increases with lower  $B_f$  because of lower physical filter damping term in Table 8.1h. All Bode plots in Figure 8.14 show that goes to  $B_f$  in the high frequency, but the high frequency behaviours change with different

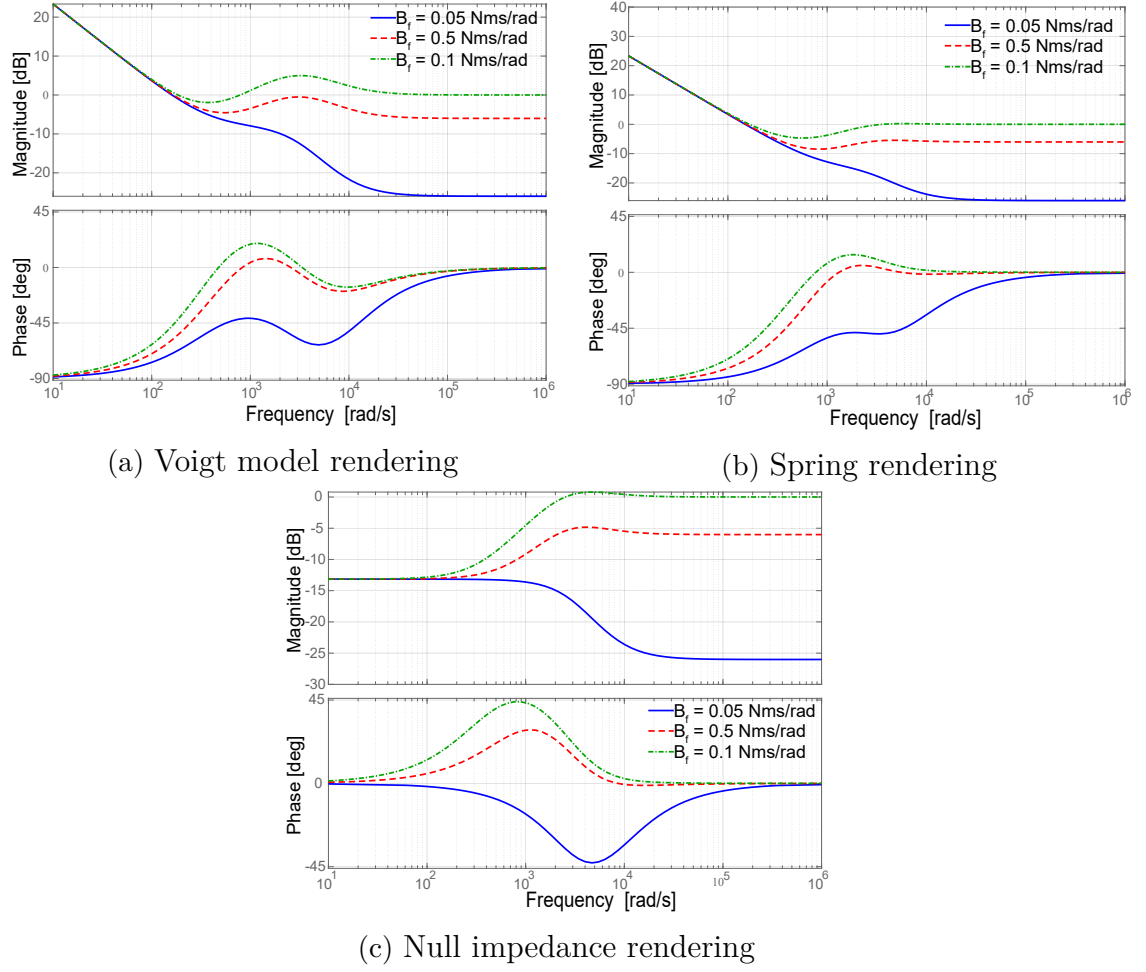


Figure 8.14 Effect of unmeasured physical parameters  $B_f$  on performance  $SDEA_{K_{fb}}$  during Voigt model rendering, spring rendering, and null impedance rendering

$B_f$ .

Figure 8.13 and 8.14 shows that higher performance increases with higher  $B_f$  for SDEA, but performance reduces with higher  $B_f$  for  $SDEA_{K_{fb}}$ . It can be verified by checking passive physical equivalents because  $B_f$  places parallel to all components for  $SDEA_{K_{fb}}$  which has disruptive effect, but  $B_f$  places parallel to physical spring for SDEA which affects performance in good way.

### 8.1.9 Performance Comparison of SDEA, $SDEA_{K_{fb}}$ , $SDEA_{K_{red}}$ , and SEA

Voigt Model Rendering: Voigt model can be passively rendered with SDEA,  $SDEA_{K_{fb}}$ , and  $SDEA_{K_{red}}$ , but SEA cannot render Voigt model which is shown before in [39]. Table 8.1a, 8.1f, and 8.1i are passive physical equivalents for Voigt model rendering for SDEA,  $SDEA_{K_{fb}}$ , and  $SDEA_{K_{red}}$ , respectively. Table 8.1a has desired virtual damping term which is parallel to desired virtual stiffness. Table 8.1f

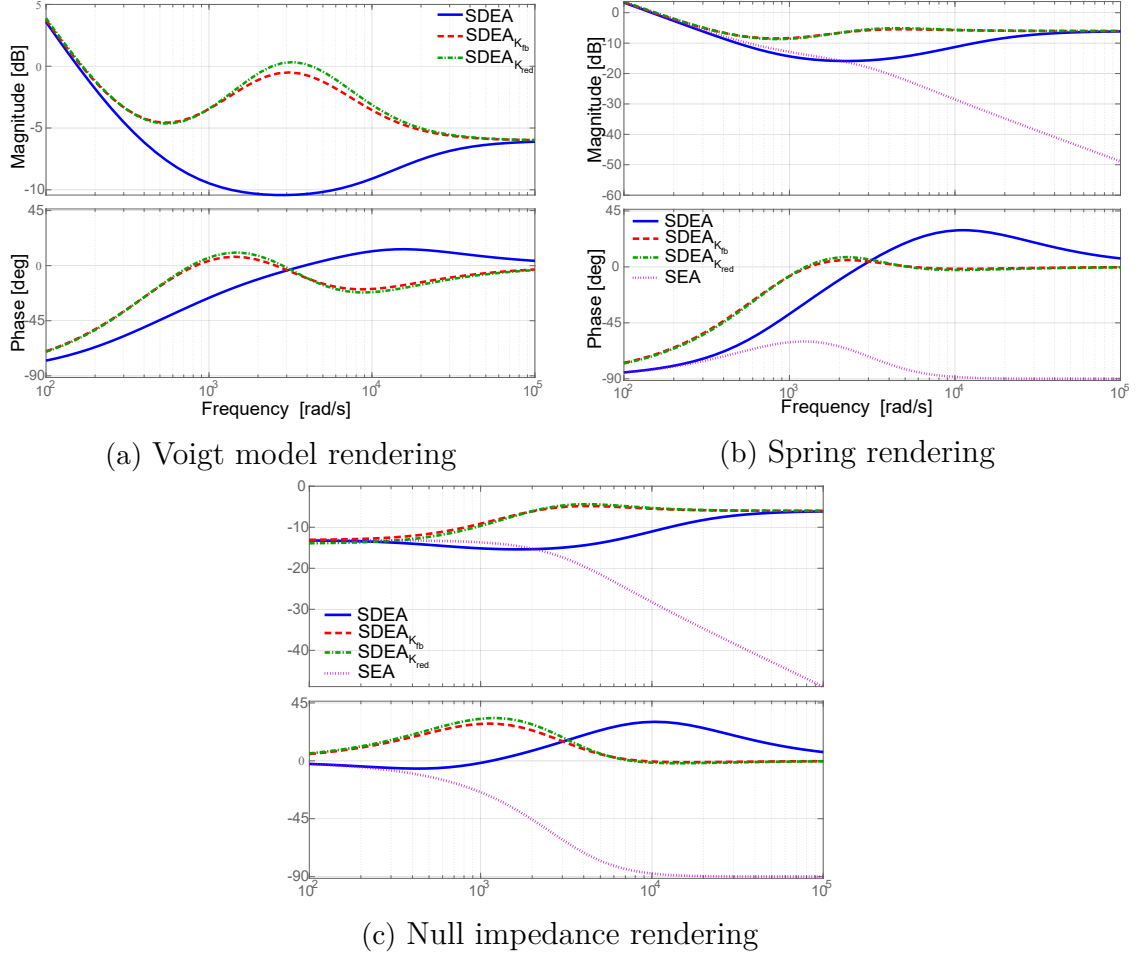


Figure 8.15 Performance comparison of SDEA,  $SDEA_{K_{fb}}$ ,  $SDEA_{K_{red}}$ , and SEA

and 8.1i have desired virtual stiffness terms like Table 8.1a, but Table 8.1f and 8.1i have physical filter damping term  $B_f$  instead of desired virtual damping which is not measured. The lack of desired virtual damping and existence of the physical filter damping term as a parallel term with the all other terms significantly affect Voigt model rendering performance for  $SDEA_{K_{fb}}$  and  $SDEA_{K_{red}}$ . Table 8.1a shows that this  $B_f$  exists in physical filter for SDEA where  $B_f$  is couple with spring. In addition to them, Table 8.1a and 8.1f have  $(\alpha K_d)/(\alpha + 1)$  as a desired virtual stiffness, but Table 8.1i have  $K_d$  as a desired virtual stiffness.

Figure 8.15a presents comparison of Voigt model rendering for SDEA,  $SDEA_{K_{fb}}$ , and  $SDEA_{K_{red}}$  when controller gains are selected to be the same. Figure 8.15a shows that SDEA has the best performance for Voigt model rendering performance. The range of desired virtual stiffness is larger for SDEA. Figures 8.15a shows that  $SDEA_{K_{fb}}$  and  $SDEA_{K_{red}}$  cannot render damping in the intermediate frequency unlike SDEA. Therefore, we can say that  $SDEA_{K_{fb}}$  and  $SDEA_{K_{red}}$  cannot render Voigt model accurately. Figure 8.15a shows that all Bode plots in Figure 8.15a goes to  $B_f$  in the high frequency. Lastly, it can be clearly seen that performance of  $SDEA_{K_{fb}}$  and

SDEA $_{K_{red}}$  are almost same.

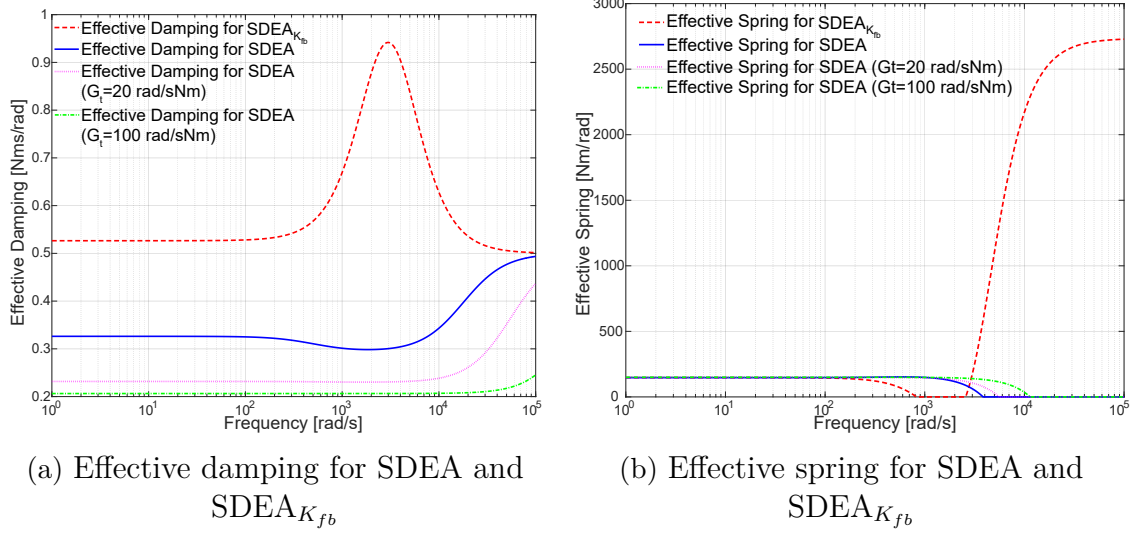


Figure 8.16 Effective damping and spring plots of SDEA and SDEA $_{K_{fb}}$  for Voigt model

Figure 8.16 shows that Voigt model performance comparison of SDEA and SDEA $_{K_{fb}}$  in terms of effective impedance analysis. Figure 8.16a shows that effective damping of SDEA gets closer the desired impedance, but SDEA $_{K_{fb}}$  goes irrelevant value with the effect of physical filter damping term in Table 8.1f. Furthermore, Figure 8.16a shows that effective damping gets closer with the choice of higher gains. SDEA and SDEA $_{K_{fb}}$  go to  $B_f$  in the high frequency range. Figure 8.16b shows that SDEA and SDEA $_{K_{fb}}$  can render virtual stiffness in the low frequency range, but SDEA's range is larger than SDEA $_{K_{fb}}$ . Figure 8.16b shows that performance increases with choice of higher controller gain. Furthermore, effective spring of SDEA goes to 0 in the low frequency range while SDEA $_{K_{fb}}$  is not equal to 0. Effective spring for SDEA in the high frequency range converges to summation of  $k_{1v}$  and  $(\alpha K_d)/(\alpha + 1)$ .

Ideal Spring Rendering: Table 8.1b, 8.1d, 8.1g, and 8.1j are passive physical equivalents for ideal spring rendering for SDEA, SEA, SDEA $_{K_{fb}}$ , and SDEA $_{K_{red}}$ , respectively. All passive physical equivalents have desired virtual stiffness as a parallel term. Table 8.1j has  $K_d$  as a desired virtual stiffness, others have  $(\alpha K_d)/(\alpha + 1)$  as a desired virtual stiffness. Table 8.1g and 8.1j have physical filter damping term  $B_f$  as a parallel term to all terms which affects performance of ideal spring rendering poorly. Table 8.1b shows that this  $B_f$  exists in physical filter for SDEA where  $B_f$  is couple with spring.

Figure 8.15b presents comparison of ideal spring rendering for SEA, SDEA, SDEA $_{K_{fb}}$ , and SDEA $_{K_{red}}$  when controller gains are selected to be the same. Figure 8.15b shows that ideal spring rendering performance of SDEA and SEA is very close and range of desired virtual stiffness in the low frequency range is better than



SDEA $_{K_{fb}}$  and SDEA $_{K_{red}}$ . All type of SDEAs go to  $B_f$  in the high frequency while SEA goes to physical stiffness in the high frequency. Accordingly, the transition from spring rendering to high frequency dynamics differs significantly for SEA, SDEA, and SDEA $_{K_{fb}}$ . Lastly, it can be clearly seen that performance of SDEA $_{K_{fb}}$  and SDEA $_{K_{red}}$  are almost same.

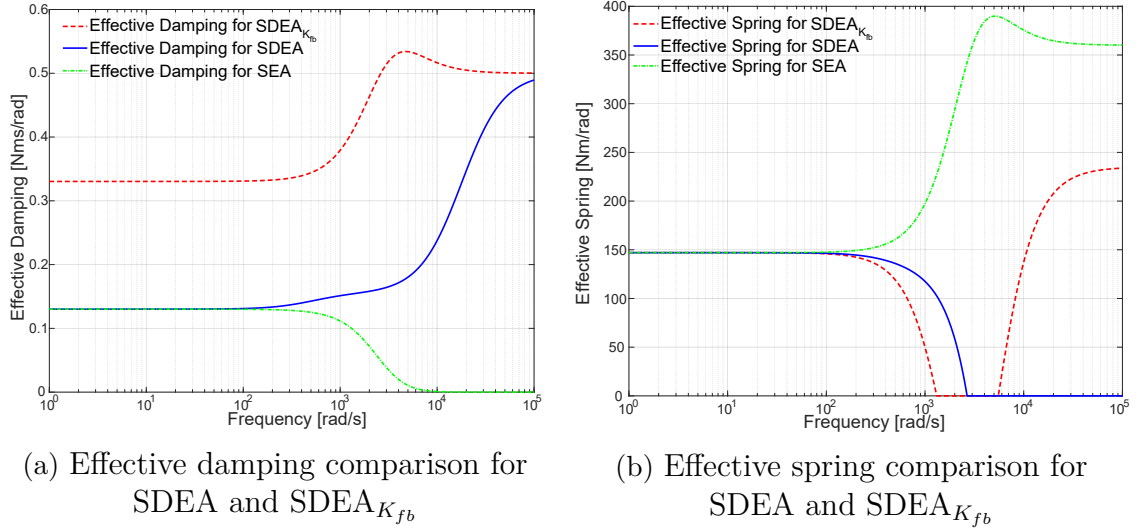


Figure 8.17 Effective impedance comparison for SDEA, SDEA $_{K_{fb}}$ , and SEA for spring rendering

Figure 8.17 shows that spring rendering performance comparison of SDEA, SDEA $_{K_{fb}}$ , and SEA in terms of effective impedance analysis. Figure 8.17a shows that effective damping of SDEA and SEA are nearly same, but effective damping of SDEA $_{K_{fb}}$  is higher. Therefore, it means that parasitic damping effect of SEA and SDEA is lower than SDEA $_{K_{fb}}$  which lead to better spring rendering performance which is verified by checking Figure 8.15b. SDEA and SDEA $_{K_{fb}}$  go to  $B_f$  in the high frequency range while SEA goes to 0. Figure 8.17b shows that SDEA, SDEA $_{K_{fb}}$ , and SEA can render virtual stiffness in the low frequency range and SDEA $_{K_{fb}}$  has the lowest range. Furthermore, Figure 8.17b shows that SDEA's effective spring is 0 while SDEA $_{K_{fb}}$  is not 0 in the high frequency range. Effective spring for SDEA in the high frequency range converges to summation of  $k_{1s}$  and  $(\alpha K_d)/(\alpha + 1)$ . Lastly, Figure 8.17b shows that SEA goes to physical stiffness in the high frequency range.

Null Impedance Rendering: Table 8.1c, 8.1e, 8.1h, and 8.1k are passive physical equivalents for null impedance rendering for SDEA, SEA, SDEA $_{K_{fb}}$ , and SDEA $_{K_{red}}$ , respectively. SDEA $_{K_{red}}$  has physical filter damper term as a parallel term to all terms which affects performance of null impedance rendering poorly. This  $B_f$  exists in physical filter for SDEA where  $B_f$  is couple with spring.

Figure 8.15c presents comparison of null impedance rendering for SEA, SDEA,

SDEA $_{K_{fb}}$ , and SDEA $_{K_{red}}$  when controller gains are selected to be the same. Figure 8.15c shows that null impedance rendering performance of SDEA and SEA is very close and better than SDEA $_{K_{fb}}$  and SDEA $_{K_{red}}$ . Range of the low frequency is larger for SEA and SDEA. All type of SDEAs go to  $B_f$  in the high frequency while SEA goes to physical stiffness in the high frequency. Accordingly, the transition from spring rendering to high frequency dynamics differs significantly for SEA, SDEA, and SDEA $_{K_{fb}}$ . Lastly, it can be clearly seen that performance of SDEA $_{K_{fb}}$  and SDEA $_{K_{red}}$  are almost same.

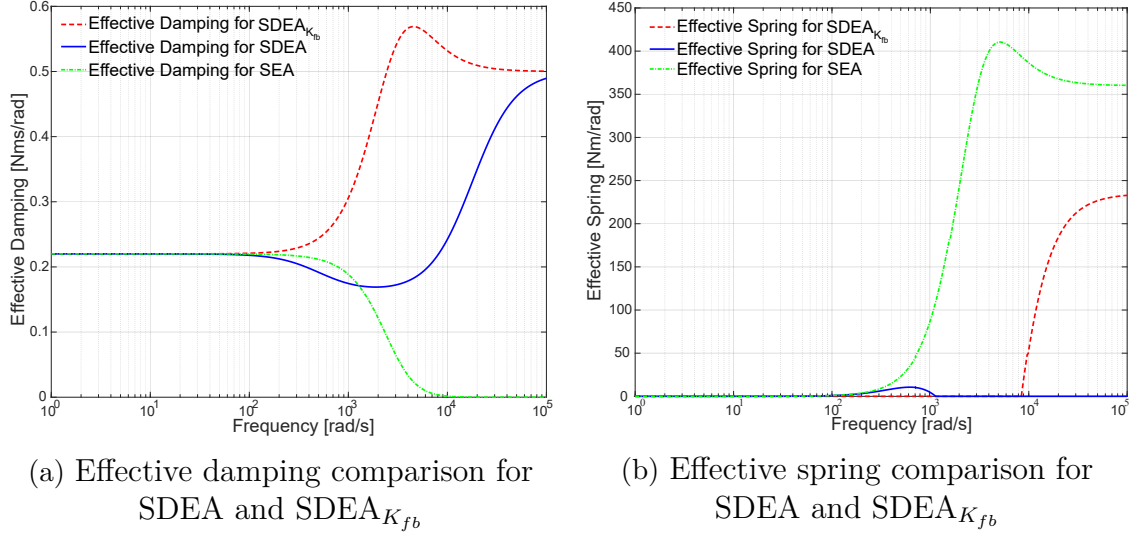


Figure 8.18 Effective impedance comparison for SDEA, SDEA $_{K_{fb}}$ , and SEA for null impedance rendering

Figure 8.18 shows that null impedance rendering performance comparison of SDEA, SDEA $_{K_{fb}}$ , and SEA in terms of effective impedance analysis. Figure 8.18a shows that effective damping of SDEA, SDEA $_{K_{fb}}$ , and SEA are nearly same in the low frequency range, but effective damping of SDEA and SEA get lower in the intermediate frequency range while SDEA $_{K_{fb}}$  increases. Furthermore, Figure 8.18b shows that SDEA's effective spring is 0 while SDEA $_{K_{fb}}$  is not 0 in the high frequency range. Effective spring for SDEA in the high frequency range converges to  $k_{1n}$  of Table 8.1h. Lastly, Figure 8.18b shows that SEA goes to physical stiffness in the high frequency range.

### 8.1.10 Maximum Renderable Virtual Stiffness Comparison for SDEA, SDEA $_{K_{fb}}$ , and SDEA $_{K_{red}}$

In this subsection, 3 systems are used to compare maximum renderable virtual stiffness SDEA, SDEA $_{K_{fb}}$ , and SDEA $_{K_{red}}$ .

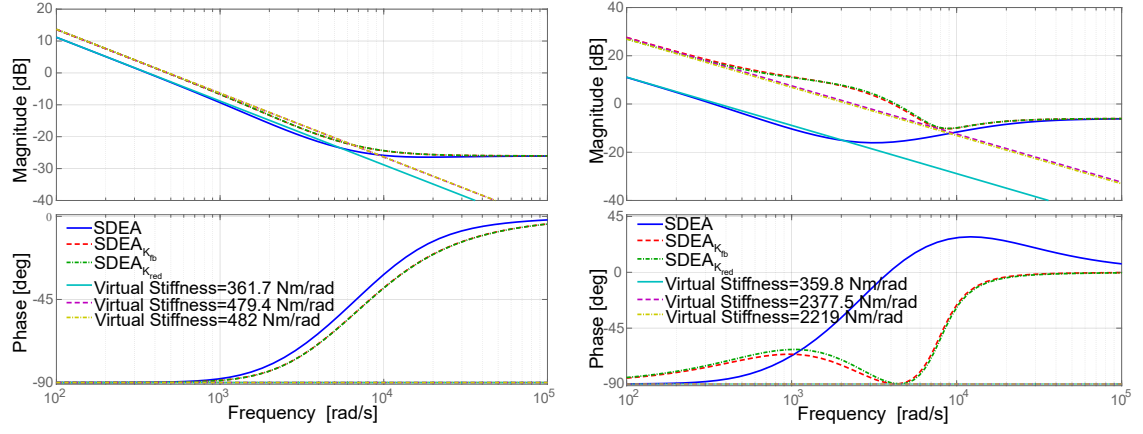
SDEA and SDEA $_{K_{fb}}$  go to  $(\alpha K_d)/(\alpha+1)$  in the low frequency range while SDEA $_{K_{red}}$

Table 8.6 Physical parameters of 3 different systems

Parameters	System-1	System-2	System-3
$J_m(kgm^2)$	$6.399e^{-4}$	0.002	$6.794e^{-4}$
$B_m(Nms/rad)$	0.169	1.22	0.0122
$K(Nm/rad)$	362	360	360
$B_f(Nms/rad)$	0.05	0.5	0.005

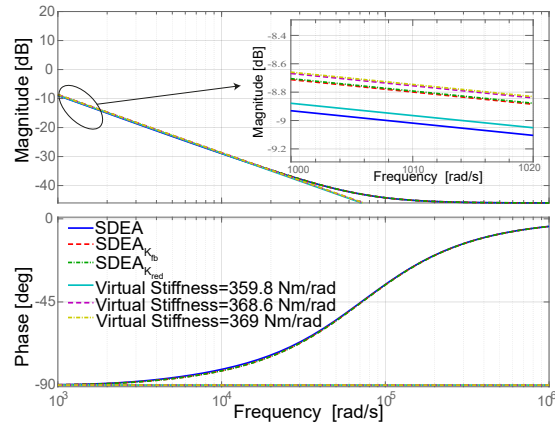
goes to  $K_d$ . In the literature SEA and SDEA cannot render virtual stiffness which is higher than physical stiffness [39, 45], but numerical evaluations show that  $SDEA_{K_{fb}}$  and  $SDEA_{K_{red}}$  can render virtual stiffness which is higher than physical stiffness.

Figure 8.19 presents maximum renderable virtual stiffness comparison for SDEA,  $SDEA_{K_{fb}}$ , and  $SDEA_{K_{red}}$  for 3 different systems when controller gains are same. These systems parameters are defined in Table 8.6. All Bode plots in Figure 8.19 show that  $SDEA_{K_{fb}}$ , and  $SDEA_{K_{red}}$  can render virtual stiffness which is higher than physical K, but SDEA cannot render virtual stiffness which is higher than K. However, as we mentioned before  $SDEA_{K_{fb}}$ , and  $SDEA_{K_{red}}$  spring rendering bandwidth can be lower because of higher  $B_f$  term as in Figure 8.19b. Figure 8.19a and 8.19c has the lower  $B_f$  term, so the low frequency range is almost same with SDEA while  $SDEA_{K_{fb}}$  and  $SDEA_{K_{red}}$  can render higher virtual stiffness.



(a) For system-1

(b) For system-2



(c) For system-3

Figure 8.19 Performance comparison of SDEA, SDEA<sub>K<sub>fb</sub></sub>, SDEA<sub>K<sub>red</sub></sub> for spring rendering for 3 different parameters set

# Chapter 9

## Experimental Evaluations

This chapter presents the experimental verification of theoretical results for passivity bounds and haptic rendering performance of S(D)EA.

### 9.1 Experimental Setup

In this section, we experimentally validate the theoretical passivity bounds and haptic rendering performance for S(D)EA using a customized version of the single degree of freedom series elastic brake pedal presented in [68, 69]. The series elastic brake pedal, presented in Figure 9.1, is actuated by a brushless DC motor equipped with a Hall-effect sensor and an optical encoder. The torque output of the motor is amplified with a gearbox and a capstan reduction featuring 1:10 and 1:3.95 transmission ratios, respectively. The series elastic element is implemented as an ideal spring through a compliant cross-flexure joint embedded into the capstan pulley. The deflections of the cross-flexure joint are measured through a linear encoder to estimate interaction torques. All controllers are implemented in real-time at 1 kHz utilizing an industrial PC connected to an EtherCAT bus.

To implement a series *damped* elastic brake pedal, linear eddy current damping is added in parallel to the compliant element of the SEA brake pedal. In particular, permanent magnets are arranged as a Halbach array to augment the magnetic field on the side of the array facing an aluminum plate. The distance between the magnet array and aluminum plate is adjusted to control the level of damping added to the system. When the magnets are removed, the SDEA brake pedal simplifies to the original SEA brake pedal.

The experimental setup is presented in Figure 9.1 which is consist of a high-torque brushless DC motor (1), gearbox (2) which increases torque capacity, the capstan

drive (3,4) which provides minimum reduction and provides more reduction, magnet holder (5), magnets (6) which arranged with considering Halbach array [70, 71], end-effector (7), an aluminum plate (8), the linear encoder (9), cross-flexure leaf spring (10), the rotational encoder (11) to measure end-effector position, and motor drive (12). If (5) is removed, the device becomes SEA which is the Figure 9.1c.

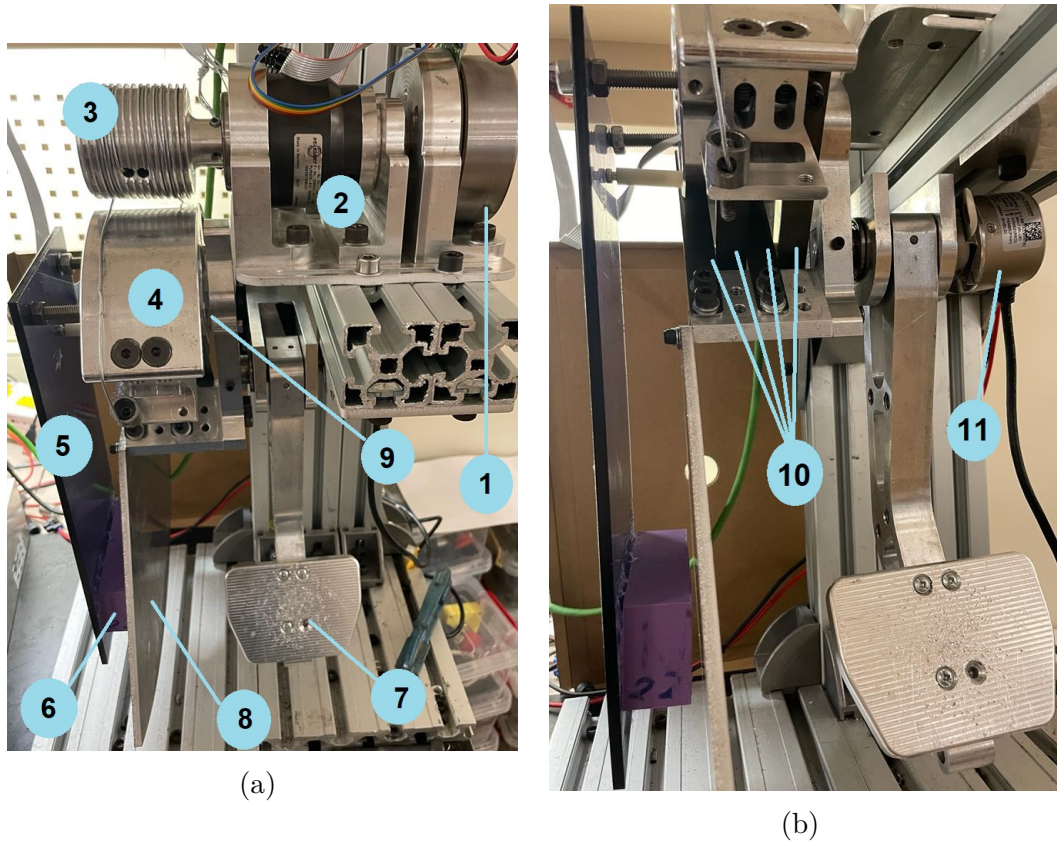


Figure 9.1 Components of experimental setup

## 9.2 System Identification

Accurate system identification is very important to find real passivity bound for the experimental setup. Passivity bounds of Chapter 4, 5, 6, 7, and 8 include physical system parameters. Therefore, there is a necessity to do convenient system identification to select proper controller gains to obtain passive system.

### Reflected Inertia and Damping of Actuator

Closed-loop system identification is utilized to experimentally determine the system parameters related to the actuator and the power transmission. The closed-loop identification enables accurate prediction of plant parameters using LTI techniques, since the robust motion controller effectively compensates for the hard-to-model nonlinear effects in the power transmission. To determine the reflected inertia and damping of the plant, the system identification is performed under the inner velocity control with  $G_m = 0.0576$  N-m s/rad. A chirp velocity reference signal with an amplitude of 7.85 rad/sec is applied to the motion control loop over the frequency range of 0.001-10 Hz, while no exogenous torque  $\tau_{sea}$  is applied to the system. A first-order transfer function is fitted to the collected data with  $R^2 = 0.88$  to determine the plant parameters as  $J_m = 0.0024$  kg-m<sup>2</sup> and  $B_m = 0.0177$  N-m s/rad. Eqn. (9.1) presents transfer function of Figure 9.2.

$$\frac{\omega_m}{\omega_d} = \frac{G_m}{J_m s + B_m + G_m} \quad (9.1)$$

We know the  $G_m$  in this model, and the rest of physical parameters can be found with the estimated transfer function.

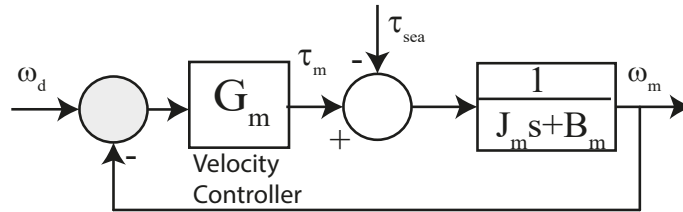


Figure 9.2 Closed loop motion controlled system

The system is excited with chirp signal between 0.009–10 Hz. The Matlab's System Identification Toolbox is used to find LTI model by using experimental data. The estimated transfer function is:

$$\frac{24}{s + 31.36} \quad (9.2)$$

Figure 9.3 presents Bode plot of the estimated transfer function.

Inertia and damping of the Table 9.1 can be achieved from Eqn. 9.2 which presents



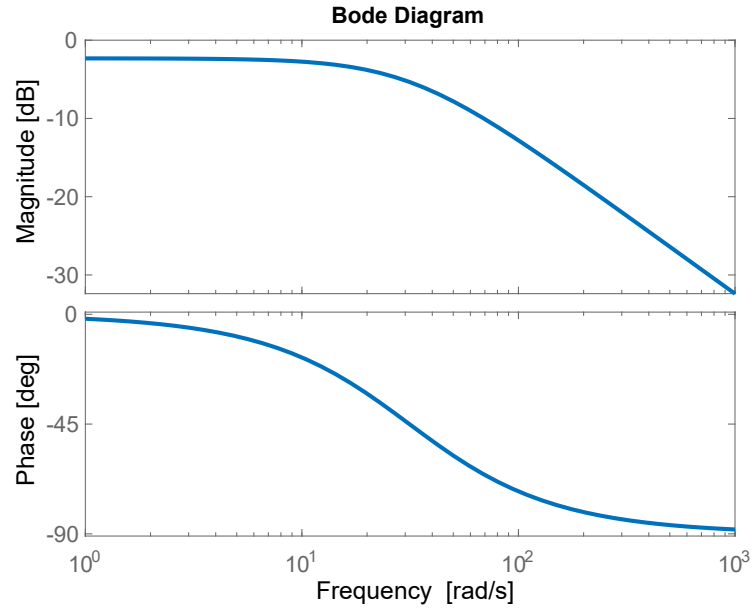


Figure 9.3 Bode plot of inner loop

the experimentally characterized parameters for the S(D)EA brake pedal system. The estimated transfer function has a fit of  $R^2$  is %87.5 with the data collected.  $R^2$  was measured in frequency domain.

## Stiffness and Damping of the Physical Filter

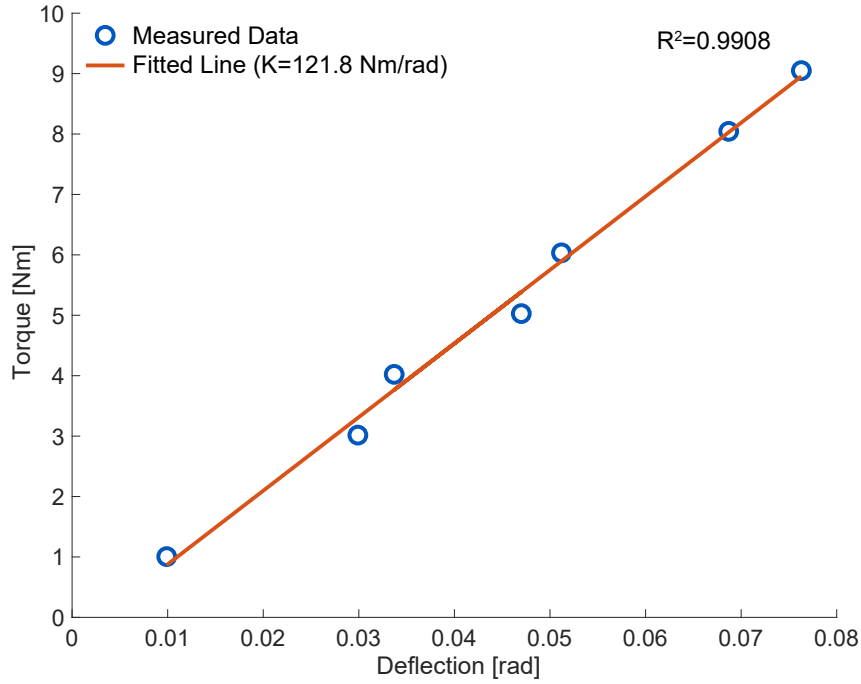


Figure 9.4 Identification of stiffness of physical filter

Identification of stiffness and damping of the physical filter are simpler than identification of reflected inertia and damping. The stiffness can be found from putting static load on the end-effector when the motor does not work. Stiffness of the elastic element can be found from the torque that occurred by the static load and deflection. Experimental result of the stiffness of the physical filter reported in Figure 9.4. The slope of the fitted line is 121.8. NRMSE of fitted line is 3.06% where RMSE is 0.24.

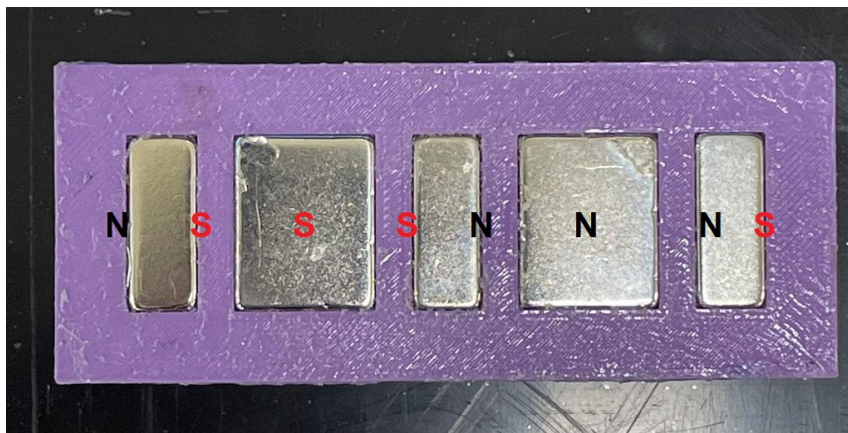
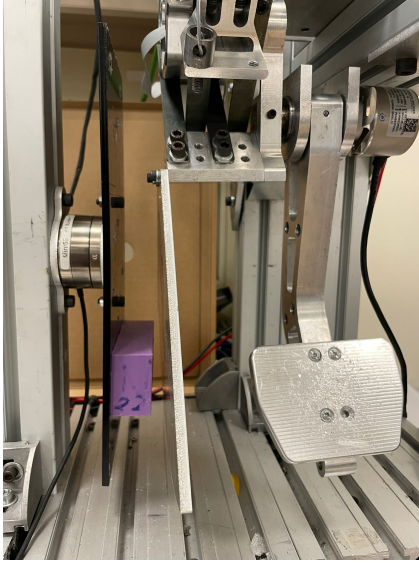


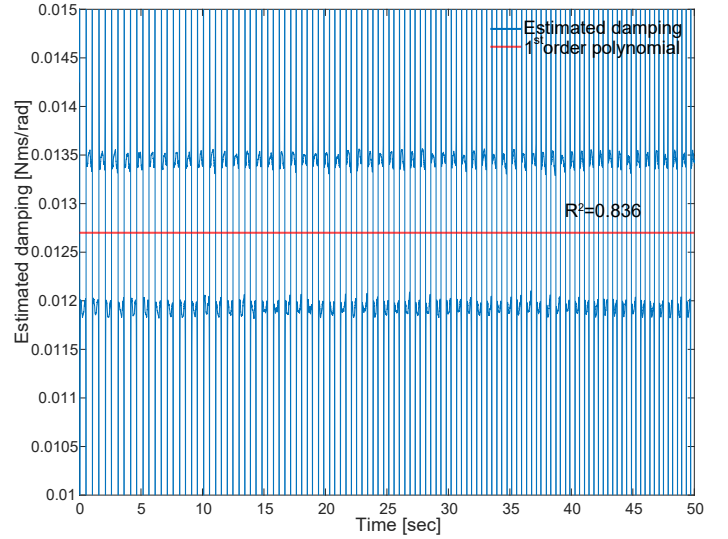
Figure 9.5 Details of arrangement of magnet

Figure 9.5 presents filter damping of SDEA. This magnets placed in logic of Halbach array. Thanks to arrangement of Halbach array as Figure 9.5, one side will be strong side and other one will be weak side. Therefore, the power of the damping can be increased with Halbach array. The damping depends on the distance between

magnets and aluminium plate. The distance in our experiment setup is 12 mm. Magnet plate is grounded with the distance of 12 mm to aluminium plate as Figure 9.6a. For the system identification of the damping coefficient, the magnet array is fixed to a force sensor and the motion of the aluminum plate is controlled to follow a reference chirp signal with an amplitude of 33.5 rad/sec over the frequency range of 0.9-1.4 Hz. The velocity is estimated through the numerical differentiation of the encoder data using the curve braking velocity estimator [72]. A least square fit to the experimental data indicates that  $B_f = 0.0127$  N-m s/rad with  $R^2 = 0.836$ .



(a) Experiment setup for damping identification



(b) Damping identification experiment result

Figure 9.6 Damping identification

Table 9.1 Experimentally characterized system parameters for the SEA brake pedal

Parameter	Value
$J_m$	0.0024 kgm <sup>2</sup>
$B_m$	0.0177 Nms/rad
$K$	121.8 Nm/rad
$B_f$	0.0127 Nms/rad

Table 9.1 presents system identification results of S(D)EA brake pedal.

### 9.2.1 Torque Controller Tuning

This section presents tuning process of force/torque controller for VSIC of S(D)EAs. As we know, we have already tuned velocity controller during system identification process. Experimental setup can catch desired torque accurately with better tuned force/torque controller. We fixed the end-effector and we gave the system desired

torque with chirp signal between 0.1–2 Hz. As a result  $G_m = 0.0576$  Nm/rad and  $G_t = 25$  rad/sNm. They are valid for the rest of the chapter unless otherwise stated. RMSE value is 0.48 and NRMSE value is 4.03% where the range of the output is used for normalization.

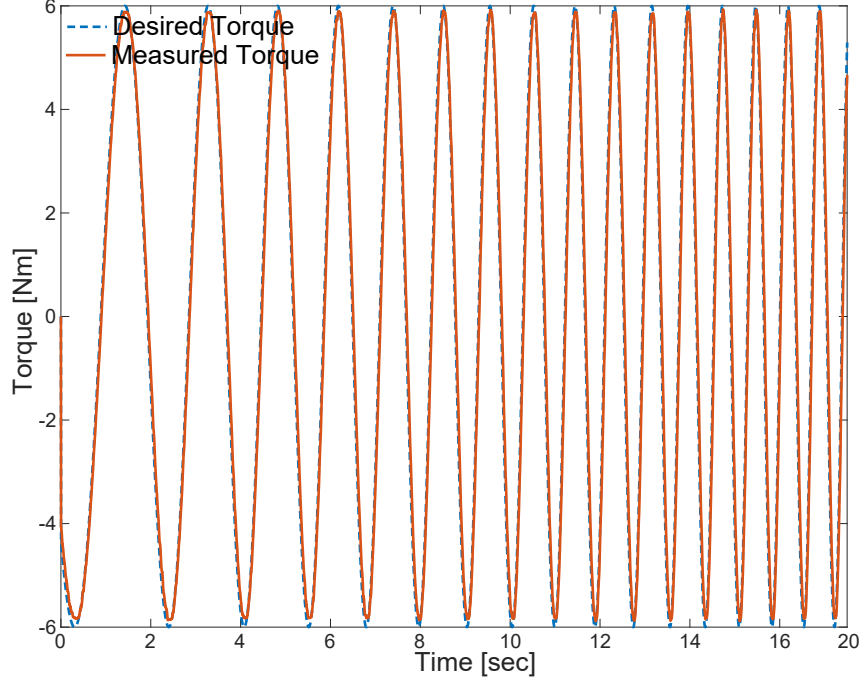


Figure 9.7 Measured torque vs desired torque

Figure 9.7 shows that experimental setup can catch desired torque well.

## 9.3 Series Elastic Actuation

In this section, theoretical verification experimentally is evaluated. Experiments of rendering performance and passivity bounds verification are conducted. Note that magnet holder (5) and magnets (6) are removed to transform device SEA as Figure 9.1c.

### 9.3.1 Impedance Rendering Performance

In this subsection, we evaluate haptic rendering performance analysis of VSIC for SEA during null impedance rendering and spring rendering.

#### 9.3.1.1 Null Impedance Rendering

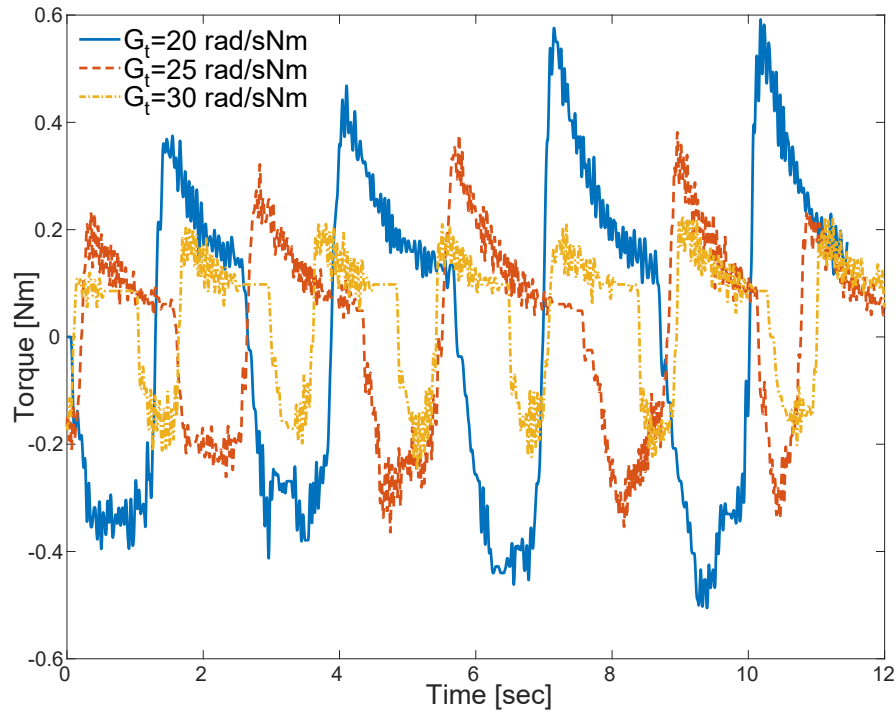


Figure 9.8 Chip test for 3 different  $G_t$

Performance of SEA under VSIC during null impedance rendering is important, as this control mode provides active backdrivability to the system.

Figure 9.8 presents null impedance rendering performance of SEA under VSIC for three distinct levels of the torque controller gain  $G_t$ . In Figure 9.8, as the torque controller gain  $G_t$  is increased from 20 rad/(s N-m) to 30 rad/(s N-m), the torque required to move the pedal decreases from 1.48% to 0.62% of 40 N-m torque output capacity of the SEA brake pedal. Note that this level of active-backdrivability is excellent for the SEA brake pedal, as evidenced by commonly employed chip test, where a potato chip is used to move the device without getting broken. The

experimental results in Figure 9.8 are also in good agreement with the analysis presented in Section 8, where the positive effect of increasing the torque controller gain  $G_t$  on the null impedance rendering performance has been shown.

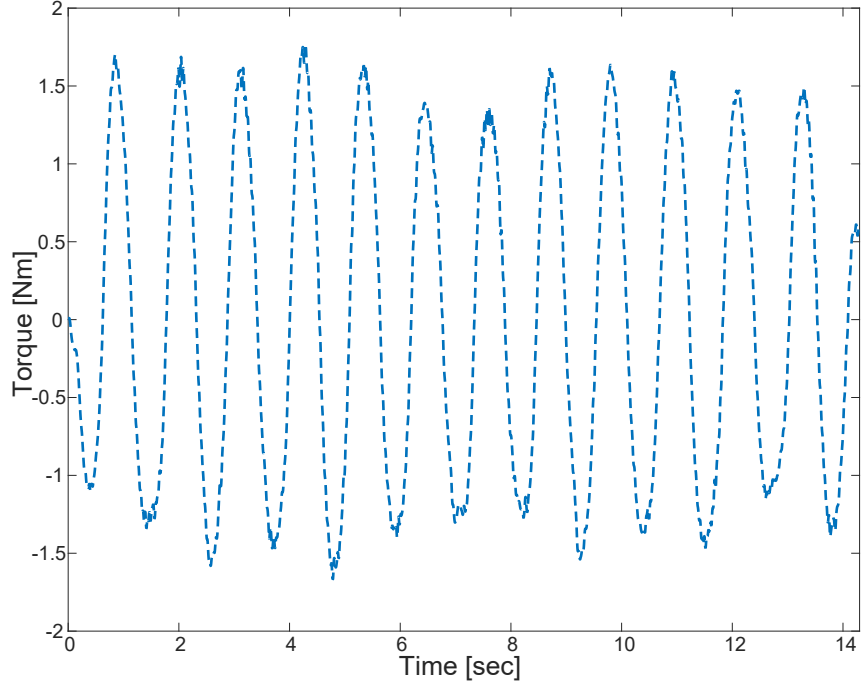


Figure 9.9 Null impedance rendering performance when interacting with human

Purpose of haptic rendering device is interacting with human. Figure 9.9 shows the performance of SEA when interacting with human.

### 9.3.1.2 Spring Rendering

Two virtual stiffness are studied where  $K_d$  selected as 50 Nm/rad and 100 Nm/rad. Static torques with known values are applied the end-effector and stiffness are calculated with knowledge of displacement. We studied these virtual stiffness for two different gains which are  $G_t = 25$  rad/sNm and  $G_t = 30$  rad/sNm. If  $G_t$  is selected as 25 rad/sNm, stiffness of virtual stiffness equal to 49.13 Nm/rad with  $K_d = 50$  Nm/rad and 98.27 Nm/rad with  $K_d = 100$  Nm/rad. If  $G_t$  is selected as 30 rad/sNm, stiffness of virtual stiffness equal to 49.27 Nm/rad with  $K_d = 50$  Nm/rad and 98.55 Nm/rad with  $K_d = 100$  Nm/rad.

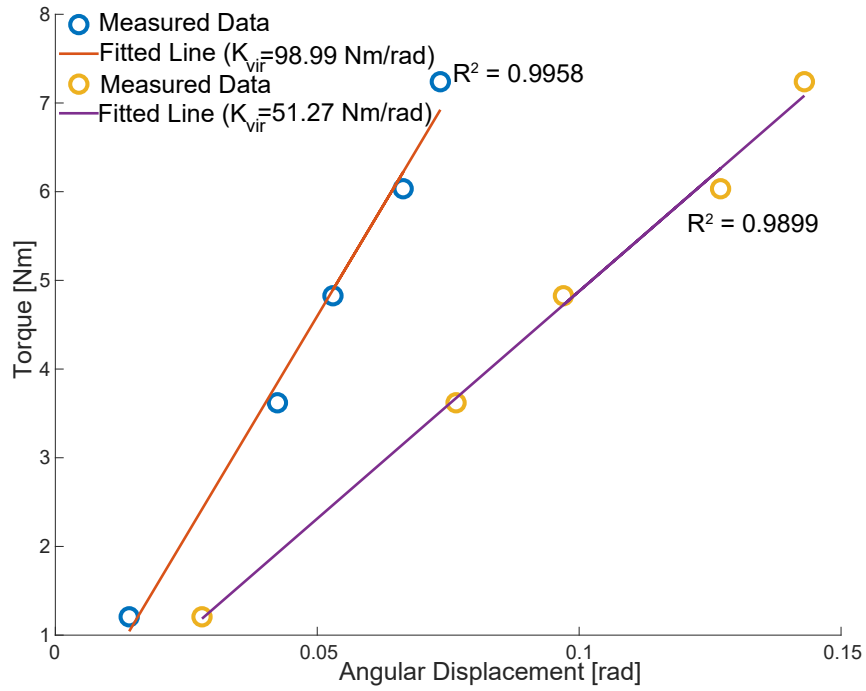


Figure 9.10 Rendering two virtual stiffness experimentally when  $G_t = 25$  rad/sNm

Figure 9.10 presents experimental verification of rendering two virtual stiffness when  $G_t = 25$  rad/sNm. When  $K_d$  is selected as 100 Nm/rad,  $K_{vir} = 98.99$  Nm/rad whose error is %0.73. When  $K_d$  is selected as 50 Nm/rad,  $K_{vir} = 51.27$  Nm/rad whose error is %4.35. Note that fitted line NRMSE of  $K_d = 100$  Nm/rad is 4.85% where RMSE is 0.28, and fitted line NRMSE of  $K_d = 50$  Nm/rad is 2.01% where RMSE is 0.11.

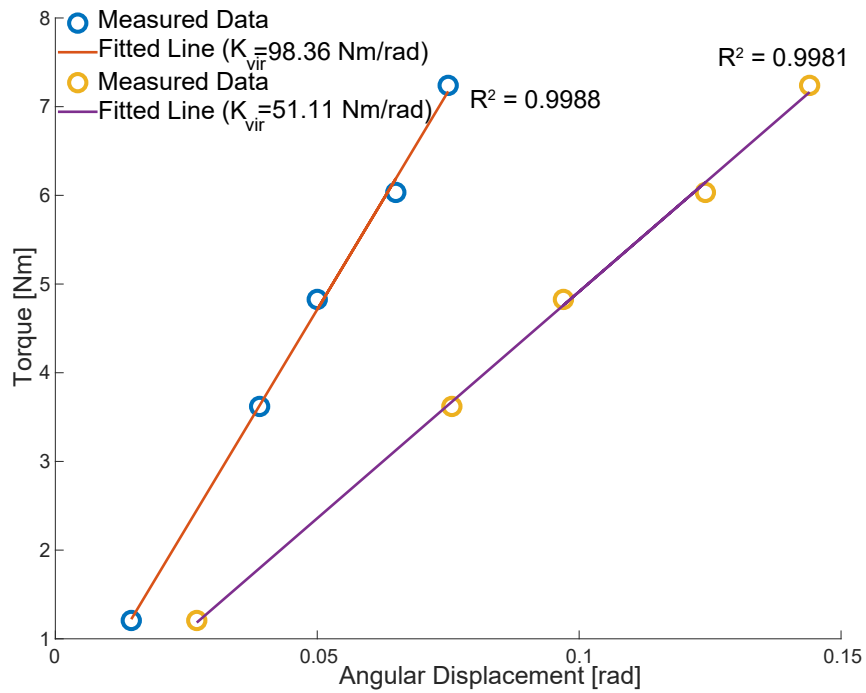


Figure 9.11 Rendering two virtual stiffness experimentally when  $G_t = 30$  rad/sNm

Figure 9.11 presents experimental verification of rendering two virtual stiffness when  $G_t = 30$  rad/sNm. When  $K_d$  is selected as 100 Nm/rad,  $K_{vir} = 98.36$  Nm/rad whose error is %0.19. When  $K_d$  is selected as 50 Nm/rad,  $K_{vir} = 51.11$  Nm/rad whose error is %3.73. Note that fitted line NRMSE of  $K_d = 100$  Nm/rad is 3.33% where RMSE is 0.19, and fitted line NRMSE of  $K_d = 50$  Nm/rad is 1.79% where RMSE is 0.10.

Figure 9.10 and 9.11 show that errors are lower for selection of  $G_t = 30$  rad/sNm for both selection of  $K_d$ . In previous chapters, we have shown that higher  $G_t$  gain increases the performance of spring rendering under VSIC through passive physical equivalents and numerical evaluation.

The SEA brake pedal is designed to interact with humans, so it is important the evaluating performance when the SEA brake pedal interacts with humans. In this experiment, a human interacted with the end-effector of the SEA brake pedal.

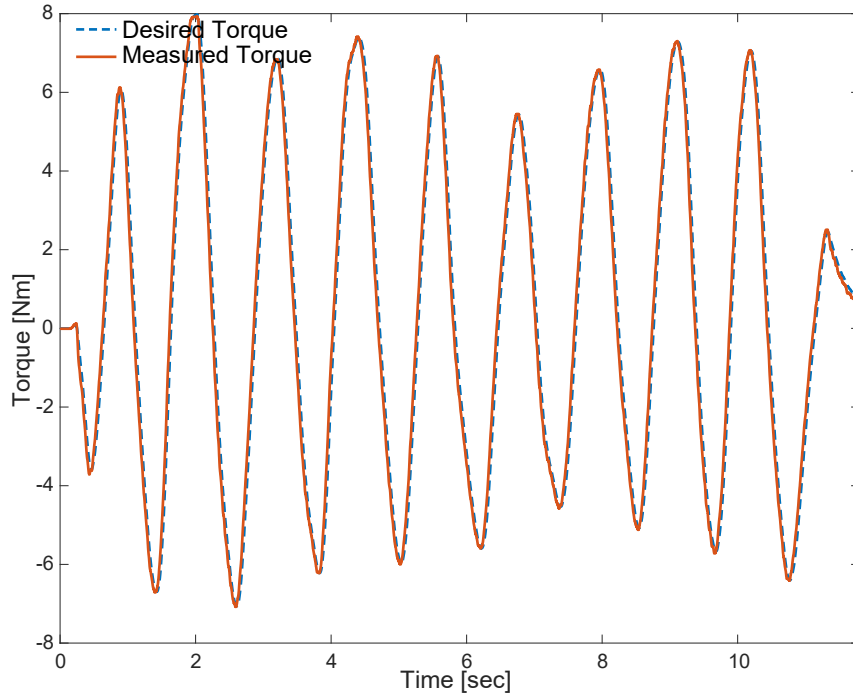


Figure 9.12 When human interacting with the SEA brake pedal when  $K_d = 50$  Nm/rad

Figure 9.12 presents desired torque and measured torque when  $K_d$  is selected as 50 Nm/rad. The human can interact the device safely while the device displays the desired virtual environment. The impedance controller computes the desired torque reference. Figure 9.12 shows that controller and device has good spring rendering performance because measured torque can catch the reference torque. NRMSE of Figure 9.12 is 3.28% where RMSE is 0.49.



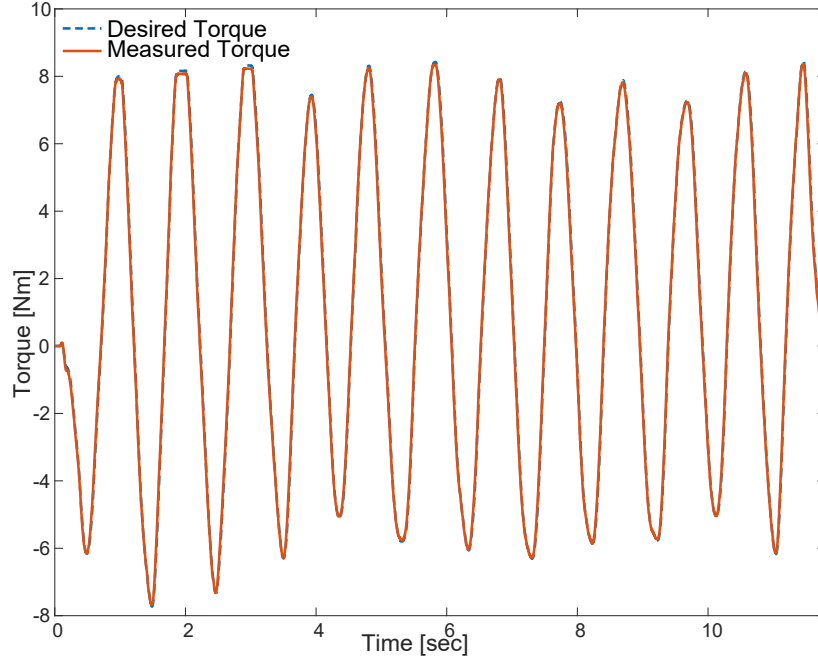


Figure 9.13 When human interacting with the SEA brake pedal when  $K_d = 100$  Nm/rad

Figure 9.13 presents desired torque and measured torque when  $K_d$  is selected as 100 Nm/rad. The human can interact the device safely while device display the desired virtual environment. The impedance controller computes the desired torque reference. Figure 9.13 shows that controller and device has good spring rendering performance because measured torque can catch the reference torque. NRMSE of Figure 9.13 is 0.94% where RMSE is 0.15.

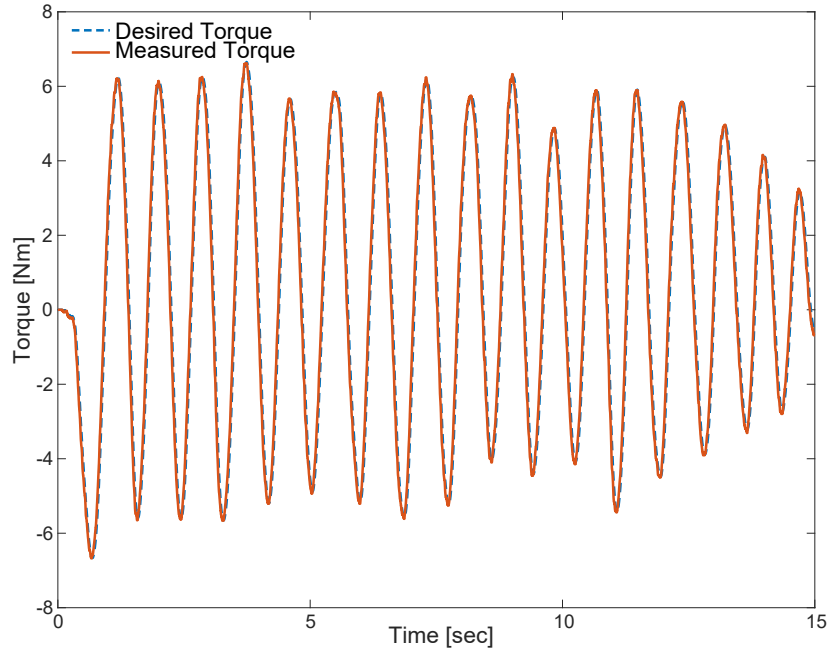


Figure 9.14 When human interacting with the SEA brake pedal when  $K_d = 50$  Nm/rad with  $G_t = 30$  rad/sNm

Figure 9.14 presents desired torque and measured torque when  $K_d$  is selected as 50

Nm/rad with  $G_t = 30$  rad/sNm. The human can interact the device safely while device display the desired virtual environment. The impedance controller computes the desired torque reference. Figure 9.14 shows that controller and device has good spring rendering performance because measured torque can catch the reference torque. NRMSE of Figure 9.14 is 3.03% where RMSE is 0.40 which is lower than selection of  $G_t = 25$  rad/sNm. Therefore, selection of higher  $G_t$  provides better tracking performance for measured torque. Also, Figure 9.12 and Figure 9.13 show that higher  $K_d$  provide better performance.

### 9.3.2 Verification of Passivity Bounds

Bode plots cannot be feasible for experimental verification because it can be challenging to obtain the system phase. There are alternative ways for passivity. When an arbitrary passive environment is coupled with a system, a passive system should hold the coupled stability. In this chapter, the system is coupled to a range of the most destabilizing environments and induces fast movements and impacts to the end-effector of the SEA brake pedal. Chatter was observed when coupled stability is violated. For simplicity, the theoretical passivity bounds in the previous sections have been derived under the non-limiting assumption that the power transmission of the system has a unity reduction ratio. Equivalent plant parameters and controller gains can be established for systems with a reduction ratio of  $n$  by introducing the following mappings:  $J_{meq} = n^2 J_m$ ,  $B_{meq} = n^2 B_m$ , and  $G_{meq} = n^2 G_m$ , and  $G_{teq} = 1/n G_t$ .

#### 9.3.2.1 Null Impedance Rendering

In this subsection, we have studied the coupled stability of SEA under VSIC during null impedance rendering when the controllers are P-PI. We have selected one passive and one active  $G_t$  gains for five distinct  $I_m$  gains according to the necessary and sufficient condition given in Eqn. (4.8).

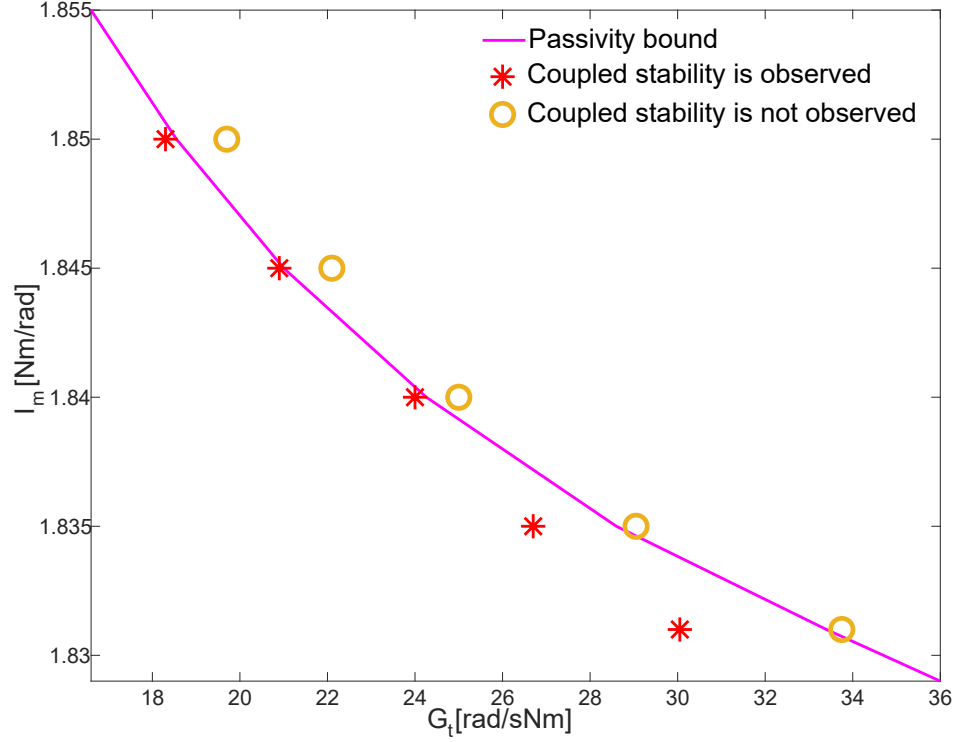


Figure 9.15  $G_t$ - $I_m$  plot for experimentally coupled stability for null impedance rendering

Figure 9.15 presents the experimental  $G_t$ - $I_m$  plot for the SEA brake pedal, together with the theoretically predicted passivity boundary depicted as the magenta line. The symbols “\*” indicate experiments where coupled stability was preserved, while symbols “o” denote experiments where coupled stability was compromised. As can be inspected from Figure 9.15, the test cases are fairly close to the analytically predicted passivity boundary and these results serve as a validation of the theoretical passivity bound. These results also indicate that the modelling assumptions considered during the derivations are reasonable and do not cause large deviations from the theoretical predictions.

### 9.3.2.2 Spring Rendering Rendering

In this subsection, we have studied the coupled stability of SEA under VSIC during spring rendering when both controllers are P. We have selected one passive and one active  $K_d$  values for four distinct  $G_t$  gains according to the necessary and sufficient condition given in Eqn. (4.2).

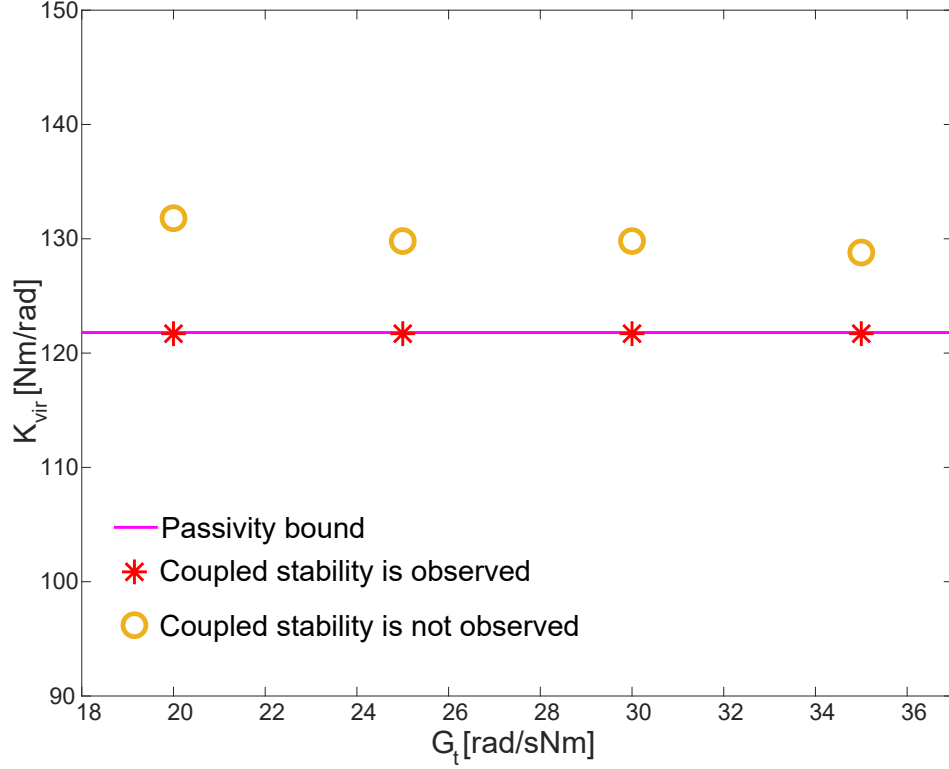


Figure 9.16  $G_t$ – $K_{vir}$  plot for experimentally coupled stability for spring rendering

Figure 9.16 presents the experimental  $K_{vir}$ – $G_t$  plot for the SEA brake pedal, where  $K_{vir} = \frac{\alpha}{\alpha+1} K_d$  denotes the stiffness of rendered spring. In the figure, the theoretical passivity boundary is depicted as the magenta line and is equal to physical stiffness of the SEA according to Eqn. (4.2). The experimental results validate the analytically predicted passivity boundary. According to the experimental results, the theoretical bound is about 7% more conservative, as the physical system is likely to have some extra dissipation effects due to unmodelled friction and hysteresis.

## 9.4 Series Damped Elastic Actuation

In this section we studied SDEA performance evaluation and passivity bounds experimentally. Torque controller tuning and all gains are same with SEA.

### 9.4.1 Impedance Rendering Performance

In this subsection, we evaluate haptic rendering performance analysis of VSIC for SDEA during null impedance rendering and spring rendering.

#### 9.4.1.1 Null Impedance Rendering

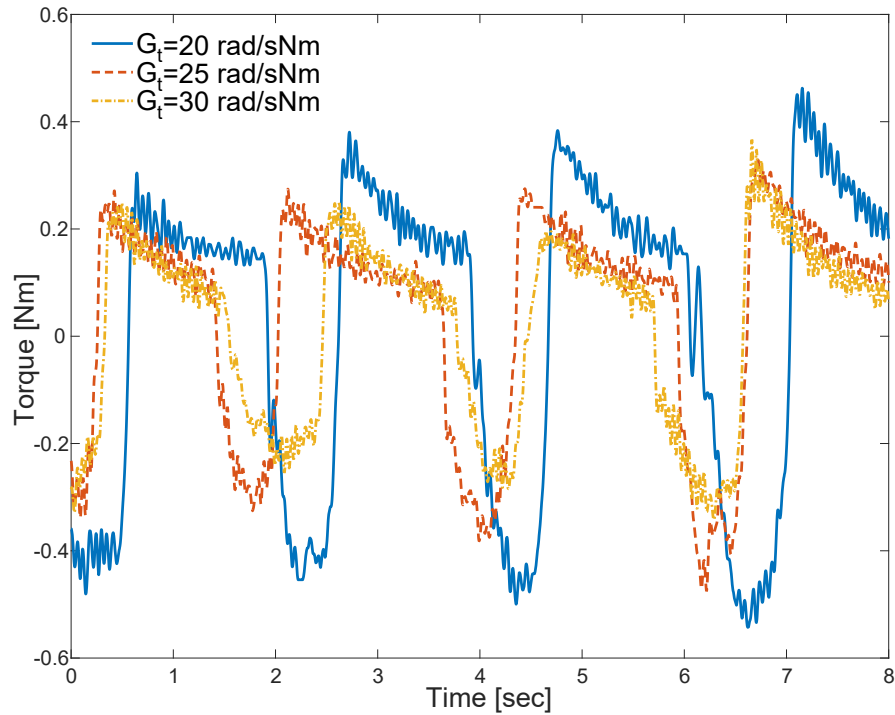


Figure 9.17 Chip test for 3 different  $G_t$  for SDEA

Performance of SDEA under VSIC during null impedance rendering is important, as this control mode provides active backdrivability to the system.

Figure 9.17 presents null impedance rendering performance of SDEA under VSIC for three distinct levels of the torque controller gain  $G_t$ . In Figure 9.17, as the torque controller gain  $G_t$  is increased from 20 rad/(s N-m) to 30 rad/(s N-m), the torque required to move the pedal decreases from 1.36% to 0.92% of 40 N-m torque output capacity of the SDEA brake pedal. Note that this level of active-backdrivability is excellent for the SDEA brake pedal, as evidenced by commonly employed chip test, where a potato chip is used to move the device without getting broken. The experimental results in Figure 9.17 are also in good agreement with the analysis

presented in Section 8, where the positive effect of increasing the torque controller gain  $G_t$  on the null impedance rendering performance has been shown.

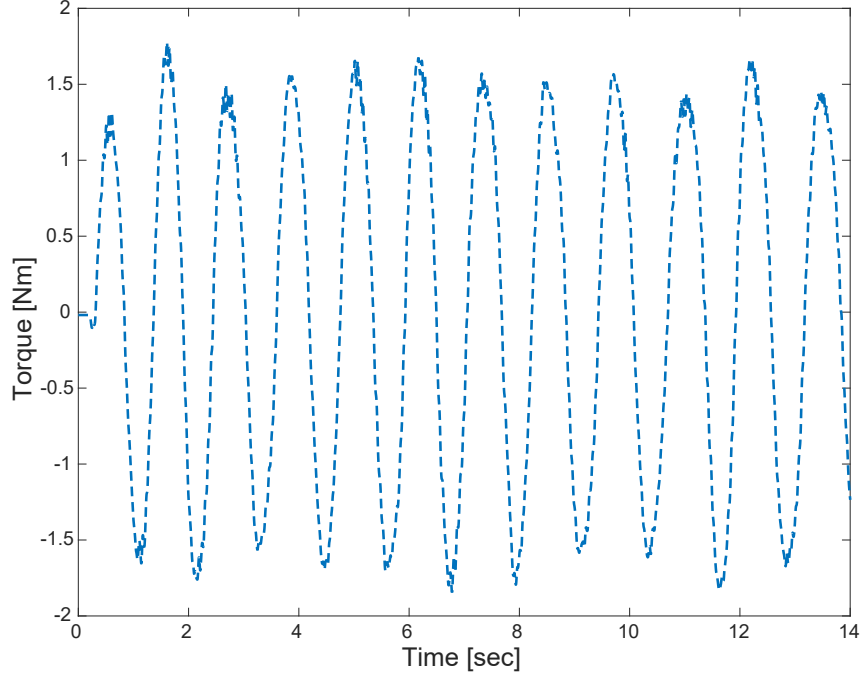


Figure 9.18 Null impedance rendering performance when interacting with human for SDEA

Purpose of haptic rendering device is interacting with human. Figure 9.18 shows the performance of SDEA when interacting with human.

#### 9.4.1.2 Spring Rendering

Two virtual stiffness are studied where  $K_d$  selected as 50 Nm/rad and 100 Nm/rad. Static torques with known values are applied the end-effector and stiffness are calculated with knowledge of displacement. We studied these virtual stiffness for two different gains which are  $G_t = 25$  rad/sNm and  $G_t = 30$  rad/sNm. If  $G_t$  is selected as 25 rad/sNm, stiffness of virtual stiffness equal to 49.13 Nm/rad with  $K_d = 50$  Nm/rad and 98.27 Nm/rad with  $K_d = 100$  Nm/rad. If  $G_t$  is selected as 30 rad/sNm, stiffness of virtual stiffness equal to 49.27 Nm/rad with  $K_d = 50$  Nm/rad and 98.55 Nm/rad with  $K_d = 100$  Nm/rad.

Figure 9.19 presents experimental verification of rendering two virtual stiffness when  $G_t = 25$  rad/sNm. When  $K_d$  is selected as 100 Nm/rad,  $K_{vir} = 97.01$  Nm/rad whose error is %1.28. When  $K_d$  is selected as 50 Nm/rad,  $K_{vir} = 50.96$  Nm/rad whose error is %3.72. Note that fitted line NRMSE of  $K_d = 100$  Nm/rad is 1.4% where RMSE is 0.08, and fitted line NRMSE of  $K_d = 50$  Nm/rad is 2.36% where RMSE is 0.13.

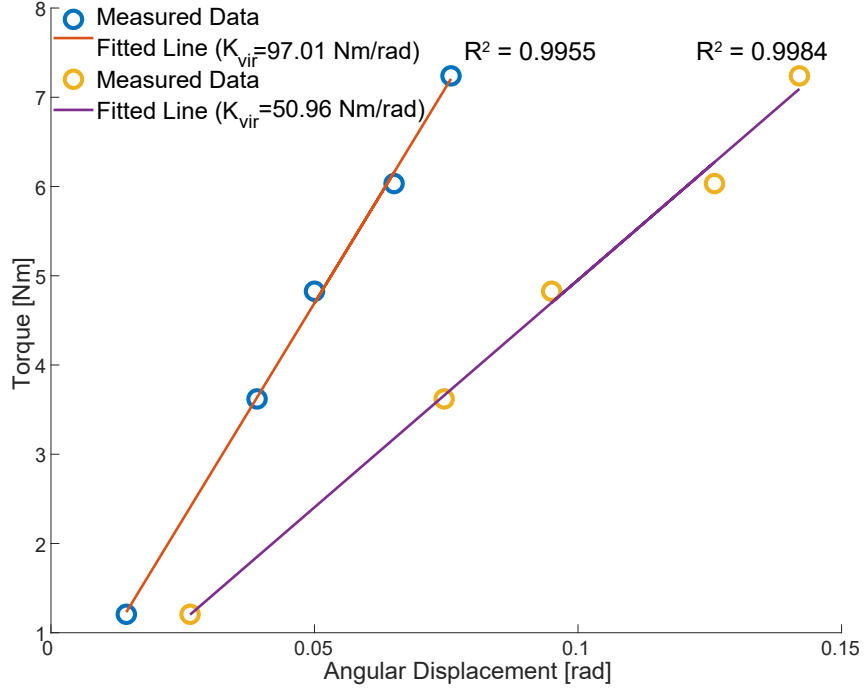


Figure 9.19 Rendering two virtual stiffness experimentally when  $G_t = 25$  rad/sNm for SDEA

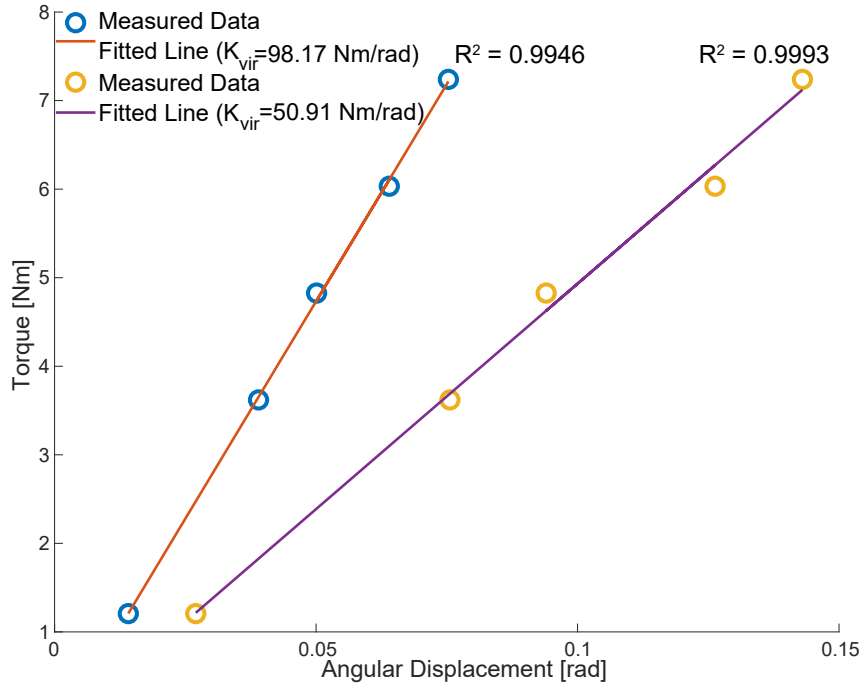


Figure 9.20 Rendering two virtual stiffness experimentally when  $G_t = 30$  rad/sNm

Figure 9.20 presents experimental verification of rendering two virtual stiffness when  $G_t = 30$  rad/sNm. When  $K_d$  is selected as 100 Nm/rad,  $K_{vir} = 98.17$  Nm/rad whose error is %0.39. When  $K_d$  is selected as 50 Nm/rad,  $K_{vir} = 50.91$  Nm/rad whose error is %3.33. Note that fitted line NRMSE of  $K_d = 100$  Nm/rad is 0.88% where RMSE is 0.05, and fitted line NRMSE of  $K_d = 50$  Nm/rad is 2.57% where RMSE

is 0.15.

Figure 9.19 and 9.20 show that errors are lower for selection of  $G_t = 30$  rad/sNm for both selection of  $K_d$ . In previous chapters, we have shown that selection of higher  $G_t$  and  $K_d$  increases the performance of spring rendering under VSIC through passive physical equivalents and numerical evaluation.

The SDEA brake pedal is designed to interact with humans, so it is important the evaluating performance when the SDEA brake pedal interacts with humans. In this experiment, a human interacted with the end-effector of the SDEA brake pedal.

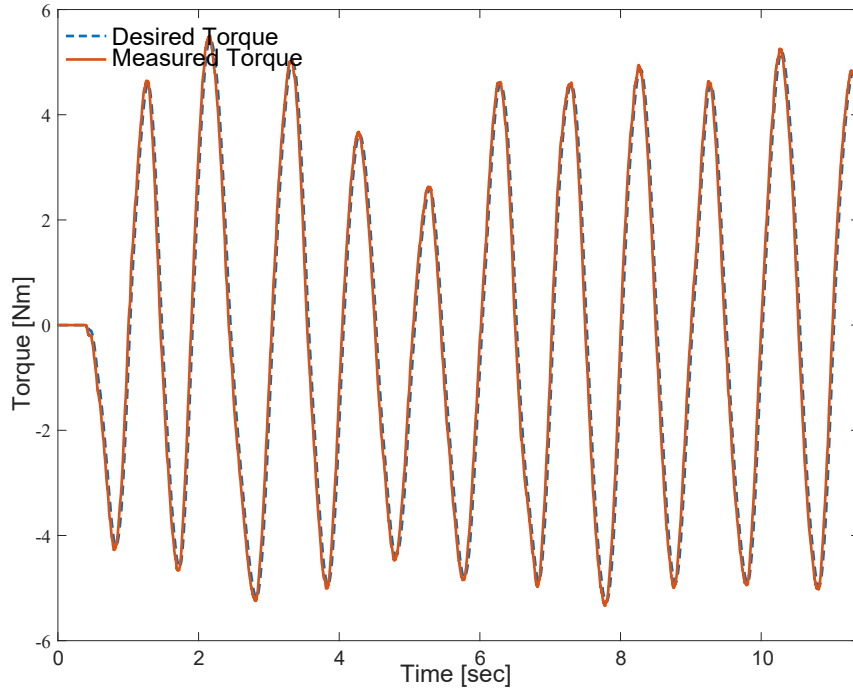


Figure 9.21 When human interacting with the SDEA brake pedal when  $K_d = 50$  Nm/rad

Figure 9.21 presents desired torque and measured torque when  $K_d$  is selected as 50 Nm/rad. The human can interact the device safely while the device displays the desired virtual environment. The impedance controller computes the desired torque reference. Figure 9.21 shows that controller and device has good spring rendering performance because measured torque can catch the reference torque. NRMSE of Figure 9.21 is 3.97% where RMSE is 0.43.

Figure 9.22 presents desired torque and measured torque when  $K_d$  is selected as 100 Nm/rad. The human can interact the device safely while device display the desired virtual environment. The impedance controller computes the desired torque reference. Figure 9.22 shows that controller and device has good spring rendering performance because measured torque can catch the reference torque. NRMSE of Figure 9.22 is 0.84% where RMSE is 0.10.



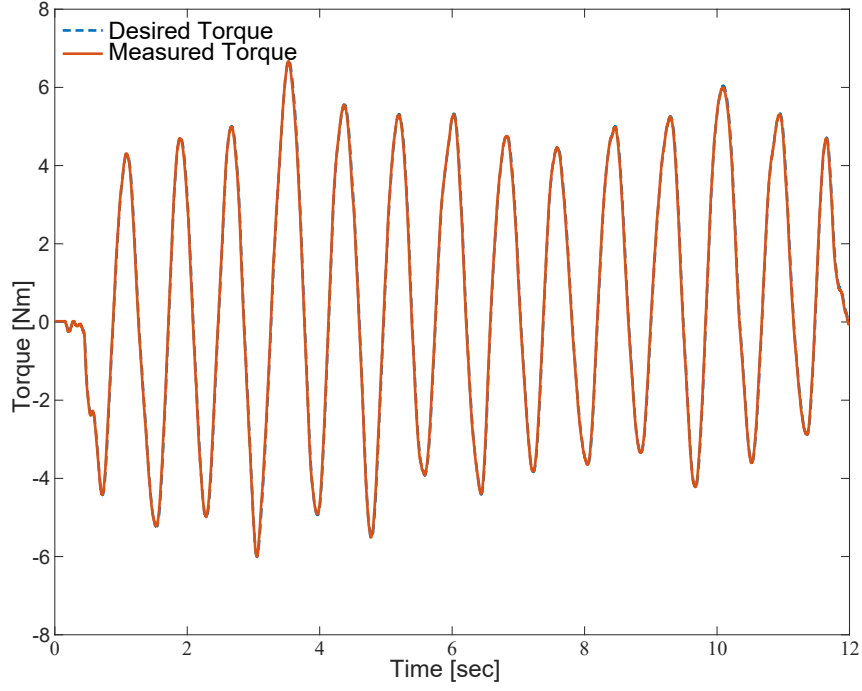


Figure 9.22 When human interacting with the SDEA brake pedal when  $K_d = 100$  Nm/rad

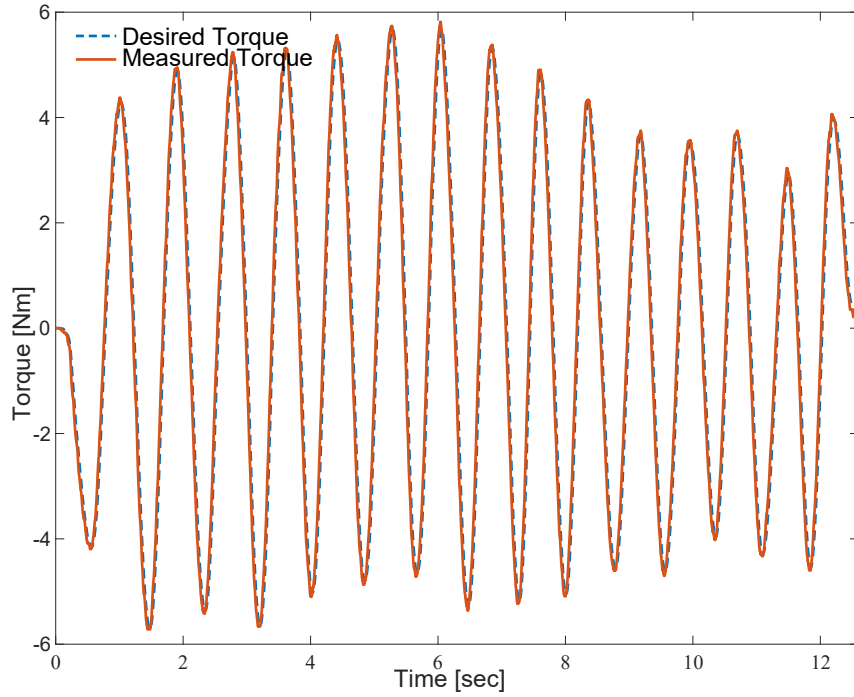


Figure 9.23 When human interacting with the SDEA brake pedal when  $K_d = 50$  Nm/rad with  $G_t = 30$  rad/sNm for SDEA

Figure 9.23 presents desired torque and measured torque when  $K_d$  is selected as 50 Nm/rad with  $G_t = 30$  rad/sNm. The human can interact the device safely while device display the desired virtual environment. The impedance controller computes the desired torque reference. Figure 9.23 shows that controller and device has good spring rendering performance because measured torque can catch the reference

torque. NRMSE of Figure 9.23 is 3.67% where RMSE is 0.42 which is lower than selection of  $G_t = 25$  rad/sNm. Therefore, selection of higher  $G_t$  provides better tracking performance for measured torque. Also, Figure 9.21 and Figure 9.22 show that higher  $K_d$  provide better performance.

#### 9.4.1.3 Voigt Model Rendering

The SDEA brake pedal is designed to interact with humans, so it is important the evaluating performance when the SDEA brake pedal interacts with humans. In this experiment, a human interacted with the end-effector of the SDEA brake pedal.

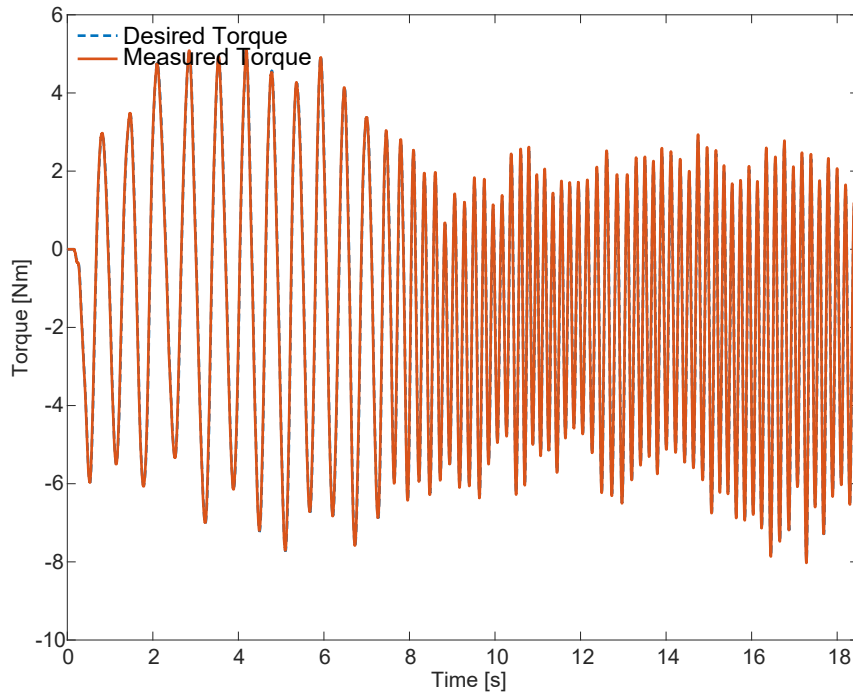


Figure 9.24 When human interacting with the SDEA brake pedal when  $K_d = 100$  Nm/rad and  $B_d = 0.01$  Nms/rad

Figure 9.24 presents desired torque and measured torque when  $K_d$  is selected as 100 Nm/rad and  $B_d$  is selected as 0.01 Nms/rad. The human can interact the device safely while the device displays the desired virtual environment. The impedance controller computes the desired torque reference. Figure 9.24 shows that controller and device has good spring rendering performance because measured torque can catch the reference torque. NRMSE of Figure 9.24 is 1.3% where RMSE is 0.16.

Figure 9.25 presents desired torque and measured torque when  $K_d$  is selected as 100 Nm/rad and  $B_d$  is selected as 0.01 Nms/rad while  $G_t = 30$  rad/sNm. The human can interact the device safely while device display the desired virtual environment. The impedance controller computes the desired torque reference. Figure 9.25 shows that controller and device has good spring rendering performance because measured

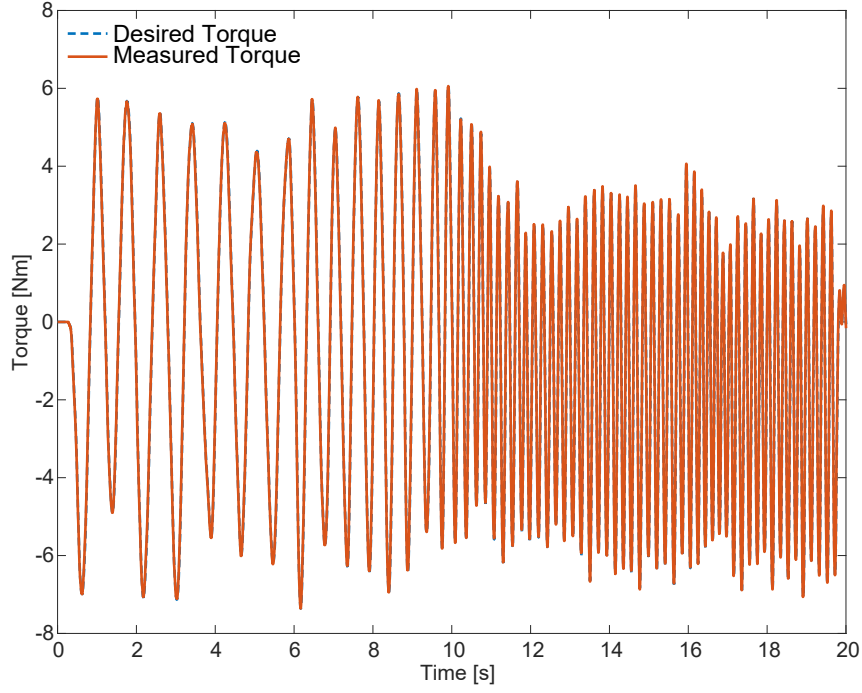


Figure 9.25 When human interacting with the SDEA brake pedal when  $K_d = 100$  Nm/rad and  $B_d = 0.01$  Nms/rad with  $G_t = 30$  rad/sNm

torque can catch the reference torque. NRMSE of Figure 9.25 is 1% where RMSE is 0.13.

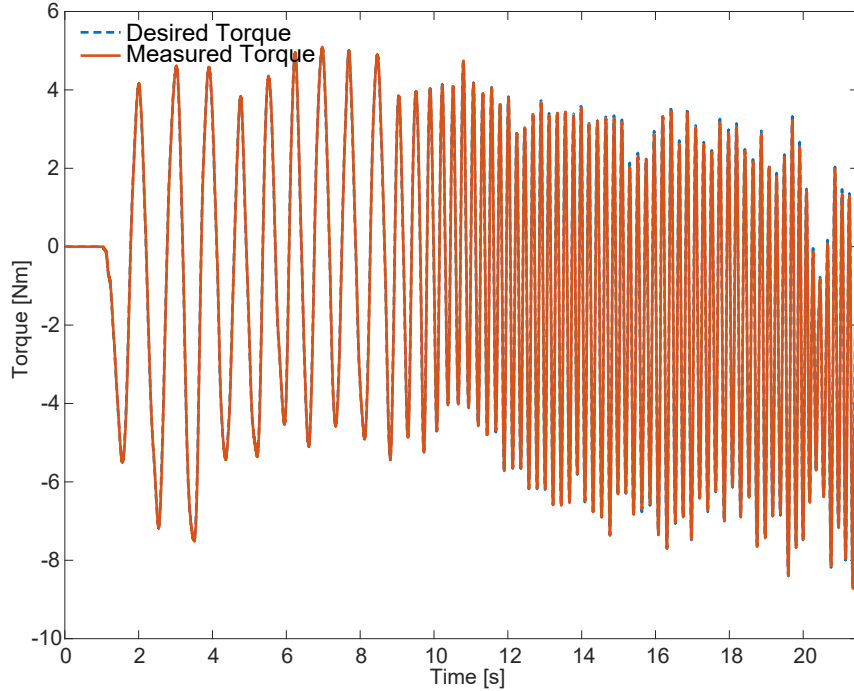


Figure 9.26 When human interacting with the SDEA brake pedal when  $K_d = 100$  Nm/rad and  $B_d = 0.05$  Nms/rad with  $G_t = 30$  rad/sNm

Figure 9.26 presents desired torque and measured torque when  $K_d$  is selected as 100 Nm/rad and  $B_d$  is selected as 0.05 Nms/rad while  $G_t = 30$  rad/sNm. The human

can interact the device safely while device display the desired virtual environment. The impedance controller computes the desired torque reference. Figure 9.26 shows that controller and device has good spring rendering performance because measured torque can catch the reference torque. NRMSE of Figure 9.26 is 0.96% where RMSE is 0.12 which is lower than selection of  $G_t = 25$  rad/sNm. Therefore, selection of higher  $G_t$  provides better tracking performance for measured torque. Also, Figure 9.25 and Figure 9.26 show that higher  $B_d$  provides better performance.

## 9.4.2 Verification of Passivity Bounds

In this subsection, we verified theoretical passivity bounds of Voigt model rendering and spring rendering experimentally for SDEA.

### 9.4.2.1 Voigt Model Rendering

In this subsection, we studied passivity bounds of Voigt model rendering for SDEA when controller are P-P. We selected 1 passive and 1 non-passive  $K_{vir}$  for different  $B_d$  gains. Necessary condition-1 is calculated from Eqn. (5.5) and necessary condition-2 is calculated from Eqn. (5.6). These 2 necessary conditions are equal to necessary and sufficient condition. Virtual stiffness  $K_{vir}$  is equal to  $K_d \frac{\alpha}{\alpha+1}$ . Note that during this experiment,  $G_t = 30$  rad/sNm.

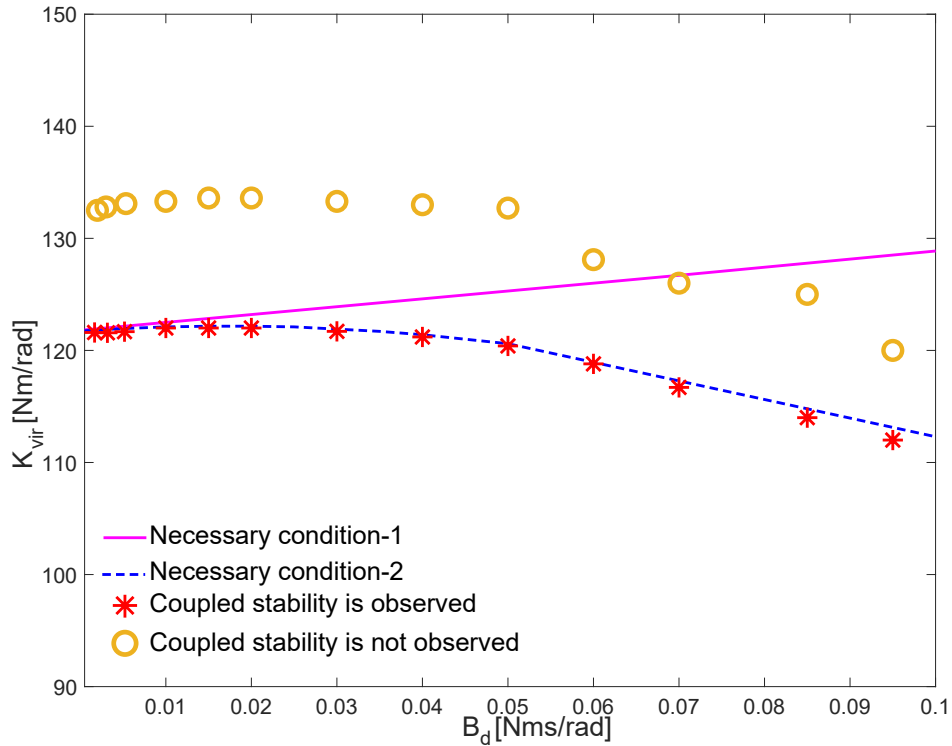


Figure 9.27  $B_d$ – $K_{vir}$  plot for experimentally coupled stability for spring rendering for SDEA

Figure 9.27 presents experimental results of  $K_{vir}$  vs  $B_d$  of the SDEA brake pedal. The passivity bounds of  $K_{vir}$  according to Eqn. (5.5) depicted as a magenta line which is the necessary condition-1 and Eqn. (5.6) depicted as a blue line which is the necessary condition-2 for Voigt model rendering for SDEA when controllers are P-P. Figure 9.27 shows that under the condition lines points hold coupled stability, but  $K_{vir}$  is over the condition lines, the chatter was observed at end-effector, so the coupled stability is violated. Figure 9.27 presents there is a difference between the condition lines and the points where coupled stability is violated. It can be caused by the omitted damping on the end-effector.

#### 9.4.2.2 Spring Rendering

In this subsection, we have studied the coupled stability of SDEA under VSIC during spring rendering when both controllers are P. We have selected one passive and one active  $K_d$  values for four distinct  $G_t$  gains according to the necessary and sufficient conditions given in Eqns. (5.22) and (5.23).

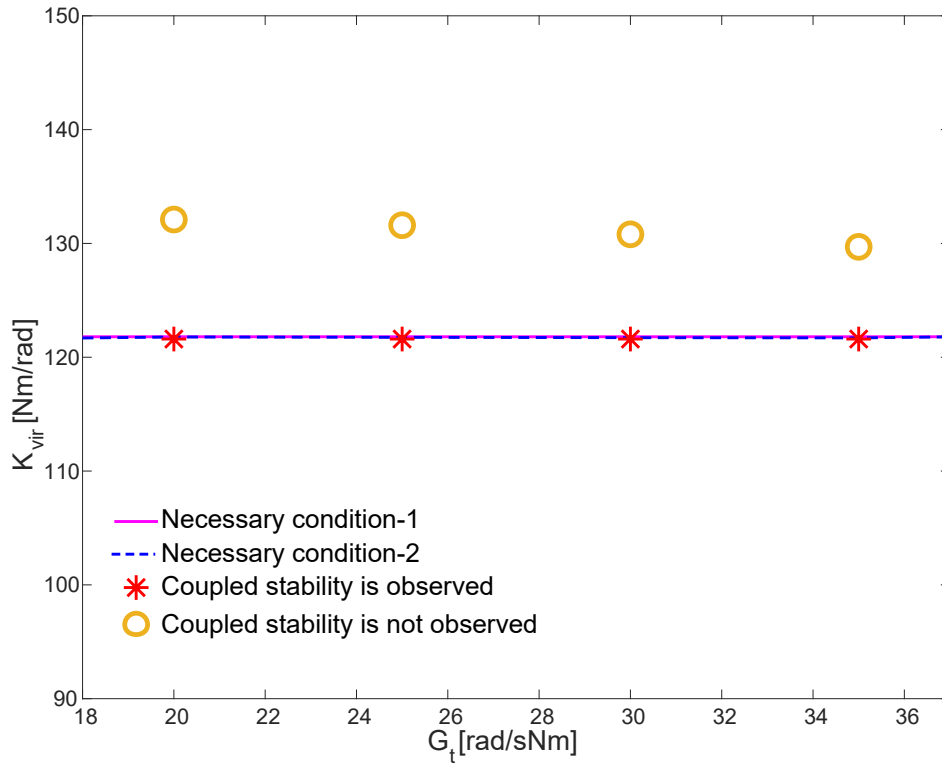


Figure 9.28  $G_t$ – $K_{vir}$  plot for experimentally coupled stability for spring rendering for SDEA

Figure 9.28 presents the experimental  $K_{vir}$ – $G_t$  plot for the SDEA brake pedal. In the figure, the theoretical passivity bound according to Eqn. (5.22) is depicted as the magenta line and is equal to physical stiffness of the SDEA, while the bound according to Eqn. (5.23) is depicted as the blue line. Figure 9.28 shows that the

two conditions are very close to each other for the parameters of the SDEA brake pedal. The experimental results validate the analytically predicted passivity boundary. According to the experimental results, the theoretical bounds are about 6.5% more conservative, as the physical system is likely to have some extra dissipation effects due to unmodelled friction and hysteresis.

## 9.5 Series Elastic Actuation with Omitted Damping Effect

In this section we studied  $SDEA_{Kfb}$  performance evaluation and passivity bounds experimentally. Torque controller tuning and all gains are same with SEA and SDEA.

### 9.5.1 Impedance Rendering Performance

In this subsection, we evaluate haptic rendering performance analysis of VSIC for  $SDEA_{Kfb}$  during null impedance rendering and spring rendering.

#### 9.5.1.1 Null Impedance Rendering

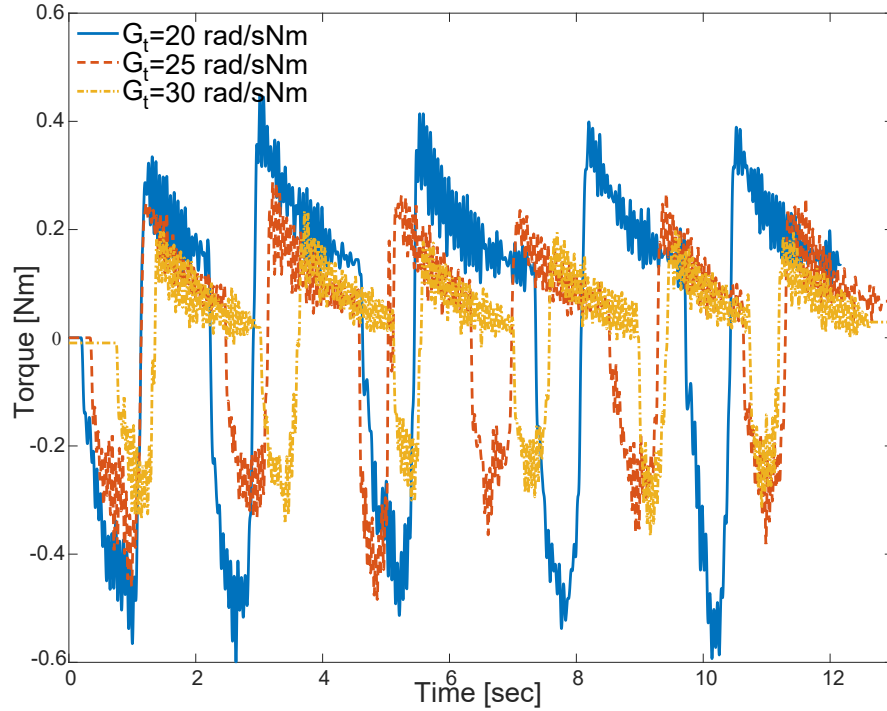


Figure 9.29 Chip test for 3 different  $G_t$  for  $SDEA_{Kfb}$

Performance of  $SDEA_{Kfb}$  under VSIC during null impedance rendering is important, as this control mode provides active backdrivability to the system.

Figure 9.29 presents null impedance rendering performance of  $SDEA_{Kfb}$  under VSIC for three distinct levels of the torque controller gain  $G_t$ . In Figure 9.29, as the torque controller gain  $G_t$  is increased from 20 rad/(s N-m) to 30 rad/(s N-m), the torque required to move the pedal decreases from 1.49% to 0.91% of 40 N-m torque output capacity of the  $SDEA_{Kfb}$  brake pedal. Note that this level of active-backdrivability is excellent for the  $SDEA_{Kfb}$  brake pedal, as evidenced by commonly employed chip test, where a potato chip is used to move the device without getting broken. The

experimental results in Figure 9.29 are also in good agreement with the analysis presented in Section 8, where the positive effect of increasing the torque controller gain  $G_t$  on the null impedance rendering performance has been shown.

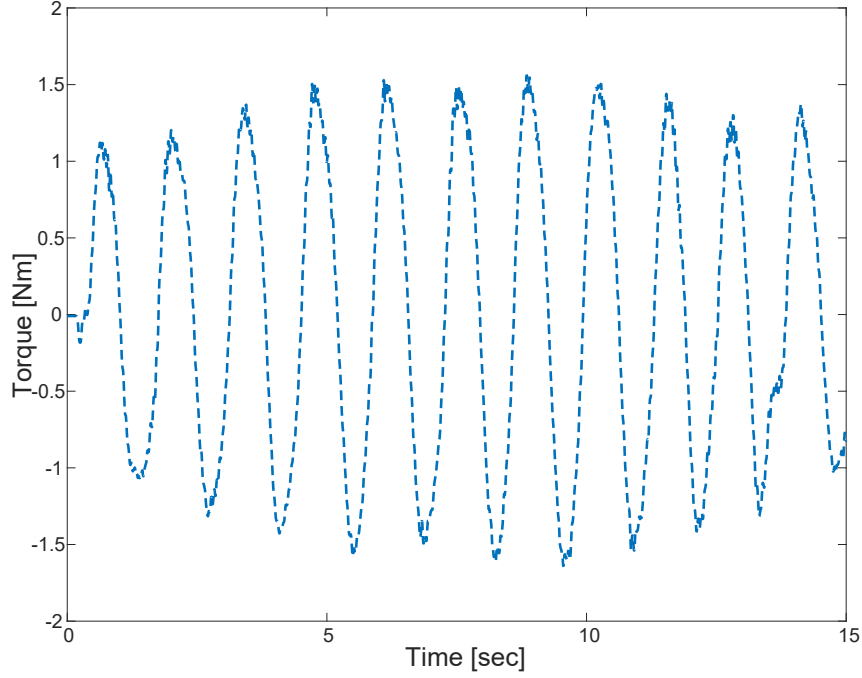


Figure 9.30 Null impedance rendering performance when interacting with human for  $SDEA_{Kfb}$

Purpose of haptic rendering device is interacting with human. Figure 9.30 shows the performance of  $SDEA_{Kfb}$  when interacting with human.

#### 9.5.1.2 Spring Rendering

Two virtual stiffness are studied where  $K_d$  selected as 50 Nm/rad and 100 Nm/rad. Static torques with known values are applied the end-effector and stiffness are calculated with knowledge of displacement. We studied these virtual stiffness for two different gains which are  $G_t = 25$  rad/sNm and  $G_t = 30$  rad/sNm. If  $G_t$  is selected as 25 rad/sNm, stiffness of virtual stiffness equal to 49.13 Nm/rad with  $K_d = 50$  Nm/rad and 98.27 Nm/rad with  $K_d = 100$  Nm/rad. If  $G_t$  is selected as 30 rad/sNm, stiffness of virtual stiffness equal to 49.27 Nm/rad with  $K_d = 50$  Nm/rad and 98.55 Nm/rad with  $K_d = 100$  Nm/rad.



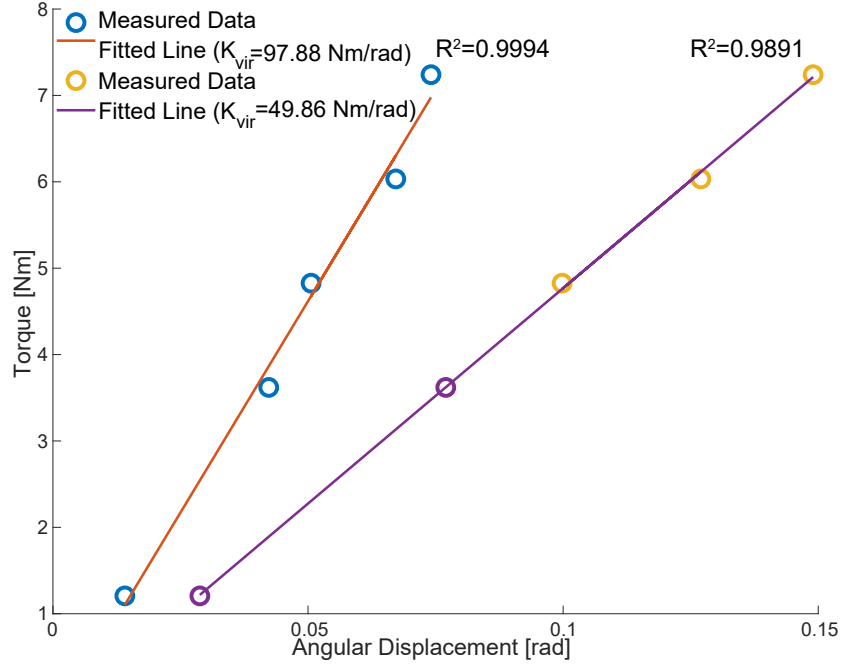


Figure 9.31 Rendering two virtual stiffness experimentally when  $G_t = 25$  rad/sNm for  $SDEA_{Kfb}$

Figure 9.31 presents experimental verification of rendering two virtual stiffness when  $G_t = 25$  rad/sNm. When  $K_d$  is selected as 100 Nm/rad,  $K_{vir} = 97.88$  Nm/rad whose error is %0.39. When  $K_d$  is selected as 50 Nm/rad,  $K_{vir} = 49.86$  Nm/rad whose error is %1.48. Note that fitted line NRMSE of  $K_d = 100$  Nm/rad is 3.6% where RMSE is 0.21, and fitted line NRMSE of  $K_d = 50$  Nm/rad is 0.82% where RMSE is 0.04.

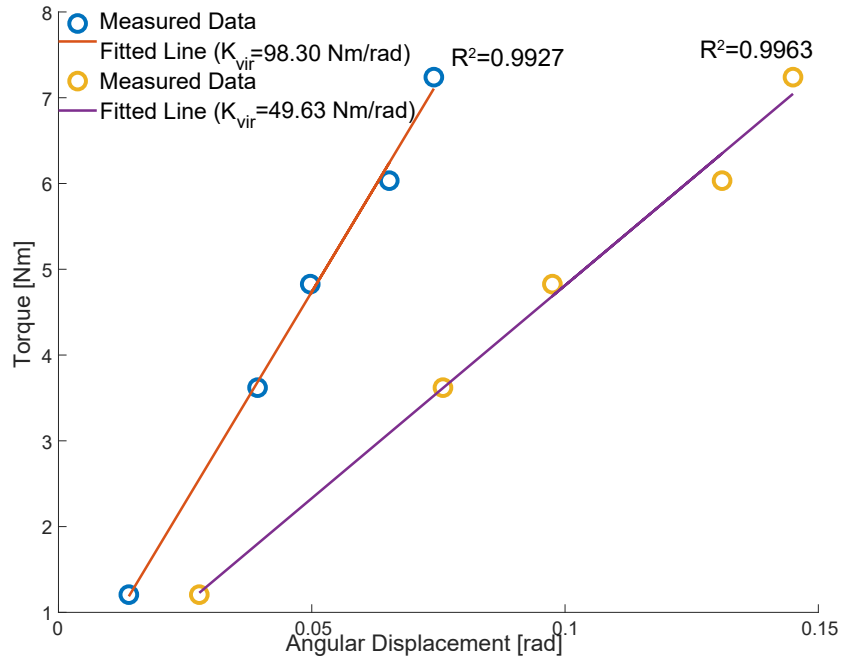


Figure 9.32 Rendering two virtual stiffness experimentally when  $G_t = 30$  rad/sNm for  $SDEA_{Kfb}$

Figure 9.32 presents experimental verification of rendering two virtual stiffness when  $G_t = 30$  rad/sNm. When  $K_d$  is selected as 100 Nm/rad,  $K_{vir} = 98.30$  Nm/rad whose error is %0.25. When  $K_d$  is selected as 50 Nm/rad,  $K_{vir} = 49.63$  Nm/rad whose error is %0.73. Note that fitted line NRMSE of  $K_d = 100$  Nm/rad is 2.13% where RMSE is 0.12, and fitted line NRMSE of  $K_d = 50$  Nm/rad is 3.05% where RMSE is 0.17.

Figure 9.31 and 9.32 show that errors are lower for selection of  $G_t = 30$  rad/sNm for both selection of  $K_d$ . In previous chapters, we have shown that selection of higher  $G_t$  and  $K_d$  increase the performance of spring rendering under VSIC through passive physical equivalents and numerical evaluation.

The  $SDEA_{Kfb}$  brake pedal is designed to interact with humans, so it is important the evaluating performance when the  $SDEA_{Kfb}$  brake pedal interacts with humans. In this experiment, a human interacted with the end-effector of the  $SDEA_{Kfb}$  brake pedal.

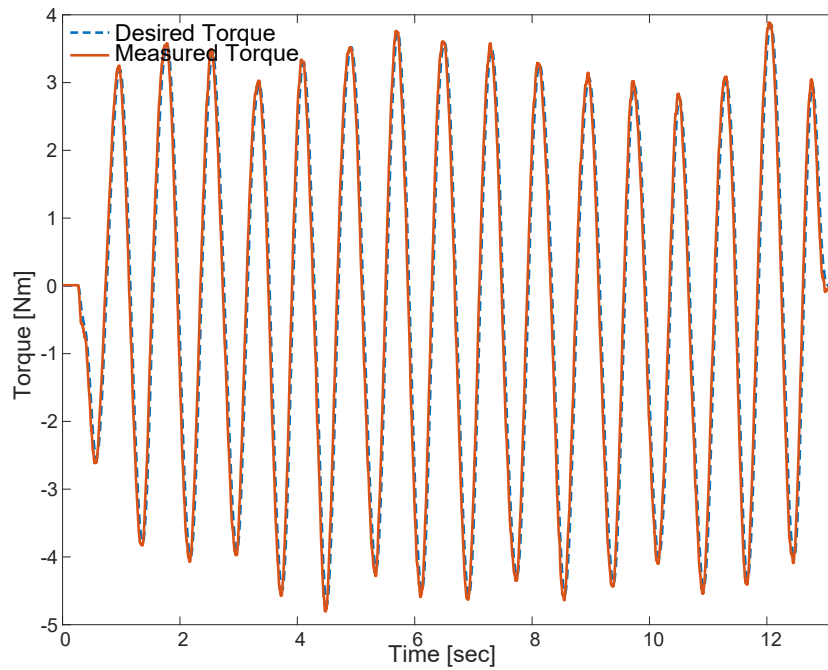


Figure 9.33 When human interacting with the  $SDEA_{Kfb}$  brake pedal when  $K_d = 50$  Nm/rad for  $SDEA_{Kfb}$

Figure 9.33 presents desired torque and measured torque when  $K_d$  is selected as 50 Nm/rad. The human can interact the device safely while the device displays the desired virtual environment. The impedance controller computes the desired torque reference. Figure 9.33 shows that controller and device has good spring rendering performance because measured torque can catch the reference torque. NRMSE of Figure 9.33 is 5.09% where RMSE is 0.43.

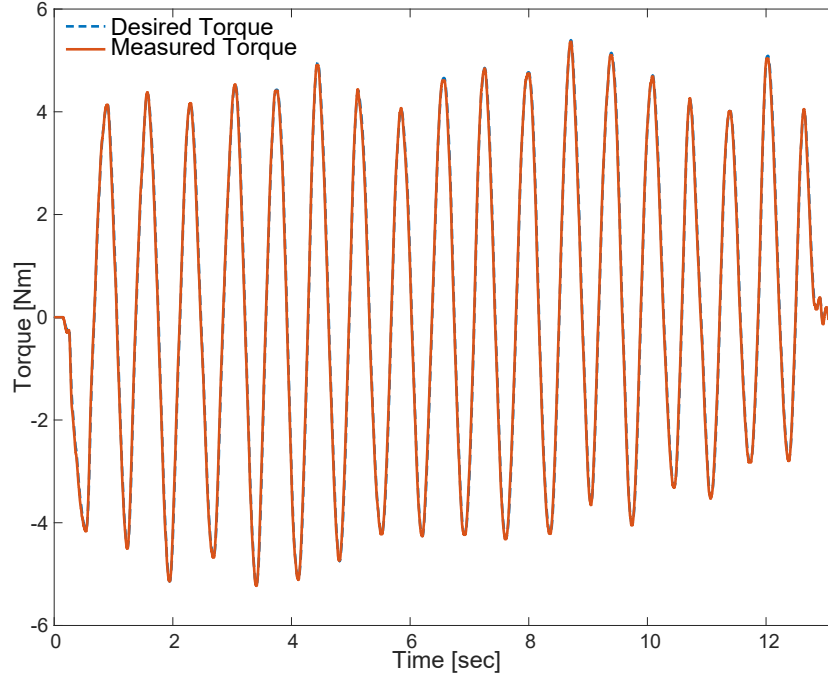


Figure 9.34 When human interacting with the SDEA $_{Kfb}$  brake pedal when  $K_d = 100$  Nm/rad for SDEA $_{Kfb}$

Figure 9.34 presents desired torque and measured torque when  $K_d$  is selected as 100 Nm/rad. The human can interact the device safely while device display the desired virtual environment. The impedance controller computes the desired torque reference. Figure 9.34 shows that controller and device has good spring rendering performance because measured torque can catch the reference torque. NRMSE of Figure 9.34 is 1.18% where RMSE is 0.12.

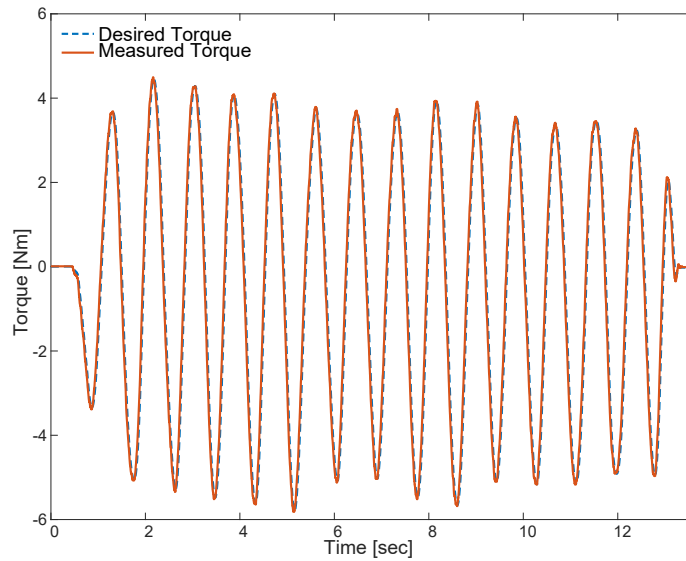


Figure 9.35 When human interacting with the SDEA $_{Kfb}$  brake pedal when  $K_d = 50$  Nm/rad with  $G_t = 30$  rad/sNm for SDEA $_{Kfb}$

Figure 9.35 presents desired torque and measured torque when  $K_d$  is selected as 50 Nm/rad with  $G_t = 30$  rad/sNm. The human can interact the device safely while device display the desired virtual environment. The impedance controller computes the desired torque reference. Figure 9.35 shows that controller and device has good spring rendering performance because measured torque can catch the reference torque. NRMSE of Figure 9.35 is 3.71% where RMSE is 0.38 which is lower than selection of  $G_t = 25$  rad/sNm. Therefore, selection of higher  $G_t$  provides better tracking performance for measured torque. Also, Figure 9.33 and Figure 9.34 show that higher  $K_d$  provide better performance.

### 9.5.1.3 Voigt Model Rendering

The  $SDEA_{Kfb}$  brake pedal is designed to interact with humans, so it is important the evaluating performance when the  $SDEA_{Kfb}$  brake pedal interacts with humans. In this experiment, a human interacted with the end-effector of the  $SDEA_{Kfb}$  brake pedal.

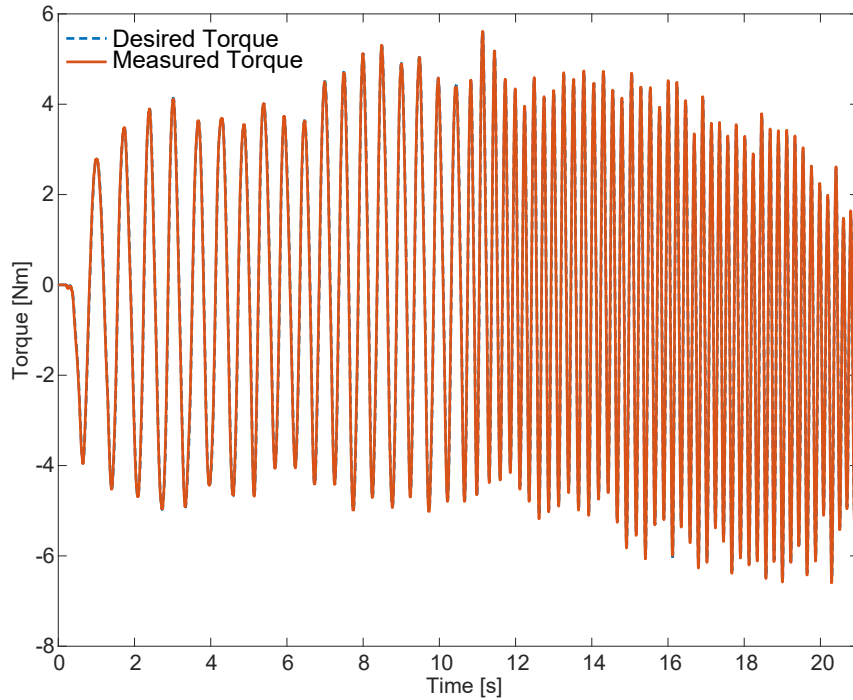


Figure 9.36 When human interacting with the  $SDEA_{Kfb}$  brake pedal when  $K_d = 100$  Nm/rad and  $B_d = 0.01$  Nms/rad

Figure 9.36 presents desired torque and measured torque when  $K_d$  is selected as 100 Nm/rad and  $B_d$  is selected as 0.01 Nms/rad. The human can interact the device safely while the device displays the desired virtual environment. The impedance controller computes the desired torque reference. Figure 9.36 shows that controller and device has good spring rendering performance because measured torque can catch the reference torque. NRMSE of Figure 9.36 is 1.21% where RMSE is 0.13.

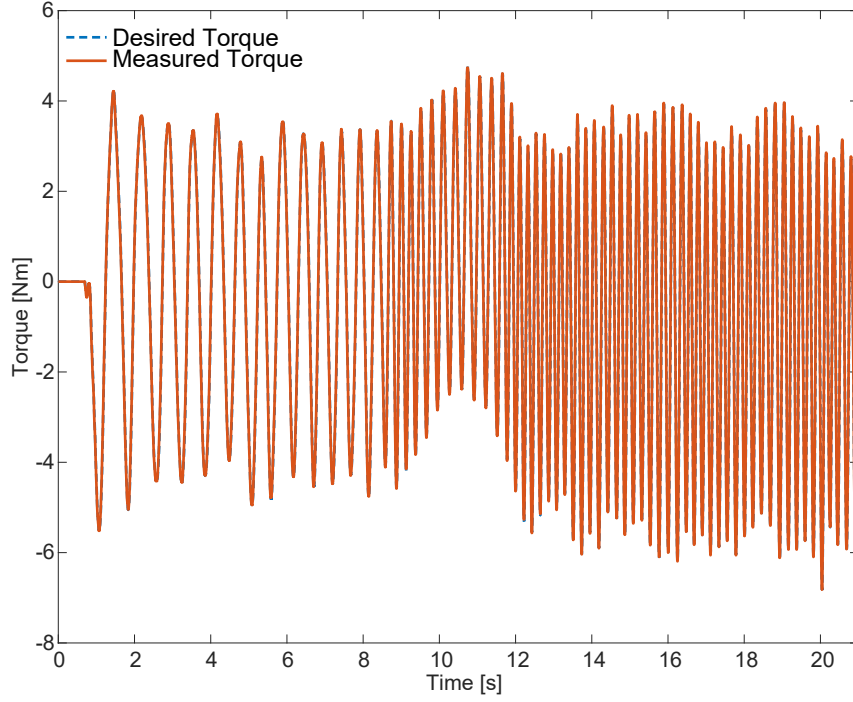


Figure 9.37 When human interacting with the  $SDEA_{Kfb}$  brake pedal when  $K_d = 100$  Nm/rad and  $B_d = 0.01$  Nms/rad with  $G_t = 30$  rad/sNm

Figure 9.37 presents desired torque and measured torque when  $K_d$  is selected as 100 Nm/rad and  $B_d$  is selected as 0.01 Nms/rad while  $G_t = 30$  rad/sNm. The human can interact the device safely while device display the desired virtual environment. The impedance controller computes the desired torque reference. Figure 9.37 shows that controller and device has good spring rendering performance because measured torque can catch the reference torque. NRMSE of Figure 9.37 is 1.1% where RMSE is 0.11.

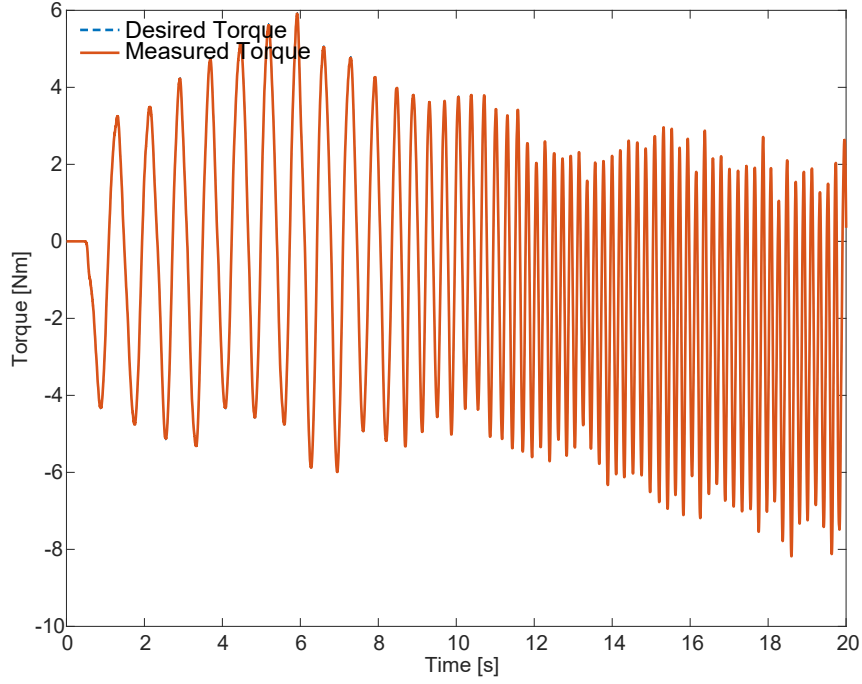


Figure 9.38 When human interacting with the  $SDEA_{Kfb}$  brake pedal when  $K_d = 100$  Nm/rad and  $B_d = 0.05$  Nms/rad with  $G_t = 30$  rad/sNm

Figure 9.38 presents desired torque and measured torque when  $K_d$  is selected as 100 Nm/rad and  $B_d$  is selected as 0.05 Nms/rad while  $G_t = 30$  rad/sNm. The human can interact the device safely while device display the desired virtual environment. The impedance controller computes the desired torque reference. Figure 9.38 shows that controller and device has good spring rendering performance because measured torque can catch the reference torque. NRMSE of Figure 9.38 is 0.95% where RMSE is 0.11 which is lower than selection of  $G_t = 25$  rad/sNm. Therefore, selection of higher  $G_t$  provides better tracking performance for measured torque. Also, Figure 9.37 and Figure 9.38 show that higher  $B_d$  provides better performance.

## 9.5.2 Verification of Passivity Bounds

### 9.5.2.1 Voigt Model Rendering

In this subsection, we studied passivity bounds of Voigt model rendering for  $SDEA_{Kfb}$  when controller are P-P. We selected 1 passive and 1 non-passive  $K_{vir}$  for different  $B_d$  gains. Necessary condition-1 is calculated from Eqn. (6.5) and necessary condition-2 is calculated from Eqn. (6.6). These 2 necessary conditions are equal to necessary and sufficient condition. Virtual stiffness  $K_{vir}$  is equal to  $K_d \frac{\alpha}{\alpha+1}$ . Note that during this experiment,  $G_t = 30$  rad/sNm.

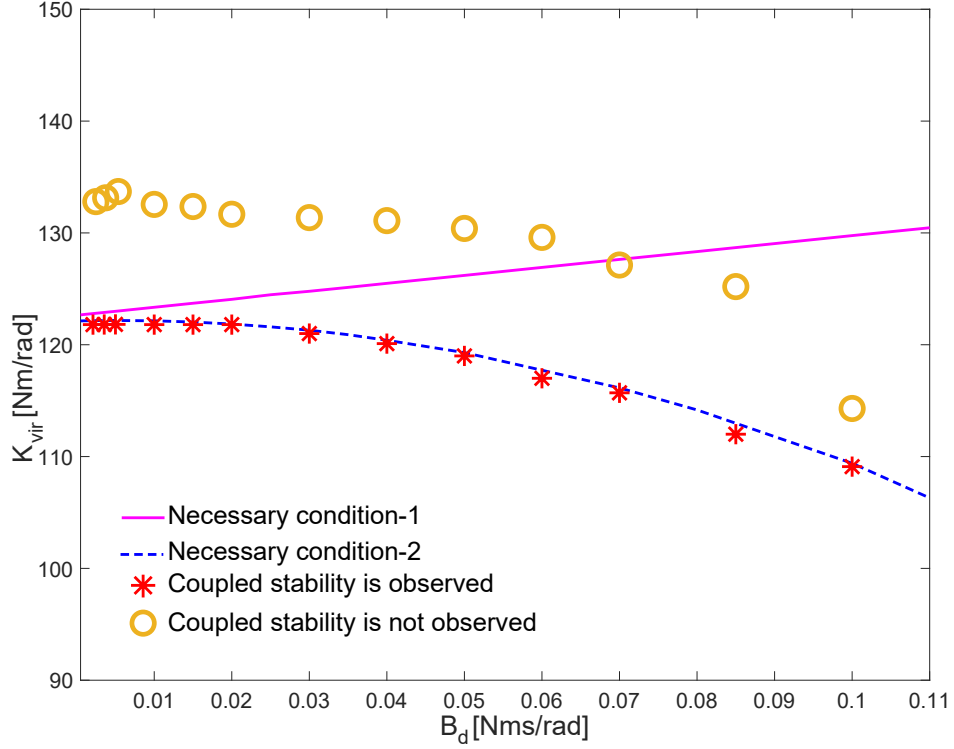


Figure 9.39  $B_d$ - $K_{vir}$  plot for experimentally coupled stability for spring rendering for SDEA $_{Kfb}$

Figure 9.39 presents experimental results of  $K_{vir}$  vs  $B_d$  of the SDEA $_{Kfb}$  brake pedal. The passivity bounds of  $K_{vir}$  according to Eqn. (6.5) depicted as a magenta line which is the necessary condition-1 and Eqn. (6.6) depicted as a blue line which is the necessary condition-2 for Voigt model rendering for SDEA $_{Kfb}$  when controllers are P-P. Figure 9.39 shows that under the condition lines points hold coupled stability, but  $K_{vir}$  is over the condition lines, the chatter was observed at end-effector, so the coupled stability is violated. Figure 9.39 presents there is a difference between the condition lines and the points where coupled stability is violated. It can be caused by the omitted damping on the end-effector and underestimation of damping.

### 9.5.2.2 Spring Rendering

In this subsection, we studied passivity bounds of spring rendering for SDEA $_{Kfb}$  when controller are P-P. We selected 1 passive and 1 non-passive  $K_{vir}$  for 4 different  $G_t$  gains. Necessary condition-1 is calculated from Eqn. (6.14) and necessary condition-2 is calculated from Eqn. (6.15). These 2 necessary conditions are equal to necessary and sufficient condition. The rendering stiffness is equal to  $K_d \frac{\alpha}{\alpha+1}$  which is depicted as  $K_{vir}$ .

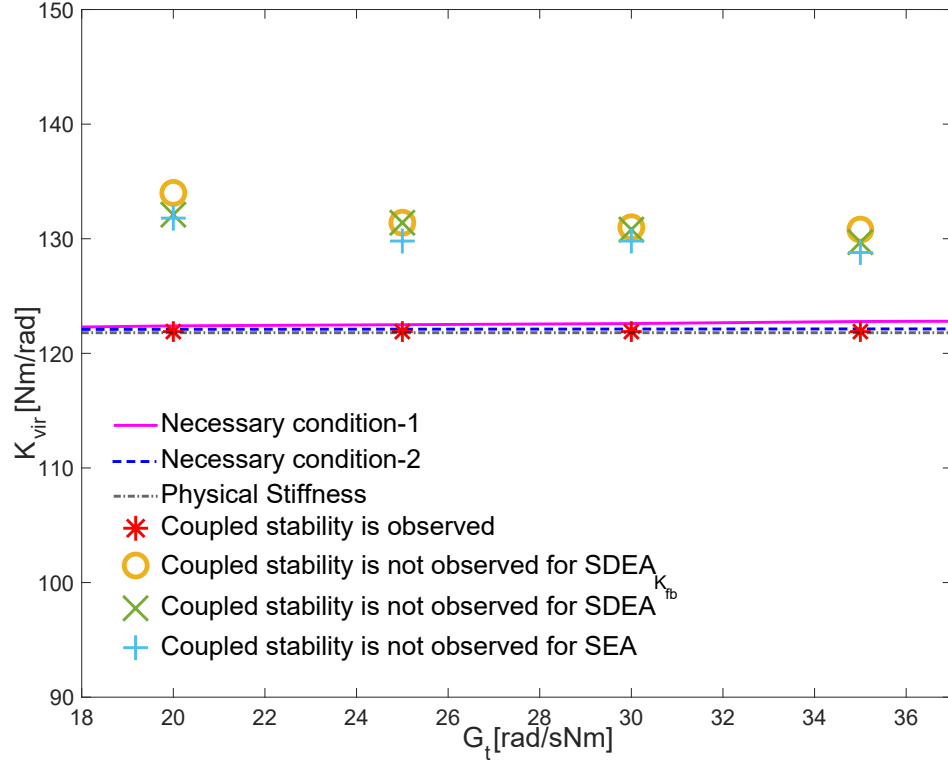


Figure 9.40  $G_t$ - $K_{vir}$  plot for experimentally coupled stability for spring rendering for SDEA $_{Kfb}$

Figure 9.40 presents experimental results of  $K_{vir}$  vs  $G_t$  of the SDEA brake pedal. The passivity bounds of  $K_{vir}$  according to Eqn. (6.14) depicted as a magenta line which is the necessary condition-1 and Eqn. (6.15) depicted as a blue line which is the necessary condition-2 for spring rendering for SDEA $_{Kfb}$  when controllers are P-P. Figure 9.40 shows that these two necessary conditions are very close and these lines provide relaxer condition than physical stiffness which is the advantage of SDEA $_{Kfb}$  over the SDEA and SEA. Figure 9.40 shows that under the condition lines points hold coupled stability, but  $K_{vir}$  is over the condition lines, the chatter was observed at end-effector, so the coupled stability is violated. Figure 9.40 presents there is a difference between the condition lines and the points where coupled stability is violated. It can be caused by the omitted damping on the end-effector. Figure 9.40 presents experimental limits for couple stability of SDEA and SEA. We can see that experimental limit of virtual spring stiffness of SDEA $_{Kfb}$  is higher than SDEA and SEA as in the theoretical results.



# Chapter 10

## Model Reference Force Control

In this chapter, we propose the use of MRFC for SEA as an alternative to VSIC and provide passivity analysis of this control scheme, under model mismatch. sufficient conditions for one-port passivity of SEA under MRFC during null impedance rendering is presented. validations of our theoretical results through a set of systematic simulations and physical experiment is provided. Also, null impedance rendering performance of MRFC is experimentally demonstrated.

### 10.1 System Description

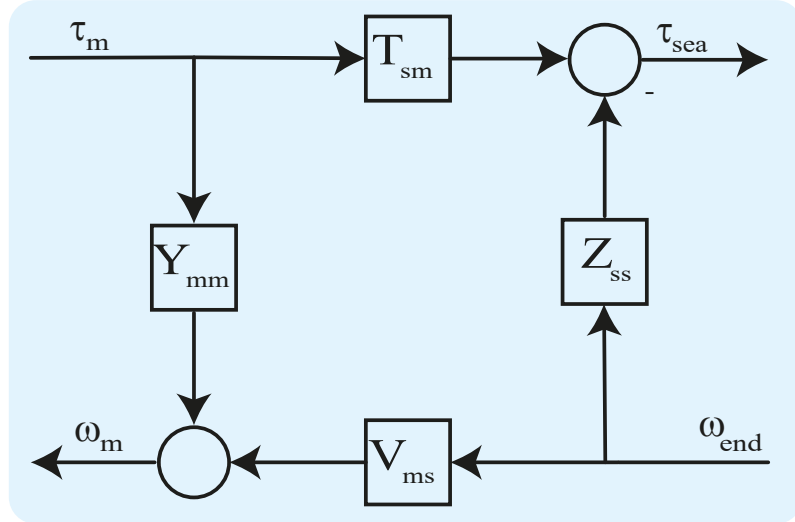


Figure 10.1 2-port impedance-admittance block diagram of uncontrolled system

Figure 10.1 depicts the model-reference force control of SEA. The figure includes elements of the 2-port hybrid immittance matrix for open loop plant as

$$\begin{bmatrix} \tau_{sea} \\ \omega_m \end{bmatrix} = \begin{bmatrix} -Z_{ss} & T_{sm} \\ V_{ms} & Y_{mm} \end{bmatrix} \begin{bmatrix} \omega_{end} \\ \tau_m \end{bmatrix} \quad (10.1)$$

with  $Z_{ss}(s) = \frac{J_m K s + K B_m}{J_m s^2 + B_m s + K}$ ,  $T_{sm}(s) = \frac{K}{J_m s^2 + B_m s + K}$ ,  $V_{ms}(s) = \frac{K}{J_m s^2 + B_m s + K}$ , and  $Y_{mm}(s) = \frac{s}{J_m s^2 + B_m s + K}$ .

If a control law is applied:

$$\tau_m = -G_f G_s G_v \omega_{end} - G_v \omega_m - G_s G_v \tau_{sea} \quad (10.2)$$

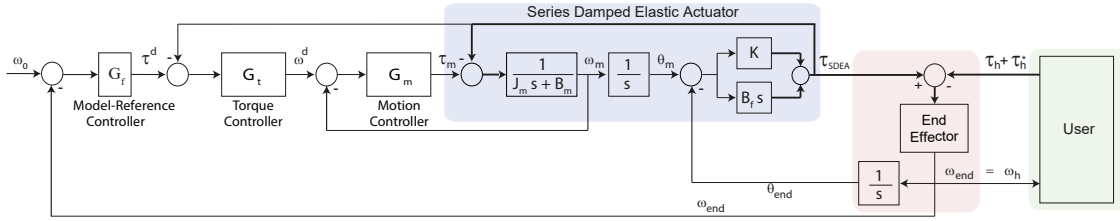


Figure 10.2 Block diagram of S(DEA) under MRFC

The terms  $G_s$  and  $G_v$  are torque controller and motion controller, respectively. From Eqn. (10.1) and Eqn. (10.2) model reference controller  $G_f$  can be computed as:

$$G_f = \frac{(G_v Y_{mm} + 1)(Z_{des} - Z_{ss})}{G_s G_v T_{sm}} - \frac{V_{ms} - G_s Z_{des}}{G_s} \quad (10.3)$$

where  $Z_{des}$  equals to  $Z_{ss} + Z_d$ . Derivation of Eqn. (10.3) is similar to [7] which is used 2-port admittance without SEA.

Figure 10.2 which consists of the plant, an inner velocity loop, an outer torque loop, and the model-reference controller. It is clearly seen that if desired impedance ( $Z_d$ ) is put instead of  $G_f$ , Figure 10.2 will have same structure with VSIC. If  $G_f$  is computed according to Eqn. (10.3),  $Z_{output}$  equals to  $Z_d + Z_{ss}$  in Figure 10.2 assuming all parameters are known. Note that  $Z_{output}$  is relation between conjugate terms which equals to  $\frac{-T_{sea}(s)}{w_{end}(s)}$ . The minus sign comes from compression. Figure 10.2 can be arranged as Figure 10.3 which depicts the model-reference force control diagram of S(D)EA. The model of the plant consists of the same elements, where  $\hat{\cdot}$  notation is used to differentiate the model parameters from those of the plant. The symbol  $G_v$  depicts the motion controller, while  $G_s$  is the force controller. The desired impedance is denoted by  $Z_d$ . In the block diagram,  $Z_d$  is multiplied by  $\frac{1}{\hat{T}_{sm}}$  to map desired end-effector torques to appropriate actuator torques. If all of the system parameters are known exactly, then  $Z_{out} = Z_{ss} + Z_d$ .

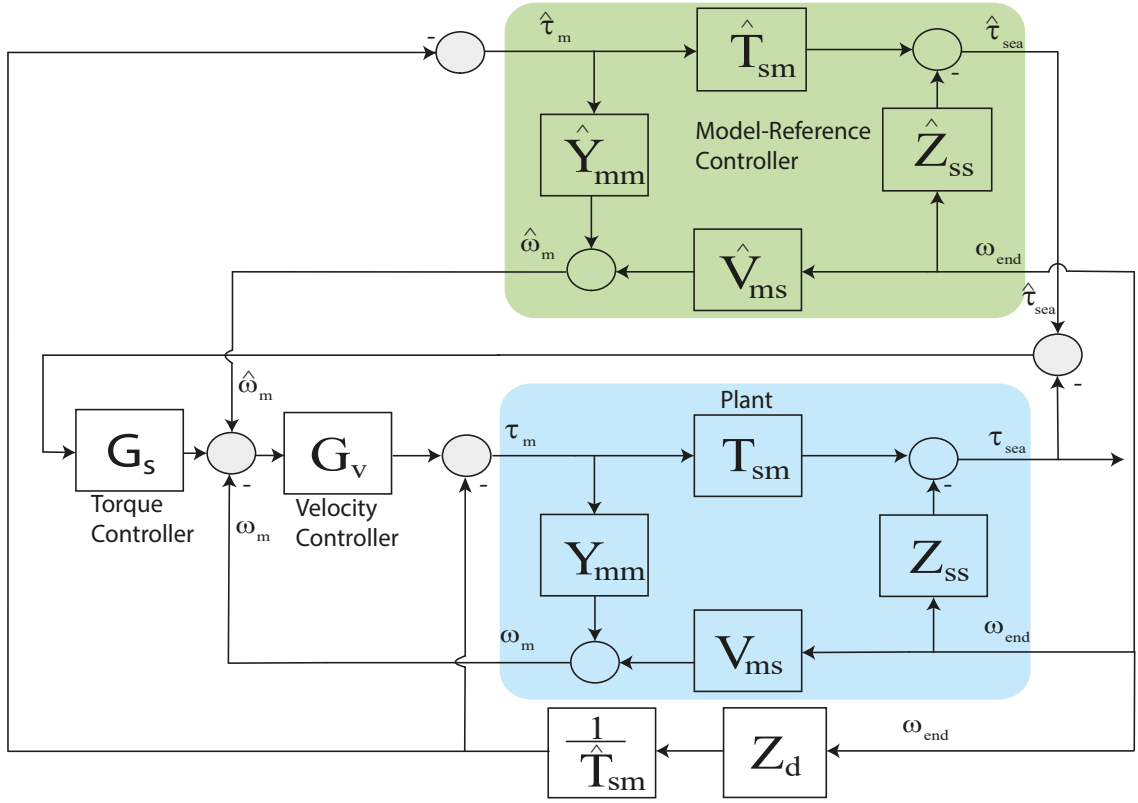


Figure 10.3 2-port block diagram of SEA under MRFC

## 10.2 Passivity Analysis

Under model uncertainty,  $Z_{out}$  for Figure 10.3 becomes

$$Z_{out}(s) = \frac{\left( G_v Y_{mm} + 1 \right) \left( Z_{ss} + \frac{T_{sm} \left( \frac{Z_d}{\hat{T}_{sm}} + G_v \left( V_{ms} - \hat{V}_{ms} + G_s (Z_d + \hat{Z}_{ss}) + \frac{\hat{Y}_{mm} Z_d}{\hat{T}_{sm}} \right) \right)}{G_v Y_{mm} + 1} \right)}{G_v Y_{mm} + G_s G_v T_{sm} + 1} \quad (10.4)$$

Passivity analysis is performed for Eqn. (10.4). In particular, we study the case for null impedance rendering, when  $Z_d=0$ . Null impedance rendering is a crucial mode for pHRI applications as it provides active backdrivability to SEA by compensating for parasitic forces acting on the system. If there exists no model uncertainty,  $Z_{out}$  becomes

$$Z_{null}(s) = \frac{J_m K s + B_m K}{J_m s^2 + B_m s + K} \quad (10.5)$$

Note that Eqn. (10.5) does not include control parameters due to the perfect cancellation of terms and this allows for selection of very high gains for aggressive and robust interaction control performance with ensured passivity. The frequency domain disturbance response can be calculated as

$$Y_f(s) = \frac{\omega_m}{F_f} \Big|_{\omega_{end}=0} = \frac{Y_{mm}}{G_v (Y_{mm} + G_s T_{sm}) + 1} \quad (10.6)$$

indicating that disturbance rejection performance of MRFC can be improved by selection of high gains for  $G_s$  and  $G_v$  without sacrificing passivity.

Under model uncertainty, a more realistic model of  $Z_{out}$  becomes  $Z_{null}(s) = \frac{N(s)}{D(s)}$ , where

$$\begin{aligned} N(s) &= \hat{J}_m J_m K s^3 + K \gamma s^2 \\ &+ (\hat{B}_m B_m K + \hat{B}_m G_v K + J_m K \hat{K} + G_s G_v \hat{J}_m K \hat{K}) s \\ &+ B_m K \hat{K} + \hat{B}_m G_s G_v K \hat{K} \\ D(s) &= \hat{J}_m J_m s^4 + \gamma s^3 \\ &+ (\hat{B}_m B_m + \hat{B}_m G_v + \hat{J}_m K + J_m \hat{K} + G_s G_v \hat{J}_m K) s^2 \\ &+ (\hat{B}_m K + B_m \hat{K} + G_v \hat{K} + \hat{B}_m G_s G_v K) s \\ &+ K \hat{K} + G_s G_v K \hat{K} \end{aligned}$$

with  $\gamma = \hat{B}_m J_m + B_m \hat{J}_m + G_v \hat{J}_m$

The passivity of  $Z_{null}(s)$  is checked according to Theorem 1. Theorem 16 presents sufficient conditions for one-port passivity of SEA under MRFC while rendering null impedance, when  $G_s$  and  $G_v$  consist of proportional gains.

**Theorem 16.** *Consider null impedance rendering for SEA under MRFC as in Figure 10.3, where  $G_s$  and  $G_v$  consist of proportional gains. Let all parameters be positive and define  $\hat{B}_m = \alpha B_m$ . Then, the following expressions constitute sufficient conditions for passivity of  $Z_{null}(s)$ .*

$$\begin{aligned} (i) \quad & \hat{K} < \left( \frac{1}{G_s G_v} + 1 \right) K, \text{ and} \\ (ii) \quad & \hat{J}_m \geq \frac{G_v J_m \hat{K}}{(B_m + G_v) (K + G_s G_v (K - \hat{K}))}, \text{ and} \\ (iii) \quad & \frac{G_v \left( \hat{J}_m K - J_m \hat{K} + G_s J_m \hat{K} (G_s \hat{J}_m K - G_s \hat{J}_m \hat{K}) \right) + B_m \left( 2 \hat{J}_m K + G_s G_v \hat{J}_m K \right)}{B_m G_v (B_m + G_v - G_s J_m \hat{K})} + \\ & \frac{G_s \hat{J}_m (K - \hat{K})}{B_m} \leq \alpha + \frac{B_m (B_m + G_v) (K + G_s G_v K - G_s G_v \hat{K})}{G_v \hat{K} (B_m + G_v - G_s J_m \hat{K})} \alpha^2 \\ & \text{with } B_m + G_v > G_s J_m \hat{K}. \end{aligned}$$

*Proof.* 1)  $Z_{null}(s)$  has no poles in the right half plane. Invoking Lemma 2, one can show that this condition can be expressed as

$$\kappa_1 + \kappa_2 \geq 0 \quad (10.7)$$

where

$$\begin{aligned} \kappa_1 &= \hat{B}_m (B_m + G_v) (\hat{B}_m^2 G_s G_v J_m K + \hat{B}_m^2 J_m K \\ &+ \hat{B}_m B_m G_s G_v \hat{J}_m K + \hat{B}_m B_m \hat{J}_m K + \hat{B}_m B_m J_m \hat{K} \\ &+ \hat{B}_m G_s G_v^2 \hat{J}_m K + \hat{B}_m G_v \hat{J}_m K + \hat{B}_m G_v J_m \hat{K} \\ &+ B_m^2 \hat{J}_m \hat{K} + 2 B_m G_v \hat{J}_m \hat{K} + G_v^2 \hat{J}_m \hat{K} + G_v^2 \hat{J}_m \hat{K}) \\ \kappa_2 &= \hat{B}_m (B_m + G_v) (\hat{J}_m K (G_s G_v + 1) - J_m \hat{K})^2 \end{aligned}$$

Here,  $\kappa_1$  is always positive, while  $\kappa_2$  is non-negative, Hence, Condition (1) of Theorem 1 is always satisfied.

2)  $Re[Z(jw)] \geq 0$  for all  $w$ . Invoking Lemma 1, the sign of  $Re[Z_{null}(s)]$  can be checked by the sign of  $H(jw) = d_4 w^4 + d_2 w^2 + d_0$ , where

$$\begin{aligned} d_4 &= K^2 (G_v \hat{J}_m^2 + B_m \hat{J}_m^2 (G_s G_v + 1) + G_s G_v^2 \hat{J}_m^2) \\ &- K \hat{K} (G_s G_v^2 \hat{J}_m^2 + G_v \hat{J}_m J_m + B_m G_s G_v \hat{J}_m^2) \end{aligned} \quad (10.8)$$

$$\begin{aligned} d_2 &= (\hat{B}_m K^2 (1 + G_s G_v) + K \hat{K} (B_m + G_v)) (\hat{B}_m B_m \\ &+ \hat{K} (\hat{B}_m G_v + J_m + G_s G_v \hat{J}_m)) - \hat{K} (B_m + \hat{B}_m G_s G_v) \\ &(J_m K \hat{K} + \hat{B}_m K (B_m + G_v) + \hat{J}_m K (K + G_s G_v K)) \\ &- K^2 \hat{K} (G_s G_v + 1) (\hat{B}_m J_m + B_m \hat{J}_m + G_v \hat{J}_m) \end{aligned} \quad (10.9)$$

$$d_0 = K^2 \hat{K}^2 (1 + G_s G_v) (B_m + \hat{B}_m G_s G_v) \quad (10.10)$$

From Lemma 3, it is necessary that  $d_0 \geq 0$ . Since all of the parameters are positive,  $d_0$  is always positive. From Lemma 3, it is also necessary that  $d_4 \geq 0$ . To check for this condition, Eqn. (10.8) can be rearranged as

$$\begin{aligned} 0 &\leq [K (G_v K + B_m K (G_s G_v + 1) + G_s G_v^2 K \\ &- G_s G_v^2 \hat{K} - B_m G_s G_v \hat{K})] \hat{J}_m^2 - (G_v J_m K \hat{K}) \hat{J}_m \end{aligned} \quad (10.11)$$

In this equation, if the coefficient of  $\hat{J}_m^2$  is not positive, then  $d_4$  is negative, due to the negative coefficient of  $\hat{J}_m$ . Therefore, to ensure a positive coefficient for  $\hat{J}_m^2$ , the following condition should hold:

$$\hat{K} < \left( \frac{1}{G_s G_v} + 1 \right) K \quad (10.12)$$

Given Eqn. (10.12) and positiveness of parameter  $\hat{J}_m$ , Condition (ii) ensures a nec-

essary condition that  $d_4$  is positive.

While Lemma 3 provides the necessary and sufficient conditions for positiveness of  $H(jw)$  an analytical solution for the third expression in Lemma 3 is cumbersome. A sufficient condition for  $Re[Z(jw)] > 0$  can be ensured by setting  $d_2 > 0$  as follows

$$\begin{aligned}
& K \hat{K} (B_m J_m \hat{K} + K(2 B_m \hat{J}_m + G_v \hat{J}_m + G_s G_v^2 \hat{J}_m \\
& + 2 B_m G_s G_v \hat{J}_m)) - K \hat{K}^2 (J_m + G_s G_v \hat{J}_m) \\
& (B_m + G_v) \leq (B_m G_v K \hat{K} (B_m + G_v - G_s J_m \hat{K}))\alpha \\
& + (B_m^2 K (B_m + G_v) (K + G_s G_v K - G_s G_v \hat{K}))\alpha^2
\end{aligned} \tag{10.13}$$

In this expression, the left hand side of Eqn. (10.13) and the coefficient of  $\alpha^2$  are always positive when Conditions (i) and (ii) hold. If  $B_m + G_v > G_s J_m \hat{K}$ , then Eqn. (10.13) can be written as Condition (iii), expressing that  $\alpha$  has a positive lower bound.

3) Any poles of  $Z(s)$  on the imaginary axis are simple with positive and real residues. This condition is always satisfied since the inequality in Lemma 2 is strictly greater than zero, as shown for Eqn. (10.7).  $\square$

**Remark (1).** *Conditions (i) and (ii) of Theorem 16 are also necessary conditions for passivity that define an upper bound for  $\hat{K}$  and a lower bound for  $\hat{J}_m$ , respectively.*

**Remark (2).** *Condition (iii) of Theorem 16 is a sufficient conditions for passivity and defines a lower bound for  $\hat{B}_m$ . This condition can be replaced by the third condition expressed in Lemma 3 to derive the necessary and sufficient conditions for passivity null impedance rendering under MRFC. However, the resulting equation is cumbersome to express in closed form<sup>1</sup>.*

**Remark (3).** *According to the necessary and sufficient conditions, it is possible to set  $\hat{B}_m = 0$  iff  $\hat{J}_m = \frac{J_m \hat{K}}{K(G_s G_v + 1) - \hat{K}(B_m G_s + G_s G_v)}$ . Note that such an exact assignment is not practically feasible, since the plant parameters cannot be determined exactly. For all other cases, it can be shown that  $\hat{B}_m$  assumes a positive lower bound to ensure passivity.*

**Remark (4).** *If the assignment for  $\hat{J}_m$  is determined, the Conditions (i) and (ii) of*

---

<sup>1</sup>A Matlab file that includes these conditions is available for download at [https://hmi.sabanciuniv.edu/Passivity\\_of\\_MRFC.m](https://hmi.sabanciuniv.edu/Passivity_of_MRFC.m)

Theorem 16 can be merged to determine the upper bound for  $\hat{K}$  as follows:

$$\hat{K} \leq \frac{\hat{J}_m (G_s G_v + 1) (B_m + G_v)}{G_v (J_m + G_s \hat{J}_m (B_m + G_v))} K \quad (10.14)$$

**Remark (5).** Since the compliant element of a series elastic actuator acts as the sensor, in general, the stiffness  $K$  is well characterized. If we evaluate conditions of Theorem 16 for  $\hat{K} = K$ , then results are simplified. In particular, Condition (i) is always satisfied, while Condition (ii) reduces to

$$\frac{G_v J_m}{B_m + G_v} \leq \hat{J}_m \quad (10.15)$$

Eqn. (10.15) is equivalent to the condition presented in [33] for a rigid manipulator. Finally, Condition (iii) becomes

$$\frac{K (2 B_m \hat{J}_m + G_v \hat{J}_m - G_v J_m + B_m G_s G_v \hat{J}_m)}{B_m G_v (B_m + G_v - G_s J_m K)} \leq \alpha + \frac{B_m (B_m + G_v)}{G_v (B_m + G_v - G_s J_m K)} \alpha^2. \quad (10.16)$$

## 10.3 Numerical Evaluations

In this section, the theoretical results are verified through Bode plots of numerical simulations.

Table 10.1 Parameters for SEA under MRFC

Parameter	Value	Parameter	Value
$J_m$	0.002 kgm <sup>2</sup>	$\hat{J}_m$	0.0022 kgm <sup>2</sup>
$B_m$	1.22 Nms/rad	$\hat{B}_m$	0.0122 Nms/rad
$K$	360 Nm/rad	$\hat{K}$	324 Nm/rad

Table 10.1 presents the parameters of the plant and the model used for MRFC. For model uncertainty,  $J_m$  is overestimated and  $K$  is underestimated by 10%, respectively. The proportional controller gains are set as  $G_v = 20$  Nms/rad and  $G_s = 5$  rad/sNm.

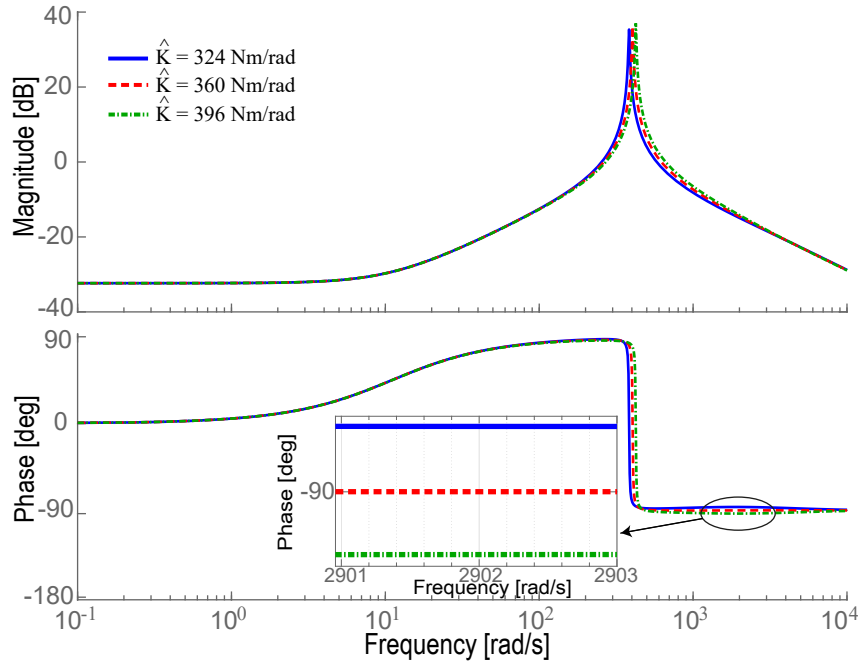


Figure 10.4 Bode plots for null rendering for various  $\hat{K}$



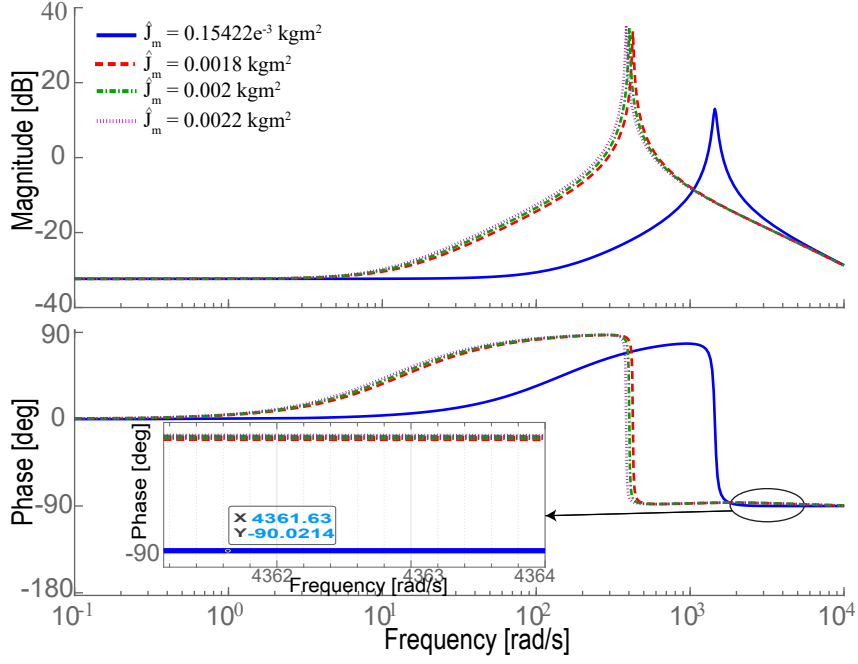


Figure 10.5 Bode plots for null rendering for various  $\hat{J}_m$

Figure 10.4 shows that the closed loop system is passive when  $K$  is underestimated 10% and passivity is lost when  $K$  is overestimated by 10%, as predicted by Condition (i) of Theorem 16. Figure 10.5 shows that the closed loop system is passive when  $J_m$  is overestimated or underestimated by 10%, as predicted by Condition (ii) of Theorem 16. One can also observe that the closed loop system is not passive when the lower limit on  $\hat{J}_m$  imposed by Condition (ii) is violated.

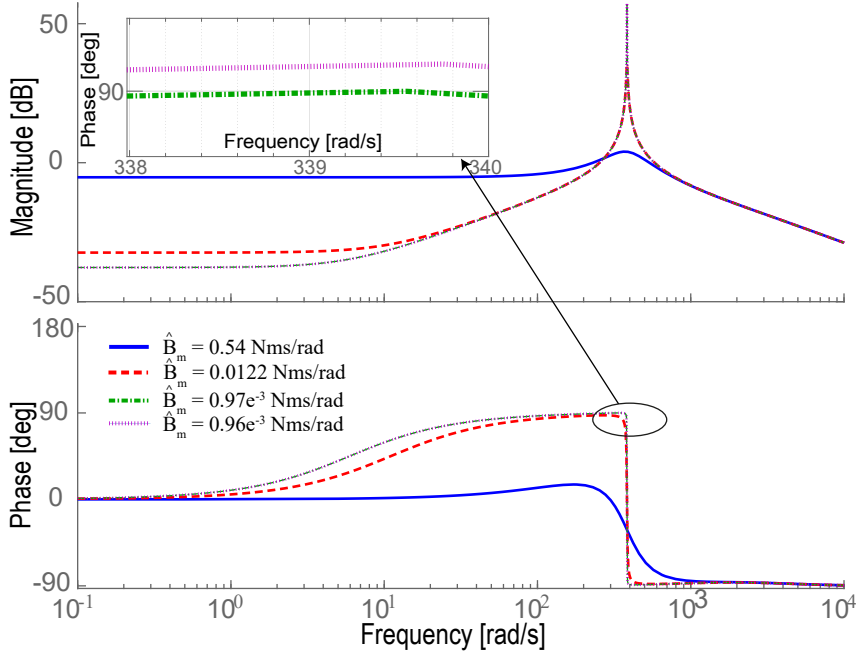


Figure 10.6 Bode plots for null rendering for various  $\hat{B}_m$

Figure 10.6 shows that the closed loop system is passive when  $\hat{B}_m = 0.01B_m$ . The lower bound on  $\hat{B}_m$  is computed as 0.54 Nms/rad according to the sufficient con-

dition in Condition (ii) of Theorem 16, while the necessary and sufficient condition imposes a significantly more relaxed lower bound of 0.00097 Nms/rad.

## 10.4 Experimental Validations

Figure 9.1 presents a solid model of the experimental setup, but there will be damper which is parallel to series elastic element. In this experiment, we removed magnets, magnet holder, and aluminium plate. Also, stiffer compliant element is used.

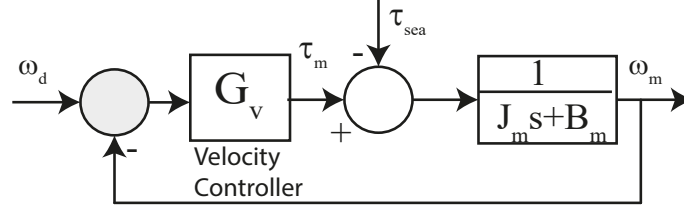


Figure 10.7 Closed loop motion controlled system

From Figure 10.7, the transfer function with  $w_d$  as input and  $w_m$  as output can be derived as

$$\frac{w_m}{w_d} = \frac{G_v}{J_m s + B_m + G_v} \quad (10.17)$$

### 10.4.1 System Identification

The closed-loop system identification is used to experimentally determine system parameters. In particular, the system is identified with the inner velocity control loop with  $G_v = 0.032$  Nms/rad. Furthermore,  $\tau_{sea}$  is taken as zero since no exogenous input is applied to the system during the system identification. Stiffness of the cross flexure joint is determined separately, by applying known forces to the SEA brake pedal and measuring the resulting deflection.

Table 10.2 presents the experimentally characterized parameters for the SEA brake pedal system. The estimated transfer function has a fit of  $R^2 = 89.5\%$  with the data collected.  $R^2$  was measured in frequency domain.

Table 10.2 Experimentally characterized system parameters for the SEA brake pedal

Parameter	Value
$J_m$	$6.794 \cdot 10^{-4} \text{ kgm}^2$
$B_m$	$0.0122 \text{ Nms/rad}$
$K$	$360 \text{ Nm/rad}$

### 10.4.2 Experimental Validation of Passivity Limits

Considering the parameters in Table 10.2, the model parameters for MRFC are selected as  $\hat{J}_m = 1.1J_m$ ,  $\hat{K} = 0.9K$  and  $\hat{B}_m = 0.05B_m$ . The motion controller gain

$G_v$  is set to 0.032 Nms/rad, as used during the system identification.

To verify the passivity limits, we tested the coupled stability of the controllers with three different  $G_s$  gains, by coupling the controlled system to a range of most destabilizing environments and inducing fast movements and impacts to the end-effector of the SEA brake pedal. A loss of coupled stability was decided, when chatter was observed.

Figure 10.8 presents the  $\hat{K}/K$  vs  $G_s$  plot of the SEA brake pedal for all the tested parameters. The passivity bound for  $\hat{K}$  according to Eqn. (10.14) is depicted as the dashed line in Figure 10.8, while the passivity bound on  $\hat{K}$  according to the necessary and sufficient condition of Lemma 3 is the presented as the magenta line. The coupled stability was tested at three  $G_s$  values for various  $\hat{K}$  selections. When  $K$  was underestimated by 10%, the coupled stability was ensured for all tested  $G_s$  gains. When  $\hat{K}$  was selected higher than the limit imposed by the passivity bound, chatter was observed at the end-effector, so the coupled stability is violated.

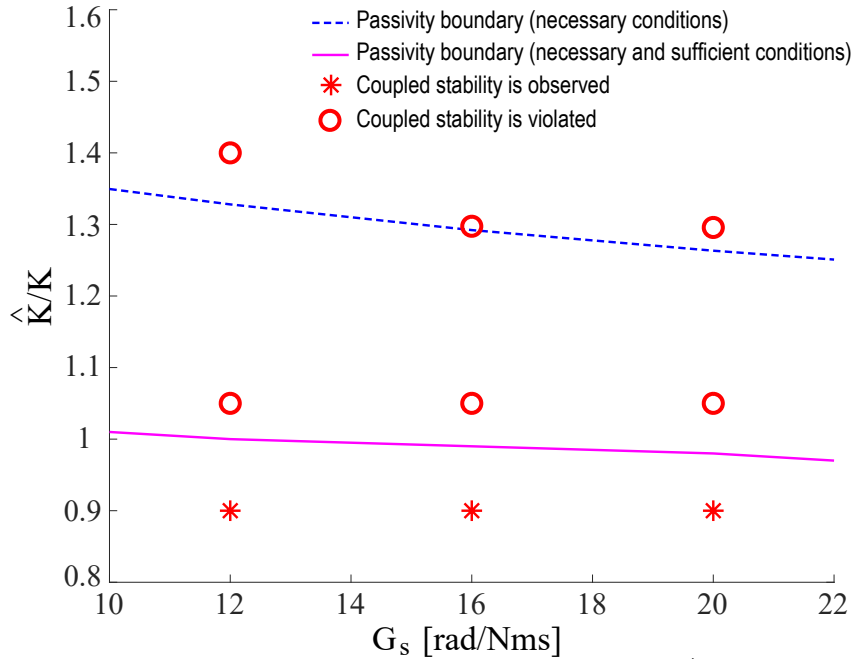


Figure 10.8 Experimental verification of the  $\hat{K}$  bound

Figure 10.9 presents the  $\hat{J}_m/J_m$  vs  $G_s$  plot of the SEA brake pedal for all the tested parameters. The passivity bound for  $\hat{J}_m$  according to Condition (ii) of Theorem 16 is depicted as the dashed line in Figure 10.9, while the passivity bound on  $\hat{J}_m$  according to the necessary and sufficient condition of Lemma 3 is the presented as the magenta line. The coupled stability was tested at three  $G_s$  values for various  $\hat{J}_m$  selections. When  $J_m$  was overestimated by 10%, the coupled stability was ensured for all tested  $G_s$  gains. When  $\hat{J}_m$  was selected lower than the limit imposed by the passivity bound, chatter was observed at the end-effector, so the coupled stability is violated.

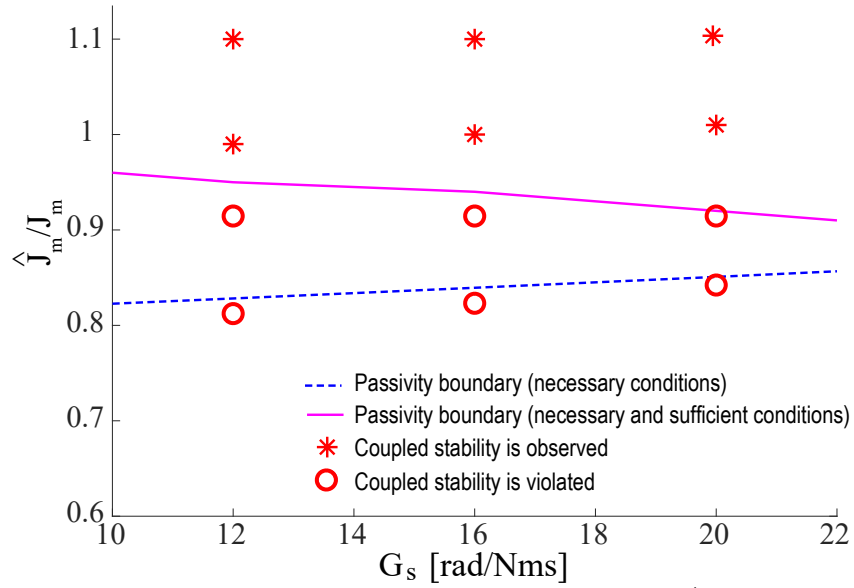


Figure 10.9 Experimental verification of the  $\hat{J}_m$  bound

### 10.4.3 Experimental Evaluation of Performance of MRFC

To demonstrate null impedance rendering performance of the SEA brake pedal under MRFC, the controller parameters were selected as  $\hat{J}_m = 1.1J_m$ ,  $\hat{K} = 0.9K$ ,  $\hat{B}_m = 0.05B_m$ ,  $G_v = 0.032$  Nms/rad, and  $G_s = 23$  rad/Nms, respectively. An active backdrivability experiment was conducted where the end-effector of the brake pedal was pushed with a potato chip. The maximum force experienced on the chip was measured as 1.2 N (0.24 Nm in torque), indicating excellent active backdrivability for a SEA capable of 40 Nm continuous torque output. Figure 10.10 presents chip test of MRFC.

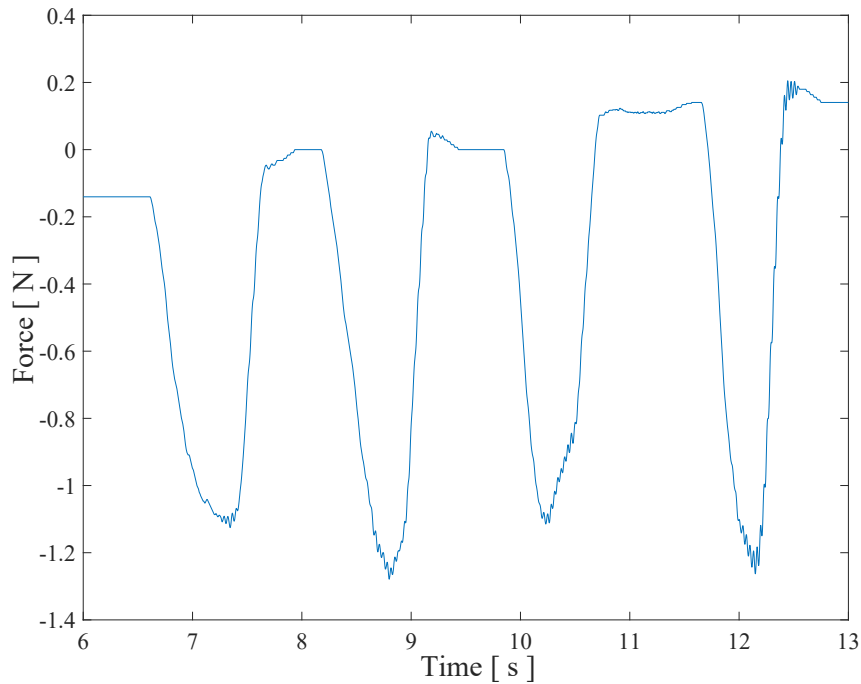


Figure 10.10 Chip test of MRFC

# Chapter 11

## Conclusion and Future Work

We have presented frequency domain passivity analysis of S(D)EA under VSIC for null impedance rendering, spring rendering, and Voigt model, and provided the necessary and sufficient conditions for passivity of these systems. These results extend earlier results on S(D)EA passivity in the literature [41, 45, 46], as the controller gains are allowed to take negative values. In addition to the passivity analysis, we have derived passive physical equivalents for these systems which provide novel insights and intuition into the closed-loop system dynamics. In particular, the passive physical equivalents make the parasitic dynamics of the system explicit and enable a rigorous study of effects of system parameters and controller gains on the rendering performance, as presented in Section 8. The limitations of rendering performance can also be understood thanks to the passive physical equivalents, which also give concrete examples of the closed-loop system's uncontrollable dynamics (for example, the physical filter's dynamics are uncontrollable during null impedance rendering under VSIC) (for instance, the stiffness of the physical stiffness provides an upper bound on virtual spring rendering under VSIC). Note that these results extend the interaction stability analysis in [17] to S(D)EA and provide easy-to-understand insights into the passivity bounds established.

We have extended this results analysis of  $\text{SDEA}_{K_{fb}}$ , the most common implementations of SEA, where the inherent damping effects on the serial elastic element is ignored in closed-loop force control. We have established the necessary and sufficient conditions for frequency domain passivity of  $\text{SDEA}_{K_{fb}}$  under VSIC and introduced passive physical equivalents for  $\text{SDEA}_{K_{fb}}$  under closed-loop control while rendering Voigt model, ideal spring, and null impedance. The passive physical equivalents not only provide a concrete understanding of uncontrollable dynamics of the closed-loop system, but also enable a fair comparisons of different plants (for instance,  $\text{SDEA}$  vs  $\text{SDEA}_{K_{fb}}$ ) on haptic rendering performance. Furthermore, we have studied a re-

duce order model  $\text{SDEA}_{K_{red}}$ , where the robust inner motion control loop is replaced by a low-pass filter, and established necessary and sufficient passivity conditions and physical equivalents for this model. We have rigorously compared the results derived with  $\text{SDEA}_{K_{red}}$  with the full order models  $\text{SDEA}_{K_{fb}}$  and  $\text{SDEA}$ . We have shown that this simplifying assumption on analysis have simpler results for passivity conditions. We have rigorously shown that if  $w_a \leq \frac{B_m+G_m}{J_m}$  and  $w_a \leq \frac{B_f\alpha}{J_m}$ , necessary and sufficient condition of  $\text{SDEA}_{K_{red}}$  provides sufficient condition of  $\text{SDEA}_{K_{fb}}$ . Also, we have shown that  $\text{SDEA}_{K_{fb}}$  and  $\text{SDEA}_{K_{red}}$  performance is nearly same for Voigt model, ideal spring, and null impedance rendering through Bode plots.

We have demonstrated that passive physical equivalents enable fair comparisons of different plants (for instance, SEA vs SDEA) and different controllers (for instance, P-P vs P-PI) on rendering performance. Unlike the case in numerical comparisons, comparisons of closed-loop system dynamics through passive physical equivalents are informative in that these conclusions can be generalized. These comparisons highlight the impact of different plant and controller terms on the closed-loop rendering performance. Also, through passive physical equivalents, we have rigorously compared the effects of measuring and omitting the damping force on the series elastic element on the closed-loop rendering performance of the system. We have shown that if the force acting on  $B_f$  is used in feedback control ( $\text{SDEA}$ ), this additional information has a beneficial effects on haptic rendering performance and enabling passive Voigt model renderings. On the other hand, if force acting on  $B_f$  is not used in feedback control ( $\text{SDEA}_{K_{fb}}$ ), then  $B_f$  has a parasitic effect on haptic performance and desired Voigt models cannot be passively rendered. We have compared  $\text{SDEA}$  and  $\text{SDEA}_{K_{fb}}$  in terms of their effective impedance and shown that parasitic damping effect is higher for  $\text{SDEA}_{K_{fb}}$ . Furthermore,  $\text{SDEA}_{K_{fb}}$  can passively render stiffer virtual spring, but always with the parasitic damping of  $B_f$ . In addition to them, we have shown that Voigt model cannot be rendered accurately with  $\text{SDEA}_{K_{fb}}$ . Also, the maximum virtual stiffness limit is the physical stiffness for ideal spring rendering which is shown theoretically and experimentally before [39, 41, 46] for SEA and SDEA. However, if there is a damping effect on the physical filter which is not measured,  $\text{SDEA}_{K_{fb}}$  can exceed the physical spring stiffness which can be seen from passivity analysis of  $\text{SDEA}_{K_{fb}}$  and Chapter 8 through Bode plots for different physical system. Furthermore, there exists continuity among realizations; for instance, one can recover the realization of null impedance rendering with SEA under P-P controller from the realization of spring rendering with SDEA under P-PI controller or  $\text{SDEA}_{K_{fb}}$  P-P controller, by setting  $B_f$ ,  $I_m$  and  $K_d$  to zero. Along these lines, the effect of each additional controller or plant dynamics can be rigorously studied. Moreover, these comparisons are symbolic in nature and do not require performance

optimization of each closed-loop system to ensure fairness, as emphasized in [30].

We have also emphasized that passive physical equivalents provide a physical realization of the effective impedance, establishing an intuitive understanding of the effective impedance analysis. For instance, realizations show how a frequency dependent damping effect in the effective impedance analysis can be realized with a serial connection of an inerter with a damper, as in [25]. We have presented passive physical realizations for S(D)EAs under VSIC while null impedance or rendering ideal springs or Voigt model in Table 8.1. It is important to note that, in general, passive physical realizations for a given impedance transfer function are not unique. The necessary conditions may not be easily established through such analysis, as it requires studying feasibility of all passive physical realizations.

We have experimentally validated our theoretical results with real life S(D)EA device. We have verified our theoretical results and we compared passivity bounds and haptic rendering performance for different type of S(D)EAs such as SEA, SDEA,  $SDEA_{K_{fb}}$ , and reduce models of S(D)EAs.

We have also studied model reference for control for SEA during null impedance when controllers are P-P. Controlling SEA with MRFC promises to improve interaction control performance compared to other commonly used controllers, as the knowledge of the model enables feed-forward action to react to inputs more quickly. Furthermore, passivity of MRFC is relatively easy to achieve, simply by overestimating the inertial effects, underestimating the compliance, and keeping the damping compensation bounded. In this study, the controllers of MRFC are considered as P-controllers to keep the closed form analytical solutions easy to follow. The derived frequency domain passivity conditions are informative, as they provide insight on how system parameters affect stability robustness of MRFC.

Our ongoing work include extension of the passivity analysis and passive realization results to S(D)EA under different controllers, such as MRFC and disturbance observer based control proposed in [73].

As part of our future work, we plan to extend passive realizations to less intuitive fractional order systems [27, 28], as physical equivalents are well-defined for fractional order terms and interpretation of these controllers can highly benefit from such physical intuition. Also, our ongoing works include extension of the passivity analysis of SDEA under MRFC to other elementary virtual environments, including linear virtual springs.

## BIBLIOGRAPHY

- [1] N. Hogan, “Impedance control: An approach to manipulation: Part i—theory,” *Journal of Dynamic Systems, Measurement, and Control*, vol. 107, no. 1, pp. 1—7, 1985.
- [2] J. E. Colgate, “The control of dynamically interacting systems,” Ph.D. dissertation, Massachusetts Institute of Technology, 1988.
- [3] R. Unal, G. Kiziltas, and V. Patoglu, “A multi-criteria design optimization framework for haptic interfaces,” in *2008 Symposium on Haptic Interfaces for Virtual Environment and Teleoperator Systems*. IEEE, 2008, pp. 231–238.
- [4] V. Hayward, J. Choksi, G. Lanvin, and C. Ramstein, “Design and multi-objective optimization of a linkage for a haptic interface,” in *Advances in robot kinematics and computational geometry*. Springer, 1994, pp. 359–368.
- [5] C. An and J. Hollerbach, “Dynamic stability issues in force control of manipulators,” in *IEEE International Conference on Robotics and Automation*, vol. 4, 1987, pp. 890–896.
- [6] S. Eppinger and W. Seering, “Understanding bandwidth limitations in robot force control,” in *IEEE International Conference on Robotics and Automation*, vol. 4, 1987, pp. 904–909.
- [7] W. S. Newman, “Stability and performance limits of interaction controllers,” *Journal of Dynamic Systems, Measurement, and Control*, vol. 114, no. 4, pp. 563—570, 1992.
- [8] R. D. Howard, “Joint and actuator design for enhanced stability in robotic force control,” Ph.D. dissertation, MIT, 1990.
- [9] G. A. Pratt and M. M. Williamson, “Series elastic actuators,” in *IEEE/RSJ International Conference on Intelligent Robots and Systems*, vol. 1, 1995, pp. 399–406.
- [10] D. W. Robinson, J. E. Pratt, D. J. Paluska, and G. A. Pratt, “Series elastic actuator development for a biomimetic walking robot,” in *IEEE/ASME International Conference on Advanced Intelligent Mechatronics*, 1999, pp. 561–568.
- [11] J. Hurst, A. Rizzi, and D. Hobbelen, “Series elastic actuation: Potential and pitfalls,” in *International conference on climbing and walking robots*, 2004.
- [12] J. Oblak and Z. Matjačić, “Design of a series visco-elastic actuator for multi-purpose rehabilitation haptic device,” *Journal of Neuroengineering and Rehabilitation*, vol. 8, no. 1, pp. 1–14, 2011.
- [13] E. Garcia, J. C. Arevalo, G. Muñoz, and P. Gonzalez-de Santos, “Combining series elastic actuation and magneto-rheological damping for the control of agile locomotion,” *Robotics and Autonomous Systems*, vol. 59, no. 10, pp. 827–839, 2011.



- [14] M. Laffranchi, N. Tsagarakis, and D. G. Caldwell, "A compact compliant actuator (compact<sup>TM</sup>) with variable physical damping," in *IEEE International Conference on Robotics and Automation*, 2011, pp. 4644–4650.
- [15] M. J. Kim, A. Werner, F. C. Loeffl, and C. Ott, "Enhancing joint torque control of series elastic actuators with physical damping," in *IEEE International Conference on Robotics and Automation*, 2017, pp. 1227–1234.
- [16] J. E. Colgate and N. Hogan, "Robust control of dynamically interacting systems," *International Journal of Control*, vol. 48, no. 1, pp. 65–88, 1988.
- [17] E. Colgate and N. Hogan, "An analysis of contact instability in terms of passive physical equivalents," in *Proceedings of International Conference on Robotics and Automation*, vol. 1, 1989, pp. 404–409.
- [18] M. C. Smith, "Synthesis of mechanical networks: the inerter," *IEEE Transactions on automatic control*, vol. 47, no. 10, pp. 1648–1662, 2002.
- [19] M. Z. Chen and M. C. Smith, "Mechanical networks comprising one damper and one inerter," in *IEEE European Control Conference*, 2007, pp. 4917–4924.
- [20] —, "Restricted complexity network realizations for passive mechanical control," *IEEE Transactions on Automatic Control*, vol. 54, no. 10, pp. 2290–2301, 2009.
- [21] M. Z. Chen, K. Wang, Y. Zou, and J. Lam, "Realization of a special class of admittances with one damper and one inerter," in *IEEE Conference on Decision and Control*, 2012, pp. 3845–3850.
- [22] —, "Realization of a special class of admittances with one damper and one inerter for mechanical control," *IEEE Transactions on Automatic Control*, vol. 58, no. 7, pp. 1841–1846, 2013.
- [23] M. Z. Chen, K. Wang, Z. Shu, and C. Li, "Realizations of a special class of admittances with strictly lower complexity than canonical forms," *IEEE Transactions on Circuits and Systems I: Regular Papers*, vol. 60, no. 9, pp. 2465–2473, 2013.
- [24] M. Z. Chen, K. Wang, Y. Zou, and G. Chen, "Realization of three-port spring networks with inerter for effective mechanical control," *IEEE Transactions on Automatic Control*, vol. 60, no. 10, pp. 2722–2727, 2015.
- [25] J. S. Mehling, J. E. Colgate, and M. A. Peshkin, "Increasing the impedance range of a haptic display by adding electrical damping," in *First Joint Eurohaptics Conference and Symposium on Haptic Interfaces for Virtual Environment and Teleoperator Systems. IEEE World Haptics Conference*, 2005, pp. 257–262.
- [26] N. Colonnese, A. F. Siu, C. M. Abbott, and A. M. Okamura, "Rendered and characterized closed-loop accuracy of impedance-type haptic displays," *IEEE Transactions on Haptics*, vol. 8, no. 4, pp. 434–446, 2015.

- [27] O. Tokatli and V. Patoglu, “Stability of haptic systems with fractional order controllers,” in *IEEE/RSJ International Conference on Intelligent Robots and Systems*, 2015, pp. 1172–1177.
- [28] ———, “Using fractional order elements for haptic rendering,” *Springer Proc. in Advanced Robotics Robotics Research*, pp. 373–388, 2018.
- [29] Y. Aydin, O. Tokatli, V. Patoglu, and C. Basdogan, “Stable physical human-robot interaction using fractional order admittance control,” *IEEE Transactions on Haptics*, vol. 11, no. 3, pp. 464–475, 2018.
- [30] ———, “A computational multicriteria optimization approach to controller design for physical human-robot interaction,” *IEEE Transactions on Robotics*, vol. 36, no. 6, pp. 1791–1804, 2020.
- [31] W. S. Newman and Y. Zhang, “Stable interaction control and coulomb friction compensation using natural admittance control,” *Journal of robotic systems*, vol. 11, no. 1, pp. 3–11, 1994.
- [32] G. D. Glosser and W. S. Newman, “The implementation of a natural admittance controller on an industrial manipulator,” in *Proceedings of the IEEE International Conference on Robotics and Automation*, 1994, pp. 1209–1215.
- [33] J. S. Hart and G. Niemeyer, “Absolutely stable model-based 2-port force controller for telerobotic applications,” *International Journal of Robotics Research*, vol. 33, no. 6, pp. 847–865, 2014.
- [34] G. Pratt, P. Willisson, C. Bolton, and A. Hofman, “Late motor processing in low-impedance robots: impedance control of series-elastic actuators,” in *American Control Conference*, 2004, pp. 3245–3251.
- [35] G. Wyeth, “Control issues for velocity sourced series elastic actuators,” in *Proceedings of the Australasian Conference on Robotics and Automation*, 2006, pp. 1–6.
- [36] ———, “Demonstrating the safety and performance of a velocity sourced series elastic actuator,” in *IEEE International Conference on Robotics and Automation*, 2008, pp. 3642–3647.
- [37] H. Vallery, R. Ekkelenkamp, H. Van Der Kooij, and M. Buss, “Passive and accurate torque control of series elastic actuators,” in *IEEE/RSJ International Conference on Intelligent Robots and Systems*, 2007, pp. 3534–3538.
- [38] H. Vallery, J. Veneman, E. Van Asseldonk, R. Ekkelenkamp, M. Buss, and H. Van Der Kooij, “Compliant actuation of rehabilitation robots,” *IEEE Robotics and Automation Magazine*, vol. 15, no. 3, pp. 60–69, 2008.
- [39] N. L. Tagliamonte and D. Accoto, “Passivity constraints for the impedance control of series elastic actuators,” *Institution of Mechanical Engineers, Part I: Journal of Systems and Control Engineering*, vol. 228, no. 3, pp. 138–153, 2014.

- [40] A. Calanca, R. Muradore, and P. Fiorini, “Impedance control of series elastic actuators: Passivity and acceleration-based control,” *Mechatronics*, vol. 47, pp. 37–48, 2017.
- [41] F. E. Tosun and V. Patoglu, “Necessary and Sufficient Conditions for the Passivity of Impedance Rendering with Velocity-Sourced Series Elastic Actuation,” *IEEE Transactions on Robotics*, vol. 36, no. 3, pp. 757–772, 2020.
- [42] A. Otaran, O. Tokatli, and V. Patoglu, “Physical human-robot interaction using HandsOn-SEA: An educational robotic platform with series elastic actuation,” *IEEE Transactions on Haptics*, vol. 14, no. 4, pp. 922–929, 2021.
- [43] C. U. Kenanoglu and V. Patoglu, “Passivity of series elastic actuation under model reference force control during null impedance rendering,” *IEEE Transactions on Haptics*, vol. 15, no. 1, pp. 51–56, 2022.
- [44] M. Focchi, G. A. Medrano-Cerda, T. Boaventura, M. Frigerio, C. Semini, J. Buchli, and D. G. Caldwell, “Robot impedance control and passivity analysis with inner torque and velocity feedback loops,” *Control Theory and Technology*, vol. 14, no. 2, pp. 97–112, 2016.
- [45] U. Mengilli, U. Caliskan, Z. O. Orhan, and V. Patoglu, “Two-port analysis of stability and transparency in series damped elastic actuation,” *CoRR*, 2020. [Online]. Available: <https://arxiv.org/abs/2011.00664>
- [46] U. Mengilli, Z. O. Orhan, U. Caliskan, and V. Patoglu, “Passivity of series damped elastic actuation under velocity-sourced impedance control,” in *IEEE World Haptics Conference*, 2021, pp. 379–384.
- [47] R. Ortega, J. A. L. Perez, P. J. Nicklasson, and H. J. Sira-Ramirez, *Passivity-based control of Euler-Lagrange systems: mechanical, electrical and electromechanical applications*. Springer Science & Business Media, 2013.
- [48] M. Z. Chen, C. Papageorgiou, F. Scheibe, F.-c. Wang, and M. C. Smith, “The missing mechanical circuit element,” *IEEE Circuits and Systems Magazine*, vol. 9, no. 1, pp. 10–26, 2009.
- [49] R. M. Foster, “A reactance theorem,” *Bell System technical journal*, vol. 3, no. 2, pp. 259–267, 1924.
- [50] O. Brune, “Synthesis of a finite two-terminal network whose driving-point impedance is a prescribed function of frequency,” Ph.D. dissertation, Massachusetts Institute of Technology, 1931.
- [51] R. Bott and R. Duffin, “Impedance synthesis without use of transformers,” *Journal of Applied Physics*, vol. 20, no. 8, pp. 816–816, 1949.
- [52] R. Kalman, *Perspectives in Mathematical System Theory, Control, and Signal Processing*. Berlin, Heidelberg: Springer, 2010, vol. 398, ch. Old and new directions of research in system theory, p. 3.

- [53] J. Z. Jiang and M. C. Smith, “Regular positive-real functions and five-element network synthesis for electrical and mechanical networks,” *IEEE Transactions on Automatic Control*, vol. 56, no. 6, pp. 1275–1290, 2011.
- [54] ———, “Series-parallel six-element synthesis of biquadratic impedances,” *IEEE Transactions on Circuits and Systems I: Regular Papers*, vol. 59, no. 11, pp. 2543–2554, 2012.
- [55] T. H. Hughes and M. C. Smith, “On the minimality and uniqueness of the bott–duffin realization procedure,” *IEEE Transactions on Automatic Control*, vol. 59, no. 7, pp. 1858–1873, 2014.
- [56] T. H. Hughes, “Why rlc realizations of certain impedances need many more energy storage elements than expected,” *IEEE Transactions on Automatic Control*, vol. 62, no. 9, pp. 4333–4346, 2017.
- [57] ———, “Minimal series–parallel network realizations of bicubic impedances,” *IEEE Transactions on Automatic Control*, vol. 65, no. 12, pp. 4997–5011, 2020.
- [58] A. Morelli and M. C. Smith, *Passive Network Synthesis: An Approach to Classification*. SIAM, 2019.
- [59] S. M. Hughes T.H., Morelli A., *Electrical Network Synthesis: A Survey of Recent Work*, ser. Lecture Notes in Control and Information Sciences. Springer, 2018, ch. Emerging Applications of Control and Systems Theory, pp. 281–293.
- [60] B. Hannaford, “A design framework for teleoperators with kinesthetic feedback,” *IEEE Transactions on Robotics and Automation*, vol. 5, no. 4, pp. 426–434, 1989.
- [61] K. Hashtrudi-Zaad and S. E. Salcudean, “Analysis of Control Architectures for Teleoperation Systems with Impedance/Admittance Master and Slave Manipulators,” *The International Journal of Robotics Research*, vol. 20, no. 6, pp. 419–445, 2001.
- [62] J. Colgate and J. Brown, “Factors affecting the Z-Width of a haptic display,” in *IEEE International Conference on Robotics and Automation*, 1994, pp. 3205–3210.
- [63] M. Dohring and W. Newman, “The passivity of natural admittance control implementations,” in *IEEE International Conference on Robotics and Automation*, vol. 3, 2003, pp. 3710–3715.
- [64] F. F. Kuo, *Network Analysis and Synthesis*. John Wiley & Sons, 1962.
- [65] A. Kamadan, G. Kiziltas, and V. Patoglu, “Co-design strategies for optimal variable stiffness actuation,” *IEEE/ASME Transactions on Mechatronics*, vol. 22, no. 6, pp. 2768–2779, 2017.
- [66] ———, “A systematic design selection methodology for system-optimal compliant actuation,” *Robotica*, vol. 37, no. 4, pp. 656–674, 2019.

- [67] S. S. Rao and F. F. Yap, *Mechanical vibrations*. Addison-wesley New York, 1995, vol. 4.
- [68] U. Caliskan, A. Apaydin, A. Otaran, and V. Patoglu, “A series elastic brake pedal to preserve conventional pedal feel under regenerative braking,” in *IEEE/RSJ International Conference on Intelligent Robots and Systems*, 2018, pp. 1367–1373.
- [69] U. Caliskan and V. Patoglu, “Efficacy of haptic pedal feel compensation on driving with regenerative braking,” *IEEE Transactions on Haptics*, vol. 13, no. 1, pp. 175–182, 2020.
- [70] Z. Yi, Z. Hong, and S. Hui-zhi, “Research of the orthoscopic permanent magnet eddy current damper in magnetic stage,” in *2010 International Conference on Computer Application and System Modeling (ICCASM 2010)*, vol. 14. IEEE, 2010, pp. V14–354.
- [71] S.-M. Jang, S.-H. Lee, and S.-S. Jeong, “Characteristic analysis of eddy-current brake system using the linear halbach array,” *IEEE Transactions on Magnetics*, vol. 38, no. 5, pp. 2994–2996, 2002.
- [72] T. K. Ghaffari and J. Kövecses, “A high-performance velocity estimator for haptic applications,” in *2013 World Haptics Conference (WHC)*. IEEE, 2013, pp. 127–132.
- [73] K. Kong, J. Bae, and M. Tomizuka, “Control of rotary series elastic actuator for ideal force-mode actuation in human–robot interaction applications,” *IEEE/ASME Transactions on Mechatronics*, vol. 14, no. 1, pp. 105–118, 2009.